

From Micro to Macro: A Study of Human Brain Structure Based on Diffusion MRI and Neuronal Networks

BY

JOHNSON JONARIS GADELKARIM
B.S., CAIRO University, EGYPT, 2004
M.S., University of Illinois at Chicago, Chicago, 2013

THESIS

Submitted as partial fulfillment of the requirements
for the degree of Doctor of Philosophy in Electrical and Computer Engineering
in the Graduate College of the
University of Illinois at Chicago, Chicago, 2013

Chicago, Illinois

Defense Committee:

Dan Schonfeld, Chair & Advisor
Alex Leow, Co-Advisor
Richard Magin, Co-Advisor
Anand Kumar, Psychiatry
Natasha Devroye

To my mother, *Nawal*, my wife *Germaine*, and my daughter *Carla*.

ACKNOWLEDGMENTS

First, I would like to express my deep gratitude to my advisors, Dan Schonfeld, Alex Leow and Richard Magin, for supervising my work and sharing their expertise during the past four years. I would also like to thank Anand Kumar for having me in his research team and giving me the opportunity to work in the prestigious and stimulating Psychiatric Institute. I am also extremely grateful to Natasha Devroye for her participation in the committee. I would also like to thank Olusola Ajilore for reviewing my thesis and taking the time to make insightful remarks and suggestions on my work.

Many people have contributed to the work presented in this thesis and I want to thank them here: Olusola Ajilore, for introducing me to the field of Connectomics, Mark Meerschaert, for his valuable mathematical inputs and for the long discussions about anomalous diffusion. Aifeng Zhang and Liang Zhan, for helping me process the data, Shaolin Yang, for his help in the acquisition of the diffusion data, Carson Ingo, for his useful comments on diffusion data processing. I also want to thank my collaborators: Jamie Feusner, Donatello Arienzo, Paul Thompsen, Tom Barrick, Silvia Capuani, Marco Palombo, and Teena Moody.

I will not forget all the friends I have made during these years: Ahmed Morsi, Bishoy Alphonse, Gergis Shenouda, Sherif Dawood and family, Nasser Boshra and family, Reda Shaker and family, Maged Saad and family, Samuel Botros and family, Fadel Azer and family, Sameh Soliman and family, and Mina Khalil.

I would also like to thank my mother and brothers for all her efforts they made for me. Finally, I would like to thank my wife, Germaine, for her love and support day-to-day during these years.

J.G.

TABLE OF CONTENTS

<u>CHAPTER</u>	<u>PAGE</u>
I. INTRODUCTION	1
1.1 Background	1
1.2 Thesis Organization.....	3
II. THE HUMAN BRAIN.....	5
2.1 The Human Brain	5
2.2 The White Matter	9
2.3 Conclusion.....	11
III. BASIC PRINCIPLES OF DIFFUSION MRI.....	12
3.1 Introduction	12
3.2 Theory of Classical Diffusion	12
3.3 Nuclear Magnetic Resonance and Diffusion Magnetic Resonance Imaging	15
3.3.1 Pulse Gradient Spin Echo	18
3.3.2 The Bloch-Torrey Equation	21
3.3.3 Diffusion-Weighted Imaging and the Apparent Diffusion Coefficient	24
3.3.4 Diffusion Tensor Imaging.....	25
3.3.5 High Angular Resolution Diffusion Imaging.....	29
3.3.5.1 Diffusion Spectrum Imaging	29
3.3.5.2 Single Shell HARD Imaging	31
3.3.5.2.1 Model-Based Approaches	31
3.3.5.2.2 Model-Free Approaches	34
3.4 Conclusion.....	35
IV. ANOMALOUS DIFFUSION	37
4.1 Introduction	37
4.2 Continuous Time Random Walk model.....	39
4.2.1 Long Jumps: Super Diffusion (Levy Flights):	42
4.2.2 Long rests: Sub Diffusion:	43
4.3 Anomalous Diffusion Magnetic Resonance Imaging.....	46
4.3.1 Isotropic Models	46
4.3.2 Anisotropic Models.....	48
4.4 Conclusion.....	50
V. NEURONAL NETWORKS.....	51
5.1 Introduction	51
5.2 Graph Theoretical Concepts for Network Analysis	52
5.3 Community Structure: A Literature Review	58
5.3.1 Traditional Methods.....	58
5.3.2 Hierarchical Clustering	59
5.3.3 Divisive Algorithms.....	59
5.3.4 Modularity Optimization.....	60
5.3.3.1 Greedy Algorithms.....	61
5.3.3.2 Simulated Annealing	62
5.3.3.3 Spectral Optimization.....	62
5.3.3.4 Limitations of Modularity	63
5.4 Conclusion.....	64

TABLE OF CONTENTS (continued)

VI. ANISOTROPIC ANOMALOUS DIFFUSION MODELS	65
6.1 Introduction	65
6.2 Anisotropic Fractional Order Anomalous Diffusion Models	65
6.2.1 Model I	65
6.2.1.1 Model I: Theory.....	66
6.2.1.2 Model I: Methods	68
6.2.1.3 Model I: Results	68
6.2.1.4 Model I: Discussion.....	77
6.2.2 Model II.....	78
6.2.2.1 Model II: Theory	79
6.2.2.1.1 Model II: Fractional Vector Calculus.....	79
6.2.2.1.2 Model II: Multidimensional Fractional Diffusion Equation.....	81
6.2.2.1.3 Model II: Fractional Order Bloch-Torrey Equation	82
6.2.2.2 Model II: Methods.....	84
6.2.2.3 Model II: Results	85
6.2.2.4 Model II: Discussion	89
6.3 Discussion	92
6.4 Conclusion.....	93
VII. USING THE TENSOR DISTRIBUTION FUNCTION	94
7.1 Introduction	94
7.2 Background on Tractography	94
7.3 TDF-TRACT Tractography Algorithm.....	97
7.4 Tractography Results.....	100
7.4.1 Graphical User Interface for TDF-Tractography.....	100
7.4.2 Tractography of the Brain Stem and Cerebellar Peduncles.....	100
7.4.3 Constructing the Dorsal Column-Medial Lemniscus (DCML) System	104
7.4.4 Constructing the Cortico-Spinal Tracts	104
7.4.5 Constructing the Main Cerebellar Efferent Fibers	104
7.4.6 Constructing the Spinocerebellar and Rubrocerebellar Pathway	105
7.4.7 Construction of the Cortico-Ponto-Cerebellar Pathway.....	105
7.5 Circular Standard Deviation	107
7.6 Conclusion.....	112
VIII. EXTRACTING THE BRAIN COMMUNITY STRUCTURES	113
8.1 Introduction	114
8.2 Methods.....	115
8.2.1 Constructing Brain Connectivity Network.....	115
8.2.2 New Graph Metrics	117
8.2.3 Path-Length Associated Community Estimation	118
8.2.3.1 Introducing Ψ^{PL}	118
8.2.3.2 Community Structure Estimation	118
8.2.3.3 Assessing group-level Community Structure Differences	119
8.2.3.4 Statistical Analysis	120
8.2.3.5 Testing for Frequency of Occurrence.....	120
8.3 Results	121
8.3.1 Applying the New Graph Metrics to Bipolar Disorder	122
8.3.2 Comparison with Q Modularity.....	124
8.3.3 Optimal Level of Hierarchical Reconstruction.....	125
8.3.4 Community Structure Alterations in Bipolar Disorder.....	126

TABLE OF CONTENTS (continued)

8.3.5	Community Structure Alterations in Depression Disorder.....	130
8.4	Discussion	132
8.5	Conclusion.....	133
IX. CONCLUSIONS AND FUTURE RESEARCH		134
APPENDICES		136
Appendix A		137
Appendix B.....		138
Appendix C.....		139
Appendix D		140
Appendix E.....		150
Appendix F		152
CITED LITERATURE.....		166
VITA.....		175

LIST OF TABLES

<u>TABLE</u>	<u>PAGE</u>
I. MATHEMATICAL NOTATION USED IN THIS THESIS.....	4
II. TIMELINE DESCRIBING THE HISTORY OF DIFFUSION MRI.	18
III. MATHEMATICAL DEFINITIONS OF NETWORK METRICS. SHADING GROUPS METRICS OF SAME FAMILY.	55
IV. MEAN AND STANDARD DEVIATION OF THE OBTAINED PARAMETERS USING THE MODEL IN EQUATION 6.8 AS WELL AS EIGENVALUES, FA AND MD ANALYSIS OF THE \mathbf{D} AND Ψ TENSORS IN THE SELECTED ROIS HIGHLIGHTED IN FIGURE 21.	76
V. MEAN AND STANDARD DEVIATION SUMMARY OF THE FITTED PARAMETERS AND THE COMPUTED METRICS ACROSS THE SLICE PRESENTED IN FIGURE 28 AND FIGURE 29.....	88
VI. INTER-HEMISPHERIC INTEGRATION ANALYSES IN THE FRONTAL, TEMPORAL, PARIETAL AND OCCIPITAL LOBES. THIS TABLE SHOWS THE MEAN AND STANDARD DEVIATION OF LOBAR INTER-HEMISPHERIC PATH LENGTH AND EFFICIENCY. ONLY GROUP DIFFERENCES REACHING STATISTICAL SIGNIFICANCE ARE SHOWN (BONFERRONI CORRECTION WITH A TOTAL OF 16 TESTS; CUT-OFF P VALUE $0.05/16=0.003$).....	123
VII. LIST OF NODES WHICH SHOWED SIGNIFICANT LOWER CONSISTENCY IN DEPRESSION RELATIVE TO HEALTHY CONTROLS AT $P < 0.01$ (UNCORRECTED). THE TABLE SHOWS MEAN AND STANDARD DEVIATION VALUES USING 2-SAMPLE T-TEST (FOR Z), AND THEIR CORRESPONDING P VALUES.	130
VIII.SOME FUNCTIONS AND THE CORRESPONDING FOURIER DERIVATIVE.....	143
IX. SOME FUNCTIONS AND THE CORRESPONDING LIOUVILLE DERIVATIVE.....	145
X. SOME FUNCTIONS AND THE CORRESPONDING RIEMANN DERIVATIVE.....	146
XI. SOME FUNCTIONS AND THE CORRESPONDING LIOUVILLE-CAPUTO DERIVATIVE	146
XII. SOME FUNCTIONS AND THE CORRESPONDING CAPUTO DERIVATIVE.....	147
XIII.SOME FUNCTIONS AND THE CORRESPONDING CAPUTO DERIVATIVE.....	148
XIV.SOME FUNCTIONS AND THE CORRESPONDING CAPUTO DERIVATIVE.....	149
XV. LIST OF BRAIN REGIONS AS DEFINED BY THE FREESURFER SOFTWARE.....	150

LIST OF FIGURES

<u>FIGURE</u>	<u>PAGE</u>
1. Nerve cell.....	6
2. Spinal gray and white matter cells, and a coronal slice of the human brain	7
3. The four lobes of the cerebral cortex and the cerebellum	8
4. The corpus callosum	10
5. The corticospinal tract.....	11
6. Diffusion of the molecules of dye in water.....	13
7. Precession of the hydrogen atom in the presence of a magnetic field	17
8. Schematic of the PGSE pulse sequence	21
9. Relaxation trajectory of the hydrogen atom.....	23
10. Diffusion ellipsoid and water Brownian motion along the fibers	28
11. Different anisotropy cases.....	28
12. Metrics derived from the diffusion tensor.....	29
13. Diffusion orientation distribution function and the apparent diffusion coefficient profile.....	30
14. Monoexponential estimate of the diffusion signal decay	38
15. A multi-scale look at neural tissue	39
16. Comparison of the trajectories of different diffusion schemes	45
17. Results of the fitted \mathbf{A} and $\mathbf{\Gamma}$ tensors in the Hall and Barrick model	49
18. Graph theoretic concepts	55
19. The diffusion tensor elements of an axial slice through the optical tracts.	70
20. Selected regions of interest highlighted on the b_0 image.....	71
21. Spatially resolved maps of the fitted parameters in Model I.....	72
22. The logarithm of the diagonal elements in $\mathbf{\Psi}$	73

LIST OF FIGURES (continued)

23. Maps of the principal eigenvector and the largest eigenvalue of the Ψ and \mathbf{D} tensors	74
24. A colormap using the fractional order parameters and the diagonal unit preserving constants....	75
25. Fitting curves to the stretched exponential model.....	75
26. Relationship between laboratory frame, DTI, and analysis in Model II coordinate systems.....	84
27. Spatially resolved maps of the unit preserving constants and the operational order parameters ..	86
28. Mean diffusivity, fractional anisotropy, mean anomalous exponent, and anomalous anisotropy	87
29. Contour plot of different versions of a 2D version of $P(\mathbf{r}, t)$	91
30. Streamline tractography	98
31. The GUI for the TDF-Tract program	102
32. The reconstructed tensor orientation distribution.....	103
33. TDF-tractography results	106
34. Visualization of multiple reconstructed fibers	107
35. The averaged FA^{DTI} values (second panel) with respect to the geodesic distance.....	110
36. FA^{TDF} versus FA^{DTI} for both low and high resolution data	111
37. CSD and average FA^{DTI} plotted against the geodesic distance	112
38. Pipeline used to generate structural brain networks.....	116
39. Community structure obtained for the Zachary club network	125
40. The average separability across	126
41. Binary trees showing mean community structures via the proposed metric	128
42. The frequencies at which several brain regions belong to the same community	129
43. Binary trees showing mean community structures via the proposed metric	131

LIST OF ABBREVIATIONS

3D	3 dimensional
AA ^{β}	Anomalous Anisotropy
AAL	Automated Anatomical Labeling
ADC	Apparent Diffusion Coefficient
AD	Anomalous Diffusion
aFA	Anomalous Fractional Anisotropy
BOLD	Blood Oxygen Level Dependent
CC	Corpus Callosum
CC	Clustering Coefficient
CNS	Central Nervous System
CPC	Cortico-Ponto-Cerebellar
CPL	Characteristic Path Length
CSD	Circular Standard Deviation
CSF	Cerebral Spinal Fluid
CST	Corticospinal Tract
CTRW	Continuous Time Random Walk
DOT	Diffusion Orientation Transform
DRTC	Dentate-Rubro-Thalamo-Cortical
DSI	Diffusion Spectrum Imaging
DT	Diffusion Tensor
DTI	DT Imaging
DW	Diffusion Weighted
DWI	DW Images
FA	Fractional Anisotropy

LIST OF ABBREVIATIONS (continued)

FACT	Fiber Assignment by Continuous Tracking
FDE	Fractional Diffusion Equation
FID	Free Induction Decay
FRT	Funk-Radon Transform
gDTI	Generalized DTI
GM	Gray Matter
HARDI	High Angular Resolution Diffusion Imaging
HOT	High Order Tensor
ICP	Inferior Cerebellar Peduncle
IID	Identically Independent Distributed
NMR	Nuclear Magnetic Resonance
NP	Non-deterministic Polynomial
MAE	Mean Anomalous Exponent
MCP	Middle Cerebellar Peduncle
MRI	Magnetic Resonance Imaging
MSD	Mean Squared Displacement
ODF	Orientation Distribution Function
PAS	Persistent Angular Structure
PDE	Partial Differential Equation
PDF	Probability Density Function
PDO	Pseudo-differential Operator
PGSE	Pulse Gradient Spin Echo
PLACE	Path Length Associated Community Estimation
PNS	Peripheral Nervous System

LIST OF ABBREVIATIONS (continued)

QBI	Q-Ball Imaging
QSI	Q-Space Imaging
RA	Relative Anisotropy
RF	Radio Frequency
ROI	Region of Interest
SA	Simulated Annealing
SCP	Superior Cerebellar Peduncle
SH	Spherical Harmonics
SNR	Signal to Noise Ratio
STR	Streamline Tracking
TDF	Tensor Distribution Function
WM	White Matter

SUMMARY

A study on the human brain is carried out through the use of diffusion weighted magnetic resonance imaging. The brain is studied at three different levels: micro, mid, and macro. At the micro-level, we utilize the theory of continuous time random walk to describe the anomalous diffusive behavior of water molecules in different brain tissues. This behavior is measured through multiple b -value diffusion weighted MRI experiments. Two anisotropic models were derived through the introduction of fractional calculus into the Bloch-Torrey equation. The obtained models are used to describe the complex structure of the brain white and gray matter tissues through the introduction of new biometrics. The models allow the quantification of the tortuosity and porosity of the brain tissues in different directions.

At the mid-level, a recent model, the tensor distribution function, is used to extract the brain white matter fiber tracts. A new algorithm is designed to extract different complex fibers in the brain. The algorithm is able to solve the fiber crossing problem at many locations. Moreover, a new metric is suggested to measure fiber incoherence. The measure is then compared to the traditional metric, fractional anisotropy, derived from the classical diffusion tensor model.

At the macro-level, the brain network community structure is studied. A new metric to extract the modular structure of networks is derived. The metric is then applied on brain networks to extract the human connectome community structure. Using the extracted connectome community structure, a framework is designed to detect alterations on the nodal and modular levels occurring in group studies. The framework is then applied on two datasets, bipolar and depression. Significant results were found in agreement with previous clinical studies revealing the importance of the modular analysis of the human connectome.

I. INTRODUCTION

1.1 Background

The human brain is considered as being one of the most complex systems ever studied. Acquiring information about the brain's anatomy is a challenging task, extracting the neuronal architecture and information about the brain white matter (WM) structure is even harder. Old methods have used dissection in order to gain access to the WM (Dejerine and Dejerine-Klumpke 1895; Gray 1936). Nowadays, diffusion weighted (DW) - magnetic resonance imaging (MRI) is considered as being the state of the art technique capable of non-invasively extracting information about the brain's WM structure. DW-MRI is based on the diffusion of water molecules. The water diffusion is isotropic in mediums with no obstacles or walls. In mediums with restricting walls and obstacles, such as the human brain WM, water molecules diffuses anisotropically and tends to be restricted by the surrounding obstacles. Using DW-MRI measurements, we are capable of describing the underlying structure of the brain WM. In this thesis, we are going to describe the human brain on three levels: micro, mid and macro.

An important task in the analysis of the acquired DW-MRI measurements is the choice of a mathematical model to describe the water diffusion. The very first model to be used in the mid 80's (Le Bihan et al. 1986) was a one dimensional *Gaussian* model. Then, a three dimensional (3D) *Gaussian* model have been proposed by Basser et al. (Basser et al. 1993; Basser et al. 1994; Basser et al. 1994) and named diffusion tensor imaging (DTI). This model has the capability of describing the main diffusion direction of water. The model assumes a 3D *Gaussian* distribution for the average diffusion of water molecules. Despite of its usefulness in describing many of the brain WM fibers pathways, it possesses a limitation manifested in the limited capabilities of resolving crossing fibers. This limitation is mainly due to the low resolution of the acquired DW-MRI signal. DW-MRI signal have a resolution between 1 to 8 mm³, while white matter fibers have diameters below 30 μ m (Poupon 1999). The existence of crossing fibers within the same voxel is then inevitable. In fact, it is now estimated to be more than one third of the imaged voxels of the human brain WM (Behrens et al. 2007). DTI limitations were the motivation to develop a family of techniques identified as

high angular resolution diffusion imaging (HARDI). In HARDI techniques, many DW signals are acquired for the same voxel and a reconstruction model is chosen to extract the fibers directions at that voxel.

Diffusion is usually described by Fick's second law which states that the rate of change of the diffusing fluid concentration is directly proportional to its laplacian and the constant of proportionality is called the *diffusion coefficient* D (mm^2/s). In that framework, diffusion depends linearly on time. This type of diffusion is called normal, *Gaussian* or *Brownian* diffusion which is previously used to model DTI. When diffusion depends non-linearly on time, we call it *anomalous diffusion* (AD). AD is usually related to diffusion in porous and complex mediums. DTI and HARDI assume that the water molecules diffusion in the human brain belongs to the non-anomalous type. Recently, researchers started to exploit the anomaly of diffusion in the human brain in order to obtain a better description of the fractal-like structure as well as the porosity of the brain tissues. Simple isotropic models were introduced by Bennett et al. (Bennett et al. 2003) and Magin et al. (Magin et al. 2008). Anisotropic models were also proposed by Hall & Barrick (Hall and Barrick 2012), and De Santis et al. (De Santis et al. 2011). However, to date, the current anisotropic models used to describe AD in the human brain do lack mathematical derivation and are presented as pragmatic models. At the micro-level, we present in this thesis two 3D models based on the modification of the Bloch-Torrey equation using fractional calculus. The models try to describe and quantify the complexity of the human brain tissues. They introduce new biometrics and prove that the AD is anisotropic.

Extracting the brain WM fibers is called *tractography*. This process tries to reconstruct the brain neural tracts as well as known fiber bundles and visualizes them using streamline tubes. At the mid-level, we are going to exploit in this thesis a recently presented HARDI reconstruction method known as tensor distribution function (TDF) (Leow et al. 2009) and use it for tractography. We are also going to study the benefits of TDF over DTI by comparing the DTI-based anisotropy metric – fractional anisotropy (FA) – with a newly TDF-based constructed one.

Tractography results can be used to extract the brain connectivity network which describes the topological structure and connections between the different gray matter (GM) regions. The brain connectivity network, also called *connectome*, was first introduced by Sporns et al. (Sporns et al. 2005). A brain structural connectome consists of *nodes* which represent GM regions and *edges* connecting nodes which represent WM

fibers. Describing the brain as a network has allowed us to use many mathematical tools from the field of graph theory to analyze it. One feature of brain networks is their “*community structure*” properties in which nodes may be grouped into different communities. This property allows us to extract the topological organization of the network and to partition it into a set of non-overlapping *communities* (also called *modules* or *clusters*). At the macro-level, we present in this thesis a new framework to extract the different brain communities and assess differences which might occur in neuropsychiatric diseases. The framework is named “Path Length Associated Community Estimation” (PLACE) and it is based on a new quality function introduced to assess the goodness of the extracted communities.

1.2 Thesis Organization

This thesis is organized in three parts. The first part includes this introduction and a brief description of the human brain in chapter 2. The second part (chapters 3-5) covers briefly the physics of diffusion as well as DW-MRI history and the different models used to describe normal diffusion in brain tissues (chapter 3). In chapter 4, we introduce the physics of AD and its relation to DW-MRI. We state different models used to describe AD in brain tissues. In chapter 5, we introduce the field of graph theory used to analyze brain networks with an emphasis on community structure extraction techniques. In the last part (chapters 6-10), we introduce the contributions of this thesis. First, in chapter 6, we present two new multi-dimensional fractional order models for the Bloch-Torrey equation. We show that AD is anisotropic in brain tissues. Second, in Chapter 7, we present the new tractography technique, and we introduce a new biomarker, the circular standard deviation (CSD) which we use to proof the dependence of DTI-based FA metric on fiber incoherence. Finally, in chapter 8, we present new graph metrics designed to measure the integration of left and right hemispheres of the brain and its application on bipolar disorder. We also present the new framework: PLACE which is validated through its application to brain networks extracted from bipolar disorder and depression. Changes in communities were assessed and results were consistent with previous clinical findings. Conclusions and future research are stated in chapter 10. Mathematical notations used in this thesis are presented in Table I.

Table I: Mathematical notation used in this thesis.

x	a scalar (italic)
\mathbf{r}	a vector (bold italic)
\mathbf{D}	a matrix (bold)
$\mathbf{r} = (x \ y \ z)^T$	a vector made out of 3 components: x y and z
$(.)^T$	transpose
$ x $	absolute value of scalar x
$\ \mathbf{r}\ $	Euclidian norm of a vector
$ \mathbf{D} $	determinant of a matrix \mathbf{D}
$\mathbf{v} \cdot \mathbf{w}$	scalar product of two vectors
$f(x)$	scalar valued function of a scalar
$f(\mathbf{x})$	scalar valued function of a vector
$\mathbf{f}(x)$	vector valued function of a scalar
$\mathbf{f}(\mathbf{x})$	vector valued function of a vector
\mathbb{R}^d	the space of d -tuples of reals $\{x_1 \dots x_d\}$
$\int \dots d_d \mathbf{x}$	the integration over multiple tuples: $\int_{\mathbb{R}^d} \dots dx_1 \dots dx_d$

II. THE HUMAN BRAIN

2.1 The Human Brain

The brain has been under extensive study for decades. It is part of the human nervous system and plays the central role in that system. The human nervous system consists of two parts: the central nervous system (CNS) which includes the brain and the spinal cord, and the peripheral nervous system (PNS) which consists of a complex network of neural cells that connects the limbs and organs to the CNS. The brain is responsible for the motor control, regulation and coordination of all our limbs and organs. It is also responsible for the perception of the external world through the processing of sensory information. Moreover, it also manages our abilities of reasoning, planning, decision-making and abstract-thought.

The main building block of the brain is the *neuron* (nerve cell) portrayed in Figure 1a. The neuron receives signals from other neurons through input terminals called *dendrites*. Dendrites are thin extensions that arise from the cell body, also called the *soma*, often extending for hundreds of micrometers and branching multiple times. The neuron also emits signals to other neurons as electrochemical waves or pulses travelling along thin fibers called *axons*. Axons are cable like structures covered by a dielectric material called *myelin* which forms a layer around it, the *myelin sheath*. This layer increases the transmission speed of electrical signals across the axon. A signal, when emitted, causes the release of chemicals called *neurotransmitters* at the axon's terminating point: *synapse* (Figure 1b). The synapse is a narrow space between the neuron and other neurons or a muscle that can be seen as a communication end (Dayan and Abbott 2001). It permits the neuron to send signals to another cell. A neuron can have over 1000 dendritic branches and around 10000 synaptic connections with other neurons. There are about 80 to 100 billion neurons in the human brain and 100 trillion synapses; they form a complex network of connections (Herculano-Houzel 2009).

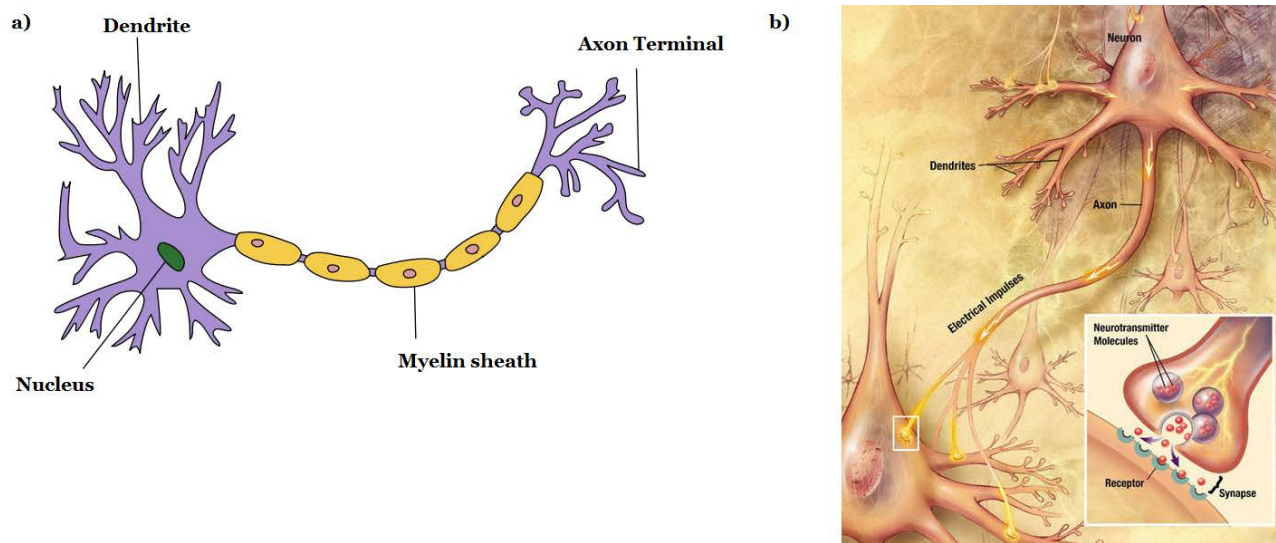


Figure 1: a) Nerve cell, b) Electrical signal propagating to the next cell through the axon and dendrites, notice the chemical reaction at the synapse. Both figures were adapted from Wikipedia.

On a larger scale, the human brain is made out of several elements. The *cerebrospinal fluid* (CSF) surrounds the brain and exists also in the ventricle system which is shown in Figure 2. It acts as a “cushion” providing the necessary mechanical and immunological protection. The brain is made out of two main types of tissues: the *gray* and *white* matters (Figure 2). The WM consists of the neuron axons. Bundles of axons are called fiber tracts. The GM is made out of the neuronal cell bodies and is full of capillary blood vessels which give it the gray-brown color. Globally, we can consider that the WM acts as a network of cables which interconnects the different regions of the GM.

On a macroscopic scale, the brain consists of three major parts: the *cerebrum*, the *cerebellum* and the *brain stem* shown in Figure 3. The cerebrum is made out of the two cerebral hemispheres separated by the central fissure and interconnected through a dense bundle of WM fibers called the corpus callosum (CC). The two hemispheres form the largest part of the human brain. The outer shell of the cerebrum, also called the cerebral cortex, is made out of highly folded GM tissues, the folding helps to increase the surface area in the

limited volume of the human skull. The cortex contains regions responsible for sensory, control of voluntary movement, speech and cognition functions.

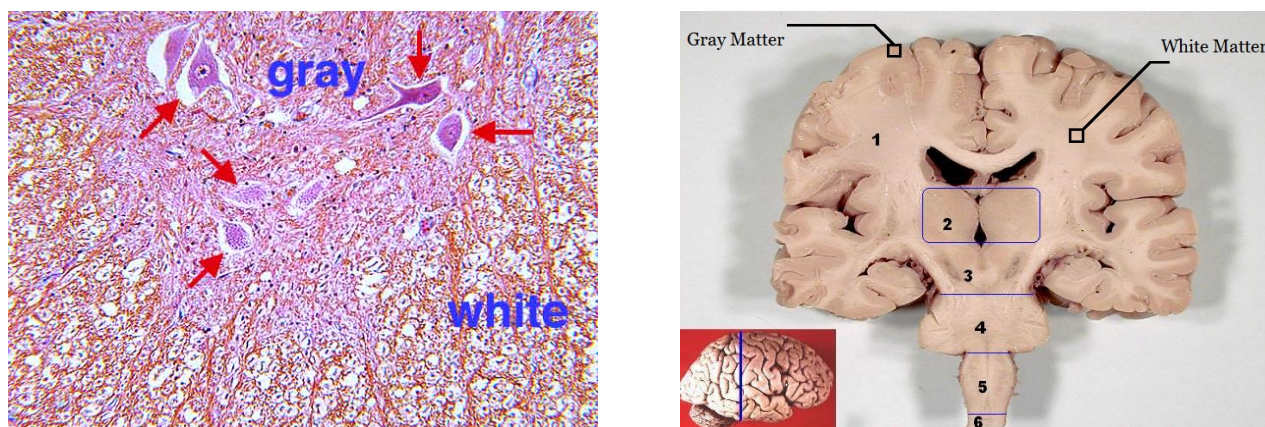


Figure 2: Spinal gray and white matter cells. Red arrows point to GM containing neuron cell bodies. WM contains cell axons, adapted from neuro-histology Atlas: <http://vanat.cvm.umn.edu/neurHistAtls/> (left). A coronal slice of the human brain, we can see the designation of the enumerated divisions is as follows: 1) Cerebrum, 2) Thalamus, 3) Midbrain, 4) Pons, 5) Medulla oblongata, 6) Spinal cord. The black regions above number two contain CSF in a living brain, they are called ventricles, adapted from Wikipedia (right).

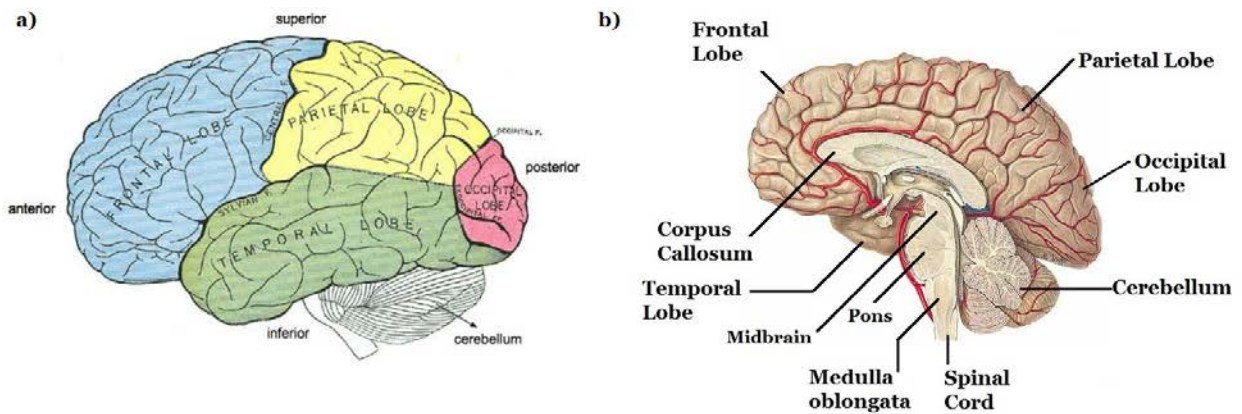


Figure 3: (a) the four lobes of the cerebral cortex and the cerebellum, adapted from (Gray 1936), (b) midsagittal cut of the human brain showing the cerebral cortex, the cerebellum and the brain stem, adapted from Wikipedia.

We can divide each of the two cerebral hemispheres cortexes into four lobes (Figure 3a). 1) The *frontal* lobe (blue region in Figure 3a) responsible for motor control, speech and memory functions. It also controls planning, reasoning and decision making actions. 2) The *temporal* lobe (green region in Figure 3a) manages the processing of audio-visual information as well as language comprehension. 3) The *parietal* lobe (yellow region in Figure 3a) integrates visual and other sensory information in order to control spatial orientation as well as arm and eyes movement. 4) Finally, the *occipital* lobe (red region in Figure 3a) which handles the primary visual processing functions.

The cerebellum (Figure 3), also called *little brain*, handles quick responses to sensory signals and equilibrium functions. It contributes to coordination, precision and accurate timing of movements. In other words, it acts as a fine tuning center for motor functions. It receives inputs through the spinal cord and other parts of the brain. The brain stem (Figure 3b) consists of three parts, first the *medulla oblongata* which controls involuntary functions such as heart rate and breathing. Second, the *midbrain* which is associated with visual reflexes control, sleep and wake, alertness and temperature regulation functions. Finally, the

pons, also called the *bridge*, consists of WM tracts which interconnect the cerebrum to the cerebellum and medulla.

This thesis tries to investigate three main aspects of the brain. First, on the micro level, we try to describe the porosity of the brain tissues using the theory of AD by proposing two different anisotropic models in chapter 6. Second, on the macro level, we try to reconstruct fiber tracts using the proposed tractography method in chapter 7. Finally, on a global level, we try to extract the underlying organizational structure, also called community structure, of the different cortical regions. We also detect alterations in that structure which might occur due to neuropsychological diseases. This is presented in chapter 8.

2.2 The White Matter

As mentioned above, the WM consists of the different fiber bundles. In this section we will describe the most important bundles which might be mentioned in this thesis. There are three types of fibers: 1) commissural fibers which interconnect the two cerebral hemispheres, 2) association tracts which interconnect the different lobes within the same hemisphere, and 3) projection fibers which interconnect the spinal cord, cerebellum and subcortical structures. We will present two main fiber bundles: the corpus callosum and the corticospinal tract.

Corpus Callosum

The CC, also known as the *colossal commissure*, is the largest and densest fibers bundle in the brain made out of about 250 million axons. It interconnects the two cerebral hemispheres. It can be considered as a flat bundle of fibers which lies beneath the cortex. The CC can be divided into four parts from anterior to posterior: *rostrum*, *genu*, *body* and *splenium* (Figure 4). We can see that the CC fibers are spread in the various parts of the cerebral cortex. Curving fibers at the genu are called *forceps minor* while fibers which curve at the splenium are called *forceps major* (Figure 4-right).

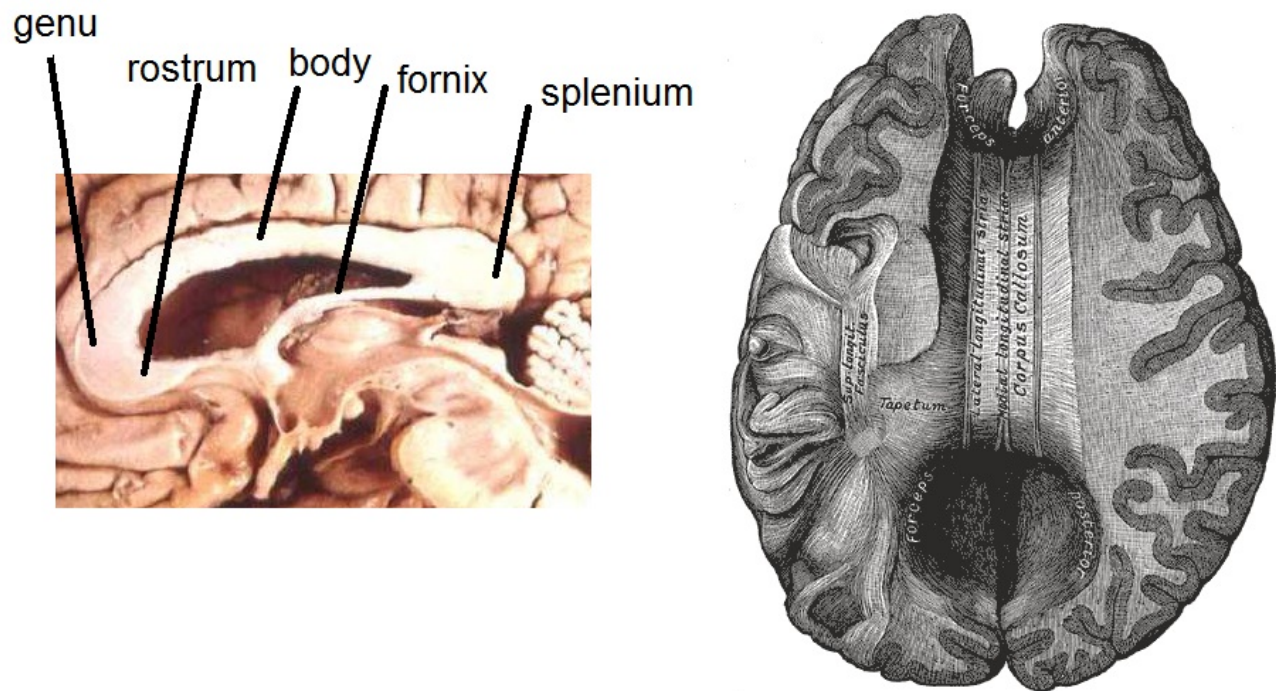


Figure 4: The corpus callosum. In the left, a sagittal cut showing the different divisions of the CC. In the right, a transverse cut showing the CC fibers interconnecting the two cerebral hemispheres. Figures adapted from Wikipedia.

Corticospinal Tract

The *Corticospinal Tract* (CST) fiber bundle runs vertically from the spinal cord to the brain. The CST contains mostly motor related tracts. Figure 5 shows the CST and how it fans out into different regions in the cerebral cortex.

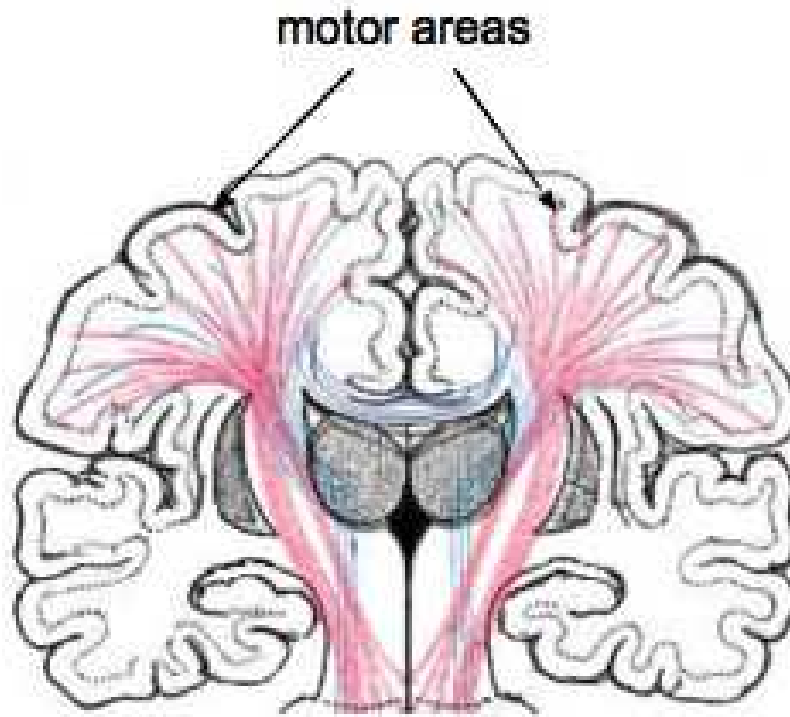


Figure 5: The corticospinal tract, adapted from (Gray 1936).

2.3 Conclusion

In this chapter, we have presented a basic description of the human brain anatomy which will be needed to understand the rest of this thesis. In the next chapter, we will introduce diffusion MRI as well as the necessary basics from physics.

III. BASIC PRINCIPLES OF DIFFUSION MRI

3.1 Introduction

DW-MRI is considered a recent technology invented in the past three decades. It is a noninvasive modality of MRI which allows us to do *in-vivo* analysis on fibrous tissues such as the brain WM and skeletal muscles such as the heart. It is based on the diffusion transport phenomena of gas and fluids. Several applications have emerged from the inspection of the DW imaging data. The most famous one is the early diagnosis of stroke. Post-processing of diffusion data have allowed us to reconstruct the brain WM fibers, the process known as tractography. Tractography has helped in charting the brain network and have deepened our understanding on the organizational structure of the human brain. In this chapter, we review the basic physics of diffusion. Then, we present different models used to describe the DW-MRI measurements of the water molecules in WM tissues. This chapter was inspired from review articles and chapters from (Le Bihan et al. 2001; Tuch 2002; Le Bihan 2003; Descoteaux 2008) which I found as great sources for the basic concepts of the diffusion MRI field.

3.2 Theory of Classical Diffusion

Gas and fluid diffusion is a transport phenomenon discovered by the botanist Robert Brown in 1827. Brown has observed the motion of pollen particles in water. He initially thought that the motion exists because the pollens are alive. Repeating his experiment with dust particles has revealed a jittery kind of motion. However, the pollens were not moving because they were alive. In fact, it was due to random collisions happening between water molecules. This was later identified as the diffusion phenomena or the *Brownian* motion. Figure 6 shows the diffusion of the molecules of dye in water. Notice that the dye molecules move from the higher concentration region to the lower concentration region. It is important to mention that diffusion will even occur in thermodynamic equilibrium state (constant temperature and pressure).

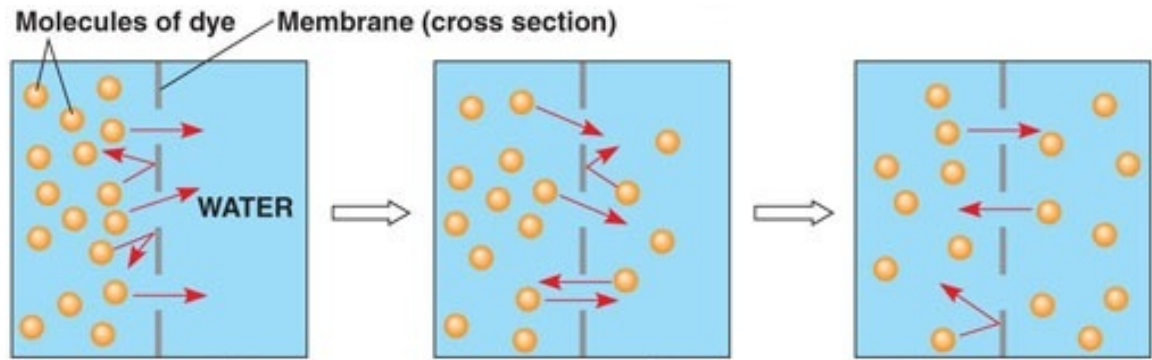


Figure 6: Diffusion of the molecules of dye in water, the dye molecules move from the higher concentration region to the lower concentration region. Notice that even at thermodynamic equilibrium state (last stage); the water molecules are still in a continuous motion across the membrane. Figure adapted from Wikipedia.

In 1855, Fick modeled diffusion as a differential equation (Fick 1855). Fick's first law states that: the net particle flux, $J(\mathbf{r})$, is related to the particle concentration, $C(\mathbf{r}, \zeta)$, at position \mathbf{r} and time ζ through the following equation:

$$J(\mathbf{r}) = -D\nabla C(\mathbf{r}, \zeta) \quad (3.1)$$

where D is the *self-diffusion coefficient* of units mm^2/sec . The ∇ sign is the gradient taken w.r.t. position. The negative sign indicates that particles flow from higher concentration region to lower concentration region. The diffusion coefficient depends on the size of the diffusing molecules, temperature and environment. Assuming an isotropic diffusion (same diffusion in all directions) enforces D to be a scalar. Using the law of conservation of mass at the crossing membrane, $\frac{\partial C(\mathbf{r}, \zeta)}{\partial t} = -\nabla J(\mathbf{r})$, and substituting in equation 3.1, we get:

$$\frac{\partial C(\mathbf{r}, \zeta)}{\partial t} = D\nabla^2 C(\mathbf{r}, \zeta) \quad (3.2)$$

This is called Fick's second law which predicts how diffusion causes the concentration to change with time. In anisotropic mediums, where the diffusion is constrained in some directions and free in the others, for

example in biological tissues where cell membranes form walls, one can replace D by the diffusion tensor (DT) \mathbf{D} . The DT is a symmetric positive definite matrix and can be written as:

$$\mathbf{D} = \begin{bmatrix} D_{xx} & D_{xy} & D_{xz} \\ D_{xy} & D_{yy} & D_{yz} \\ D_{xz} & D_{yz} & D_{zz} \end{bmatrix} \quad (3.3)$$

Hence, equation 3.2 can be then generalized in the form:

$$\frac{\partial C(\mathbf{r}, \zeta)}{\partial t} = \nabla^T \mathbf{D} \nabla C(\mathbf{r}, \zeta) \quad (3.4)$$

where $[\cdot]^T$ represents transpose. In 1905, Einstein re-described diffusion in a statistical framework in the context of a *random walk* scenario (Einstein and Fürth 1956). He hypothesized that if one could observe the movement of a single molecule in a fluid, one could observe a random trajectory of motion. Furthermore, this trajectory is independent of neighboring molecules motion trajectories. However, one cannot describe trajectories for all molecules. So, Einstein suggested the following: on a macro scale, if the number of molecules is large and they have the freedom to diffuse anywhere, one could characterize their *mean squared displacement* (MSD) from a starting point over a time τ . He then described diffusion by a probability density function (PDF), $P(\mathbf{r}, \tau)$, which represents the probability of finding a particle at location \mathbf{r} and at time τ . This PDF is currently known by the name of *diffusion propagator*. Einstein proved that the MSD averaged over all diffusing molecules in an isotropic medium is proportional to the diffusing time τ and the constant of proportionality is the *self-diffusion coefficient* D . He expressed this in the form:

$$\langle \mathbf{r}^T \mathbf{r} \rangle = 6D\tau \quad (3.5)$$

where $\langle \cdot \rangle$ denotes the ensemble average and \mathbf{r} is the net displacement position vector: $\mathbf{r} = \mathbf{r}_\tau - \mathbf{r}_0$ with \mathbf{r}_0 is the original position of a particle and \mathbf{r}_τ is the position after time τ . Einstein has reached equation 3.2 with the particle concentration $C(\mathbf{r}, \zeta)$ replaced by the diffusion PDF. In current literature discussing diffusion, the propagator usually replaces $C(\mathbf{r}, \zeta)$ in equations 3.1 to 3.4. His equation can be generalized to the DT model similar to equation 3.3. Experimentally, one could measure the value of D for water at a temperature of 30°C

to be $2.6 \times 10^{-3} \text{ mm}^2/\text{s}$. In other words, in 1 ms, water molecules will move, on average, 4 μm in all directions. The general solution of the DT model is a Gaussian distribution given by:

$$P(\mathbf{r}, \tau) = \frac{1}{\sqrt{(4\pi|\mathbf{D}|\tau)^3}} \exp\left(-\frac{1}{4\tau} \mathbf{r}^T \mathbf{D}^{-1} \mathbf{r}\right) \quad (3.6)$$

where $|\mathbf{D}|$ is the determinant of the DT. In that context, \mathbf{D} can be considered as the covariance matrix of the 3-variate Gaussian *diffusion propagator* describing the motion of the diffusing molecules. In isotropic mediums when D is a scalar, we can write:

$$P(\mathbf{r}, \tau) = \frac{1}{\sqrt{(4\pi D\tau)^3}} \exp\left(-\frac{\|\mathbf{r}\|^2}{4D\tau}\right) \quad (3.7)$$

where $\|\cdot\|$ is the norm. Further analysis of the DT model will be discussed later in this chapter when discussing the DTI model. From above, one could notice that D is a scalar constant which makes us to wonder about how this can be used to describe different tissues in DW-MRI. In fact, due to the presence of obstacles such as cell membranes and macromolecules, biological tissues do possess a hindering nature which will lower the values of the measured D . In this case, the measured D in DW-MRI is called the *apparent diffusion coefficient* (ADC) (Le Bihan et al. 1986). We now start describing how we do actually measure the ADC.

3.3 Nuclear Magnetic Resonance and Diffusion Magnetic Resonance Imaging

We will start by presenting a brief history about MRI. Before MRI and DW-MRI, people have measured diffusion using nuclear magnetic resonance (NMR) spectroscopy. NMR spectroscopy is a method by which one can use the magnetic properties of atoms in order to determine their physical and chemical properties. It is based on the phenomenon of NMR first discovered in 1938 by Isidor Rabi et al. (Rabi et al. 1992) who won the Nobel Prize in Physics in 1944 for this work. In 1946, Felix Bloch (Bloch 1946) and Edward Mills Purcell (Purcell et al. 1946) simultaneously presented a new expansion for Rabi's technique to be used on gas and liquid. They both won the Nobel Prize in Physics in 1956 for their discovery. Rabi, Bloch and Purcell hypothesized that in the presence of a strong homogenous magnetic field, hydrogen atoms, ^1H ,

will precess around the same axis of the applied magnetic field at a specific frequency, also called the *Larmor* frequency, which characterizes the hydrogen atom and depends on the applied field strength (Figure 7a). This state was then called *equilibrium*. They noticed that a perturbation to this state using a radio frequency (RF) pulse could be absorbed by the atom only if its frequency matched the Larmor frequency. This was called the *resonance* state of the atom shown in Figure 7b. The RF pulse is usually called a 90 degree pulse because it tips the hydrogen atom in the transverse plane perpendicular to the applied magnetic field (Figure 7b). After the end of the RF pulse, an oscillatory damped signal is emitted from the ensemble of hydrogen atoms in resonance, this signal is characterized by the Larmor frequency and is called the free induction decay (FID) shown in Figure 7c.

In 1973, Paul Lauterbur designed a technique to generate 2D MR images which made him won the Nobel Prize in Physiology and Medicine jointly with Peter Mansfield in 2003. In 1950, Hahn introduced spin-echo to NMR. He suggested a technique to rebuild the damped FID signal by applying another RF pulse for twice the duration of the 90 degree pulse following to the application of the initial 90 degree pulse (Hahn 1950). He observed that the emitted signal by the hydrogen builds-up after a certain period (Figure 7d). This was a very essential step in the development of DW-MRI. In 1956, Torrey have introduced a new term in the Bloch equation to account for diffusion (Torrey 1956). Using the spin-echo pulse sequence, Edward Stejskal and John Tanner have developped in 1965 the pulse gradient spin-echo (PGSE) sequence which allows the measurement of the ADC (Stejskal and Tanner 1965). In the next section, we are going to discuss the PGSE in more details. Table II shows a timeline which describes briefly the diffusion MRI history.

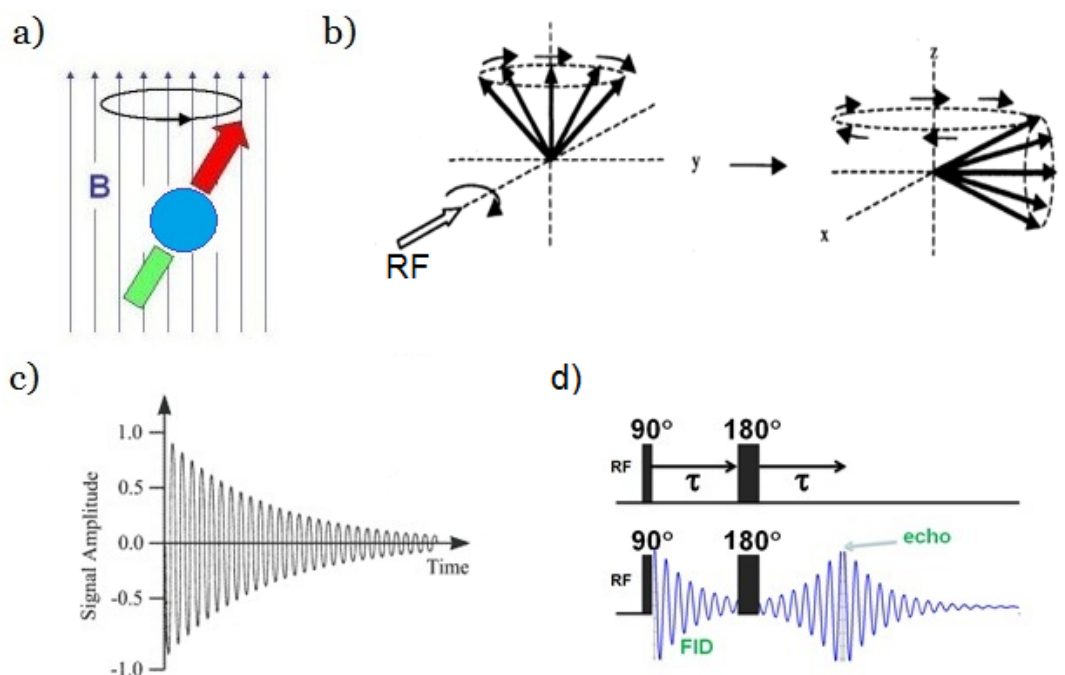












Figure 7: a) Precession of the hydrogen atom (proton) in the presence of a magnetic field B , red and green colors represent positive and negative polarities respectively, b) The application of a 90 degree tipping RF pulse will cause the hydrogen atom to precess in the transverse plane perpendicular to the main applied magnetic field, c) Free induction decay, notice that the signal exhibits a damping oscillatory behavior, d) Spin-echo pulse sequence, notice how the echo signal builds-up after the 180 degree pulse. Figure adapted from Wikipedia.

Table II: Timeline describing the history of diffusion MRI.

1938	1946	1950	1956	1965	1973	1985	1990-1991	1992
 Isidor Rabi	 Felix Bloch  Edward Purcell	 Erwin Hahn	 H.C. Torrey	 Edward Stejskal & John Tanner	 Paul Lauterbur	Taylor & Bushell  Denis Le Bihan & Breton	 Maichel Moseley et al., Douek et al.	 Peter Basser et al.
Principles of NMR		Spin-echo	Diffusion in NMR	PGSE	2D MRI	Scalar DW-MRI, ADC and Trace Imaging		DTI

3.3.1 Pulse Gradient Spin Echo

In 1965, Stejskal and Tanner have designed the *pulsed gradient spin echo* (PGSE) sequence in order to acquire information about the diffusion of particles (Stejskal and Tanner, 1965). Before discussing the PGSE sequence, we would like to present the notion of a gradient. From the previous discussion, we recall the dependence of the hydrogen atoms precessional frequency on the strength of the applied magnetic field. This fact describes what is known to be the Larmor equation which states that the precessional frequency of the hydrogen atom is directly proportional to the applied magnetic field and the constant of proportionality is called the gyromagnetic ratio, γ , a unique characteristic for every element, and have units of rad/sec/Tesla. The application of a linearly space-varying magnetic field, i.e. a gradient, imposed on the originally applied

strong static magnetic field, will cause a position dependence for the hydrogen atoms precessional frequency. In other words, each atom will precess at a different frequency according to the strength of the magnetic field present at its location which will cause each atom to gain a different phase along time. Applying the gradient field for a period of time will create a gradient of phase over the volume under study. This phase gradient can be reversed by the application of a 180 degree RF pulse followed by a gradient with exactly the same amplitude, duration and polarity.

Since water consists of two hydrogen atoms, one can apply NMR principles to a water specimen. The PGSE pulse sequence illustrated in Figure 8 can be used to measure the diffusion of water molecules at a specific direction \mathbf{g} (a unit vector). By default a strong magnetic field \mathbf{B} is applied on the specimen to allow the exploitation of its NMR properties. The PGSE consists of four steps. First, a 90 degree pulse is applied which will tip all the atoms in the transverse plane, recall Figure 7b. Second, a *dephasing* gradient is then applied in direction \mathbf{g} with strength G and duration δ will cause a phase gradient to build-up across the specimen. Third, a 180 degree RF pulse is applied. Finally, we apply a second *rephasing* gradient in direction \mathbf{g} with the same amplitude and duration – as the first gradient – after a time Δ from the first gradient. In the absence of the water molecules displacement, the second rephasing gradient should cancel the phase shift of the static molecules. However, under the random walk of water molecules, i.e. diffusion, a distribution of phase occurs due to the displacement of different molecules. This distribution will cause a loss in the signal coherence which can be observed as a loss of the spin-echo signal amplitude when compared to the no-diffusion experiment. Please note that the applied gradient pulses were assumed to be short enough so that the water diffusion is negligible during that time (δ).

In their 1965 paper, Stejskal and Tanner have showed that the acquired NMR signal, $S(\mathbf{q}, \tau)$, in the PGSE experiment is the 3D Fourier transform, \mathcal{F} , of the diffusion propagator PDF, $P(\mathbf{r}, \tau)$, mentioned in section 3.2. Assuming an initial delta distribution of material at $\mathbf{r} = \mathbf{0}$ and $\tau = 0+$, (i.e. $P(\mathbf{r} = \mathbf{0}, \tau) = \delta(\mathbf{r})$), we can write:

$$\frac{S(\mathbf{q}, \tau)}{S_0} = \int_{\mathbb{R}^3} P(\mathbf{r}, \tau) \exp(-i2\pi \mathbf{q}^T \mathbf{r}) d\mathbf{r} = \mathcal{F}\{P(\mathbf{r}, \tau)\} \quad (3.8)$$

where the value of \mathbf{q} is given by $\mathbf{q} = \gamma \delta \mathbf{G} \mathbf{g} / 2\pi$, with γ being the nuclear gyromagnetic ratio for water protons, \mathbf{G} is the applied gradient amplitude and \mathbf{g} is a unit vector in its direction, S_0 is the baseline image acquired without any diffusion gradients (also called $b = 0$ image). In diffusion MRI, we seek out the reconstruction of the diffusion propagator PDF. An exhaustive model-free solution is to sample all possible \mathbf{q} vectors or the so-called \mathbf{q} -space which have been realised in \mathbf{q} -space imaging (Callaghan, 1991). A simple solution is to assume that the propagator takes the form of a Gaussian distribution. In that case, equation 3.8 could be worked out analytically and one could reach the following equation:

$$S(\mathbf{g}, \tau) = S_0 \exp(-\tau \|\mathbf{q}\|^2 D \mathbf{g}^T \mathbf{g}) = S_0 \exp(-b \cdot \text{ADC}) \quad (3.9)$$

where b is called the b -value given by $b = \tau \|\mathbf{q}\|^2$ with units of s/mm^2 and was first introduced by Le Bihan et al. (Le Bihan et al. 1986) and the ADC is the *apparent diffusion coefficient*. From the above equation, we can see that increasing the b -value will decrease the amplitude of the acquired signal, thus decreasing the signal to noise ratio (SNR). Notice that D here is scalar since the measurement was assumed to be in only one direction which assumes an isotropic medium under test. In anisotropic mediums, the DT \mathbf{D} could be used instead. In the next section we will try to obtain equation 3.9 using a different approach starting from the Bloch-Torrey equation (Torrey 1956).

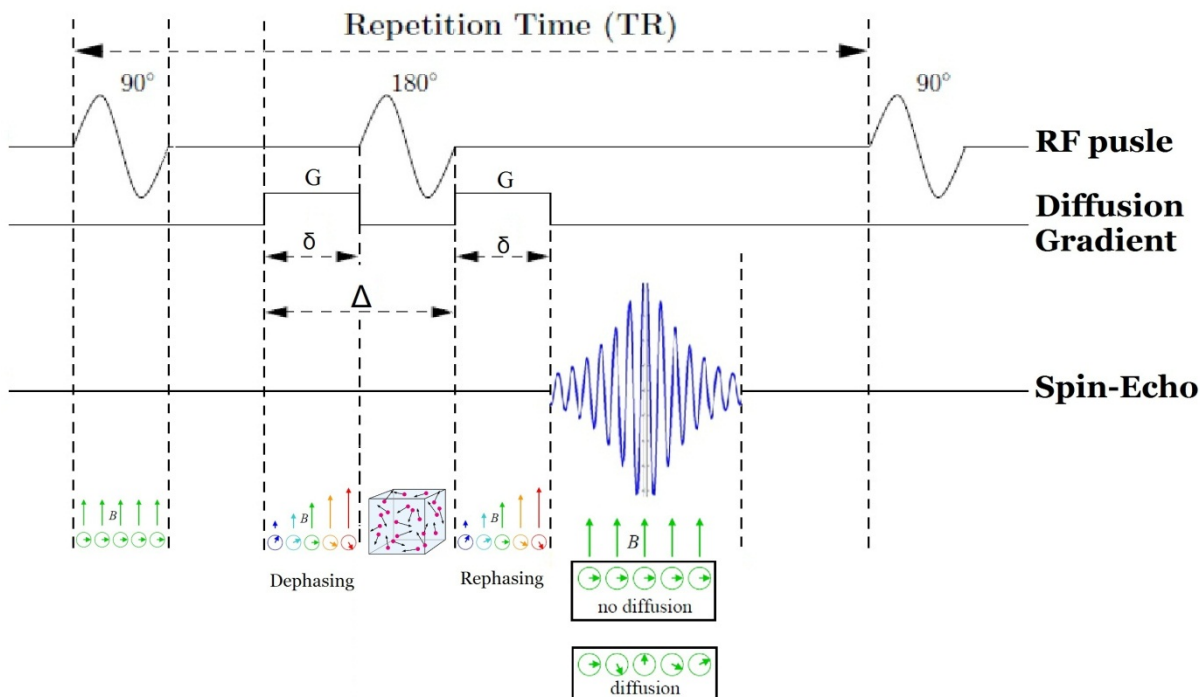


Figure 8: Schematic of the PGSE pulse sequence. At the 90° pulse, the ensemble of hydrogen atoms are tipped in the transverse plane to the applied magnetic field B and they precess with the Larmor frequency. After the application of the first gradient, atoms start dephasing (each atom will precess at different frequency) due to dependence of the precession frequency on the field strength. Each atom will experience a different field strength which will depend on its location. After the application of the second gradient following the 180° degree RF pulse, the atoms undergo a rephasing process (they restore their original phase). This rephasing is complete only when the atoms are still in their locations. However, due to the diffusion phenomena which occurs in the time between the two gradients, the rephasing is not complete and the signal will lose some of its amplitude.

3.3.2 The Bloch-Torrey Equation

In 1946, Felix Bloch has described the magnetization change of the hydrogen atom in the NMR experiment (Bloch 1946). We recall that the NMR experiment starts by the application of a strong static magnetic field to hydrogen atoms which react by precessing along their axis in the direction of the applied field at the Larmor frequency. The application of the 90° degree RF pulse tips the hydrogen atom in the

transverse plane (Figure 7b). The atom, however, recovers its orientation in the direction of the applied magnetic field (the equilibrium state), we call this: *relaxation* (Figure 9). There are two types of relaxation in the NMR experiment: 1) T_1 -relaxation, also called *spin-lattice* relaxation, where the hydrogen atoms give back the absorbed energy from the RF pulse to the surrounding environment or lattice. 2) T_2 -relaxation, also called *spin-spin* relaxation, where the hydrogen atoms start dephasing due to the energy exchange between them. Both relaxation types will cause the measured net magnetization (the detected signal) in the transverse plane to decay. The net magnetization of an ensemble of atoms in a specimen can be detected by means of coils surrounding it as shown in Figure 9.

The Bloch equation describes the decay of the transverse net magnetization moment \mathbf{M} as a function of the T_1 and T_2 relaxation times. The Bloch equation states:

$$\frac{d\mathbf{M}}{dt} = \underbrace{\mathbf{M} \times \gamma \mathbf{B}}_{\text{Precession}} - \underbrace{\frac{M_x \mathbf{i} + M_y \mathbf{j}}{T_2}}_{\text{spin-spin relaxation}} - \underbrace{\frac{(M_z - M_0) \mathbf{k}}{T_1}}_{\text{spin-lattice relaxation}} \quad (3.10)$$

where $\mathbf{M} = [M_x \ M_y \ M_z]^T$ is the net magnetization moment of the ensemble of hydrogen atoms in the specimen, $\mathbf{B} = [0 \ 0 \ B_0]^T$ is the static magnetic field and it is assumed to act in the z direction, \mathbf{i} , \mathbf{j} and \mathbf{k} are unit vectors in the x, y and z directions. The first part of the equation describes the precessional effect due to the applied static magnetic field. The second and third parts describe the effect of the T_1 and T_2 relaxations.

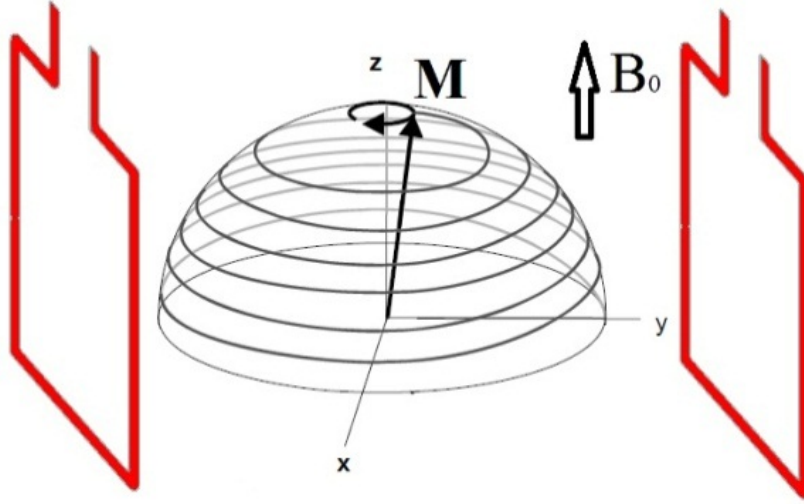


Figure 9: Relaxation trajectory of the hydrogen atoms in a specimen present in a static magnetic field B_0 after the end of the RF excitatory pulse. The net magnetization \mathbf{M} is detected by means of horizontal coils. The atoms return to the equilibrium state where they are oriented parallel to the applied static field.

In 1956, Henry Torrey introduced a diffusion term in equation 3.10 (Torrey 1956). Ignoring the T_1 and T_2 relaxation and considering only the transverse magnetization \mathbf{M}_{xy} to be the combination of M_x and M_y in the form: $M_{xy} = M_x + iM_y$ where $i = \sqrt{-1}$, he wrote:

$$\frac{\partial M_{xy}}{\partial t} = -i\gamma(\mathbf{r} \cdot \mathbf{G})M_{xy} + \nabla^T \mathbf{D} \nabla M_{xy} \quad (3.11)$$

where $\mathbf{r} = [x \ y \ z]^T$ is a position vector, $\mathbf{G} = [G_x \ G_y \ G_z]^T$ is the applied gradient in the PGSE sequence, $\nabla = \left[\frac{\partial}{\partial x} \ \frac{\partial}{\partial y} \ \frac{\partial}{\partial z} \right]^T$ and \mathbf{D} same as equation 3.3. Equation 3.11 is known as the *Bloch-Torrey* equation. Using the method of separation of variables, a solution of the following form can be assumed:

$$M_{xy}(\mathbf{r}, t) = A(t) \exp(-i\gamma \mathbf{r} \cdot \mathbf{F}(t)) \quad (3.12)$$

where $\mathbf{F}(t) = \int_0^t \mathbf{G}(t') dt'$. Substituting 3.12 in 3.11 and noting that

$\nabla \exp(-i\gamma \mathbf{r} \cdot \mathbf{F}(t)) = -i\gamma \mathbf{F}(t) \exp(-i\gamma \mathbf{r} \cdot \mathbf{F}(t))$ we obtain:

$$\frac{\partial[A(t)]}{\partial t} = -\gamma^2 (\mathbf{F}(t)^T \mathbf{D} \mathbf{F}(t)) A(t) \quad (3.13)$$

Integrating, we get:

$$A(t) = A_0 \exp\left(-\gamma^2 \int_0^t \mathbf{F}(t')^T \mathbf{D} \mathbf{F}(t') dt'\right) \quad (3.14)$$

Hence, one can write:

$$M_{xy} = M_0 \exp\left(-\gamma^2 \int_0^t \mathbf{F}(t')^T \mathbf{D} \mathbf{F}(t') dt'\right) \quad (3.15)$$

Performing the integration on the PGSE pulse using square gradients, we get:

$$\begin{aligned} M_{xy} &= M_0 \exp\left(-(\gamma\delta\|\mathbf{G}\|)^2\left(\Delta - \delta/3\right)\mathbf{g}^T \mathbf{D} \mathbf{g}\right) \\ &= M_0 \exp(-b\mathbf{g}^T \mathbf{D} \mathbf{g}) \end{aligned} \quad (3.16)$$

where $\mathbf{g} = \frac{\mathbf{G}}{\|\mathbf{G}\|}$, $b = (\gamma\delta\|\mathbf{G}\|)^2\left(\Delta - \delta/3\right)$ is the b -value mentioned in section 3.3.1 computed for the PGSE sequence. In light of equation 3.16, we can describe the acquired diffusion signal in the form:

$$S(\mathbf{g}, t) = S_0 \exp(-b\mathbf{g}^T \mathbf{D} \mathbf{g}) \quad (3.17)$$

where S_0 is the signal acquired at $b = 0$. The last equation describes the DT model applied in anisotropic mediums. In isotropic mediums, a scalar diffusion coefficient will be used and we will reach equation 3.9. Equation 3.19 is considered to be the basis of the DTI model.

3.3.3 Diffusion-Weighted Imaging and the Apparent Diffusion Coefficient

The beginnings of diffusion MRI dates back to 1985 when Taylor and Bushell acquired the first DW images (DWI) of a small hen's egg (Taylor and Bushell 1985). The images were the acquired data of the

applied PGSE pulse sequence in one gradient direction. In the next year, Le Bihan et al. presented the first *in-vivo* DWI acquisition of a human brain (Le Bihan et al. 1986). In that study, he introduced the notion of the b -value and provided the formulation to compute the ADC from the acquired DWI using equation 3.9 with b computed for the PGSE sequence as in 3.16. Two acquisitions were needed: one with no diffusion, also called $b0$ image, and another one with the PGSE applied. He noted changes in ADC in different tissues in the brain. He has also observed that GM tissues possess a higher ADC compared to WM tissues. However, both tissue types had an ADC lower than the self-diffusion coefficient of water. The ADC of CSF was found to vary according to location. In general, it has a value close to the self-diffusion coefficient of water and it was significantly higher in the ventricles.

The usage of different gradient directions appeared in 1990 when Moseley et al. measured the ADC along the x and z axis in a cat brain (Moseley et al. 1990). At that time, it became clear that diffusion in biological tissues is anisotropic. Moseley et al. suggested the ratio ADC_z/ADC_x to characterize the level of anisotropy in tissues and it was called the *anisotropy index*. Unfortunately, this metric was rotationally variant and it depended on the gradient direction used in the PGSE sequence. In the next section we will introduce the DTI model which is rotationally invariant.

3.3.4 Diffusion Tensor Imaging

Many of the fibrous biological tissues such as the heart muscle and the brain WM exhibit anisotropic water diffusion. Basser et al. have proposed the DT model (equation 3.6) to describe the diffusion propagator PDF (Basser et al. 1993; Basser et al. 1994; Basser et al. 1994). In that case, equation 3.17 is used to describe the acquired diffusion signal. From equation 3.3, we can see that the DT, \mathbf{D} , is made out of 6 unknowns (since it is symmetric). Hence, we need to acquire at least 6 DWI in 6 non-collinear gradient directions in addition to the $b0$ image (S_0) to be able to compute the DT. A system of linear equations can then be formed by rewriting equation 3.17 in the form:

$$-\frac{1}{b} \log \left(\frac{S(\mathbf{g}, t)}{S_0} \right) = g_x^2 D_{xx} + g_y^2 D_{yy} + g_z^2 D_{zz} + 2g_x g_y D_{xy} + 2g_x g_z D_{xz} + 2g_y g_z D_{yz} \quad (3.18)$$

An over determined problem can also be solved when acquiring more than 6 DWI acquisitions. In that case the method of least squares can be used to find the best solution of the DT. In the DT, the 3 diagonal elements represent the ADC along the three orthogonal axes of the MRI scanner. However, the 3 off diagonal elements does not represent ADC along directions between the orthogonal axes. If we regarded the DT as a covariance matrix for the Gaussian PDF chosen to model the diffusion propagator, the off diagonal elements of the DT will represent the correlation between displacements along the three orthogonal axes.

Diagonalizing the DT by extracting its eigenvalues (e_1 , e_2 and e_3) and eigenvectors (λ_1 , λ_2 and λ_3 in units of mm^2/s) provides valuable information about the basic axes of diffusion. This is possible since the 3-variate Gaussian model chosen to describe the diffusion propagator does have isosurfaces of constant values in the form of ellipsoids. The eigenvectors will determine the orientation of the ellipsoid's basic axes and the square root of the eigenvalues will scale their lengths (Figure 10). Moreover, the eigenvalues can be considered as the ADC along the principal directions of diffusion represented by the eigenvectors. In a single fiber bundle with no crossing fibers such as the CST, one eigenvalue will be larger than the other two. In that case, the eigenvector corresponding to the largest eigenvalue will point to the principal direction of diffusion along the bundle's orientation. This case is called *linear anisotropy* (Figure 11a). Two other cases exist: *planar anisotropy* which can be seen in crossing fibers where two eigenvalues are larger than the third one (Figure 11b), and *spherical anisotropy* which occurs in isotropic mediums where the three eigenvalues are equal in value (Figure 11c).

Using the eigenvalues, we can compute several metrics which might provide valuable information about tissue microstructure while being rotationally invariant to the applied coordinate system of the scanner (Westin et al. 2002). Examples on such metrics are the *trace* ($\text{TR} = \lambda_1 + \lambda_2 + \lambda_3 = D_{xx} + D_{yy} + D_{zz}$) and the *mean diffusivity* (MD) ($\text{MD} = \text{TR}/3$). The most famous metrics which have been extensively studied are the *fractional anisotropy* (FA) and the *relative anisotropy* (RA), (Basser and Pierpaoli 1996), defined as:

$$FA = \sqrt{\frac{(\lambda_1 - \lambda_2)^2 + (\lambda_1 - \lambda_3)^2 + (\lambda_2 - \lambda_3)^2}{2(\lambda_1^2 + \lambda_2^2 + \lambda_3^2)}} \quad (3.19)$$

$$RA = \frac{\sqrt{(\lambda_1 - \lambda_2)^2 + (\lambda_1 - \lambda_3)^2 + (\lambda_2 - \lambda_3)^2}}{\sqrt{2}(\lambda_1 + \lambda_2 + \lambda_3)} \quad (3.20)$$

They both vary from 0 to 1. A value of zero FA indicates an isotropic medium and 1 indicates an anisotropic diffusion along one axis (Figure 12a, b). The DT can be visualized by plotting the components of the eigenvector corresponding to the largest eigenvalue as a Red-Green-Blue (RGB) colormap which represents the orientation in x, y and z directions (Figure 12c).

The DT model has helped in quantifying the anisotropy of diffusion in different brain tissues as well as in estimating the principle direction of diffusion at every voxel which enabled the extraction of different WM fibers throughout the brain using the process of tractography. However, DTI possesses a main limitation in its inability of recovering crossing fibers within voxels since fibers diameter are much lower (1-30 μm) than the DWI voxel resolution (vary from 1 to 9 mm^3). Crossing fibers do appear in the form of planar anisotropy (Figure 11b) when two fibers are crossing or in the form of spherical anisotropy when three or more fibers cross which affects profoundly the results of tractography. The limitations of the DT model have led to the development of richer models that may provide more directional information and solve the crossing fibers issue. In the next section we are going to briefly discuss a sample of such models. We are also going to present the TDF model which is being used as the basis of the tractography algorithm presented in this thesis.

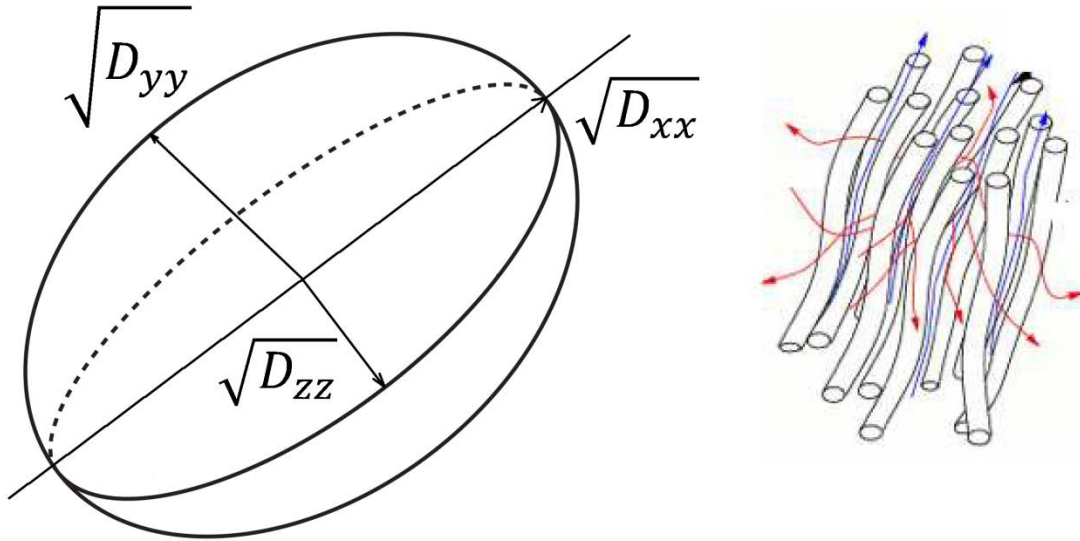


Figure 10: (left) Diffusion ellipsoid, the axes are the eigenvectors of the DT. The ellipsoid axes are proportional to the square roots of the eigenvalues of the DT. (right) Water Brownian motion along the fibers.



Figure 11: Different anisotropy cases: a) Linear when $\lambda_1 \gg \lambda_2, \lambda_3$ which happens in single fiber bundles such as CST, b) Planar when $\lambda_1 \sim \lambda_2 \gg \lambda_3$ which happens in crossed fiber bundles, c) Spherical when $\lambda_1 \sim \lambda_2 \sim \lambda_3$ which happens in isotropic mediums.

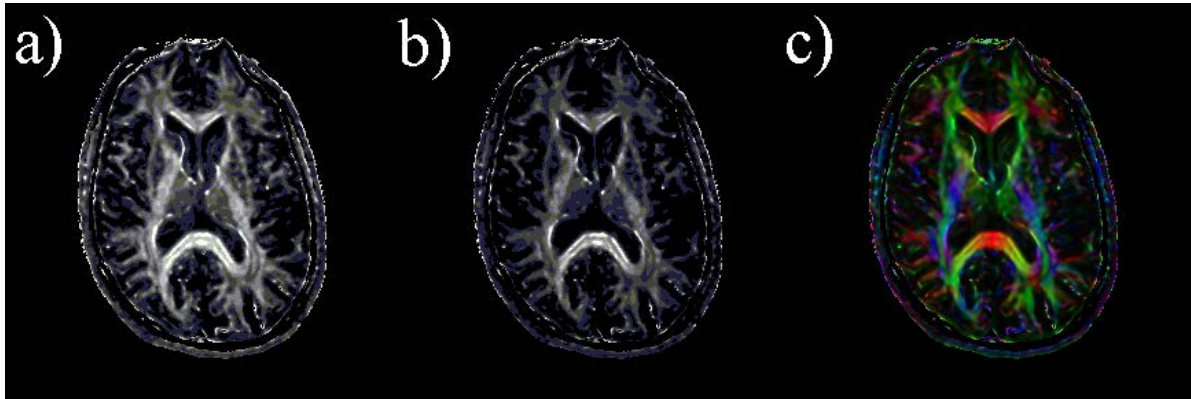


Figure 12: Scalar metrics derived from the DT. In (a), the FA is shown for an axial slice, while (b) represents the RA for the same slice. In (c), the eigenvector corresponding to the largest eigenvalue is visualized as an RGB colormap.

3.3.5 High Angular Resolution Diffusion Imaging

To overcome the fibers crossing problem, a lot of models have been developed based on the idea of sampling the q -space in as many directions as possible. This allows a better reconstruction of the true diffusion propagator PDF. These techniques are called High Angular Resolution Diffusion Imaging (HARDI). Two strategies have emerged: 1) sampling the q -space in a Cartesian grid, and 2) sampling the q -space at a single spherical shell (fixed b value).

3.3.5.1 Diffusion Spectrum Imaging

In 2000, Wedeen et al. (Wedeen et al. 2000) developed the *diffusion spectrum imaging* (DSI) technique based on the previously developed q -space imaging (QSI) technique by Callaghan et al. (Callaghan et al. 1988; Callaghan 1991). He sampled the q -space at a large number of points ($N > 500$) in the 3D Cartesian space using different gradients directions and magnitudes (i.e., different b -values: $500 \leq b \leq 20000$ s/mm²). He computed the diffusion PDF by numerically computing the 3D inverse Fourier transform of the

measured DWI signals. It is important to note that this technique does not impose a specific model on the diffusion PDF. The fibers directions are obtained through the computation of the diffusion *orientation distribution function* (ODF) in the polar coordinates as shown in Figure 13a by projecting the computed PDF on a sphere. Fibers are found at the maxima directions of the ODF defined in (Tuch 2002) as:

$$\psi(\theta, \phi) = \int_0^\infty P(r, \theta, \phi) dr \quad (3.21)$$

where $\theta \in [0, \pi]$, $\phi \in [0, 2\pi]$. Despite of its efficiency in the determination of crossing fibers (Weeden et al., 2005), DSI requires a long acquisition time. One will be forced to acquire lower resolution DWI in order to shorten the required acquisition time. This has given rise to the other clinically practical approach: single shell HARDI imaging (Tuch et al. 1999; Tuch 2002; Tuch et al. 2002).

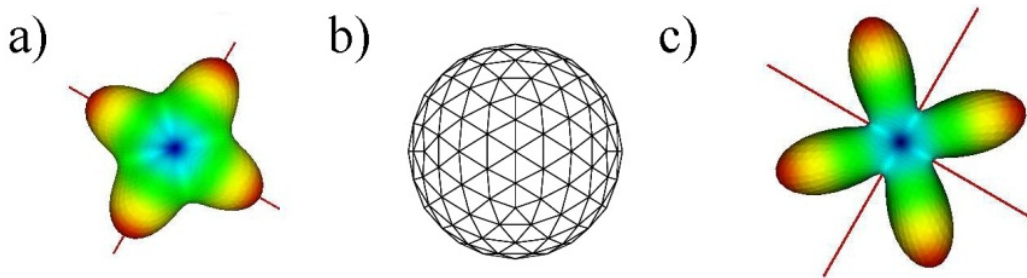


Figure 13: a) Diffusion orientation distribution function, b) 320 points on a sphere representing gradients directions, c) Apparent diffusion coefficient profile, adapted from Wikipedia.

3.3.5.2 Single Shell HARD Imaging

Many models were built on the idea of sampling the DWI signal on a single spherical shell in \mathbf{q} -space (fixed b -value) at N points corresponding to N different gradient directions as shown in Figure 13b. These models are characterized by a much shorter imaging time than DSI. Single shell HARDI methods are nowadays used to solve fibers crossing and are widely used in tractography. Two approaches have emerged to model the water diffusion propagator: model-based and model-free methods. In the next section, we will perform a literature review for the different models which currently exist.

3.3.5.2.1 Model-Based Approaches

A Mixture Models

A simple method for modeling the water propagator is to assume that the HARDI signal comes from a mixture of functions. Tuch (Tuch 2002) have modeled the water propagator PDF as a mixture of n Gaussians which is known as the *multi-Gaussian* or the *multi-Tensor* model. It can be written in the form:

$$P(\mathbf{r}, \tau) = \sum_{i=1}^n a_i \frac{1}{\sqrt{(4\pi|\mathbf{D}_i|\tau)^3}} \exp\left(-\frac{1}{4\tau} \mathbf{r}^T \mathbf{D}_i^{-1} \mathbf{r}\right) \quad (3.22)$$

where $a_i \in [0,1]$, $\sum_{i=1}^n a_i = 1$. Hence the acquired signal can be written as:

$$S(\mathbf{g}, b) = S_0 \sum_{i=1}^n a_i \exp(-b \mathbf{g}^T \mathbf{D}_i \mathbf{g}) \quad (3.23)$$

The crucial concern in that model is the choice of n at every voxel. Several constraints have been applied to assure the stability of tensors estimation such as imposing symmetry of eigenvalues, forcing certain magnitude and ratios of eigenvalues or imposing positive definiteness of the \mathbf{D}_i (Alexander et al. 2001; Tuch 2002; Tuch et al. 2002; Blyth et al. 2003; Maier et al. 2004; Yunmei et al. 2004; Peled et al. 2006).

A special case when $n = 2$ is the *Ball & stick* model (Behrens et al. 2003; Hosey et al. 2005) which assumes that brain tissues contain two compartments for the diffusion of water: an anisotropic compartment

due to the fibers restrictive nature to diffusion (slow or intracellular diffusion in and around the fiber) which is modeled as an anisotropic Gaussian PDF P_r and an isotropic one which is not affected by the fibers (fast or extracellular diffusion) which is modeled as an isotropic Gaussian PDF P_f . The propagator is then assumed to be in the form: $P = \alpha P_f + (1 - \alpha)P_r$, where $0 < \alpha < 1$. P_r was modeled as Gaussian in which the DT has only one non-zero eigenvalue since it only has one preferred direction along the fiber. Note that this model should not be confused with the *bio-exponential* model (Clark and Le Bihan 2000; Mulkern et al. 2000) which also describes the diffusion signal as a mixture of two Gaussians representing slow and fast compartments since it is considered a deviation of the ADC technique described in equation 3.9 and it uses only one gradient. It estimates two ADC(s): ADC_{slow} and ADC_{fast} by varying the b -value instead of acquiring numerous DWI in different directions.

A similar approach to the *Ball & Stick* model but with a higher complexity is the *composite hindered and restricted model of diffusion* (CHARMED) (Assaf et al. 2004; Assaf and Basser 2005). It assumes the existence of two diffusion processes: a restricted non-Gaussian (intra-axonal compartments) one and a hindered one that can be approximated to Gaussian (cells and extracellular compartments). The hindered part is modeled by a full DT, while the restricted part is modeled using Neuman's model for restricted diffusion in a cylinder (Neuman 1974).

To overcome the main drawback in the multi-Gaussian, Ball & Stick and CHARMED models, which is the choice of the number of compartments, a recent model which does not impose any constraint on the number of tensors was proposed by Leow et al. (Leow et al. 2009). The *tensor distribution function* (TDF) proposed by Leow et al. assumes a distribution of tensors and tries to numerically estimate a PDF which weights every possible tensor in the four dimensional (4D) space of symmetric positive definite three-by-three matrices \mathbf{D} . The reason \mathbf{D} is a 4D space is the assumption that fibers are cylindrical which allows us to enforce two eigenvalues to be equal. To complete the definition of a tensor, we need a unit vector which can be defined by two angles on the unit sphere. Thus, a tensor \mathbf{D} can be expressed as a function of two eigenvalues and two angles: $\mathbf{D}(\lambda_1, \lambda_2, \theta_1, \theta_2)$ which makes \mathbf{D} a 4D space. Hence, we need to compute a PDF

$P(\mathbf{D})$ at every voxel which weights all possible tensors in the 4D space, \mathbf{D} . The acquired signal at each voxel is then assumed to be in the form:

$$S_{calc}(\mathbf{g}) = \int_{\mathbf{D} \in \mathcal{D}} P(\mathbf{D}) \exp(-b \mathbf{g}^T \mathbf{D} \mathbf{g}) d\mathbf{D} \quad (3.24)$$

Notice that the sum in equation 3.23 is now replaced by the integration sign since the TDF $P(\mathbf{D})$ is a continuous function. To estimate an optimal solution for $P(\mathbf{D})$, we need to acquire many DWI at different gradient direction \mathbf{g}_i and solves the least squares equation:

$$P^*(D) = \underset{P}{\operatorname{argmin}} \sum_i [S_{obs}(\mathbf{g}_i) - S_{calc}(\mathbf{g}_i)]^2 \quad (3.25)$$

where $S_{obs}(\mathbf{g}_i)$ is the observed signal at the gradient direction \mathbf{g}_i . To assure that $P(\mathbf{D})$ represents a good PDF, two constraints must be enforced. First, the non-negativity constraint which can be enforced by assuming that $P(\mathbf{D}) = \exp(R(\mathbf{D}))$ and solving for $R(\mathbf{D})$. Second, ensuring that $\int P(\mathbf{D}) d\mathbf{D} = 1$. The method of gradient descent was used to solve for $R(\mathbf{D})$ in combination of Lagrange multiplier with the second constraint. After the numerical estimation of the TDF, one can determine dominant fiber directions on the unit sphere by computing the tensor orientation distribution (TOD) obtained by integrating out the eigenvalues from the TDF:

$$TOD(\theta_1, \theta_2) = \iint_{\lambda_1, \lambda_2} P(\theta_1, \theta_2, \lambda_1, \lambda_2) d\lambda_1 d\lambda_2 \quad (3.26)$$

In chapter 7, we will use this model for tractography. The technique shows great results in extracting various fiber bundles.

B Spherical Deconvolution

Spherical Deconvolution assumes that the acquired HARDI signal is a result of the convolution of a presumed *single fiber response* function with a *fiber distribution* function specific for the imaged voxel. The

fiber response function was assumed to be Gaussian in (Alexander 2005) and a symmetric diffusion tensor estimated from real datasets in (Tournier et al. 2004; Anderson 2005). In (Jian and Vemuri 2007; Jian et al. 2007), a *mixture of Wishart* model was proposed in order to resolve the fiber crossing problem. Equation 3.8 was rewritten such that the diffusion signal was thought to be the Laplace transform on the space of positive definite tensors. They used a non-linear Levenberg-Marquardt (LM) optimization technique in order to obtain a solution.

3.3.5.2.2 Model-Free Approaches

A The Apparent Diffusion Coefficient

The *apparent diffusion coefficient* (ADC) profile tries to model the intravoxel fiber crossing without assuming a Gaussian diffusion. The ADC tries to find a model which fits equation 3.27 using the acquired DWI measurements of the HARDI data without imposing a model on the diffusion propagator. Hence, it is assumed to be a model-free technique. Unlike the ODF, it was found that the ADC profile have maxima at an angle midway between the crossed fibers not along them as shown in Figure 13c. The ADC profile was modeled with spherical harmonics (SH), high order tensors (HOT) and generalized DTI (gDTI) at (Alexander et al. 2002; Frank 2002; Hirsch et al. 2003; Ozarslan and Mareci 2003; Zhan et al. 2003; Chen et al. 2004; Liu et al. 2004).

$$ADC := D(\mathbf{g}) = -\frac{1}{b} \log \left(\frac{S(\mathbf{g}, t)}{s_0} \right) \quad (3.27)$$

B Q-Ball Imaging (QBI)

In 2002, Tuch presented the Q-ball imaging (QBI) technique (Tuch 2002; Tuch 2004) in which he tries to estimate the ODF by approximating it using the funk-radon transform (FRT). FRT maps spherical functions on a sphere from one function to another. QBI has a numerical solution (Tuch 2004) and a faster analytical solution using spherical harmonic reconstruction which was also found to be more robust to noise (Anderson 2005; Hess et al. 2006; Descoteaux and Deriche 2007).

C Persistent Angular Structure MRI (PAS-MRI)

Jansons and Alexander have proposed a model-free method to estimate the ODF by reconstructing a statistic called: the radially *persistent angular structure* (PAS), \tilde{p} , of the diffusion PDF (Jansons and Alexander 2003). PAS can be described as the function p of the sphere which has a Fourier transform that best describes the normalized diffusion measurements and represents the relative mobility of water in each direction. The problem is formulated by assuming non-zero probabilities only on a spherical shell of radius r_0 and assuming independence of the angular and radial structure of the diffusion PDF:

$$P(\mathbf{r}) = \frac{\tilde{p}(\tilde{\mathbf{r}})}{r_0^2} \delta(|\mathbf{r}| - r_0) \quad (3.28)$$

where $\tilde{\mathbf{r}}$ is a unit vector in the direction of \mathbf{r} . Using a maximum entropy parameterization, $\tilde{p}(\tilde{\mathbf{r}})$ can be reconstructed by fitting the HARDI data with a non-linear optimization algorithm. The method was reported to produce sharper ODF than QBI (Alexander 2005), however it is computationally demanding. A faster solution was found by replacing the maximum entropy by a linear basis of spherical harmonics (Alexander 2005; Seunarine and Alexander 2006).

D Diffusion Orientation Transform

The last model-free approach to present is the *diffusion orientation transform* (DOT) proposed by Özarslan et al. (Özarslan et al. 2006). The DOT can be considered as a variant of QBI. It maps the ADC profile to the diffusion PDF, and then the ODF can be easily obtained using equation 3.21. While the QBI is a smoothed version of the ODF, the DOT is considered to be an exact representation of the diffusion PDF.

3.4 Conclusion

In this chapter, we presented a brief history about the evolution of diffusion MRI. We have also presented different methods used to model the acquired diffusion signal from DWI, DTI and HARDI. We have performed a literature review on different methods used in HARDI to solve the fibers crossing problem.

We have clustered the methods into model-based and model-free. In this thesis, we are going to use the TDF presented in section 3.3.5.2.1 for the tractography application which will be presented in chapter 7.

IV. ANOMALOUS DIFFUSION

4.1 Introduction

Although all the HARDI models are able to resolve fibers crossing to some extent, all but DSI are usually acquired at low b -values ($b \leq 1500$ s/mm²). Studying the DW signal behavior at high b -value ($b > 1500$) has revealed that the signal decay does not follow an exponential decay as was presumed in the Gaussian mono-exponential decay model. Instead, it was found that the decay follows a stretched exponential behavior as shown in Figure 14. In fact, the measured ADC will depend on the experiment time when the water molecules are moving in a restricted or porous medium, which is called *hindered* diffusion. In short times, when molecules do not encounter any boundaries, diffusion may be modeled by the Gaussian model. However, in the long time limit, the motion of a molecule may depend on the starting position and the surrounding environment. In this case, another statistic should be used in order to scale the diffusion constant which gives rise to *anomalous* diffusion (AD).

In order for the brain to carry out its functions, neurons need to transmit electrochemical signals to various neighbor cells and to respond to incoming signals from other cells. Various complex biochemical and metabolic processes controls the electrical properties of neurons. On the micro level, the brain WM tissues are made out of a large amount of myelinated axons which vary in diameter from 2 to 15 μ m. The axons are made out of many neurofilaments with diameters that vary from 10 to 20 nm (Figure 15). This complex structure creates a porous medium in which the water molecules may exhibit AD.

Anomalous (*non-Gaussian*) diffusion is the kind of diffusion which results from the porosity and tortuosity of the diffusive media. It assumes a power law relationship between the MSD and the diffusion time in the form:

$$\langle |r|^2 \rangle \sim Dt^H \quad (4.1)$$

where the *Hurst index* H can be viewed as a measure of the complexity of the medium. When $H > 1$ we call it super-diffusion and when $H < 1$ we call it sub-diffusion and at $H = 1$ we recover the Gaussian model. In the

mathematics of fractals literature, the H is replaced by $2/d_w$ where d_w is called the *fractal dimension* (Metzler 2000). Many frameworks have been developed in order to describe AD. The most famous model is a stochastic framework called the *continuous time random walk* model (CTRW) (Metzler and Klafter 2000). The CTRW model gives rise to a *fractional diffusion equation* (FDE) that can be considered as a fractionalization of Fick's second law, (for information about *Fractional Calculus*, refer to Appendix D).

In this chapter, we are going to present the theory of AD including the CTRW model as well as the fractionalized Fick's law. We are also going to present proposed models in the area of DW-MRI to describe AD in brain tissues. Both, isotropic and anisotropic models are going to be discussed. In chapter 6, we are going to present two new models constructed through a multidimensional fractional order version of the Bloch-Torrey equation. The models are going to be used to study the tortuosity and complexity of the brain tissues.

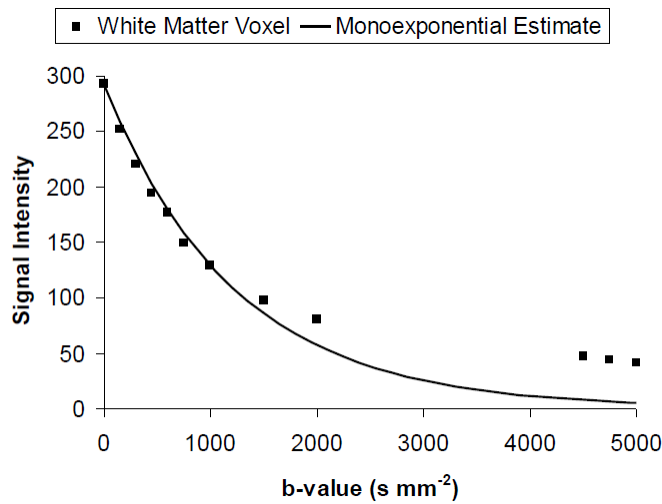


Figure 14: Monoexponential (Gaussian) estimate of the diffusion signal decay plotted on actual DW-MRI measurements for b -values up to 5000 s/mm². Notice the failure of the estimate at high b -values.

Brain white matter

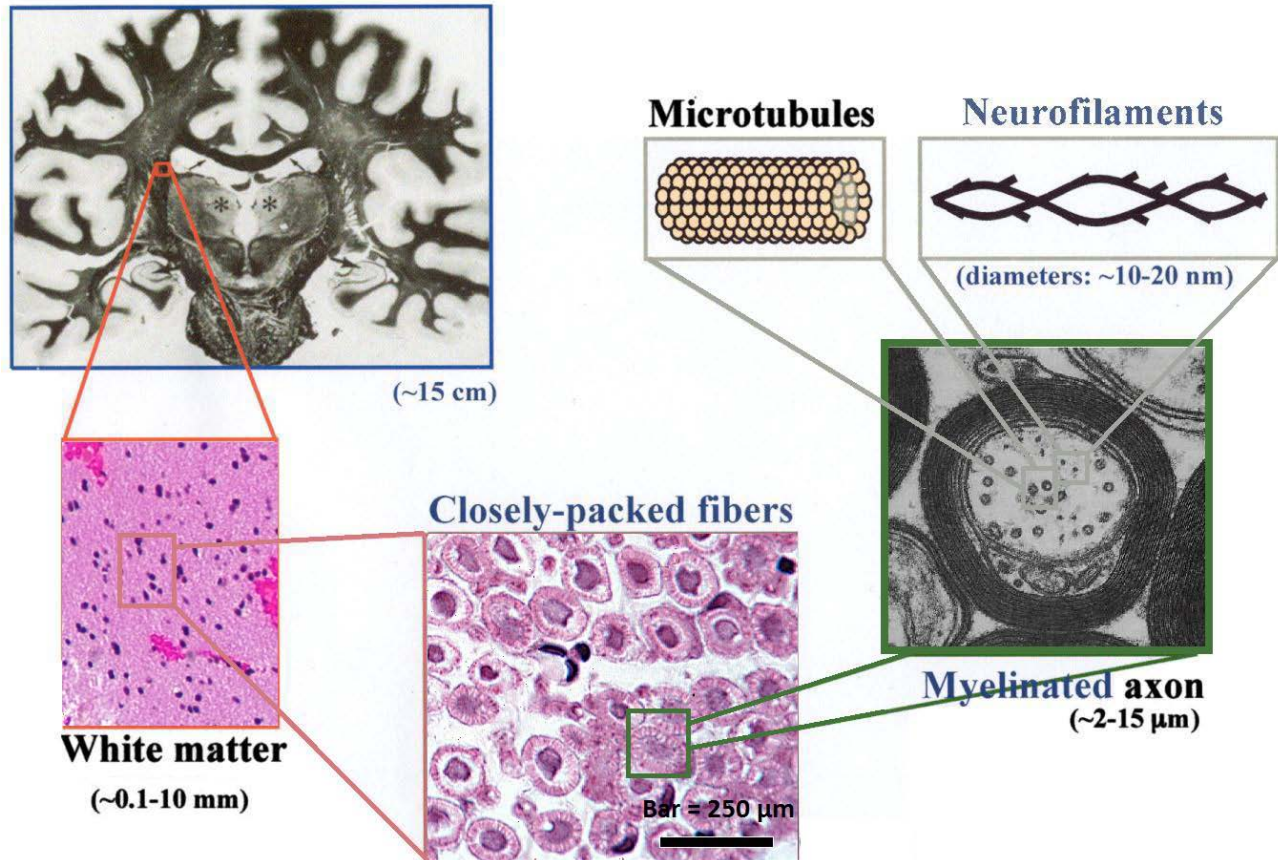


Figure 15: A multi-scale look at neural tissue. The figure is collaged from Wikipedia and the HistoWeb website (<http://www.kumc.edu/instruction/medicine/anatomy/histoweb/index.htm>).

4.2 Continuous Time Random Walk model

The stochastic formulation of diffusion goes back to the random walk model first introduced by Karl Pearson in 1905 (Pearson 1905) and the reformulation done by Albert Einstein in the same year (Einstein and Fürth 1956). AD was studied in the transport theory since the late 1960s. The CTRW model describes the random behavior of a particle in a diffusive medium (Metzler and Klafter 2000). The model was first

introduced by Montroll and Weiss in (Montroll and Weiss 1965). For a detailed review on the model, please review (Metzler and Klafter 2000).

The model starts by considering the random motion of a particle in a medium. The particle is assumed to perform discrete jumps of distances Δx that vary according to a PDF $P(x)$ and waits at each location a period of time Δt according to a PDF $\psi(t)$. The waiting times and displacement PDFs are assumed to be independent in the *separable* CTRW model. Assuming the particle will start moving at time $t = 0$, the total displacement of a particle, $X(t)$, after N identically independent distributed (IID) random jumps in the time interval $[0, t]$ is given by:

$$X(t) = \sum_{i=1}^{N(t)} \Delta x_i \quad (4.2)$$

which is a random sum of random variables. The PDF for waiting time of the N^{th} step:

$$\psi_N(t) = \psi(t)^{*N} \quad (4.3)$$

where $[.]^{*N}$ denotes N times convolution. We define the *survival probability*, $\Psi(t)$, as the probability that no step was taken in the interval $0 \leq t' \leq t$, hence:

$$\Psi(t) = 1 - \int_0^t \psi(t') dt' = \int_t^\infty \psi(t') dt' \quad (4.4)$$

Hence, we can define the probability that the particle have performed N jumps in time t , $P(t, N)$, to be the convolution that the N^{th} step was taken in the interval $[0, t]$ and no steps were taken afterward:

$$\begin{aligned} P(t, N) &= \int_0^t \psi_N(t') \Psi(t - t') dt' \\ &= (\psi_N * \Psi)(t) \\ &= (\psi_1 * \psi_2 * \dots * \psi_N * \Psi)(t) \end{aligned} \quad (4.5)$$

The probability of finding a particle at location x and time t , also called the *motion propagator*, is given by:

$$P(x, t) = \sum_{N=0}^{\infty} P(t, N) P(x)^{*N} \quad (4.6)$$

where, $P(x)$ is the PDF of finding the particle at location x . Taking the Laplace-Fourier transform to the above equation (the Laplace transform w.r.t. time designated with the \sim symbol and the Fourier transform w.r.t. space designate with the \wedge symbol), we get:

$$\hat{P}(k, s) = \sum_{N=0}^{\infty} \tilde{P}(s, N) (\hat{P}(k))^N \quad (4.7)$$

Taking Laplace transform of equation (4.5), we can write:

$$\begin{aligned} \hat{P}(k, s) &= \sum_{N=0}^{\infty} \left(\tilde{\psi}(s) \right)^N \left(\frac{1 - \tilde{\psi}(s)}{s} \right) (\hat{P}(k))^N \\ &= \frac{1 - \tilde{\psi}(s)}{s \left(1 - \tilde{\psi}(s) \hat{P}(k) \right)} \end{aligned} \quad (4.8)$$

The above is known as the *Montroll-Weiss* equation. We can categorize different CTRW processes by defining the characteristic waiting time:

$$T = \int_0^{\infty} t \psi(t) dt \quad (4.9)$$

and the jump length variance

$$\Sigma^2 = \int_{-\infty}^{\infty} x^2 P(x) dx \quad (4.10)$$

As example, consider for instance a finite T and Σ^2 with a Poissonian waiting time PDF in the form $\psi(t) = \frac{1}{T} \exp\left(-\frac{t}{T}\right)$ and a Gaussian jump length PDF in the form $P(x) = \frac{1}{\sqrt{4\pi\sigma^2}} \exp\left(\frac{-x^2}{4\sigma^2}\right)$ with $\Sigma^2 = 2\sigma^2$. Hence, one could rewrite equation 4.8 in the form:

$$\hat{\tilde{P}}(k, s) = \frac{1}{s + \frac{\sigma^2}{T} k^2} \quad (4.11)$$

by approximating $\tilde{\psi}(s) \sim 1 - sT + O(T^2)$ and $\hat{P}(k) = 1 - \sigma^2 k^2 + O(k^4)$, and using the differentiation theorems of Fourier and Laplace transforms, one could simply recover Fick's second law by computing the inverse Laplace-Fourier transform. In fact, the choice of any finite T and Σ^2 leads to the same result (Metzler and Klafter 2000). In the next two sections, we are going to discuss two types of AD: super and sub diffusion.

4.2.1 Long Jumps: Super Diffusion (Levy Flights):

First coined by Benoît Mandelbrot (Mandelbrot 1982) to describe continuous random walks defined by the *survivor* function (commonly known as the *survival* function). The term *Lévy flight* is used nowadays by researchers to describe random walks on lattice with the step-lengths possess a PDF that is heavy tailed or have a stable distribution. The Lévy flight is known to be a Markovian process in nature.

A stable distribution is a continuous probability distribution with a PDF defined as:

$$f(x) = \mathcal{F}^{-1}\{\varphi(t)\} \quad (4.12)$$

where $\varphi(t)$ is the characteristic function (Fourier transform) of the stable distribution given by:

$$\varphi(t) = \exp(it\mu - |ct|^\alpha (1 - i\beta \text{sgn}(t)\Phi)) \quad (4.13)$$

where $i = \sqrt{-1}$, $\Phi = \tan\left(\frac{\pi\alpha}{2}\right)$ for all α , except at $\alpha = 1$ where $\Phi = -\frac{2}{\pi i} \log(t)$, $\mu \in \mathbb{R}$ is a *shift* parameter, $\beta \in [-1, 1]$ is called the *skewness* parameter, a measure of asymmetry, and $c \in [0, \infty]$ is a *scale* parameter. This family of functions cannot be expressed analytically except for the special cases of the Gaussian ($\alpha = 2$), and the Cauchy ($\alpha = 1$) distributions. With the exception of the normal distribution, the variance of a stable distribution is infinite.

In the CTRW model, consider the case when T is finite, $\Sigma^2 = \infty$, and $P(x) = P(-x)$ (i.e. $\mu = \beta = 0$ in 4.13), we can write:

$$\hat{P}(k) = \exp(-a|k|^\alpha) \sim 1 - B|k|^\alpha, k \rightarrow 0, 0 < \alpha < 2 \quad (4.14)$$

Consider $\tilde{\psi}(s) \sim 1 - sT, s \rightarrow 0$, substituting in 4.8, we obtain:

$$\hat{\tilde{P}}(k, s) = \frac{1}{s + \frac{B}{T}|k|^\alpha} \quad (4.15)$$

Taking the Laplace-Fourier inverse transform, one obtains the FDE:

$$\frac{\partial P(x, t)}{\partial t} = \frac{B}{T} {}_{RZ}D^\alpha P(x, t) \quad (4.16)$$

where ${}_{RZ}D^\alpha$ is Riesz fractional derivative having the property $\mathcal{F}\{{}_{RZ}D^\alpha f(x)\} = -|k|^\alpha \mathcal{F}\{f(x)\}$ (see Appendix D). One can compute the Fourier transform of the motion propagator, obtaining:

$$\hat{P}(k, t) = \exp\left(-\frac{B}{T}|k|^\alpha\right) \quad (4.17)$$

which is the characteristic function of a centered and symmetric Lévy distribution.

4.2.2 Long rests: Sub Diffusion:

Sub-diffusion is characterized by an infinite average waiting time T and a finite jump length variance Σ^2 . We introduce a long-tailed waiting time PDF with the asymptotic behavior described by:

$$\psi(t) \sim \left(\frac{t_0}{t}\right)^{1+\gamma}, 0 < \gamma < 1 \quad (4.18)$$

using Tauberian theorems, which relate the power-law scaling of a Laplace transform at small s to the scaling in original space for large t , the corresponding asymptotic Laplace can be written in the form:

$$\tilde{\psi}(s) = 1 - (t_0 s)^\gamma, s \rightarrow 0 \quad (4.19)$$

Assuming a Gaussian jump length PDF with the Fourier transform is in the form:

$$\hat{P}(k) \sim 1 - \frac{\sigma^2 k^2}{2}, k \rightarrow 0 \quad (4.20)$$

Substituting in 4.8, one obtains:

$$\hat{\hat{P}}(k, s) = \frac{1}{s \left(1 + t_0 \left(\frac{\sigma^2 k^2}{2} s \right)^\gamma \right)} \quad (4.21)$$

Computing the inverse Laplace transform, one would get:

$$\hat{P}(k, t) = E_\gamma \left(- \left(\frac{t}{E(k)} \right)^\gamma \right) \quad (4.22)$$

where $E_\gamma(z)$ is the Mittag-Leffler function described in Appendix D. It can be proven that $P(x, t)$ satisfies the FDE in the form:

$$\frac{\partial P(x, t)}{\partial t} = \left(\frac{\sigma^2}{2t_0^\gamma} \right) {}^{RL}D_t^{1-\gamma} \left\{ \frac{\partial^2 P(x, t)}{\partial x^2} \right\} \quad (4.23)$$

where ${}^{RL}D_t^{1-\gamma}$ is the Riemann-Liouville fractional derivative described in Appendix D.

To summarize, we have presented the separable CTRW model which can be used to describe AD in porous mediums. The model is based on the construction of two probability distributions. The first, $P(x)$, represents the probability that a particle moving on a lattice will omit a jump Δx . The second, $\Psi(t)$, represents the probability that the particle will remain in the current location for a time Δt . A general form for the motion propagator was developed using the Laplace-Fourier transform. Two cases were discussed according to the average waiting time and the variance of the jump lengths. A finite average waiting time and infinite variance of the jump lengths would lead to a super-diffusive process (*Lévy flight*) characterized by long jumps while an infinite average waiting time and a finite variance of the jumps length would result into a sub-diffusive process characterized by long rests between jumps. A simulation to both cases is illustrated in Figure 16.

In the next section, we are going to review different models for DW-MRI that took into consideration the anomalous diffusive behavior of water molecules in brain tissues. Models will be categorized by being either isotropic which cares only about modeling AD in one gradient direction. Other anisotropic models try to describe AD in different directions of space in order to test its dependence on the gradient direction.

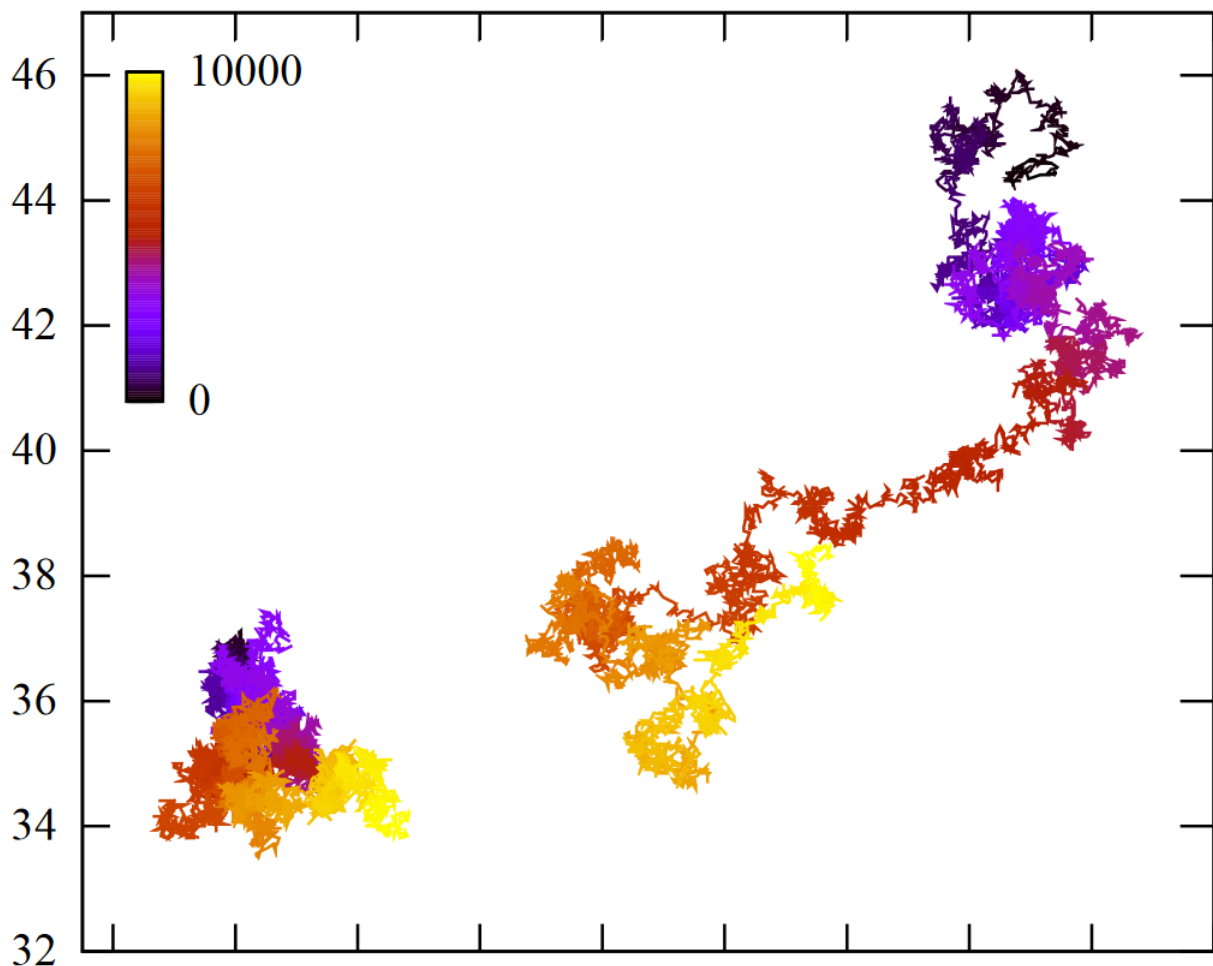


Figure 16: Comparison of the trajectories of a Brownian or sub-diffusive random walk (left) and a Lévy walk with index $H = 1.5$ (right). Whereas both trajectories are statistically self-similar, the Lévy walk trajectory possesses a fractal dimension, characterizing the island structure of clusters of smaller steps, connected by a long step. Both walks are drawn for the same number of steps (10000). Figure is adapted from Wikipedia.

4.3 Anomalous Diffusion Magnetic Resonance Imaging

4.3.1 Isotropic Models

An early model was the *mixture of Gaussians* or so called *bio-exponential* model which was previously described in section (3.3.5.2.1-A). Bennett et al. proposed a *stretched exponential* model (Bennett et al. 2003) and he introduced the “*stretching parameter*” α which takes a value from 0 to 1 in the equation:

$$S = S_0 \exp(-(bD)^\alpha) \quad (4.24)$$

Bennett et al. found that his model performs better than the bio-exponential one in 20% of the voxels even though it has less parameters for tuning. The stretching parameter was found to be linked with the heterogeneity of the diffusive media. Later, it has been observed that it is different in different directions.

Magin et al. (Magin et al. 2008) fractionalized the Bloch-Torrey equation and introduced two new parameters: μ to preserve units and β simultaneously acting as the fractional order of derivative in the proposed FDE and as the stretched exponent in the solution. He wrote the transverse magnetization in the rotating frame in the form:

$$\frac{dM_{xy}}{dt} = -i\gamma(\mathbf{r} \cdot \mathbf{G})M_{xy} + D\mu^{2(\beta-1)}\nabla^{2\beta}M_{xy} \quad (4.25)$$

where $\nabla^{2\beta} = (D_x^{2\beta} \quad D_y^{2\beta} \quad D_z^{2\beta})$ is a sequential Riesz fractional order Laplacian operator in space (see Appendix D). Solving the above equation for a Stejskal-Tanner pulse sequence allows us to write the DW signal in the form:

$$S = S_0 \exp\left(-|q|^{2\beta}\mu^{2\beta-2}D\left(\Delta - \frac{2\beta-1}{2\beta+1}\delta\right)\right) \quad (4.26)$$

The new parameter μ (mm) was found to be directly proportional with tortuosity while β which varies from 0.5 to 1 was found to be inversely proportional with the complexity of the surroundings. In Zhou et al. (Zhou et al. 2010) β and μ brain maps were created. The scalar ADC, D , was first computed at low b -value ($b =$

1000 s/mm²). Then, non-linear least squares method based on the LM algorithm was used to fit for μ and β using multiple b -values. A great correlation between brain tissues complexity and low beta values was found. In precise, β values for CSF was found to follow a value near to unity driving equation 4.4 back to the Gaussian model, while β for WM and GM was 0.64 ± 0.01 and 0.82 ± 0.01 respectively indicating a slower decay for WM compared to GM.

Equation 4.26 was also applied to sephadex gel, a material made of a chemically cross-linked network making it an excellent medium with uniform pore size (Magin et al. 2011). Different pore sizes were tested with different diffusing time Δ (recall equation 3.16) in order to test the effect on β and μ . Beta was found to decrease with increasing gel complexity (smaller pore diameter) while μ was found to increase with diffusion time as well as with tortuosity.

Recently, Hanyga and Seredyńska have used a pseudo-differential operator, Q , in the Bloch-Torrey equation to describe AD in DW-MRI (Hanyga and Seredynska 2012). A pseudo-differential operator (PDO) is simultaneously an extension of the concept of differential operator and of that of a singular integral operator. They are used extensively in the theory of partial differential equations. A PDO, Q , acting on a function $f(\mathbf{x})$ is only defined in the Fourier domain. Hence, we can write $Q f(\mathbf{x}) = \mathcal{F}^{-1}\{Q(\mathbf{k})f(\mathbf{k})\}$. For more information about PDOs, we refer the reader to (Hörmander 1987; Sato 1999). In their work, Hanyga and Seredyńska wrote the Bloch-Torrey equation in the form:

$$\left(D + i\gamma(\mathbf{G}(t) \cdot \mathbf{x}) + \frac{1}{T_2}\right)^\beta M_{xy} = Q M_{xy} \quad (4.27)$$

where D^β denotes the Caputo derivative (see Appendix D), β is a parameter satisfying $0 < \beta \leq 1$, Q is the PDO defined in the Fourier domain as $Q(\mathbf{k}) = -\int_S |\mathbf{k} \cdot \mathbf{y}|^\alpha m(dy)$ where S denotes the surface of the unit sphere centered at 0, m is a measure on the unit sphere and α is a parameter satisfying the inequalities $0 < \alpha \leq 2$. Solving the above equation, we get:

$$M_{xy} = M_0 E_{\beta, 1 + \frac{\alpha}{\beta}} \left(-\gamma^\alpha t^{\alpha + \beta} \int_S |\mathbf{g} \cdot \mathbf{y}|^\alpha m(d\mathbf{y}) \right) \quad (4.28)$$

where E is the Mittag-Leffler function described in Appendix D, \mathbf{g} is a unit vector in the direction of the applied gradient. In the special case when $\beta = 1$, the Mittag-Leffler falls into an exponential. When $\beta = 1$ and $\alpha = 2$, we recover the DTI model. A solution based on the replacement of the measure m by a series of spherical harmonics was suggested. However, the solution was not tested on real DW data. Though this model has suggested a solution to the fiber crossing problem by the introduction of spherical harmonics, however, it treated AD as an isotropic problem through the utilization of the parameter α .

4.3.2 Anisotropic Models

Recently, Hall and Barrick (Hall and Barrick 2012) suggested a two-step anomalous diffusion tensor imaging scheme based on an old scalar model they have previously developed (Hall and Barrick 2008). Their old model starts from equation (3.9) and represents the signal decay as:

$$S(b) = S_0 \exp(-Ab^\gamma) \quad (4.29)$$

where A is a constant and γ is the stretched exponential previously suggested by Bennett. They tried to investigate the anisotropy in the stretched exponential term by fitting multi-directional DW data on a generalized tensorial version of the stretched exponential model which reads:

$$S(b) = S_0 \exp(-[b\mathbf{A}(\mathbf{r})]^\Gamma) \quad (4.30)$$

where \mathbf{r} is a unit vector defined on the unit sphere, \mathbf{A} and Γ are rotationally invariant tensors called *distributed diffusivity tensor* and *anomalous exponent tensor* respectively (Figure 18). Both tensors are symmetric and assumed to be well described by Gaussian ellipsoids. Using the gradient direction vector \mathbf{g} they can be described as follow:

$$\mathbf{A} = \begin{bmatrix} g_x & g_y & g_z \end{bmatrix} \begin{bmatrix} A_{xx} & A_{xy} & A_{xz} \\ A_{xy} & A_{yy} & A_{yz} \\ A_{xz} & A_{yz} & A_{zz} \end{bmatrix} \begin{bmatrix} g_x \\ g_y \\ g_z \end{bmatrix} \quad (4.31)$$

$$\mathbf{\Gamma} = [g_x \quad g_y \quad g_z] \begin{bmatrix} \Gamma_{xx} & \Gamma_{xy} & \Gamma_{xz} \\ \Gamma_{xy} & \Gamma_{yy} & \Gamma_{yz} \\ \Gamma_{xz} & \Gamma_{yz} & \Gamma_{zz} \end{bmatrix} \begin{bmatrix} g_x \\ g_y \\ g_z \end{bmatrix} \quad (4.32)$$

Decomposition of both tensors to eigenvalues and eigenvectors has shown similar behavior of \mathbf{A} to the diffusion tensor and the eigenvector corresponding to the largest eigenvalue of the $\mathbf{\Gamma}$ tensor points to the direction of the greatest environment complexity.

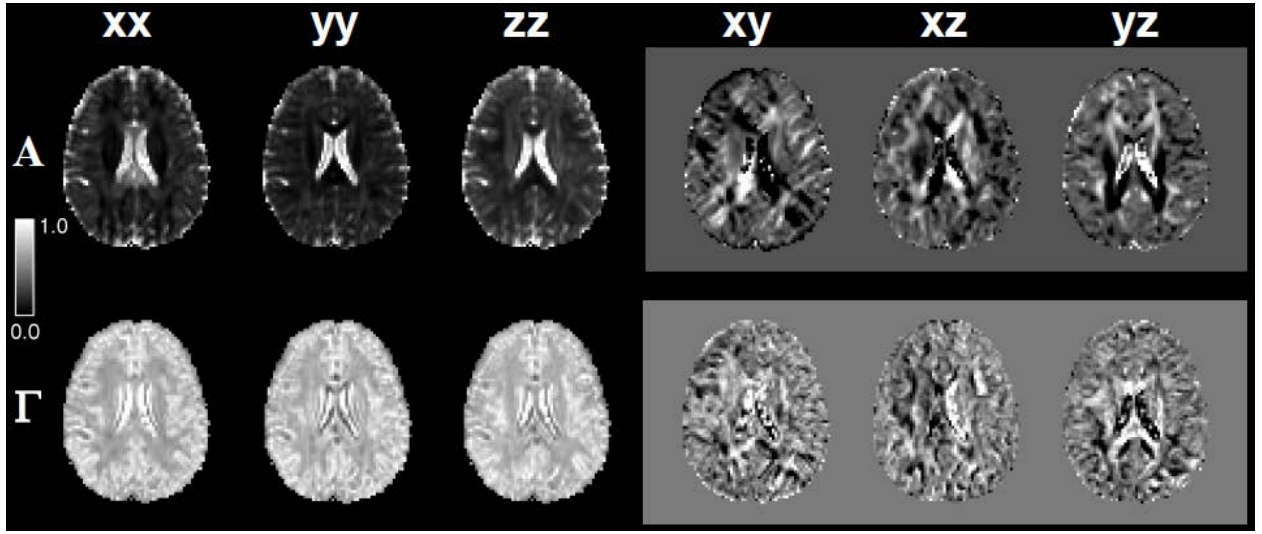


Figure 17: Results of the fitted \mathbf{A} and $\mathbf{\Gamma}$ tensors in the Hall and Barrick model. Figure adapted from Tom Barrick presentation at the Interpore 2012 conference.

De Santis et al. (De Santis et al. 2011) have assumed that the DW signal is combined from three stretched exponentials existing along the three main axes of diffusion. She wrote:

$$S(b) = S_o \prod_{i=1}^3 \exp(-A_i b \gamma^i) \quad (4.33)$$

where A_i ($\text{mm}^{2\gamma_i}/\text{s}^{\gamma_i}$) is a generalization of the diffusion constant. De Santis et al. have proposed the following protocol to compute the six unknowns in equation (4.31): first the eigenvectors were computed from the classical DTI tensor. Then, the rotation matrix that links the laboratory frame with the DTI orthogonal eigenvectors was computed. Finally, equation (4.31) was fit to compute the six unknowns. Their protocol implies the coincidence of both the DTI and AD coordinates. A strong correlation between anomalous anisotropy (γA) (the mean squared difference between the stretching exponents and their mean values) and DTI FA was found. Anomalous anisotropy was computed using (3.19) by replacing λ_i by γ_i . Moreover, a positive correlation was found between DTI MD and the mean value of the stretched exponents ($M\gamma$).

4.4 Conclusion

In this chapter, we have presented the theory of AD, the CTRW model and discussed two main special cases: super and sub diffusion. We have also presented isotropic and anisotropic AD-MRI models. We can notice that all of the anisotropic models lack a mathematical derivation emerging from the Bloch-Torrey equation. In summary, the work to date suggests that there is additional information in the directional dependence of the stretched or anomalous diffusion exponent. In chapter 6, we will present two anisotropic models based on the fractionalization of the Bloch-Torrey equation in a multidimensional formulation that separates the tissue anisotropy from the directional dependence of the stretched exponential parameters.

V. NEURONAL NETWORKS

5.1 Introduction

Neuroscience has known the concept of networks since the second half of the 19th century. The hypothesis of the “*disconnection syndromes*” suggested by Wernicke, Lichtheim, Liepmann, Dejerine and others based on clinico-pathological correlations (Catani and Mesulam 2008). Since then, the concept was left for a decade until its reintroduction by Norman Geschwind in 1965 (GESCHWIND 1965). Modern imaging techniques have allowed us to study the human brain as a complex system by modeling the brain as a network. Inspired by the sequencing project of the human genetic code, the genome, the term *connectome*, first introduced in (Hagmann 2005; Sporns et al. 2005), describes the map of neural connections in the brain. A connectome, also called *brain connectivity network*, consists of *nodes* which represent gray matter regions and *edges* connecting nodes which represent WM fibers in structural networks, or correlations between two BOLD (blood oxygen level dependent) time sequences in the case of functional networks. Mathematical tools have been borrowed from the field of graph theory and applied to connectomes in order to analyze them (Sporns et al. 2005; Rubinov and Sporns 2010).

In this chapter we are going to present the basics of graph theory used to analyze brain networks. Moreover, we are going to focus on a specific property of sparse networks (networks having the number of nodes in the order of the number of edges) called *community structure*. In chapter 8, we argue that to better measure a community structure, one has to consider not only connections within communities, but also connections between communities (in that one seeks to balance interactions within versus between communities). A novel metric is introduced to better measure community structure by jointly maximizing within-community integration and minimizing between-community separation. We use this metric to study the topological structure of the human brain by extracting the community structure of brain networks. Moreover, we perform group studies to detect changes in that structure due to various neuropsychological diseases.

5.2 Graph Theoretical Concepts for Network Analysis

The first notion of graph theory dates back to 1736 when Euler tried to solve the seven bridges of Königsberg's problem. Nowadays called Kaliningrad, the city of Königsberg included two large islands interconnected with each other and the mainland by seven bridges. The problem was to find a path through the city that would cross each bridge only once. By representing the problem into a graph, Euler has proven that this was impossible. His paper (Euler 1741) is considered to be the foundation of graph theory in mathematics. Later on, the graph theoretic concepts have found use in different fields such as electrical circuit analysis, computer science, and sociology.

A *graph* is made out of a set of *nodes* or *vertices* connected by *edges* (lines) and can be abstracted into a network. Networks can be *directed* or *undirected*, and *weighted* or *unweighted* (binary). A path is a walk through the graph where each node is visited only once. An *unweighted* network made of n nodes can be described by an $n \times n$ adjacency matrix A , where every non-diagonal entry a_{ij} is of value 1 if an edge exists between vertex i and vertex j and zero otherwise. On the other hand, a *weighted* network made of n nodes can be described by an $n \times n$ distance matrix W , where every non-diagonal entry w_{ij} describes the weight between vertex i and vertex j . *Undirected* networks possess a symmetric adjacency or distance matrices. Figure 18 shows different definitions used in graph theory. A weighted network can be converted into an unweighted network using a threshold. In that case, connections are only established if the weight d_{ij} is above that threshold. Unweighted networks simplify the calculation of many network measures. However, the choice of a threshold can be very problematic. A fixed threshold would lead to a different number of edges in different networks. On the other hand, comparing unweighted networks with the same number of edges means that a different threshold may be used for each network. In this thesis, we are going to focus on weighted undirected networks. For a structural brain network, nodes could be neurons or cortical regions and edges could be axons or WM tracts. Alternatively, edges could signify correlations between the activity patterns of nodes forming functional brain networks. Network analysis techniques can be applied to the analysis of brain networks. In this thesis, we focus only on structural weighted networks.

One can measure the network *topological* properties from its matrix representation using various metrics. A first metric is the node *degree* which is simply its number of edges. The *degree distribution* is defined as being the probability distribution of nodal degrees over all the nodes in the network. It can be used as a measure for the network development and resilience. This metric can be used to test the ability of anatomical brain connectivity to resist decay due to different neuropsychiatric diseases such as Alzheimer's disease. Another measure of resilience is the node's *average neighbor degree* defined as the ratio between the sum of its neighbors' degrees and the number of neighbors.

An important characteristic in graphs is *functional integration* which is defined as the ability to combine information from the various parts of the network. The concept of a path is well prominent in metrics used to measure network integration. A key metric is the *shortest path length* defined as the shortest path between two nodes. The *characteristic path length* (CPL) is the average path length over all possible pairs of nodes. Networks with longer CPL exhibit information flows that are “impeded” or “slower” compared to those with shorter CPL, and are thus less efficient. A related global metric, the *global efficiency* (E_{glob}), calculates the average inverse shortest length between all pairs of nodes. Thus the higher E_{glob} , the more efficient is the network. It has been suggested that E_{glob} may be advantageous over CPL in measuring network integration as CPL values can be heavily influenced by very long path lengths (Achard and Bullmore 2007).

Another important family of metrics for graphs is measures of network *clustering* or *segregation* such as the *clustering coefficient* and *transitivity*. These metrics try to quantify the existence of groups and clusters in the network. Such groups could be considered as dedicated processing units or centralized functional centers in the case of brain networks. The *clustering coefficient* (CC) of a node is defined as the percentage of its neighbors that are also connected among them. Thus, nodes with high CC form locally interconnected clusters. The CC of the whole network averages CC across all nodes. A related metric to network clustering, *transitivity*, is only defined on the whole network by modifying the mathematical formulation of CC such that its values are less susceptible to outliers.

It has been shown that brain networks are sparse (Bassett and Bullmore 2006). In sparse networks, the ability to collect nodes in communities is called the network *community structure*. Using this feature, we try to extract groups and find their exact size and composition revealing valuable information about the network topological and functional structure. A widely used metric for measuring and extracting the community structure of a network is called *modularity* (Newman 2004). In this thesis we are going to present a new method to extract community structures of networks and we are going to apply it to brain networks. In the next section, we are going to perform a literature review about the different methods used to extract community structures, a focus will be given to the modularity metric.

Important nodes (hubs) that play an interactive role with different clusters can be detected by measures of *centrality* such as nodal *degree* and *betweenness centrality*. The *betweenness centrality* measures the density of nodes surrounding the node under test. A node betweenness is larger when it lies between many pairs of nodes. This is done by computing the ratio between shortest paths that pass through the node under test and all shortest paths in the network.

Lastly, networks with *small-world* properties have been theorized to exhibit an optimal balance between functional integration and local clustering (Watts and Strogatz 1998). Mathematically, the *small-worldness* which computes the normalized CC divided by the normalized CPL, both normalized against random networks with globally the same number of connections. Random networks are generated by establishing each potential connection between nodes with a probability p and have low clustering and short path length, (Erdős and Rényi 1960). A higher value of small-worldness indicates a higher level of clustering with a short path length compared to a randomly generated network. It has been shown that the brain exhibits small-worldness which indicates that segregated processing exists in locally specialized and highly clustered nodes as well as globally distributed processing throughout the network with a short CPL (Sporns and Zwi 2004). The mathematical definition of the graph theory metrics described above is presented in Table III.

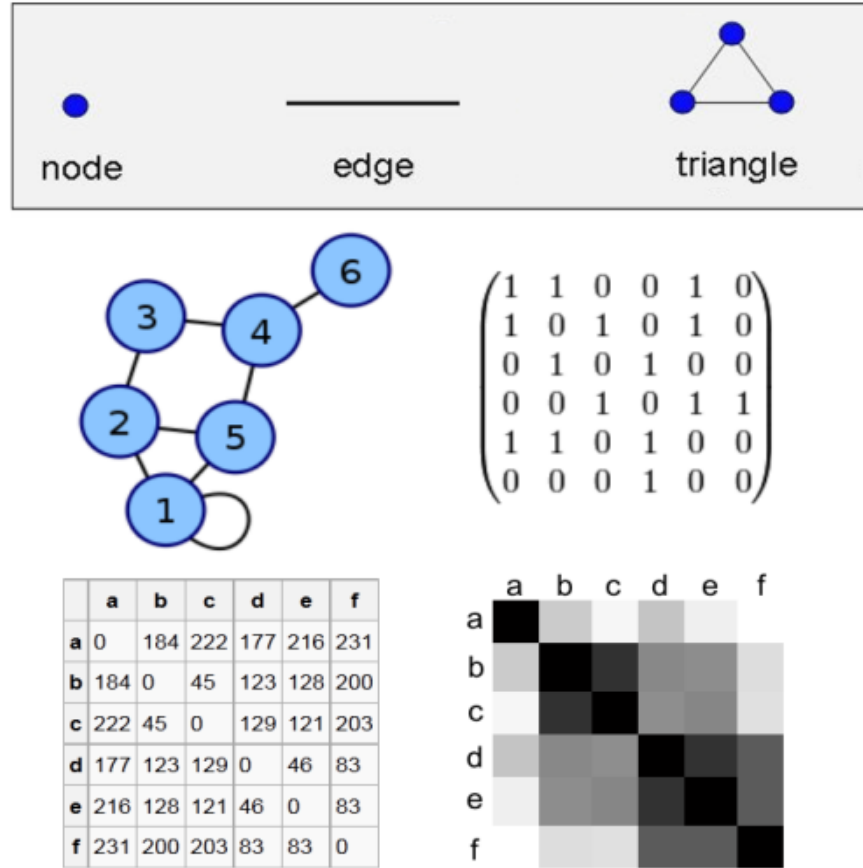


Figure 18: Top row shows the definition of a node, an edge, a triangle, and a connected triplet. Second row shows an unweighted undirected graph and its adjacency matrix. Third row shows a weighted undirected distance matrix and a grayscale visualization of its entries. The figure is adapted from Wikipedia.

Table III: Mathematical definitions of network metrics. Shading groups metrics of same family.

Metric	Definition
Basic concepts and notation	N is the set of all nodes in the network, and n is the number of nodes.
	L is the set of all links in the network, and l is number of links.
	(i, j) is a link between nodes i and j , $(i, j \in N)$.
	Links (i, j) are associated with connection weights w_{ij} .
	W is the sum of all weights in the network, computed as $W = \sum_{i,j \in N} w_{ij}$

Number of triangles around a node i ,

Number of triangles

$$t_i = \frac{1}{2} \sum_{j,h \in N} (w_{ij} w_{ih} w_{jh})^{\frac{1}{3}}$$

Degree

for node i : $k_i = \sum_{j \in N} w_{ij}$

Betweenness centrality of node i (Freeman 1979),

Betweenness centrality

$$b_i = \frac{1}{(n-1)(n-2)} \sum_{\substack{h,j \in N \\ h \neq i, h \neq j, i \neq j}} \frac{\rho_{hj}(i)}{\rho_{hj}}$$

where ρ_{hj} is the number of shortest paths between h and j , and $\rho_{hj}(i)$ is the number of shortest paths between h and j that pass through i .

Cumulative degree distribution of the network (Barabási and Albert 1999),

Degree distribution

$$P(k) = \sum_{k' \geq k} p(k')$$

where $p(k')$ is the probability of a node having degree k' .

Average neighbor degree (modified from (Barrat et al. 2004)),

Average neighbor degree

$$k_{nn,i} = \frac{\sum_{j \in N} w_{ij} k_j}{k_i}$$

Shortest path length (distance), between nodes i and j ,

Shortest path length

$$d_{ij} = \sum_{a_{uv} \in g_{i \leftrightarrow j}} f(w_{ij})$$

where f is a map from weight to length and $g_{i \leftrightarrow j}$ is the shortest path between i and j .

Characteristic path length of the network (Watts and Strogatz 1998),

Characteristic path length

$$L = \frac{1}{n} \sum_{i \in N} L_i = \frac{1}{n} \sum_{i \in N} \frac{\sum_{i \in N, i \neq j} d_{ij}}{n-1}$$

where L_i is the average distance between node i and all other nodes.

Local efficiency of the network, generalized from (Latora and Marchiori 2001),

Local efficiency

$$E_{loc} = \frac{1}{2} \sum_{i \in N} \frac{\sum_{i,h \in N, i \neq j} (w_{ij} w_{ih} [d_{ij}(N_i)]^{-1})^{\frac{1}{3}}}{k_i(k_i - 1)}$$

Global efficiency	<p>Global efficiency of the network, generalized from (Latora and Marchiori 2001),</p> $E = \frac{1}{n} \sum_{i \in N} E_i = \frac{1}{n} \sum_{i \in N} \frac{\sum_{j \in N, i \neq j} d_{ij}^{-1}}{n-1}$ <p>where E_i is the efficiency of node i.</p>
Clustering coefficient	<p>Clustering coefficient of the network (Onnela et al. 2005),</p> $C = \frac{1}{n} \sum_{i \in N} C_i = \frac{1}{n} \sum_{i \in N} \frac{2t_i}{k_i(k_i - 1)}$ <p>where C_i is the clustering coefficient of node i ($C_i = 0$ for $k_i < 2$).</p>
Transitivity	<p>Transitivity of the network, generalized from (Newman 2003),</p> $T = \frac{\sum_{i \in N} 2t_i}{\sum_{i \in N} k_i(k_i - 1)}$
Modularity	<p>Modularity of the network, generalized from (Newman 2004),</p> $Q = \frac{1}{W} \sum_{i,j \in N} \left(w_{ij} - \frac{k_i k_j}{W} \right) \delta(i, j)$ <p>where the network is fully subdivided into a set of non-overlapping modules M, $\delta(i, j)$ is 1 if nodes i and j are in the same module and zero otherwise.</p>
Measure of network small-worldness.	<p>Network small-worldness, generalized from (Humphries and Gurney 2008),</p> $S = \frac{C/C_{rand}}{L/L_{rand}}$ <p>where C and C_{rand} are the clustering coefficients, and L and L_{rand} are the characteristic path lengths of the respective tested network and a random network. Small-world networks often have $S \gg 1$.</p>

5.3 Community Structure: A Literature Review

We define *community structure* as being the topological organization of sparse networks in which they are partitioned into a set of non-overlapping communities, also referred to as *modules* or *clusters*. Another definition for communities is that they are partitions of the graph (subgraphs) in which the number of links (edges) inside is much larger than the number of edges linking its nodes with the rest of the graph. Extracting the community structure of a network has been an important and challenging task for different fields of science such as sociology, biology and computer science (Fortunato 2010). Community structure is considered to be a measure of network segregation. It helps in understanding the organizational and functional aspects of complex networks. It is believed that nodes within a community will probably share common properties and/or play similar roles within the graph. The problem is usually considered a class of non-deterministic polynomial time (NP)-hard problem whose solution could only be reached in a polynomial time using approximation (rather than exact) algorithms in order to lower the computational complexity (Fortunato 2010). While in this thesis we will address only the case of partitioning undirected graphs into non-overlapping communities (i.e. assigning each node to only one community), it should be noted that algorithms that take into account overlapping communities have been proposed, but they are computationally demanding (Fortunato 2010). A big challenge in finding different clusters in a network is that the number of communities is usually unknown. However, several methods and algorithms have been developed for that purpose with different computational complexity and varying levels of success.

5.3.1 Traditional Methods

The *minimum-cut*, also called *graph partitioning*, is considered the oldest technique used to extract the community structure. It was used in parallel computing for load balancing in order to minimize communication between processors. In this technique, a network is usually divided into a predetermined number of clusters of approximately the same size such that the number of edges between them is minimized. The need of a predetermined number of clusters in this method is considered a limitation when it comes to

community structure extraction, as it will result into communities regardless of whether they are implicit in the network or not (Newman 2004).

5.3.2 Hierarchical Clustering

To reveal the multi-level structure of a system, one could use *hierarchical clustering* algorithms (Hastie et al. 2001). There exist two main types of hierarchical clustering techniques: the *agglomerative* and the *divisive*. The *agglomerative* method starts bottom-up. At the first level, every node is a community by itself. In each subsequent level, two communities that are considered closest (with respect to a similarity measure) are merged into one, until all nodes are in one community. The *divisive* method follows the opposite or a top-down approach. It starts with all nodes belonging to one single community, and at each level, each community is further split into several sub-communities (unlike the agglomerative method, the divisive clustering usually uses a dis-similarity measure). It should be noted that one may choose to stop the clustering process at a pre-specified level (stopping criteria can be a given number of communities or the optimization of a quality function (Fortunato 2010). Dendrograms are often used in order to illustrate the resultant tree-structure. Hierarchical clustering have been widely used due to its advantage that it does not require a previous knowledge on the number and size of communities. However, due to the dependence of the procedure on the chosen similarity (or dissimilarity) measure, one would not be able to choose which partitions better represent the community structure of the graph (Fortunato 2010). Moreover, the constructed hierarchical structure may be artificial on the graph under analysis which might not possesses a hierarchical structure at all.

5.3.3 Divisive Algorithms

Another algorithm was presented by Girvan and Newman in (Girvan and Newman 2002) depends on edge betweenness. Using the edge betweenness centrality metric, the algorithm identifies nodes that lie between communities and then removes the interconnecting edges, thus isolating the communities. The algorithm gives good results but it suffers from a slow runtime of order $O(m^2n)$ for a network of n nodes and m edges due to the heavy calculations needed to compute the betweenness metric. In order to improve its

speed, a variation of the algorithm based on Monte-Carlo estimation was suggested in (Tyler et al. 2003; Wilkinson and Huberman 2004). Another speeded version was presented by Rattigan et al. (Rattigan et al. 2007) in which an approximation of the edge betweenness was instead computed.

5.3.4 Modularity Optimization

One of the most widely used techniques for community structure extraction is the modularity maximization, presented in Table III. The Q modularity was first introduced by Newman and Girvan in (Newman and Girvan 2004) as a quality metric for a particular partitioning of a network. Then, it was suggested that its maximization would yield the community structure of the network (Newman 2004). The modularity maximization method detects communities by searching over possible divisions of a network for one or more that have particularly high modularity. Modularity was designed based on the idea that a graph has a community structure cannot be a *random graph*. As proposed by Erdős and Renyi (Erdős and Rényi 1960), a *random graph* is defined as being networks with the probability of edges between nodes is of value p , where $0 \leq p \leq 1$. Hence, a random graph is not expected to have a community structure since no connectional preference exists between nodes in order to form groups. Starting from the random graph definition, one can introduce the notion of the *null model* as being a random graph with some structural features of a given network. The modularity is defined by comparing the actual density of edges and the expected density in case of a null model. Hence, one can write modularity in the form:

$$Q = \frac{1}{2W} \sum_{ij} (w_{ij} - P_{ij}) \delta(i, j) \quad (5.1)$$

where the sum runs over all pairs of vertices, w_{ij} is the weight of the edge connecting nodes i and j , W is the sum of all weights in the network, P_{ij} represents the expected number of edges between nodes i and j in the null model, and $\delta(i, j)$ yields one if vertices i and j are in the same community and zero otherwise. Newman and Girvan have proposed a null model where the edges of the original network are randomly rewired such that the expected degree of each node remains the same (Newman and Girvan 2004). Imposing this null model on the definition of Q , and under independency assumption, the probability that nodes i and j with

degrees k_i and k_j are connected is given by: $p_i p_j = \left(\frac{k_i}{2W}\right) \left(\frac{k_j}{2W}\right)$. Hence, the expected number $P_{ij} = 2W p_i p_j = \frac{k_i k_j}{2W}$, and we can re-write Q in the form:

$$Q = \frac{1}{2W} \sum_{ij} \left(w_{ij} - \frac{k_i k_j}{2W} \right) \delta(i, j) \quad (5.2)$$

It is important to state that modularity was first defined on adjacency (binary) matrices then it was adapted for weighted networks. The value of Q usually lies in the range $[-0.5, 1]$. An exhaustive search for the maximum modularity is impossible since the problem is of type NP-complete (Brandes et al. 2006). In the next sections, we are going to state various techniques used for the maximization of modularity.

5.3.3.1 Greedy Algorithms

The very first algorithm used for modularity maximization was a greedy method based on agglomerative hierarchical clustering suggested by Newman (Newman 2004). In this method, nodes are joined to form larger clusters under the condition of an increase in modularity. Variations of that algorithm exist in order to improve speed and efficiency in (Clauset et al. 2004; Danon et al. 2006; Newman 2006; Pujol et al. 2006; Du et al. 2007; Wakita and Tsurumi 2007; Schuetz and Caflisch 2008; Schuetz and Caflisch 2008; Ye et al. 2008; Mei et al. 2009; Noack and Rotta 2009; Xiang et al. 2009). These algorithms can work on networks with a maximum of 10^6 nodes.

A very fast, yet greedy agglomerative algorithm was proposed by Blondel et al. (Blondel et al. 2008) and consists of two steps. In the first step, each node is assigned to a community, and then we perform a random sweep on all nodes to compute the gain in modularity, ΔQ , when node i is joined with node j , the largest positive gain is chosen. In the second step, communities are replaced by supernodes, and the edges interconnecting each two communities are summed to yield one edge between each two supernodes. Then the two steps of the algorithm are repeated until no gain in modularity can be achieved. This algorithm can work on large networks in the order of 10^9 edges.

5.3.3.2 Simulated Annealing

Simulated Annealing (SA) (Kirkpatrick et al. 1983) is a generic probabilistic metaheuristic optimization technique that enables one to find *global* optimum of a given function without getting trapped in *local* minima. By exploring the space of possible states, SA searches for the local maxima of a function F . In this sense, SA mimics the annealing process in metallurgy, a technique involving heating and controlled cooling of a material to increase the size of its crystals and reduce their defects. At every iteration of the SA algorithm, a random new state is chosen. The new state is then accepted with respect to the following acceptance probability:

$$P(\text{accept}) = \begin{cases} 1, & \text{if } F_{\text{new}} > F_{\text{current}} \\ \exp\left(\frac{1}{T}(F_{\text{new}} - F_{\text{current}})\right), & \text{if } F_{\text{new}} < F_{\text{current}} \end{cases} \quad (5.3)$$

where F_{new} is the current value of our cost function under optimization computed in the new state, F_{current} is the last accepted value, and T is the artificial cooling temperature. SA was first used by Guimera et al. (Guimerà et al. 2004) to maximize modularity. A modified version with local (randomly moving nodes from one cluster to another) and global (randomly merging and splitting communities) changes was implemented by Guimera and Amaral in (Guimera and Amaral 2005). This technique was found to give higher modularity than simple local moves in (Massen and Doye 2005; Medus et al. 2005). Despite of the high modularity outcome from the SA algorithm, its slow performance restricts it to small networks of up to 10^4 nodes.

5.3.3.3 Spectral Optimization

Another technique for modularity maximization can be attained through the definition of the modularity matrix \mathbf{B} whose elements are defined in the form:

$$b_{ij} = w_{ij} - \frac{k_i k_j}{2W} \quad (5.4)$$

In the case of two communities, we define S_i to be 1 in case node i belongs to the first group and -1 otherwise. Hence, we can rewrite equation 8.2 in the form.

$$Q = \frac{1}{4W} \sum_{ij} b_{ij} S_i S_j = \frac{1}{4W} \mathbf{S}^T \mathbf{B} \mathbf{S} \quad (5.5)$$

where \mathbf{S} is the column vector with S_i as elements. By decomposing \mathbf{B} into its eigenvectors and eigenvalues, the previous equation can be written in the form:

$$Q = \frac{1}{4W} \sum_i a_i \mathbf{u}_i^T \mathbf{B} \sum_j a_j \mathbf{u}_j = \frac{1}{4W} \sum_{i=1}^n (\mathbf{u}_i^T \cdot \mathbf{S})^2 \beta_i \quad (5.6)$$

where the vector \mathbf{S} is decomposed on the basis eigenvectors \mathbf{u}_i ($i = 1, \dots, n$) of the \mathbf{B} matrix, $\mathbf{S} = \sum_i a_i \bar{\mathbf{u}}_i$, and β_i is the eigenvalue of \mathbf{B} corresponding to the eigenvector \mathbf{u}_i . From equation 8.6, we can deduct that a single cluster would exist only if \mathbf{B} have no positive eigenvalues ($Q = 0$). Otherwise, a bisection of the graph can be obtained by searching for the eigenvector of \mathbf{B} corresponding to the largest positive eigenvalue \mathbf{u}_1 , and then the nodes can be grouped according to the signs of the components of \mathbf{u}_1 . This procedure can then be repeated for the resultant clusters as long as the modularity increases (Newman 2006). Note that the modularity should always be computed from the distance matrix corresponding to the full graph, since Q is maximized globally. Variations of the spectral optimization exist in (White and Smyth 2003; Ruan and Zhang 2007; Wang et al. 2008; Richardson et al. 2009; Sun et al. 2009).

5.3.3.4 Limitations of Modularity

In general, we are certain that a non-negative maximum value for the modularity exists (since the single cluster with all nodes in the graph would yield zero modularity). However, some random networks which are not supposed to possess a community structure would yield a large value of modularity. The basic definition of modularity was based on the hypothesis that community structures are detected by comparing the current graph with a random one with equal size and expected degree. Due to non-homogeneous

fluctuations in the distribution of edges in the random graph, concentrations of links might be created in some parts of the graph and can be detected as communities (Fortunato 2010).

Another matter of concern is the resolution limit of the modularity which might affects the detection of small communities in large graphs even if they are well defined such as cliques (communities with all nodes are interconnected) (Fortunato and Barthelemy 2007). The problem was traced back to the null model on which the modularity was constructed. The model assumes that every node interacts with all the other nodes in the graph which is not correct for large graphs (e.g. Web graphs). A better assumption would be that every node has a limited region (territory) of interaction instead of including the whole graph. However, it is still unknown how to define such region.

5.4 Conclusion

In this chapter, we have introduced graph theory, the notions of graph, node and edge as well as various metrics used to measure networks topological, integration and clustering properties. We made an emphasis on the community structure feature of sparse networks. In chapter 8, a novel metric is introduced to better measure community structure by jointly maximizing within-community integration and minimizing between-community separation. We use this metric to study the topological structure of the human brain by extracting the community structure of brain networks. Moreover, we perform group studies to detect modular changes due to various neuropsychological diseases.

VI. ANISOTROPIC ANOMALOUS DIFFUSION MODELS

Parts of the work in this chapter have been presented in:

Johnson GadElkarim, Richard Magin, Mark M. Meerschaert, Silvia Capuani, Marco Palombo, and Alex Leow. ‘Fractional order generalization of anomalous diffusion as a multidimensional extension of the transmission line equation.’ IEEE Journal on Emerging and Selected Topics in Circuits and Systems, 19 June (2013), doi: 10.1109/JETCAS.2013.2265795.

6.1 Introduction

As previously discussed in chapter 4, it was found that the DW signal decay does not follow the presumed mono-exponential model, especially at high b -value ($b > 1500$). Instead, the decay was found to follow a stretched exponential behavior (Figure 14) which was linked to the existence of an anomalous diffusive behavior exhibited by the water molecules in the complex tissue structure of the brain. The complexity of this structure can be revealed at the micro-level where thin neurofilaments construct the axons of the neurons (Figure 15). This structure creates a porous medium in which the water molecules may exhibit AD.

In this chapter, we will focus on studying brain tissues at the micro-level. This will be done via two models which will be constructed using novel mathematical tools derived from the theory of fractional calculus. The models aim to study the anisotropy of water molecules AD in brain tissues and to present new directional dependent biomarkers which can describe the environment tortuosity and complexity and their dependence on direction. Results from both models are shown to be consistent.

6.2 Anisotropic Fractional Order Anomalous Diffusion Models

6.2.1 Model I

Several groups have investigated fractional order generalizations of the Bloch-Torrey equation (Magin et al. 2008; Yu et al. 2011; Hanyga and Serebnytska 2012). However, in these studies, the proposed forms of the fractional gradient operator were assumed to have the same order of fractional differentiation in

all directions. This restriction is a limitation, since the anomalous diffusive behavior could possibly vary with location as well as direction. Here, we extend the vector fractional calculus approach of Meerschaert et al. (Meerschaert et al. 2006) and employ a fractional gradient operator expressing a different order of fractional derivative in each coordinate direction. This model is considered as a generalization of the work of Magin et al. (Magin et al. 2008) in order to generate an anisotropic 3D AD model.

6.2.1.1 Model I: Theory

We start from a modified FDE version of the Block-Torrey equation written in the form:

$$\frac{\partial M_{xy}(\mathbf{r}, t)}{\partial t} = -i\gamma(\mathbf{r}, \mathbf{G}(t))M_{xy}(\mathbf{r}, t) + (\nabla^\beta)^T [\mathbf{D}_F] \nabla^\beta M_{xy}(\mathbf{r}, t) \quad (6.1)$$

where

$$\mathbf{D}_F = \begin{bmatrix} D_{F_{xx}} & D_{F_{xy}} & D_{F_{xz}} \\ D_{F_{xy}} & D_{F_{yy}} & D_{F_{yz}} \\ D_{F_{xz}} & D_{F_{yz}} & D_{F_{zz}} \end{bmatrix} \quad (6.2)$$

is a symmetric 3×3 tensor with elements in the form whose elements are in the form:

$D_{F_{ij}} = \mu_{ij}^{\beta_i + \beta_j - 2} D_{ij}$; $i, j = \{x, y, z\}$, μ (μ_{xx} , μ_{yy} , μ_{zz} , μ_{xy} , μ_{xz} , μ_{yz}) are unit preserving constants (mm) and

$\nabla^\beta = \left(\frac{\partial^{\beta_x}}{\partial x^{\beta_x}}, \frac{\partial^{\beta_y}}{\partial y^{\beta_y}}, \frac{\partial^{\beta_z}}{\partial z^{\beta_z}} \right)^T$ is a fractional nabla operator using the Feller fractional derivative with the

fractional order, β , varying from 0.5 to 1 (see Appendix D). We assume a solution in the form:

$$M_{xy}(\mathbf{r}, t) = A(t)e^{-i\gamma\mathbf{r} \cdot \mathbf{F}(t)} \quad (6.3)$$

where $\mathbf{F}(t) = \int_0^t \mathbf{G}(t') dt'$. Substituting 6.3 in equation 6.1, we get:

$$\frac{\partial \ln(A(t))}{\partial t} e^{-i\gamma\mathbf{r} \cdot \mathbf{F}(t)} = (\nabla^\beta)^T [\mathbf{D}_F] \nabla^\beta A(t) e^{-i\gamma\mathbf{r} \cdot \mathbf{F}(t)} \quad (6.4)$$

Using the definition of the Feller fractional derivative, the fractional derivative of the exponential is defined as $D_x^{\beta_x}(e^{iax}) = -|a|^{\beta_x} i^{\theta \text{sgn}(a)} e^{iax}$, where $\text{sgn}(a)$ returns the sign of a , $-1 \leq \theta \leq 1$ (see Appendix D).

Applying the differential operator and integrating w.r.t. time, we obtain:

$$A(t) = \exp \left(\int_0^t (\mathbf{L}'(t''))^T [\mathbf{D}_F] (\mathbf{L}'(t'')) dt'' \right) \quad (6.5)$$

where $\mathbf{L}' = \left(i^{\theta \text{sgn}(L_x)} |L_x|^{\beta_x} \quad i^{\theta \text{sgn}(L_y)} |L_y|^{\beta_y} \quad i^{\theta \text{sgn}(L_z)} |L_z|^{\beta_z} \right)^T$. Finally, if we again consider a Stejskal–Tanner gradient pulse pairs, as described in chapter 3, we get:

$$M_{xy} = M_0 \exp \left((\boldsymbol{\phi}(q))^T \boldsymbol{\Psi}(\boldsymbol{\phi}(q)) \right) \quad (6.6)$$

where $\boldsymbol{\phi}(q) = \left(i^{\theta \text{sgn}(q_x)} |q_x|^{\beta_x} \quad i^{\theta \text{sgn}(q_y)} |q_y|^{\beta_y} \quad i^{\theta \text{sgn}(q_z)} |q_z|^{\beta_z} \right)^T$, whose j^{th} element $q_j = \gamma G_j \delta q_i = \gamma G_i \delta$ with $j = \{x, y, z\}$, and

$$\boldsymbol{\Psi} = \begin{bmatrix} \Psi_{xx} & \Psi_{xy} & \Psi_{xz} \\ \Psi_{xy} & \Psi_{yy} & \Psi_{yz} \\ \Psi_{xz} & \Psi_{yz} & \Psi_{zz} \end{bmatrix} \quad (6.7)$$

$\bar{\bar{\Psi}} = \begin{bmatrix} \Psi_{xx} & \Psi_{xy} & \Psi_{xz} \\ \Psi_{xy} & \Psi_{yy} & \Psi_{yz} \\ \Psi_{xz} & \Psi_{yz} & \Psi_{zz} \end{bmatrix}$ is a 3×3 symmetric positive semi-definite matrix with elements in the form $\Psi_{ij} =$

$D_{Fij} \left(\Delta - \delta \frac{\beta_i + \beta_j - 1}{\beta_i + \beta_j + 1} \right)$; $i, j = \{x, y, z\}$. Further on, we will refer to $\boldsymbol{\Psi}$ by the *anomalous diffusion tensor* (aDT). In order to express the decay in the acquired signal, we substitute θ by 1 in equation 6.6. Hence, we can describe it as follows:

$$S(q) = S_0 \exp \left(-(\boldsymbol{\phi}'(q))^T \boldsymbol{\Psi}(\boldsymbol{\phi}'(q)) \right) \quad (6.8)$$

where $\boldsymbol{\phi}'(q) = \left(\text{sgn}(q_x) |q_x|^{\beta_x} \quad \text{sgn}(q_y) |q_y|^{\beta_y} \quad \text{sgn}(q_z) |q_z|^{\beta_z} \right)^T$. Note that when all the beta values are set to 1, we will recover the classical DTI model.

6.2.1.2 Model I: Methods

Equation 6.8 was fitted with the multiple b values dataset 1 described in Appendix C. The analysis process consists of multiple steps. First, all DW images were corrected for eddy currents distortions using automatic image registration (AIR) built-in the DTISTUDIO program (<http://www.mristudio.org>). Second, the DT calculations were obtained using the DTISTUDIO program with a $b = 1000 \text{ s/mm}^2$ subset of the acquired data in order to compute \mathbf{D} . In diagonalizing \mathbf{D} , the eigenvalues were organized such that: $\lambda_1 \leq \lambda_2 \leq \lambda_3$. Third, the whole spectrum of b -values was used to fit for different μ and β values in the aDT using the LM algorithm implemented in MATLAB. The initial β values were chosen as 0.75, and the initial μ values were computed from equation 6.8, with μ being the only unknown. Finally, equation 6.8 was used to analyze the set of DW images to yield the final values of β and μ on a voxel-by-voxel basis (the fitted results were insensitive to the chosen initial β values). In applying the LM algorithm, the bounds on the computed parameters were taken as: $0.5 < \beta \leq 1$ and $0 < \mu < 0.025 \text{ mm}$. To perform the analysis on the resolved parameters of the different types of tissues, WM, GM and CSF masks were generated using the segmentation tool embedded in the Statistical Parametric Mapping (SPM8) software (<http://www.fil.ion.ucl.ac.uk/spm/>).

6.2.1.3 Model I: Results

Generalizing the fractional order Bloch-Torrey equation into the multi-dimensional version provides a new model to study the anisotropy of AD. The slice presented in the following figures is an axial slice taken at the optical fiber level. Figure 19 displays maps of the classical DT elements. Figure 20 shows the $b0$ image with selected ROIs in the WM, GM and CSF areas. It also indicates the chosen coordinate system where X is left-right, Y is anterior-posterior, and Z is superior-inferior. Notice that the WM ROI was chosen parallel to the Y direction to facilitate data analysis. Figure 21 shows the fitted parameters in the aDT: the dimensionless operational order parameters, β ($\beta_x, \beta_y, \beta_z$), and the unit preserving space constants μ ($\mu_{xx}, \mu_{yy}, \mu_{zz}, \mu_{xy}, \mu_{xz}, \mu_{yz}$). Qualitatively, high contrast can be noticed between GM and WM tissues in the β maps.

Figure 22 shows maps of the aDT elements described in equation 6.8. In order to test for anisotropy, we compute a new *anomalous FA* (aFA) by diagonalizing the aDT into eigenvectors (V_1, V_2, V_3) and

eigenvalues ($\lambda_1^a \leq \lambda_2^a \leq \lambda_3^a$). The aFA is computed using equation 3.19. Figure 23 shows colormaps of the principal eigenvectors – corresponding to the largest eigenvalue – of the diagonalized Ψ and \mathbf{D} tensors as well as maps of their corresponding eigenvalues in (a) and (b) respectively. A comparison between the aFA versus conventional FA is shown in (c). Interestingly, the colormap of the principal eigenvector of the aDT possesses sharp edges compared to its counterpart from the DT.

Figure 24a plots the inverse fitted β values ($1 - \beta$) in different directions as a colormap. Since the inverse is plotted, the dominant color emphasizes the direction of the smallest beta: red is equivalent to right-left (β_x), green is equivalent to anterior-posterior (β_y), and blue is equivalent to superior-inferior (β_z). The optical fibers can be traced through the green line travelling vertically which indicates a lower beta (β_y) in the Y direction than the other two directions ($\beta_y < \beta_x, \beta_z$). The previous result can also be seen in Table IV which shows that ($\beta_y = 0.57 \pm 0.14$) is much smaller than ($\beta_x = 0.76 \pm 0.16$ and $\beta_z = 0.71 \pm 0.12$) for the chosen WM ROI parallel to the Y direction. Voxels colored in gray indicate similar betas in all directions (isotropic) which appear in GM, and black voxels have isotropic betas close to one which appear in CSF. Figure 24b shows a colormap of the diagonal unit preserving constants ($\mu_{xx}, \mu_{yy}, \mu_{zz}$). Here, the dominant color emphasizes the direction of the largest mu. We can trace the optical fibers through the green line travelling vertically which indicates a larger mu (μ_{yy}) in the Y direction than in the other two directions (μ_{xx}, μ_{zz}). This result can also be traced in Table IV which shows that ($\mu_{yy} = 17.4 \pm 4.2$) is larger than ($\mu_{xx} = 15.2 \pm 5.3$ and $\mu_{zz} = 14.9 \pm 5.1$) in the WM ROI.

In order to test for the result presented in Figure 24a – the smallest stretched exponent is along the WM fiber – we have chosen three subsets of the DW data each having the gradient aligned along one of the principal directions – X, Y, and Z. Then, we averaged the data of each subset at the chosen ROIs indicated in Figure 20. Finally, we fitted the averaged data to equation 4.24 in order to obtain a unique stretched exponent at each direction and ROI pair. The fitted curves are shown in Figure 25. Indeed, the stretched exponent (β) along the WM fiber – in the Y direction – is the lowest when compared to its value across the WM – in the X and Z directions. Moreover, the value of β is isotropic in GM and CSF regions.

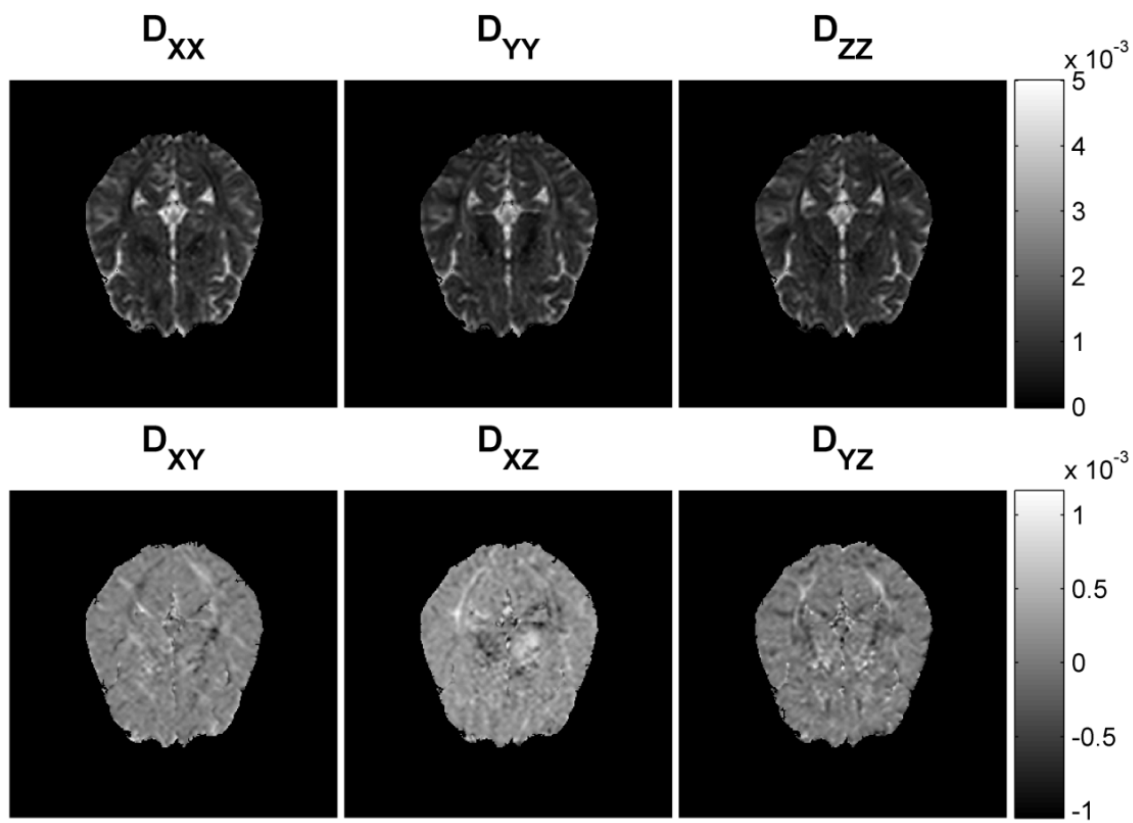


Figure 19: The computed diffusion tensor elements of an axial slice through the optical tracts.

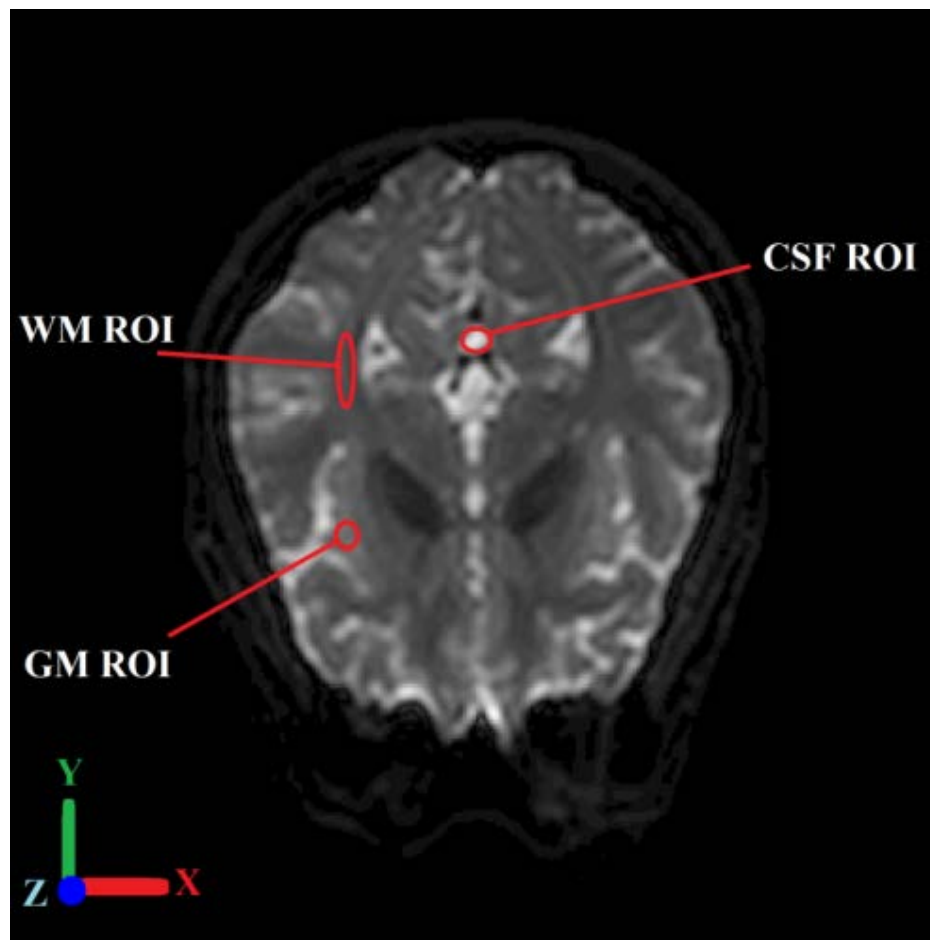


Figure 20: Selected regions of interest in the WM, GM and CSF areas highlighted on the b0 image. The WM ROI was selected parallel to the Y axis at the optical fiber.

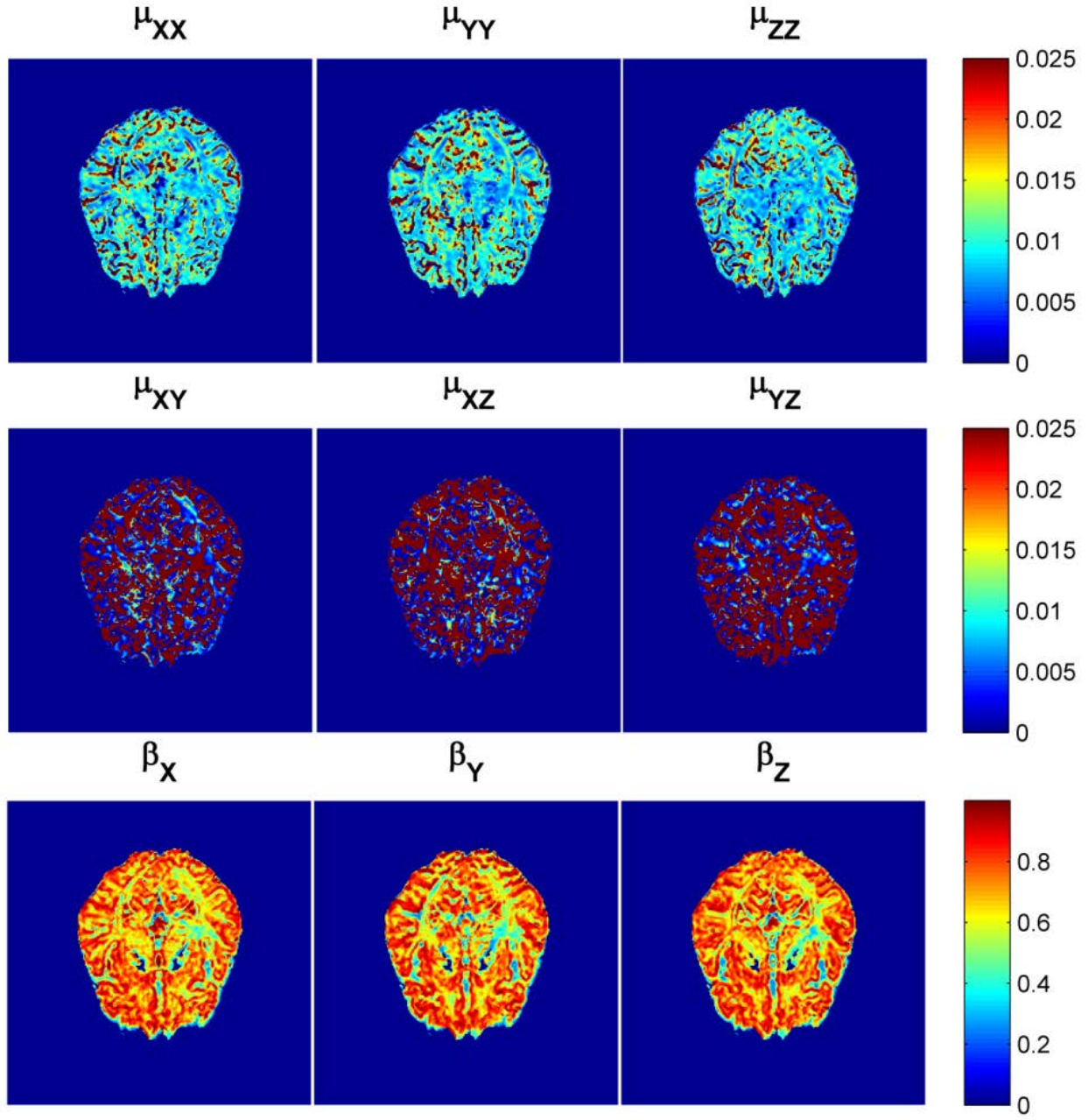


Figure 21: Spatially resolved maps of the unit preserving space constants (μ_{xx} , μ_{yy} , μ_{zz} , μ_{xy} , μ_{xz} , μ_{yz}) (top two rows), and the dimensionless operational order parameters, (β_x , β_y , β_z) (bottom row) in the model described by equation 6.7.

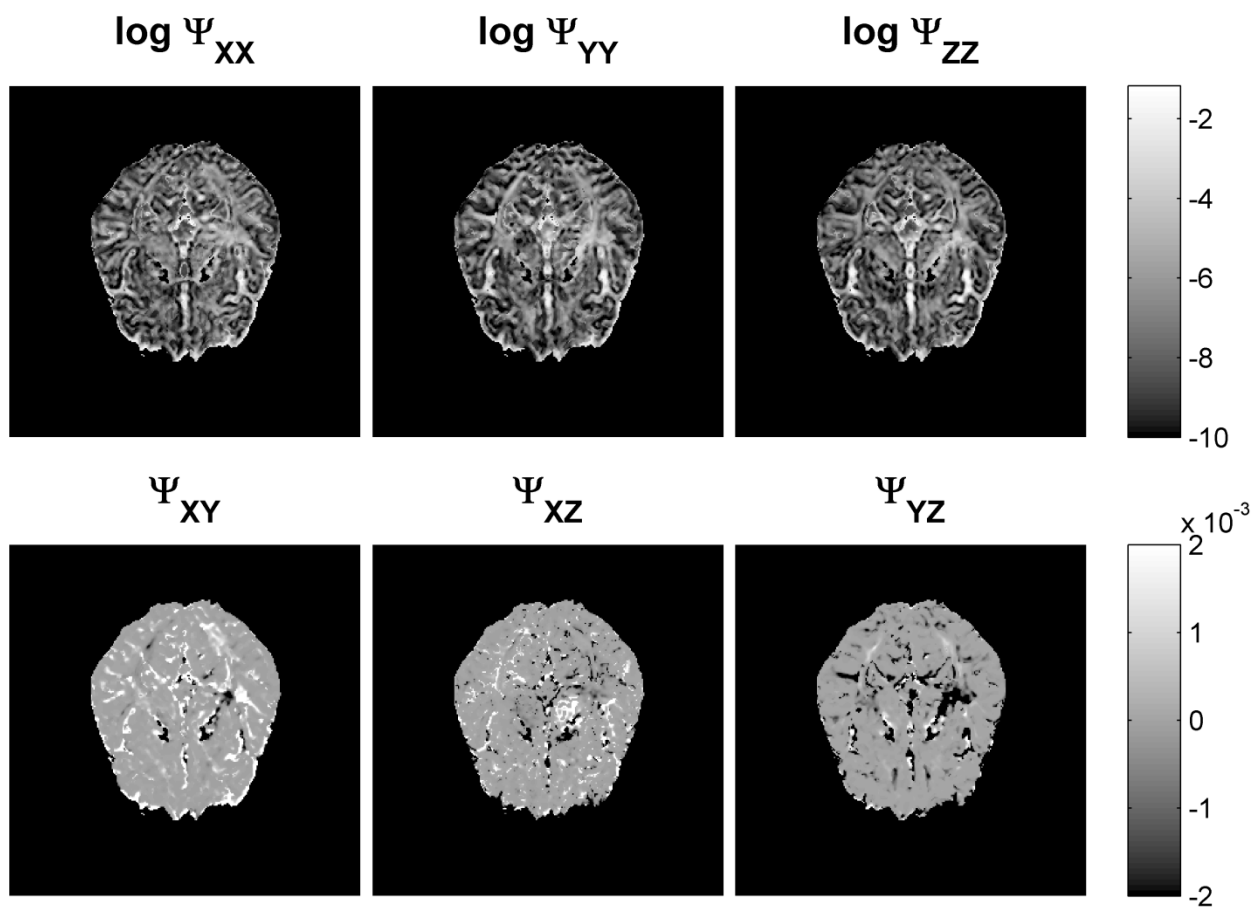


Figure 22: The logarithm of the diagonal elements in Ψ (top row) and the off-diagonal elements in Ψ (bottom row). The logarithm was taken in order to increase contrast of the images.

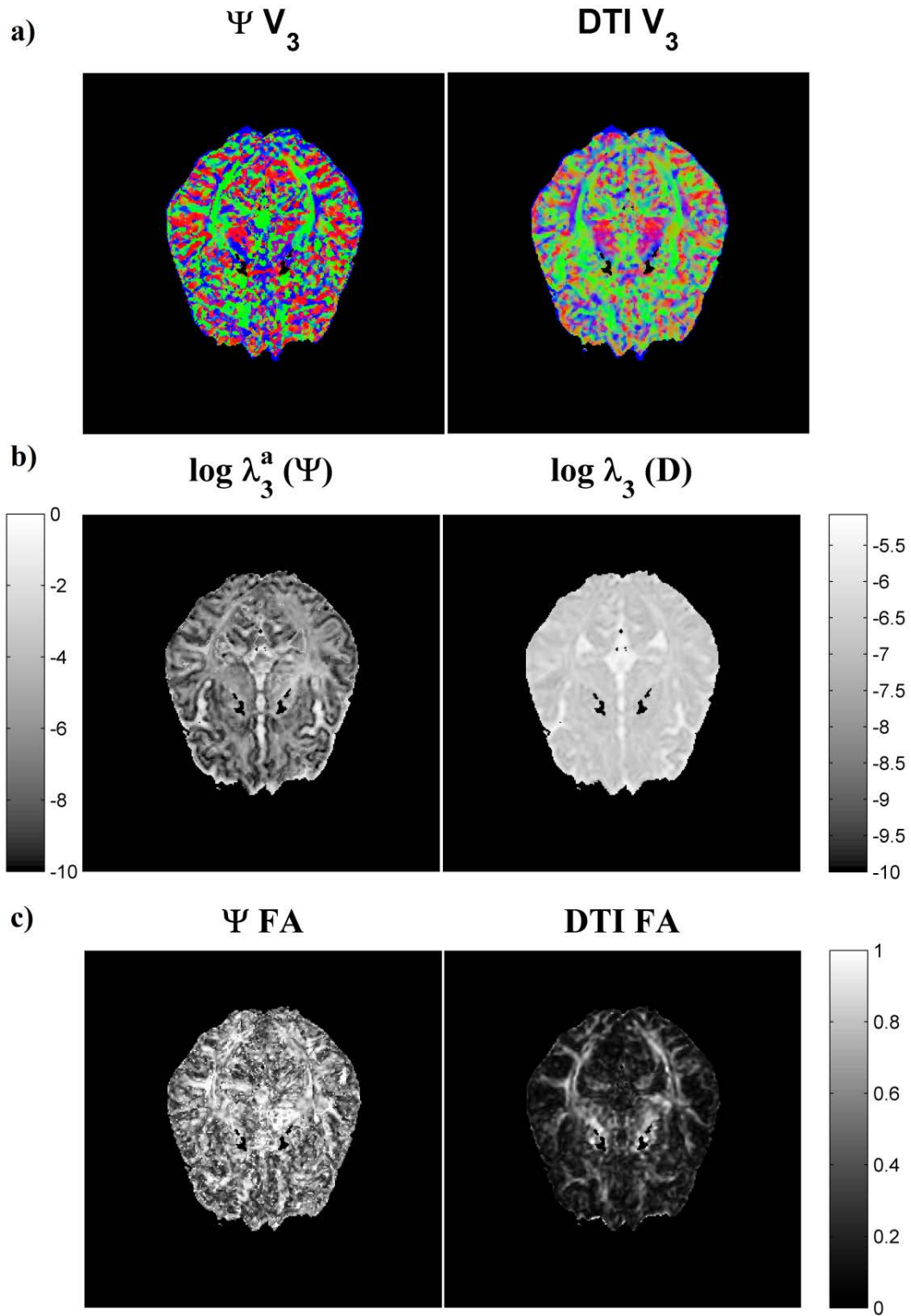


Figure 23: Maps of the principal eigenvector (the one corresponding to the largest eigenvalue) (a) and the largest eigenvalue (b) computed by diagonalizing the Ψ and D tensors. Notice the sharp edges of the white matter directions in the principal eigenvector of the Ψ tensor. Also, notice the high contrast in the largest eigenvalue of the Ψ tensor. (c) FA maps computed using eigenvalues extracted from Ψ and D tensors.

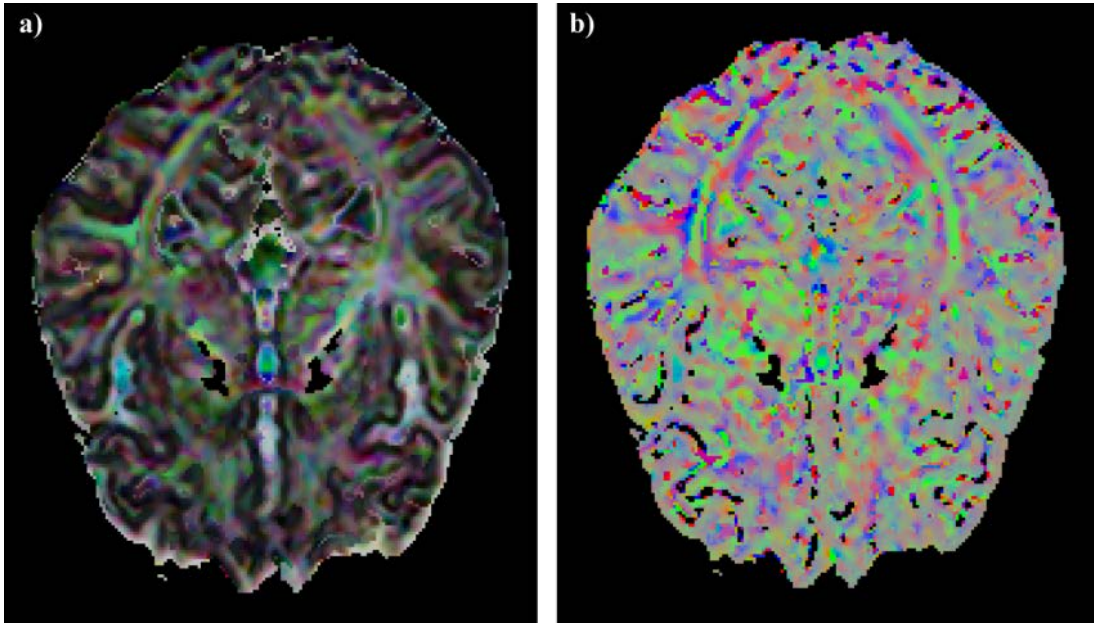


Figure 24: (a) A colormap using the inverted values of the fractional order parameters ($1 - \beta$) in different directions to weight the RGB color code. The dominant color emphasizes the direction of the smallest beta (since the inverse of β is used): red is equivalent to right-left (β_x), green is equivalent to anterior-posterior (β_y), and blue is equivalent to superior-inferior (perpendicular to the slice) (β_z). Gray and black colors indicate isotropic β values (same in all directions) which appears in areas such as GM and CSF. (b) A colormap using the normalized diagonal unit preserving constants (μ_{xx} , μ_{yy} , μ_{zz}) to weight the RGB color code. The dominant color emphasizes the direction of the largest mu: red is equivalent to right-left (μ_x), green is equivalent to anterior-posterior (μ_y), and blue is equivalent to superior-inferior (perpendicular to the slice) (μ_z). Gray and black colors indicate isotropic μ values (same in all directions) which appears in areas such as GM and CSF.

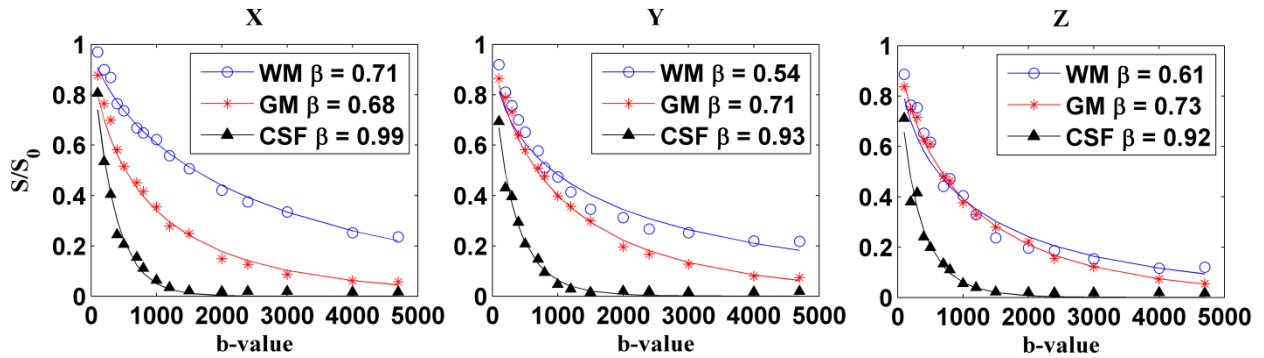


Figure 25: Fitting curves to the stretched exponential model in equation 4.24 of averaged diffusion weighted data acquired along the principal directions shown in Figure 20 in different tissues (WM, GM and CSF) corresponding to highlighted regions of interest in Figure 20. The legends indicate the value of the stretched exponent.

Table IV: Mean and standard deviation of the obtained parameters using the model in equation 6.8 as well as eigenvalues, FA and MD analysis of the \mathbf{D} and $\mathbf{\Psi}$ tensors in the selected ROIs highlighted in Figure 20.

	GM	WM	CSF
$\mu_{xx} (\mu\text{m})$	11.7 ± 2.8	15.2 ± 5.3	11.2 ± 6.3
$\mu_{yy} (\mu\text{m})$	12.3 ± 4.4	17.4 ± 4.2	12.8 ± 7.3
$\mu_{zz} (\mu\text{m})$	11.1 ± 3.1	14.9 ± 5.1	11.0 ± 6.0
β_x	0.80 ± 0.08	0.76 ± 0.16	0.92 ± 0.08
β_y	0.81 ± 0.05	0.57 ± 0.14	0.91 ± 0.07
β_z	0.80 ± 0.07	0.71 ± 0.12	0.92 ± 0.10
$\lambda_1 (\text{mm}^2/\text{s})$	0.88 ± 0.14	0.39 ± 0.14	2.80 ± 0.63
$\lambda_2 (\text{mm}^2/\text{s})$	1.09 ± 0.19	0.69 ± 0.17	3.47 ± 0.74
$\lambda_3 (\text{mm}^2/\text{s})$	1.35 ± 0.15	1.44 ± 0.23	4.18 ± 0.71
$\lambda_1^a (\text{mm}^{2\beta})$	0.17 ± 0.08	0.47 ± 0.24	2.41 ± 0.68
$\lambda_2^a (\text{mm}^{2\beta})$	0.28 ± 0.10	1.09 ± 0.26	3.66 ± 0.91
$\lambda_3^a (\text{mm}^{2\beta})$	0.51 ± 0.25	3.33 ± 0.41	4.12 ± 1.21
FA	0.22 ± 0.07	0.57 ± 0.12	0.21 ± 0.07
MD (D) (mm^2/s)	1.11 ± 0.15	0.85 ± 0.13	3.49 ± 0.66
aFA	0.45 ± 0.17	0.87 ± 0.16	0.49 ± 0.17
MD (Ψ) ($\text{mm}^{2\beta}$)	0.32 ± 0.10	1.73 ± 0.99	3.38 ± 0.75

6.2.1.4 Model I: Discussion

The new aDT incorporates two new sets of parameters in addition to the conventional DT: the dimensionless operational order parameters β : β_x , β_y and β_z , and the unit preserving space constants μ : μ_{xx} , μ_{yy} , μ_{zz} , μ_{xy} , μ_{xz} and μ_{yz} (in units of mm). The operational order parameters can be thought as a generalization of the stretched exponent in the stretched exponential model. In (Magin et al. 2008), the operational order parameter, β , was related to the complexity of the surrounding medium when studied in phantoms as well as in biological tissues. It was noted that a decrease in β is correlated to an increase in Sephadex gel complexity. Moreover, β was found to be lower in brain WM tissues compared to GM. The presented model follow the same trend, the β values were found here to be lower in WM ($\sim 0.7 \pm 0.1$) than in GM ($\sim 0.8 \pm 0.1$) suggesting a higher complexity in WM, while in CSF the values were around unity ($\sim 0.9 \pm 0.1$) (Table IV).

The anisotropy of the stretched exponent was studied in (Hall and Barrick 2008; De Santis et al. 2011; Hall and Barrick 2012) where it was found to be anisotropic in WM. Indeed, here we report anisotropy of the stretched exponents, identified here as the fractional order parameters, which appear in Figure 21 and Figure 25a. More precisely, the stretched exponents are found to be lowest in the same direction of the WM fibers illustrated in Figure 24a by the dominated green color tracing the optical fiber running vertically (anterior-posterior). Unlike WM, the β values were the same in all directions in GM tissues as well as the CSF which is indicated by the gray and black colors in Figure 20a. Black regions indicate CSF where the stretched exponents are closer to unity. This can also be verified through Table IV.

The unit preserving constants, μ , were found to follow the same trend previously reported in (Zhou et al. 2010; Gao et al. 2011), although they did not show a high tissue contrast (Figure 21) unlike what have been reported for the μ map in (Zhou et al. 2010). The μ parameters exhibit higher values in WM compared to GM tissues in all directions as demonstrated in Table IV. High instability was seen in fitting CSF voxels where the diffusion process approaches the Gaussian case with β values closer to unity which can be seen by the large standard deviations in Table IV. Moreover, anisotropy was found in the diagonal μ parameters (μ_{xx} ,

$\mu_{yy}, \mu_{zz})$ where the largest μ was found to be in the direction of the WM fibers as shown by the green line vertically tracing the optical fiber in Figure 24b.

Diagonalizing the aDT presented in Figure 22 has revealed interesting features. First, the principal eigenvector of both tensors (Ψ and \mathbf{D}) exhibit similar qualitative behavior, with sharper edges found in the principal eigenvector of the aDT as shown in Figure 22a. This was expected since AD is guided by the geometry of the surrounding media which is affected by the WM fibers direction. This result is compatible with the one found in (Hall and Barrick 2012) where the principal eigenvector of the distributed diffusivity tensor, \mathbf{A} , was found to be similar to its counterpart in the DT. Second, the computed aFA exhibits a similar behavior compared to the classical DTI-based FA – higher FA in WM compared to GM and CSF – as shown in Figure 22c and demonstrated in Table IV.

Although this model provides valuable information about the anisotropic AD behavior of water in brain tissues, it lacks the positivity preserve feature. In other words, we are not sure that the solution in equation 6.8 is the characteristic function of a certain multivariate PDF. This comes from the fact that the applied operator in equation 6.1 does not guarantee to preserve positivity. Thus, an explanation of the results cannot be given in light of the CTRW model since the model does not clearly describe the underlying propagator. Proving that the inverse Fourier of the solution in equation 6.8 is a PDF is not a trivial task. In order to prove that a function $F(\mathbf{k})$ is the characteristic function of a PDF, one needs to prove three points. First, we need to prove that the inverse Fourier of $F(\mathbf{k})$ integrates to 1, which is trivial in our case since $S(\mathbf{q} = 0)/S_0 = 1$. Second, we need to prove that the inverse Fourier of $F(\mathbf{k})$ is real, which is also trivial in our case since $S(\mathbf{q}) = S(-\mathbf{q})$ and S is real. Finally, one needs to prove that the inverse Fourier of $F(\mathbf{k})$ is non-negative, which is the hard part. Due to this limitation in this model, another model that passes the positivity test was developed. We will develop this model in the next section.

6.2.2 Model II

This model tries to surpass the limitation in Model I presented in the previous section. A new multidimensional fractional operator that guarantees to preserve positivity is first presented. Then, the

operator is used to fractionalize the Bloch-Torrey equation. A new anisotropic AD model is then produced and applied to DW brain data. Though the results are similar to those found in Model I, the existence of a well-defined diffusion propagator underlying the model allows a better explanation for the findings.

6.2.2.1 Model II: Theory

6.2.2.1.1 Model II: Fractional Vector Calculus

In this section, we extend the theory of fractional vector calculus, presented in (Meerschaert et al. 2006), to allow the order of the fractional derivative to change with the coordinate direction, in an arbitrary orthogonal coordinate system. We advise the reader to review Appendix D in order to obtain the required background on fractional calculus needed for this section. We start by recalling the usual model for anisotropic diffusion described by the ordinary diffusion equation given by:

$$\frac{\partial P(\mathbf{r}, t)}{\partial t} = \nabla^T \mathbf{D} \nabla P(\mathbf{r}, t) \quad (6.9)$$

$\frac{dM}{dt} = \nabla^T \bar{\bar{D}} \nabla M$ where \mathbf{D} is a symmetric positive definite matrix. The simplest case is when \mathbf{D} is $D\mathbf{I}$, where \mathbf{I} is a 3×3 identity matrix, and D is a scalar, then we can write:

$$\frac{\partial P(\mathbf{r}, t)}{\partial t} = D \nabla^T \nabla P(\mathbf{r}, t) = D \Delta P(\mathbf{r}, t) \quad (6.10)$$

Since the gradient has Fourier symbol $(i\mathbf{k})$, we can write $(i\mathbf{k}) \cdot \mathbf{F}(\mathbf{k})$ as the Fourier transform of $\nabla \mathbf{f}(\mathbf{r})$ where $\mathbf{F}(\mathbf{k})$ is the vector Fourier transform of the function $\mathbf{f}(\mathbf{r})$ in terms of the wave vector $\mathbf{k} = (k_x \ k_y \ k_z)^T$, $\mathbf{k} = [k_x \ k_y \ k_z]^T$. Then, the Laplacian has the Fourier symbol $(i\mathbf{k})^T (i\mathbf{k}) = -(k_x^2 + k_y^2 + k_z^2)$. If \mathbf{D} is a diagonal tensor:

$$\mathbf{D} = \begin{bmatrix} D_x & 0 & 0 \\ 0 & D_y & 0 \\ 0 & 0 & D_z \end{bmatrix} \quad (6.11)$$

Then $\nabla^T \mathbf{D} \nabla$ has the Fourier symbol: $(i\mathbf{k})^T \mathbf{D} (i\mathbf{k}) = -(D_x k_x^2 + D_y k_y^2 + D_z k_z^2)$. $(i\mathbf{k})^T [\bar{\mu}] (i\mathbf{k}) = -(\mu_{xx} k_x^2 + \mu_{yy} k_y^2 + \mu_{zz} k_z^2)$. Let the fractional dispersion tensor \mathbf{D}_F be a fractional integration tensor of order $2\beta-2$. More generally, to allow the order of the fractional derivative to vary with the coordinate, we can take \mathbf{D}_F to be the operator with Fourier symbol:

$$\mathcal{F}\{\mathbf{D}_F\} = \begin{bmatrix} \mu_x^{2\beta_x-2} D_x |k_x|^{2\beta_x-2} & 0 & 0 \\ 0 & \mu_y^{2\beta_y-2} D_y |k_y|^{2\beta_y-2} & 0 \\ 0 & 0 & \mu_z^{2\beta_z-2} D_z |k_z|^{2\beta_z-2} \end{bmatrix} \quad (6.12)$$

Then, it follows that the dispersion operator $\nabla^T \mathbf{D}_F \nabla$ has a Fourier symbol:

$$\mathcal{F}\{\nabla^T \mathbf{D}_F \nabla\} = - \sum_{j=\{x,y,z\}} \mu_j^{2\beta_j-2} D_j |k_j|^{2\beta_j} \quad (6.13)$$

This operator applies a one-dimensional fractional Riesz derivative of a different order in each coordinate. As an example, we apply this operator on a complex exponential function, $f(\mathbf{r}) = e^{-i\mathbf{r} \cdot \mathbf{a}}$, to obtain:

$$\nabla^T [\mathbf{D}_F] \nabla e^{-i\mathbf{r} \cdot \mathbf{a}} = \left(- \sum_{j=\{x,y,z\}} \mu_j^{2\beta_j-2} D_j |a_j|^{2\beta_j} \right) e^{-i\mathbf{r} \cdot \mathbf{a}} \quad (6.14)$$

The operator described in 6.12 guarantees positivity. In other words, if it operates on a non-negative function with non-negative initial conditions, positivity will be preserved. This is due to the fact that it applies three independent one-dimensional fractional Riesz derivatives each in a different coordinate. This operator can also be linked to the theory of pseudo-differential operators mentioned in chapter 4. We recall the PDO Q used in (Hanyga and Serebrynska 2012) defined as $Q(\mathbf{k}) = - \int_S |\mathbf{k} \cdot \mathbf{y}|^\alpha m(d\mathbf{y})$. A generalization of this operator can be written in the form (Magin et al. 2013):

$$Q(\mathbf{k}) = - \int_S |\mathbf{k} \cdot \mathbf{y}|^{\beta(\mathbf{y})} m(d\mathbf{y}) \quad (6.15)$$

where $\beta(\mathbf{y})$ is a distribution of the exponent on the unit sphere S such that $0 \leq \beta(\mathbf{y}) \leq 2$. It can be shown that the operator in 6.13 is a special case of the operator in 6.15 by assuming that we are only concerned by 3

orthonormal directions y_1 , y_2 , and y_3 . We will also define the values of the exponent distribution and the measure to be: $\beta(y_i) = \beta_i$ and $m(dy_i) = \delta(y)$ for $i=1,2,3$ and zero otherwise. By doing this, the operator in 6.15 converges to the one defined in 6.13 with a minor exception of the scaling factor $\mu_j^{2\beta_j-2} D_j$.

6.2.2.1.2 Model II: Multidimensional Fractional Diffusion Equation

In this section we will define a new FDE based on the mathematical notations introduced in the previous section. In the next section, this FDE will be used to define a new multidimensional fractional order Bloch-Torrey equation. Let $P(\mathbf{r}, t)$ be the diffusion propagator of the diffusing particles which represents the probability of finding a particle at location \mathbf{r} and time t such that $P(\mathbf{r}, t=0) = \delta(\mathbf{r})$. Assuming that the principal directions of diffusion coincide with the laboratory coordinates, the new FDE can be written in the form:

$$\frac{\partial P(\mathbf{r}, t)}{\partial t} = \nabla^T \mathbf{D}_F \nabla P(\mathbf{r}, t) \quad (6.16)$$

where $\mathbf{D}_F = [\bar{\mu}^{[\beta]} \bar{D}] = \begin{bmatrix} \mu_{xx}^{2(\beta_x-1)} D_{xx} & \mu_{xy}^{(\beta_x-1)+(\beta_y-1)} D_{xy} & \mu_{xz}^{(\beta_x-1)+(\beta_z-1)} D_{xz} \\ \mu_{xy}^{(\beta_x-1)+(\beta_y-1)} D_{xy} & \mu_{yy}^{2(\beta_y-1)} D_{yy} & \mu_{yz}^{(\beta_z-1)+(\beta_y-1)} D_{yz} \\ \mu_{xz}^{(\beta_x-1)+(\beta_z-1)} D_{xz} & \mu_{yz}^{(\beta_z-1)+(\beta_y-1)} D_{yz} & \mu_{zz}^{2(\beta_z-1)} D_{zz} \end{bmatrix}$ is a fractional dispersion

tensor as defined in 6.12. Taking the Fourier transform of equation 6.16, we obtain:

$$\frac{\partial P(\mathbf{k}, t)}{\partial t} = \left(- \sum_{j=\{x,y,z\}} \mu_j^{2\beta_j-2} D_j |k_j|^{2\beta_j} \right) P(\mathbf{k}, t) \quad (6.17)$$

where the β_j are dimensionless operational order parameters, and the μ_j are unit preserving space constants.

Assuming $P(\mathbf{k}, 0) = 1$, the solution to equation 6.17 is:

$$P(\mathbf{k}, t) = \exp \left(-t \sum_{j=\{x,y,z\}} \mu_j^{2\beta_j-2} D_j |k_j|^{2\beta_j} \right) \quad (6.18)$$

Equation 6.18 describes the characteristic function of a multidimensional operator stable Lévy distribution with independent alpha stable distributions in each coordinate, each with a different stretched exponent. This

is a more general form than the conventional multivariate alpha stable PDF which applies the same stretched exponent in all directions.

6.2.2.1.3 Model II: Fractional Order Bloch-Torrey Equation

We start by assuming that the coordinate system described by the principal directions of diffusion $\mathbf{r}' = (\theta \ \varphi \ \psi)^T$ can be related to the laboratory coordinates $\mathbf{r} = (x \ y \ z)^T$ using a unitary transformation \mathbf{Q} . Further, let \mathbf{Q} be the unitary matrix that diagonalizes the classical DT: $\mathbf{D} = \mathbf{Q}\mathbf{\Lambda}\mathbf{Q}^T$, where \mathbf{Q} is the matrix whose columns are the eigenvectors of \mathbf{D} : $\mathbf{V}_\theta, \mathbf{V}_\varphi, \mathbf{V}_\psi$, and $\mathbf{\Lambda}$ (mm²/s) is a diagonal matrix whose entries are the corresponding eigenvalues of \mathbf{D} : $D_\theta, D_\varphi, D_\psi$ (Figure 26). Hence, as described in the previous section, the fractional order Bloch-Torrey equation can be written in the \mathbf{r}' coordinate system in the form:

$$\frac{\partial M_{xy}(\mathbf{r}, t)}{\partial t} = -i\gamma(\mathbf{r}' \cdot \mathbf{G}'(t))M_{xy}(\mathbf{r}, t) + \tilde{\nabla}^T[\mathbf{D}_F]\tilde{\nabla}M_{xy}(\mathbf{r}, t) \quad (6.19)$$

where $\mathbf{G}' = \mathbf{Q}^T\mathbf{G}$, and $\tilde{\nabla}$ is the gradient operator applied in the \mathbf{r}' coordinate system, with Fourier symbol $\mathcal{F}\{\tilde{\nabla}\} = i\mathbf{k}' = i(k_\theta \ k_\varphi \ k_\psi)^T$, and \mathbf{D}_F is the fractional integral operator as defined in the previous acting in the \mathbf{r}' coordinate system and having the Fourier symbol:

$$\mathcal{F}\{\mathbf{D}_F\} = \begin{bmatrix} \mu_\theta^{2\beta_\theta-2} D_\theta |k_\theta|^{2\beta_\theta-2} & 0 & 0 \\ 0 & \mu_\varphi^{2\beta_\varphi-2} D_\varphi |k_\varphi|^{2\beta_\varphi-2} & 0 \\ 0 & 0 & \mu_\psi^{2\beta_\psi-2} D_\psi |k_\psi|^{2\beta_\psi-2} \end{bmatrix} \quad (6.20)$$

The mu parameters (mm) in the \mathbf{D}_F operator are space constants needed to preserve units (Magin et al. 2008).

We assume a solution to equation 6.20 in the form:

$$M_{xy} = M_0 A(t) \exp(-i\mathbf{r}' \cdot \mathbf{L}'(t)) \quad (6.21)$$

where $\mathbf{L}'(t) = \gamma \int_0^t \mathbf{G}'(t'') dt''$. Substituting (6.21) into (6.19), and applying the above operator, we obtain:

$$A(t) = \exp \left(- \int_0^t \sum_{h=\{\theta, \phi, \psi\}} \mu_h^{2\beta_h-2} D_h |(L_h'(t''))|^{2\beta_h} dt'' \right) \quad (6.22)$$

where $L_h'(t) = \mathbf{G}^T(t) \mathbf{V}_h$, and $0 < \beta_h \leq 1$ are the stretched exponents. Finally, if we again consider the Stejskal-Tanner gradient pulse pairs, we find:

$$M_{xy} = M_0 \exp \left(- \sum_{h=\{\theta, \phi, \psi\}} \mu_h^{2\beta_h-2} D_h |\gamma \mathbf{G}^T \mathbf{V}_h|^{2\beta_h} \left(\Delta - \delta \frac{2\beta_h - 1}{2\beta_h + 1} \right) \right) \quad (6.23)$$

Using equation 6.23, one can describe the acquired DW signal as follows:

$$S(\mathbf{g}, t) = S_0 \exp \left(- \sum_{h=\{\theta, \phi, \psi\}} \mu_h^{2\beta_h-2} D_h |\gamma \delta \mathbf{G}^T \mathbf{V}_h|^{2\beta_h} \left(\Delta - \delta \frac{2\beta_h - 1}{2\beta_h + 1} \right) \right) \quad (6.24)$$

Note that when h equals only θ , we recover Magin's et al. model described in equation 4.26. Moreover, when all of the beta values are set to one, we recover the classical DTI model since equation 6.23 becomes

$$S(\mathbf{g}, t) = S_0 \exp(-b(\mathbf{Q}^T \mathbf{g})^T \mathbf{\Lambda}(\mathbf{Q}^T \mathbf{g})) = S_0 \exp(-b \mathbf{g}^T \mathbf{D} \mathbf{g}) \quad (6.25)$$

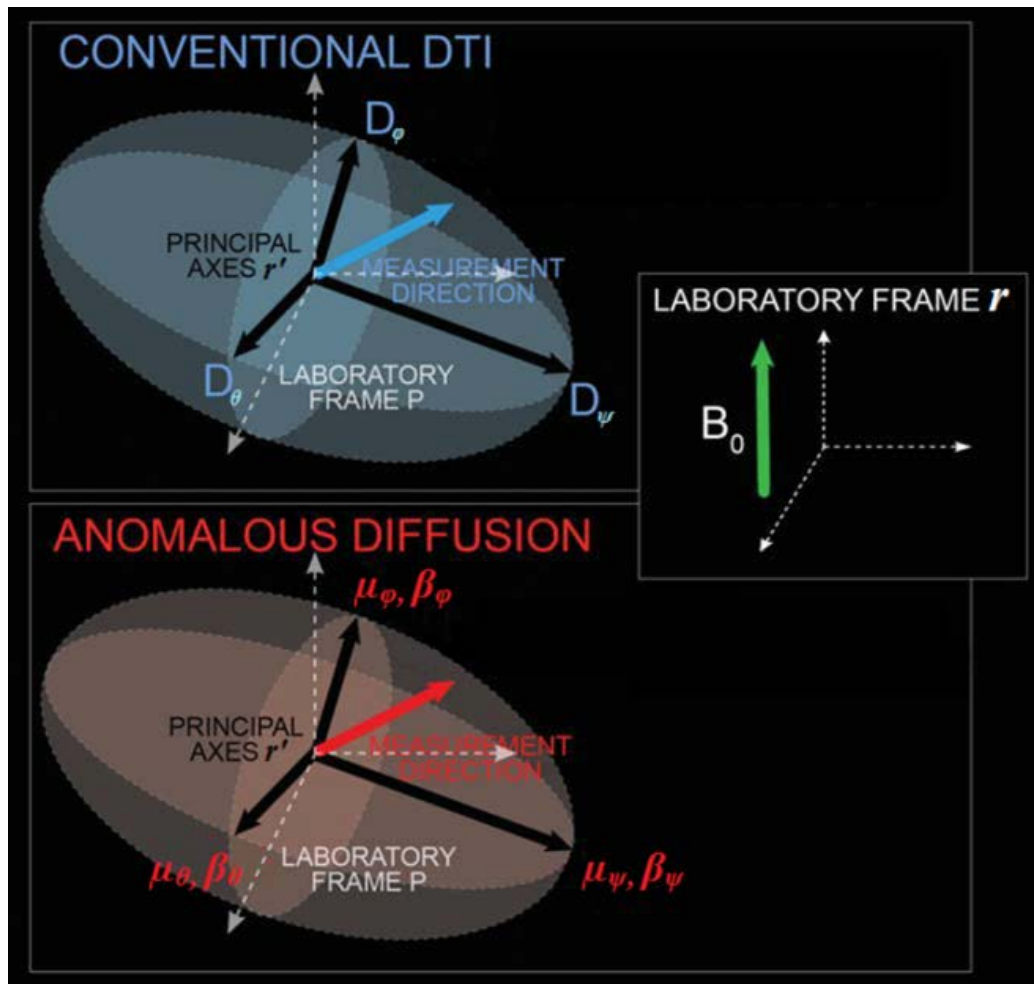


Figure 26: Relationship between laboratory frame, DTI, and analysis in Model II coordinate systems. We can notice that in Model II, we assumed that AD follows the same coordinate system extracted from the diagonalization of the DT.

6.2.2.2 Model II: Methods

Equation 6.24 was fitted with the multiple b values dataset 2 described in Appendix C. The analysis process consists of multiple steps. All DW images were corrected for eddy current distortions using FSL version 4 software package (<http://www.fmrib.ox.ac.uk/fsl>). Tensor calculations were performed using the

DTISTUDIO program (<http://www.mristudio.org>) using the $b = 1000 \text{ s/mm}^2$ subset of the acquired data in order to compute \mathbf{D} . Afterward, the whole spectrum of b values was used to fit different μ and β values in equation 6.24 using the LM algorithm implemented in MATLAB R2011a (MathWorks Inc, Natick, MA). The initial β values were chosen as 0.75, and the initial μ values were computed from equation 6.24 with μ being the only unknowns. Afterward, equation 6.24 was used to analyze the set of DW images to yield the final values of β and μ on a voxel-by-voxel basis (the fitted results were insensitive to the chosen initial β values). In applying the LM algorithm, the bounds on the computed parameters were taken as: $0.5 < \beta \leq 1$ and $0 < \mu < 0.05 \text{ mm}$. It is assumed that the eigenvalues of the DT are ordered such that: $D_\theta \leq D_\phi \leq D_\psi$. The same order is followed in the eigenvector matrix \mathbf{Q} . To perform the analysis on the resolved parameters of the different types of tissues, WM, GM and CSF masks were generated using the segmentation tool embedded in the well-known Statistical Parametric Mapping (SPM8) software (<http://www.fil.ion.ucl.ac.uk/spm/>).

6.2.2.3 Model II: Results

Figure 27 displays maps for the six fitted parameters using the model described in equation 6.24 $\bar{\Psi}$: the three dimensionless operational order parameters β ($\beta_\theta, \beta_\phi, \beta_\psi$), and the unit-preserving space constants μ ($\mu_\theta, \mu_\phi, \mu_\psi$) (with units of mm). A high contrast exists between the GM and WM tissues in the β maps. It is qualitatively clear from Figure 27 that both β_θ and β_ϕ are larger than β_ψ in the WM regions, which is presented in Table V. This result indicates a lower value for the stretched exponent in the principal direction of diffusion along the WM fibers similar to what have been found in Model I.

In order to test the previous result, we have computed *anomalous anisotropy* (AA^β) of the stretched exponent β using equation 3.19. Figure 28 shows maps of the DTI FA, DTI MD, *mean anomalous exponent* (MAE) (computed by averaging the stretched exponents: β), as well as *anomalous anisotropy* (AA^β) in order to compare our results with De Santis' et al. mean γ ($M\gamma$) and *anomalous anisotropy* (γA) presented chapter 4 (De Santis et al. 2011). Indeed, qualitatively, one can see that AA^β has higher values in WM fibers and lower values in GM. These results are similar to what has been found in γA , which can also

be assessed quantitatively through Table V. Moreover, we report a high correlation between the AA^β and the FA in the WM region with the correlation coefficient being 0.8 and a p-value < 0.0001 .

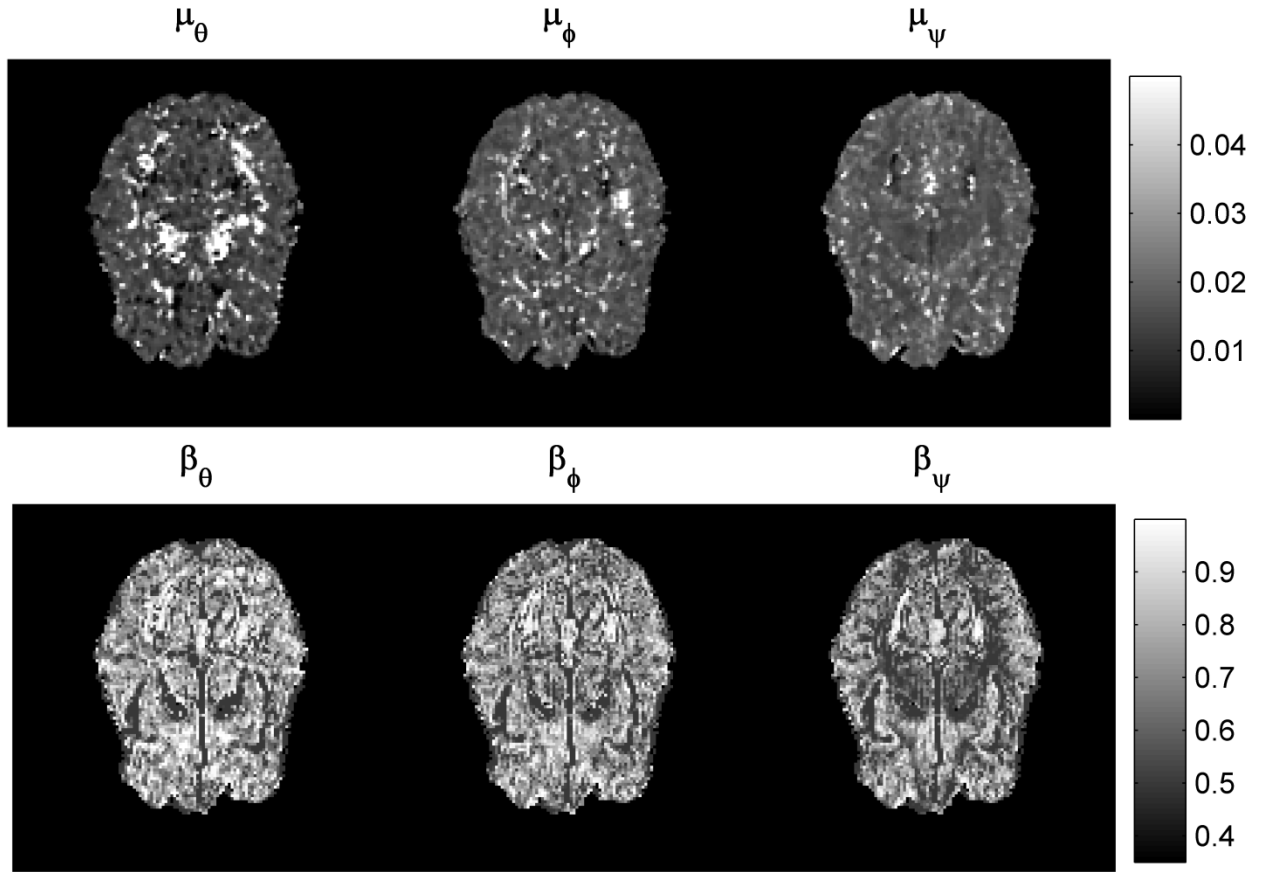


Figure 27: Spatially resolved maps of the unit preserving space constants (μ_θ , μ_ϕ , and μ_ψ) (top row), and the dimensionless operational order parameters, (β_θ , β_ϕ and β_ψ) (bottom row) in the model described by 6.23.

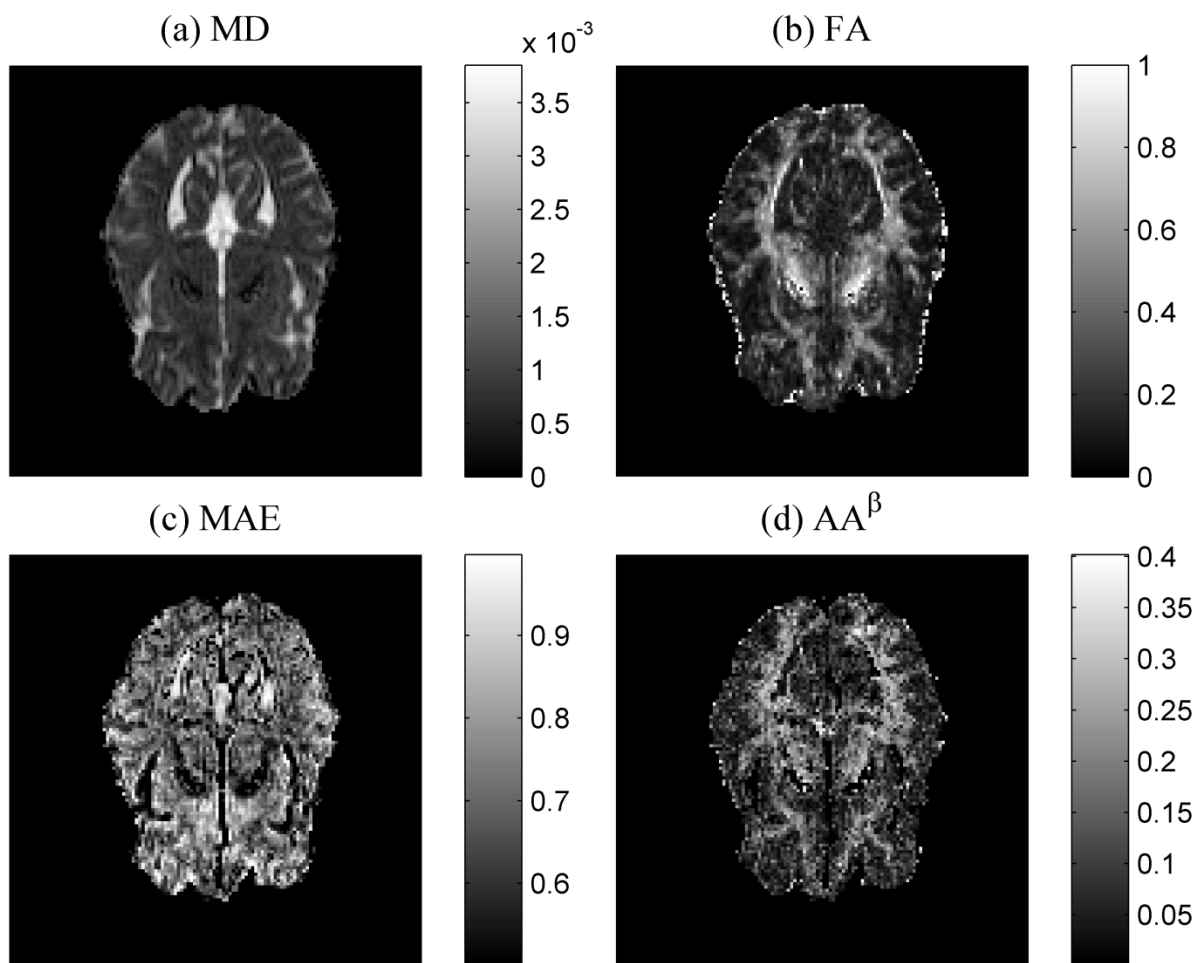


Figure 28: (a) Mean diffusivity (MD), (b) fractional anisotropy (FA), (c) mean anomalous exponent (MAE), and (d) anomalous anisotropy (AA^β) maps.

Table V: Mean and standard deviation summary of the fitted parameters and the computed metrics across the slice presented in Figure 27 and Figure 28.

	GM	WM	CSF
β_θ	0.77 ± 0.1	0.68 ± 0.1	0.87 ± 0.1
β_φ	0.77 ± 0.1	0.68 ± 0.1	0.91 ± 0.02
β_ψ	0.78 ± 0.1	0.59 ± 0.1	0.88 ± 0.1
$\mu_\theta (\mu\text{m})$	18.7 ± 5.5	21.6 ± 5.4	12.7 ± 8.3
$\mu_\varphi (\mu\text{m})$	19.8 ± 5.6	23.1 ± 6.3	23.7 ± 12.5
$\mu_\psi (\mu\text{m})$	19.5 ± 5.3	26.1 ± 6.1	26.6 ± 14.3
MD ($\mu\text{m}^2/\text{ms}$)	0.98 ± 0.18	0.65 ± 0.07	2.66 ± 0.8
FA	0.17 ± 0.08	0.42 ± 0.18	0.13 ± 0.05
MAE	0.77 ± 0.09	0.65 ± 0.07	0.9 ± 0.08
AA ^β	0.07 ± 0.02	0.15 ± 0.05	0.1 ± 0.02
$D_\theta (\mu\text{m}^2/\text{ms})$	0.82 ± 0.18	0.45 ± 0.18	2.33 ± 0.75
$D_\varphi (\mu\text{m}^2/\text{ms})$	0.97 ± 0.18	0.7 ± 0.18	2.64 ± 0.83
$D_\psi (\mu\text{m}^2/\text{ms})$	1.16 ± 0.21	1.11 ± 0.25	3.0 ± 0.96

6.2.2.4 Model II: Discussion

Similar to what have been found in Model I, our β values (Table V) were found to be lower in WM ($\sim 0.65 \pm 0.1$) than in GM ($\sim 0.77 \pm 0.1$), suggesting a higher complexity in WM. In CSF, the β values were found to be close to unity ($\sim 0.9 \pm 0.1$) as expected. We have also found that the stretched exponents were lowest in the direction of the WM fibers, as illustrated in Figure 27 and Figure 28. In particular, β_ψ , which represents the stretched exponent in the direction of the principal eigenvector, was found to be lower than β_θ and β_ϕ in WM ($\beta_\psi \sim 0.59 \pm 0.1$). Moreover, β_θ and β_ϕ were found close in values ($\sim 0.68 \pm 0.1$) in WM regions, which explain the higher anisotropy along WM tracts in the AA^β map (Figure 28).

The existence of low beta values along the WM fibers may first seem counter intuitive, especially when we try to connect it with the concept of complexity discussed in (Magin et al. 2008). However, a deeper understanding of the underlying distribution, described in equation 6.18, can explain our result in light of the CTRW model. The stretched exponential model of AD can be explained through the Long jumps model, also called Lévy flight, presented in section 4.2.1, which will result in an alpha stable distribution for the diffusion propagator $P(x,t)$. In this model particles are allowed to occasionally perform large jumps in their random walks. Alpha stable distributions are heavy tailed functions having power law probability tails $P(|X| > x) \sim x^{-2\beta}$ and their Fourier transform is known to be a stretched exponential (Metzler and Klafter 2000). It has been proven that a Fourier relationship exists between the diffusion propagator and the normalized DW signal (S/S_0) under the short pulse assumption (when the pulse separation period $\Delta \gg$ pulse duration δ which holds in the current experiment setup) (Stejskal 1965). Hence, it is expected that a stretched exponential relationship in the q -space ($q = \gamma\delta G$ is assumed to be the spatial Fourier frequency of units mm^{-1}) will describe the acquired DW signal.

In order to gain a better understanding of the solution in equation 6.18, which represents the Fourier transform of the solution of equation 6.16, we need to take a closer look at the propagator PDF $P(\mathbf{r},t)$ that underlies the model. For simplicity, we write the characteristic function of a 2D version of the propagator $P(\mathbf{r},t)$ with $t = 1$ oriented at a rotated coordinate system $\{\phi, \psi\}$ by an angle Ω in the form:

$$P(\mathbf{k}, t = 1) = \exp \left(- \left[A_\phi |k_\phi|^{2\beta_\phi} + A_\psi |k_\psi|^{2\beta_\psi} \right] \right) \quad (6.26)$$

where A_ϕ and A_ψ are scale constants ≥ 0 , β_ϕ and β_ψ are the stretched exponents, and

$$\begin{bmatrix} k_\phi \\ k_\psi \end{bmatrix} = \begin{bmatrix} \cos(\Omega) & \sin(\Omega) \\ -\sin(\Omega) & \cos(\Omega) \end{bmatrix} \begin{bmatrix} k_x \\ k_y \end{bmatrix} \quad (6.27)$$

The characteristic function, $P(\mathbf{k}, t=1)$, was numerically evaluated in MATLAB by varying the five parameters: A_ϕ , A_ψ , Ω , β_ϕ , and β_ψ in equation 6.18 and then the inverse Fourier transform was computed in order to display the PDF value in the space domain. Note that the rotation matrix (equation 6.27) used as the relationship between the $\{k_x, k_y\}$ and $\{k_\phi, k_\psi\}$ coordinate systems in the Fourier domain can be used to relate the $\{x, y\}$ and $\{\phi, \psi\}$ coordinate systems in the space domain. It is clear from Figure 29 that increasing the scale parameters will increase the spread in the corresponding direction (b compared to a), while lowering one of the stretched exponents will elongate the tail in the corresponding direction (c compared to a). Finally the change of the rotation angle will change the principal axes of the function (d compared to a, b and c).

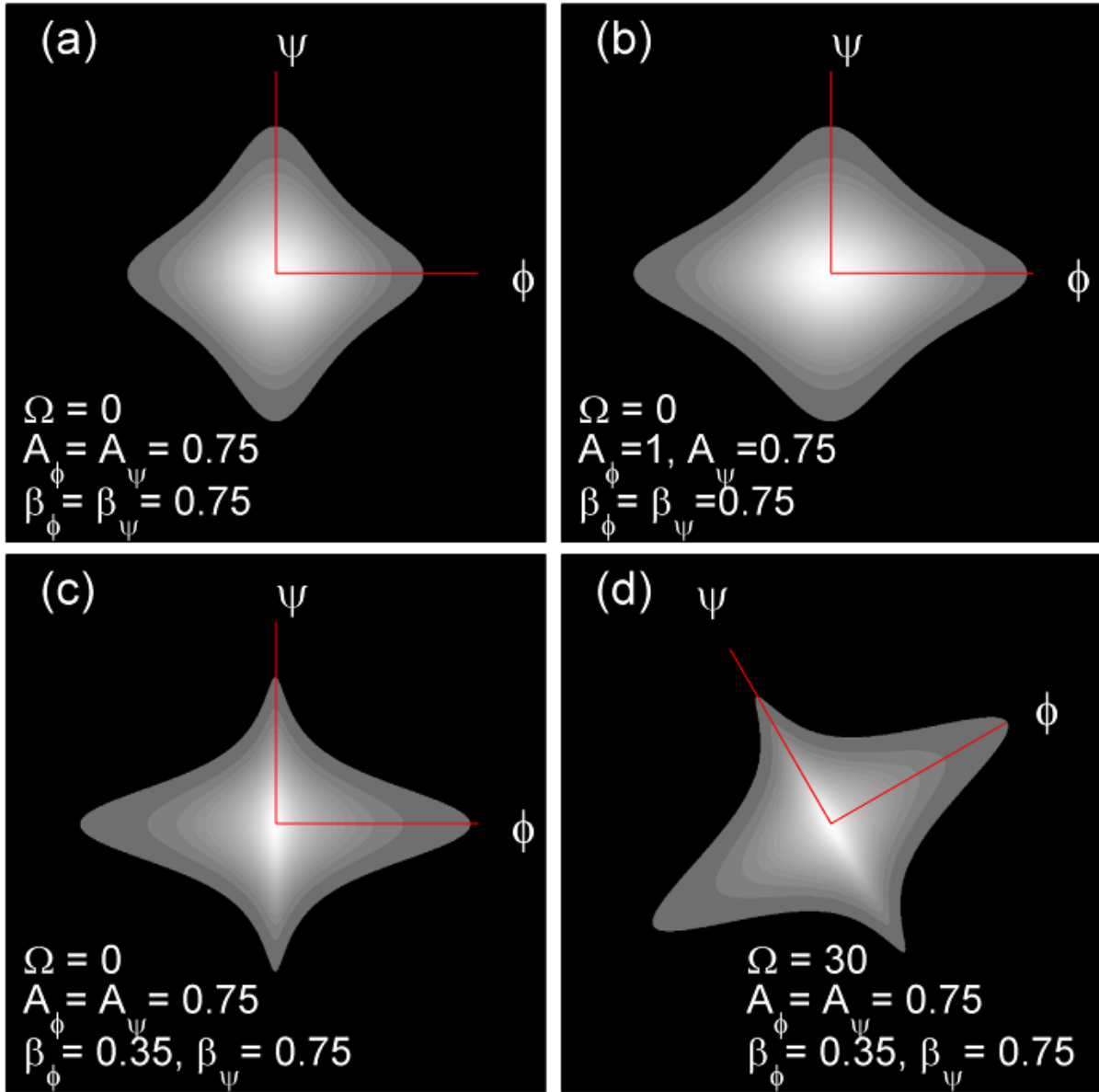


Figure 29: Contour plot (isomap) of different versions of a 2D version of $P(\mathbf{r}, t)$ by varying five parameters (2 scale parameters: A_ϕ and A_ψ , rotation angle: Ω , and 2 stretched exponents: β_ϕ and β_ψ). The coordinate system is shown in red.

According to the CTRW model, the heavy tailed solution for the space fractional diffusion model reflects the probability that distant randomly walking particles could jump to the current position (Schumer et al. 2009). From the above analysis, we can deduce that it is more likely for particles along the WM fibers to perform long jumps than particles randomly walking in the transverse directions, which explains the lower beta value found in the principal direction of diffusion along the optical fibers in Figure 27. In order to tie this result to the anatomy of the brain, we postulate the entrapment of water molecules along the WM fibers. When the molecules are freed, they might commit long jumps. Unlike WM, β values were isotropic in GM tissues as well as the CSF appearing as low AA^β values in Figure 28 and similar average values for the stretched exponents in Table V.

The unit preserving constants, μ , were found to follow the same trend similar to Model I, although they did not show a good tissue contrast (Figure 27) unlike what have been reported for the μ map in (Zhou et al. 2010). Similar to Model I, the μ parameters exhibit higher values in WM compared to GM tissues in all directions. Instability was seen in the fitting for CSF voxels where the diffusion process approaches the normal case with β values closer to unity, as evidenced by the large standard deviations in Table V. The blurriness in the μ maps may be due to the low SNR (around 1.25 in GM and around 1.4 for WM at a b value of 5000 s/mm²) of the acquired data compared to that used in (Zhou et al. 2010) (reported to be around 3.5 in GM and around 6 for WM at a b value of 4700 s/mm²). Indeed fitting this data to Magin *et al.*'s model resulted in a blurred μ map. In general, we posit that both fitting the μ parameter in the isotropic model or the μ parameters in our anisotropic models are sensitive to the SNR of the data. Moreover, increasing SNR without sacrificing resolution requires averaging multiple acquisitions, which increases the acquisition time.

6.3 Discussion

Our results from both models reflect the existence of three different diffusion phenomena occurring in brain tissue. The first – diffusion in anisotropic media – depends on the structure and composition of the environment in which the water molecules move. Barriers such as macromolecules, membranes, and bundles of axons will create a restricted diffusive medium in which the directions of allowed motion are constrained

causing a reduction in the measured ADC, when compared with a barrier-free environment. Although Model I suffers from the lack of positivity guarantee, however, using the principal eigenvector of the aDT, Ψ , we were able to detect the medium anisotropy without any assumptions. The second – diffusion in multi-scale or fractal structures – has been demonstrated to occur in brain tissue that exhibits fractal-like appearance (Smith et al. 1991; Caserta et al. 1995; Havlin et al. 1995; Ozarslan et al. 2006), and thus it has been linked to the use of fractional order stretched exponents (which quantify sub-diffusion processes in terms of random walk particle trajectories). Such a process could shed light on the relationship between AD and the anisotropy found in the fractional order parameters (Ozarslan et al. 2006; Hall and Barrick 2008; Magin et al. 2008; Ozarslan et al. 2012). The third – diffusion in porous heterogeneous media – is related to the AD description for which the Hurst index $H > \frac{1}{2}$ or $< \frac{1}{2}$ (Metzler and Klafter 2000). This could be due to the complexity of the random walk executed by the spins (water protons) caused by magnetic susceptibility differences between different tissues, water compartments and chaotic travel paths (Palombo et al. 2011; Capuani et al. 2012; Palombo et al. 2012).

6.4 Conclusion

In this chapter, we have presented two new models to study the anisotropy of AD in DW-MRI. The models were applied to DW-MRI brain data to study AD in the different types of brain tissues. It is important to note that both models suffer from partial volume contamination as do DTI. Inside a voxel, multi-fiber crossings are known to influence the principal direction of diffusion. A suggested solution is the utilization of spherical harmonics in order to solve for fiber crossing. This could be applied through the generalized PDO Q suggested in equation 6.15. However, this would complicate the formulation of the problem.

VII. USING THE TENSOR DISTRIBUTION FUNCTION

Parts of the work in this chapter have been presented in:

J.J. GadElkarim, L. Zhan, S.L. Yang, A.F. Zhang, L. Altshuler, M. Lamar, O. Ajilore, P.M. Thompson, A. Kumar, A. Leow, “TDF-TRACT: PROBABILISTIC TRACTOGRAPHY USING THE TENSOR DISTRIBUTION FUNCTION”, International Symposium of Biomedical Imaging, ISBI, 2010.

7.1 Introduction

In this chapter, we are going to study the brain on the mid-level using the TDF presented in section 3.3.5.2.1 for the tractography application. We are going to start by presenting a brief literature review about different tractography algorithms. Algorithms are categorized in two main families: *deterministic-based* and *probabilistic-based*. This is followed by presenting our tractography algorithm TDF-TRACT based on the TDF. We then exploit a new property of the TDF by presenting a new metric, circular standard deviation (CSD) and we show that it is capable of measuring fibers incoherence. We also show that FA values depend on the spatial resolution during the acquisition process which puts a barrier in comparisons across studies. This dependence can be solved using HARDI-based methods.

7.2 Background on Tractography

Early tractography trials dates back to 1997 (Jones et al. 1997; Basser 1998; Mori et al. 1998; Mori and Barker 1999; Mori et al. 1999), at that time it presented the first non-invasive tool to probe information on the WM architecture of the human brain and it remained the only one up-to-date. Clinical applications for tractography vary from the characterization of neuro-degenerative diseases to surgical planning (Mori and van Zijl 2002). Recent utilization of full brain tractography combined with GM automatic segmentation algorithms have allowed us to form structural connectivity maps also known as connectome (Sporns et al. 2005). As we mentioned above, algorithms fall in one of two categories: deterministic or probabilistic. Early trials were deterministic algorithms based on the DTI model, they were unsuccessful to extract crossing information due to resolution limitations discussed in chapter 3. Many algorithms were adapted to take advantage of the additional information provided by the HARDI-based models. Probabilistic tractography

algorithms possess a greater advantage in that they are based on the full probability distribution under study which describes fibers orientation (ODF, PAS, etc...) and not only on the extracted maxima. In tractography, a single fiber pathway is made by the interconnection of consecutive voxels while following a preferred direction at each voxel determined by the underlying model used to describe the DW measurements until certain stopping criteria are met. One can use a ROI as a starting seed for the tractography process or choose all WM brain voxels (using a mask) as seed points which is called full brain tractography.

The first deterministic techniques were based on the streamline tracking (STR) algorithm proposed by (Basser 1998; Mori et al. 1998; Conturo et al. 1999; Basser et al. 2000; Basser and Jones 2002) in which a fiber tract is represented by a 3D space-curve. Since diffusion data are defined on a grid as discrete samples (voxels), one needs to find a way to infer fiber orientation at locations away from voxel centers. Mori et al. (Mori et al. 1999) have used a nearest neighbor approach in their algorithm *fiber assignment by continuous tracking* (FACT) algorithm, while Lazar and Alexander have used a better approach by using smooth interpolation in their *bootstrap white matter tractography* (BOOT-TRACT) algorithm (Lazar and Alexander 2005). Another approach in the direction update procedure is the *tensor deflection* (TEND) algorithm proposed by (Westin et al. 2002; Lazar et al. 2003) in which one can use the entire DT to estimate the propagation direction of the next step. This technique gives smoother tracts due to the limits put on the deflection curvature when using the full DT. An important issue in tractography is the choice of termination criteria. Two important criteria were widely used. Since it is less likely that WM axons bend sharply within the scale of an imaging voxel, one could use the angle of curvature as the first stopping criteria. Hence, one can predetermine a curvature threshold which acts as a termination condition for the tractography process. Typical angles in literature vary from 25 to 45 degrees. The second stopping criterion is the anisotropy within the voxel. One can stop the tracking procedure when diffusion anisotropy is insufficient. This is estimated using the FA value at the current voxel, generally the tracking process is stopped when $FA \leq 0.15$.

HARDI-based tracking algorithms started to appear with the work of (Tuch 2002; Hagmann et al. 2004) who proposed an adaptation for the streamline algorithm using the principal direction of diffusion ODF computed from DSI. The STR was also adapted to the QBI-based diffusion ODF in the work of

Campbell et al. (Campbell et al. 2005; Campbell et al. 2006) which approached the issue of fibers crossing using a curvature constraint. Descoteaux proposed a modification to the STR algorithm in which he exhaustively scanned for all possible splitting following different maxima of the diffusion ODF in order to extract fanning and branching fibers (Descoteaux 2008). The STR was also adapted to the multi-Gaussian model in the work of (Parker and Alexander 2003). The FACT algorithm was adapted in (Kreher et al. 2005; Bergmann et al. 2007) by using a multi-tensor model and in (Chao et al. 2007; Chao et al. 2008) by using multiple maxima of the q-ball ODF (M-FACT).

In probabilistic tractography, a connectivity index is usually produced to indicate how probable two voxels are connected instead of using stopping criteria to terminate the propagation process. This can be used to assess the reliability of the generated pathways from the tractography process. DTI-based probabilistic tractography algorithms were proposed in (Koch et al. 2002; Behrens et al. 2003; Parker and Alexander 2003; Jbabdi et al. 2004; Lazar and Alexander 2005; Friman et al. 2006; Lenglet 2006; Ramirez-Manzanares et al. 2007; Jbabdi et al. 2008). Bayesian DTI-based algorithm (Behrens et al. 2003) was adapted in the work of (Kaden et al. 2007) using parametric spherical deconvolution and in (Behrens et al. 2007) using the multi-Gaussian model. Full brain tractography was generated in (Jbabdi et al. 2007) using a Bayesian framework. Stochastic frameworks based on particle filters were used in the work of (Björnemo et al. 2002; Brun et al. 2002; Zhang et al. 2009) in order to extract full brain tractography. Tractography algorithms based on Monte-Carlo estimation appear in the work of (Perrin et al. 2005) in which they used the Q-ball diffusion ODF and in (Parker and Alexander 2005; Haroon and Parker 2007) based on PAS. A connection probability map was produced using M-FACT algorithm in (Yi-Ping et al. 2007). Branching and fanning was taken into account in the work of (Seunarine and Alexander 2006; Savadjiev et al. 2007; Descoteaux 2008).

In the next section we are going to present our new tractography algorithm based on the TDF. Although it is a deterministic algorithm, it does possess a probabilistic aspect by sampling the TOD function and using a random seed point for every tracking trial. The algorithm captures crossing, fanning and branching fibers.

7.3 TDF-TRACT Tractography Algorithm

We start by extending the STR algorithm. The tangent to the streamline at any point is assumed to be parallel to the fiber orientation vector field \mathbf{v} . If one parameterized the location of the tract pathway \mathbf{r} by the arc length s of the trajectory, we can write:

$$\frac{d\mathbf{r}(s)}{ds} = \mathbf{v}(\mathbf{r}(s)) \quad (7.1)$$

hence

$$\mathbf{r}(s) = \int_{s_0} \mathbf{v}(\mathbf{r}(s)) ds \quad (7.2)$$

where $\mathbf{r}(s = s_0) = \mathbf{r}_0$ represents the seed point, $\mathbf{r}(s) = [x(s) \ y(s) \ z(s)]^T$. In order to realize the integration in equation 7.2, one can start from a seed point \mathbf{r}_0 , calculate $\mathbf{v}(\mathbf{r}_0)$, propagate in space for a predefined step of size Δs in order to obtain the next point $\mathbf{r}_1 = \mathbf{r}_0 + \mathbf{v}(\mathbf{r}_0)\Delta s$ on the fiber pathway (Figure 30). This is called the Euler's method in which we construct the fiber by propagating iteratively according to the following update equation:

$$\mathbf{r}_{i+1} = \mathbf{r}_i + \mathbf{v}(\mathbf{r}_i)\Delta s \quad (7.3)$$

To decrease the accumulating propagation error of the numerical integration, one can use the Runge-Kutta scheme to perform the integration in equation 7.2, in that case we can write:

$$\mathbf{r}_{i+1} = \mathbf{r}_i + \mathbf{v}\left(\mathbf{r}_i + \frac{\Delta s}{2}\mathbf{v}(\mathbf{r}_i)\right)\Delta s \quad (7.4)$$

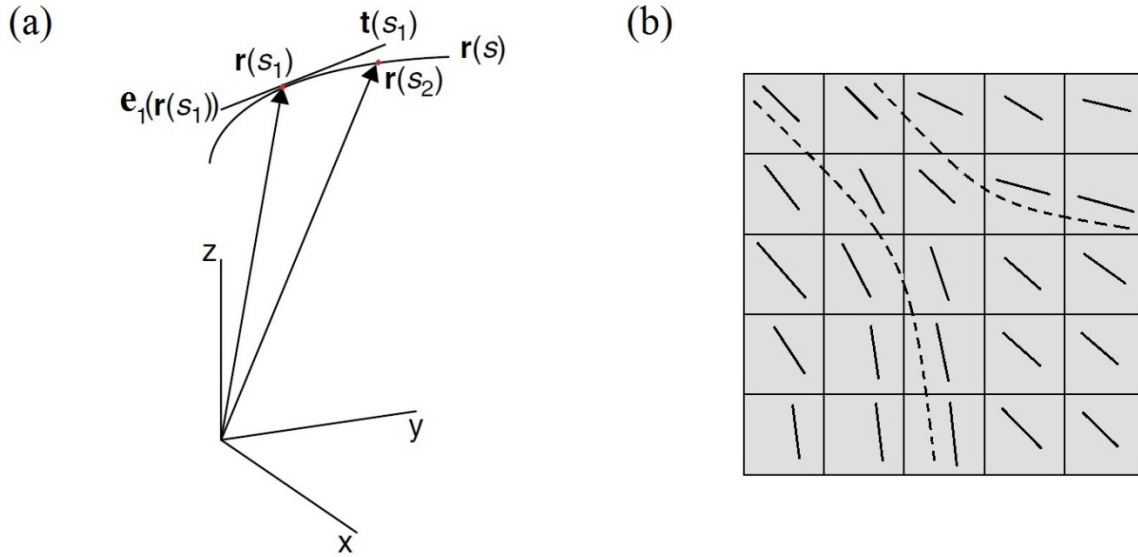


Figure 30: Streamline tractography. (a) Mathematical representation of streamline tractography, the streamline location is parameterized as a vector \mathbf{r} which is a function of length along the streamline s . The tangent to the streamline $\mathbf{t}(s)$ is the estimate of local fiber orientation. (b) The dotted streamline follows the orientations of the principal axes of diffusion tensors.

Due to the heuristic nature of our algorithm, we perform a linear interpolation in order to infer fiber orientation at locations away from voxel centers. Other schemes such as cubic or spline interpolation will be computationally expensive. The input to our tractography algorithm is as follow:

- A table of the sampled directions on the unit sphere (\mathbf{q} -table), usually we do a low and high resolution sampling of 27 and 81 directions respectively. This table should not be confused with the gradient table which comes from the HARDI data. Each direction represents a different tensor (recall from chapter 3 that one needs 2 eigenvalues and a unit vector to represent a DT in the TDF scheme).
- A TOD map which represents the PDF of every DT represented by the directions found in the \mathbf{q} -table at every voxel. One usually can put thresholds on the TDF to eliminate directions with very low weights. Typical used thresholds are: 0.05, 0.1, and 0.15.

- Number of tensors at every voxel, since many directions will be weightless after applying a threshold on the TOD, we record the number of survived tensors.
- A binary mask for the WM voxels
- Number of tracts per seed point N_{tps}
- A step size Δs
- Maximum number of points per tract N_p
- A maximum curvature threshold Θ_t
- A starting point \mathbf{r}_0

The algorithm can be described as follow:

Loop from 1 to N_{tps}

Start from: $\mathbf{r}_0' = \mathbf{r}_0 + \mathbf{r} - 0.5$, \mathbf{r} is a random vector with elements in the interval $[0, 1]$.

Tract1 = **GenerateTracts**: Inputs are \mathbf{r}_0' and $\mathbf{v} = [0 \ 0 \ 0]^T$

Tract2 = **GenerateTracts**: Inputs are \mathbf{r}_0' and $\mathbf{v} = \mathbf{r}_0' - \mathbf{r}_l$

Concatenate Tract1 and Tract2

End Loop

where

Function **GenerateTracts**: Inputs are \mathbf{r}_i and $\mathbf{v}(\mathbf{r}_{i-1}) = \mathbf{v}$

If mask = 0 or \mathbf{r}_i outside brain size \rightarrow stop tractography

* Randomly sample the TOD at nearest neighbor of \mathbf{r}_i to get $\mathbf{v}(\mathbf{r}_i)$ from the \mathbf{q} -table

If $\text{acos}(\mathbf{v}(\mathbf{r}_i) \cdot \mathbf{v}(\mathbf{r}_{i-1})) > \theta_t$ \rightarrow stop tractography

If $\mathbf{v}(\mathbf{r}_i) \cdot \mathbf{v}(\mathbf{r}_{i-1}) < 0$ \rightarrow $\mathbf{v}(\mathbf{r}_i) = -\mathbf{v}(\mathbf{r}_i)$

Propagate using equation 7.3

If number of points $> N_p$ \rightarrow stop tractography

Go to (*) with $\mathbf{r}_i = \mathbf{r}_{i+1}$ and $\mathbf{v}(\mathbf{r}_{i-1}) = \mathbf{v}(\mathbf{r}_i)$

Return tract

In the implementation we allowed $\Delta s = 0.5$ mm, $\Theta_t = 60$ degree, $N_p = 500$. Although the algorithm is categorized as of a deterministic type, a probabilistic aspect can be observed by the random choice of starting seed points as well as the sampling process of the TOD PDF.

7.4 Tractography Results

7.4.1 Graphical User Interface for TDF-Tractography

The graphical user interface (GUI) for the TDF-TRACT algorithm is shown in Figure 31. The program is called: CoNECt. It was first implemented in the Matlab environment. Afterward, it was translated into C++ in the cross-platform GUI framework known as Qt. The user interface has the capabilities of displaying the TOD along with the colored fiber orientation (red denotes left-right, green denotes anterior-posterior, and blue denotes top-down orientation), as well as various slice views of the corresponding structural image. This allows the user to easily navigate between structural anatomy and local fiber directional information, making it easier to identify and trace ROIs. The “AND/NOT” function is implemented such that the user may perform virtual dissections of WM structures in an interactive manner. In addition, the user may specify the number of random samplings of trajectories per seed point as well as the cut-off bending angle. Figure 31 shows the different views available in the software. In the TOD view (Figure 31b), the user can inspect the different fiber directions by using the zoom capabilities. The user can also filter fibers by length, ROI, and color.

7.4.2 Tractography of the Brain Stem and Cerebellar Peduncles

To demonstrate the power of TDF-TRACT, we attempted to reconstruct all major neuronal pathways to and from the brainstem, a structure where multiple fiber bundles are mostly condensed and aligned adjacent to each other. While previous studies (Habas and Cabanis 2007; Kamali et al. 2010) have concluded that high spatial resolution (~ 1 mm) is necessary in assessing the WM architecture of the brain stem, here we demonstrate that TDF tractography is successful in reconstructing these fibers at a clinically typical yet lower spatial resolution (~ 2 mm). The visualization of the TDF framework is introduced in Figure 32 which shows the reconstructed TOD overlaid with the color map representing overall fiber orientation at each voxel as

calculated using the mean fiber direction vector \mathbf{R} . The TOD is a voxel-wise vector plot, in which multiple vectors were plotted indicating different fiber directions. On the other hand, the color codes of the mean fiber direction \mathbf{R} (presented in the next section) are similar to the RGB coding used in DTI tensor visualization with green, red, and blue representing anterior-posterior, left-right, and superior-inferior orientation respectively. Visually, the \mathbf{R} color map provides a gross or macro representation of the WM structure, while TOD vector plot represents finer details of the WM structure with the ability to resolve fiber crossing. Fiber crossing, for example, can be readily appreciated at the level of the pons (Figure 32c).

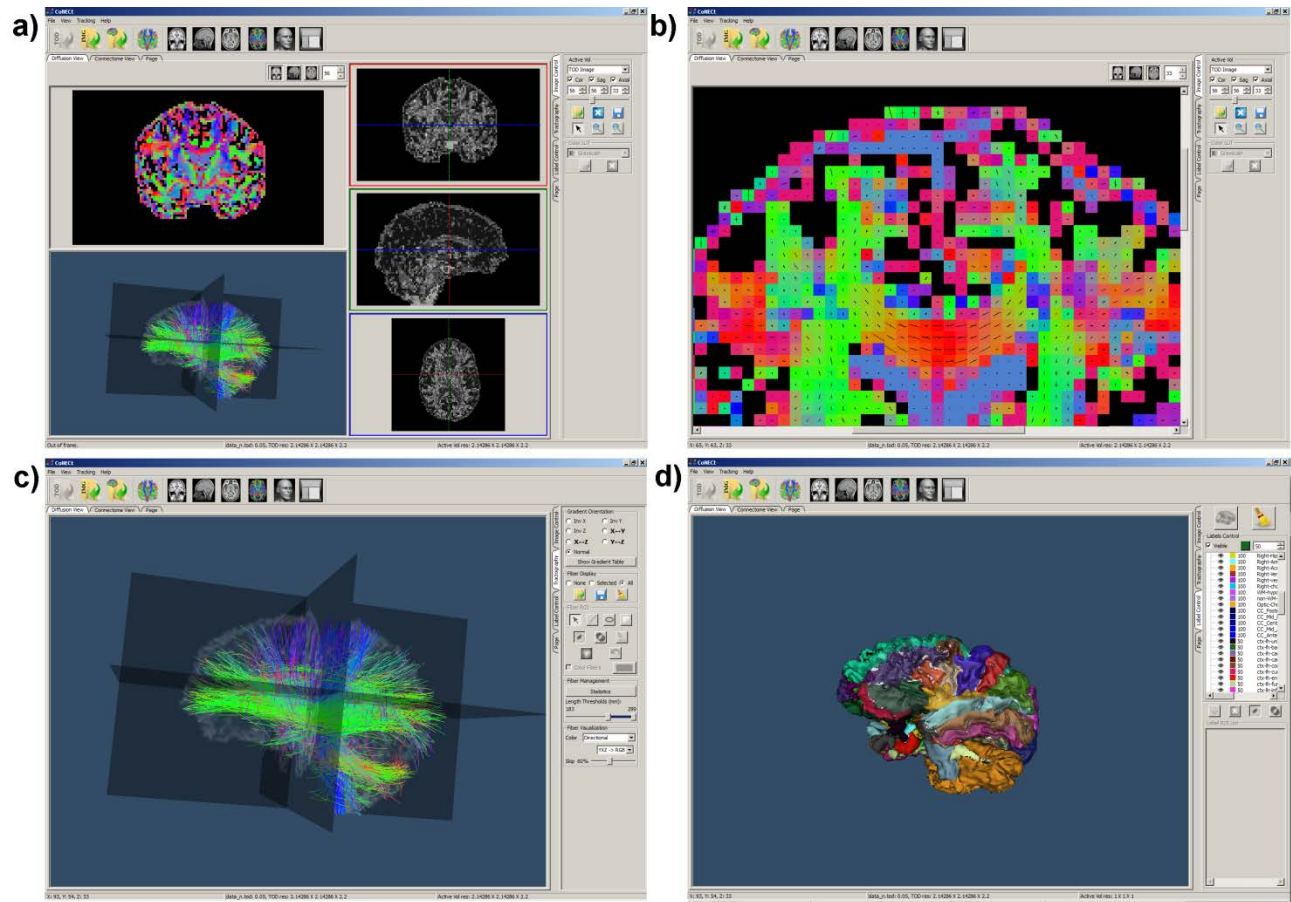


Figure 31: The GUI for the CoNECT program. There are three main views available: the global view (a), TOD view (b), and 3D view the tract view (c, d).

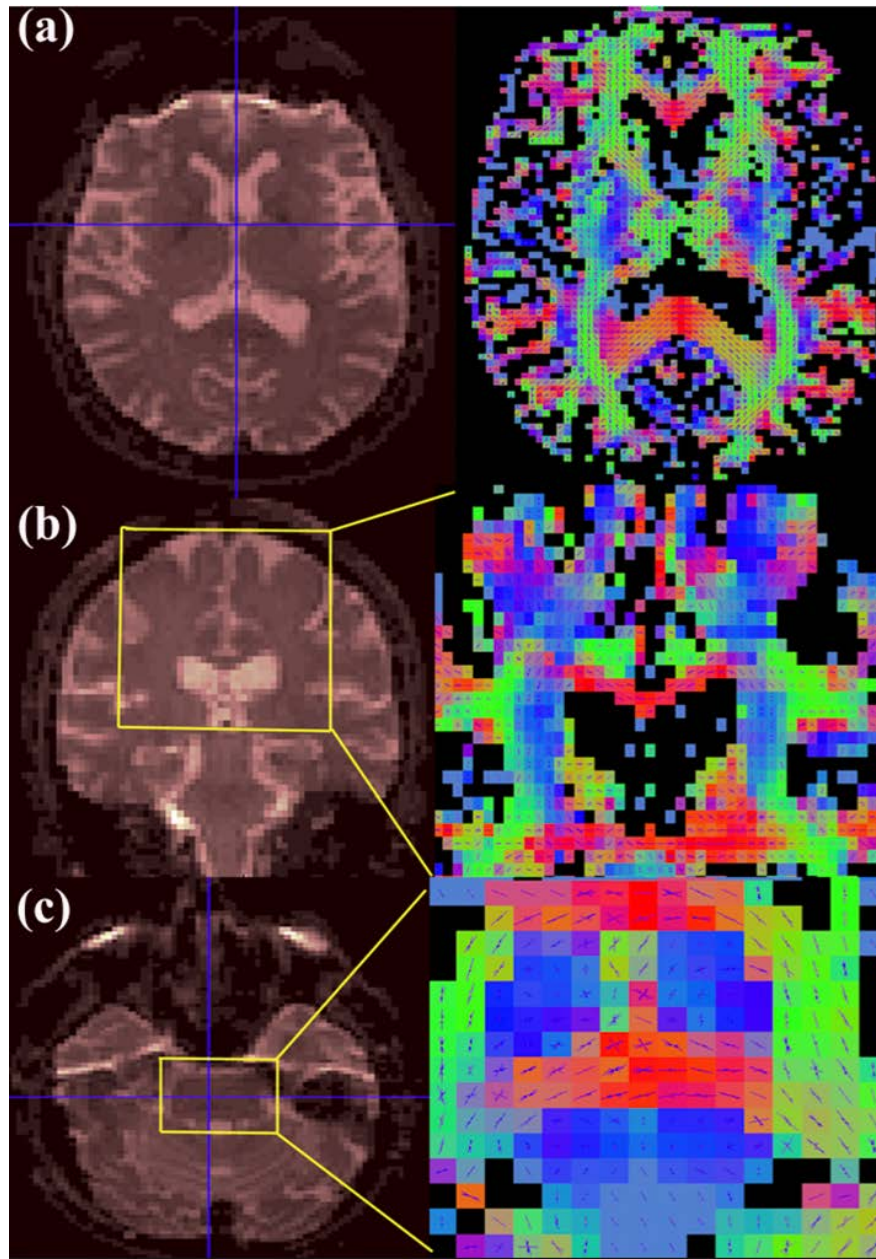


Figure 32: The reconstructed tensor orientation distribution (TOD; right panel) and the color map representing overall fiber orientation at each voxel, as calculated using the RGB coloring of the mean fiber direction vector \mathbf{R} (Eq. 7.8). The TOD is a voxel wise vector plot, in which multiple vectors may be present that indicate reconstructed fiber directions. On the other hand, the color codes of \mathbf{R} are similar to those used in DTI tensor visualization with green, red, and blue representing anterior-posterior, left-right, and superior-inferior orientation respectively. Top panel shows the TOD and \mathbf{R} color map at the level of the thalamus. Here the \mathbf{R} color map provides a gross or macro representation of the white matter structure, while voxel wise TOD vector plot represents finer details of the white matter structure with the ability to resolve fiber crossing. Examples are shown in the middle and bottom rows, where complex white matter structure including fiber crossing can be seen. In (c), at the level of the pons, the ponto-cerebellar tracts (PCT; coded red) cross to the contra-lateral side to reach the cerebellum via the middle cerebellar peduncle (MCP). Visually, the complex white matter architecture is evident in this region.

7.4.3 Constructing the Dorsal Column-Medial Lemniscus (DCML) System

The DCML pathway relays information to the sensory cortex for senses including light touch, vibration, and proprioception. Neurons carrying touch information synapse at the gracile and cuneate nuclei in the spinal cord, and axons from secondary neurons decussate at the level of the open medulla and travel up the brainstem as the medial lemniscus on the contralateral side, reaching the ventral posterolateral (VPL) nucleus of the thalamus. The VPL nucleus then further relays the sensory information to the somatosensory cortex in the postcentral gyrus. Figure 33a shows the reconstructed DCML pathway, which extends from the medulla/rostral spinal cord to the somatosensory cortex. Here the seeding ROI was placed by identifying the rostral end of the dorsal column, followed by a second “and” ROI at the pontine tegmentum.

7.4.4 Constructing the Cortico-Spinal Tracts

CST can be easily constructed by recognizing these tracts in the pons (Figure 32), where we place the seeding ROI. This is followed by placing a second “and” ROI at the primary motor cortex in the precentral gyrus. Figure 33 (b) and (c) show the reconstructed CST using TDF-tractography.

7.4.5 Constructing the Main Cerebellar Efferent Fibers

The superior cerebellar peduncle (SCP) contains major cerebellar efferent fibers. These fibers originate in the deep cerebellar nuclei and cross the midline in the decussation of SCP with termination either at the contra-lateral red nucleus or the ventrolateral (VL) and ventroanterior (VA) thalamic nuclei. The VL and VA nuclei then further relays cerebellar output information to the motor, pre-motor, and supplementary motor cortices, thus completing the dentate-rubro-thalamo-cortical (DRTC) pathway that plays an important role in the modulation, timing, and coordination of motor control. Here we reconstruct the DRTC pathway by placing a first seeding ROI using a coronal slice covering the entire cerebellum followed by a second “and” ROI placed in SCP bilaterally. Here, TDF-Tract is able to reconstruct the whole dentate-rubro-thalamo-cortical pathway with final termination in the cerebral cortex (Figure 33c). Also, we note in passing that often the term cerebello-cortical pathway is alternatively used to describe the projection from the cerebellum to the cortical cortex, and thus will be used somewhat interchangeably.

7.4.6 Constructing the Spinocerebellar and Rubrocerebellar Pathway

The cerebellum receives input from the spinal cord via the spinothalamic/cuneocerebellar tract as well as the inferior olive. These fibers enter the cerebellum via the inferior cerebellar peduncle (ICP). In addition to these afferent fibers, the fastigial nucleus of the cerebellum sends most of its efferent fibers inferiorly through the ICP to the vestibular nucleus. In Figure 32d, we reconstructed these fibers by placing the seeding ROI in the medulla, and a second “and” ROI using a coronal ROI of the cerebellum. Some aberrant fiber contaminations (mostly from middle cerebellar peduncle or MCP) were then removed by using the “not” function with additional ROIs.

7.4.7 Construction of the Cortico-Ponto-Cerebellar Pathway

The cerebellum receives its main input fibers from the contralateral pontine nuclei via the ponto-cerebellar tracts, the pontine nuclei in turn receives cortical input via the corticopontine tracts. Together, these two tracts complete the Cortico-Ponto-Cerebellar (CPC) pathway, a major pathway connecting the cerebral cortex to the cerebellum. Figure 33e reconstructs the CPC pathway by placing a seeding ROI using a coronal slice of the entire cerebellum, followed by a second “and” ROI placed at bilateral MCP, and a last “and” ROI placed in the centrum semi-ovale.

In Figure 34, we plot and visualize these reconstructed fibers (green-corticospinal or pyramidal tract; red-DCML and other ascending sensory pathways; yellow-fibers passing through SCP representing main cerebellar efferent output to the cerebral cortex, the DRTC or cerebello-cortical pathway; light blue- tracts passing through ICP; magenta-CPC pathway passing through MCP). To better appreciate the anatomy of interest, all fibers were reconstructed bilaterally except for the CPC pathway, shown here to originate in one side of the cortex and reach the contralateral cerebellum. From the posterior view in Figure 34c, the DRTC pathway lies laterally to the fiber tracts of the ICP. This is consistent with known neuroanatomy as the dentate nucleus, most lateral among all deep nuclei of the cerebellum (from lateral to medial: the dentate, interposed, and fastigial nuclei), accounts for most of the cerebellar efferent output. Moreover, our

tractography results suggest that fibers in SCP are organized into more than one bundle, aligned in an overall anterior-posterior fashion (Figure 34a and Figure 34b).

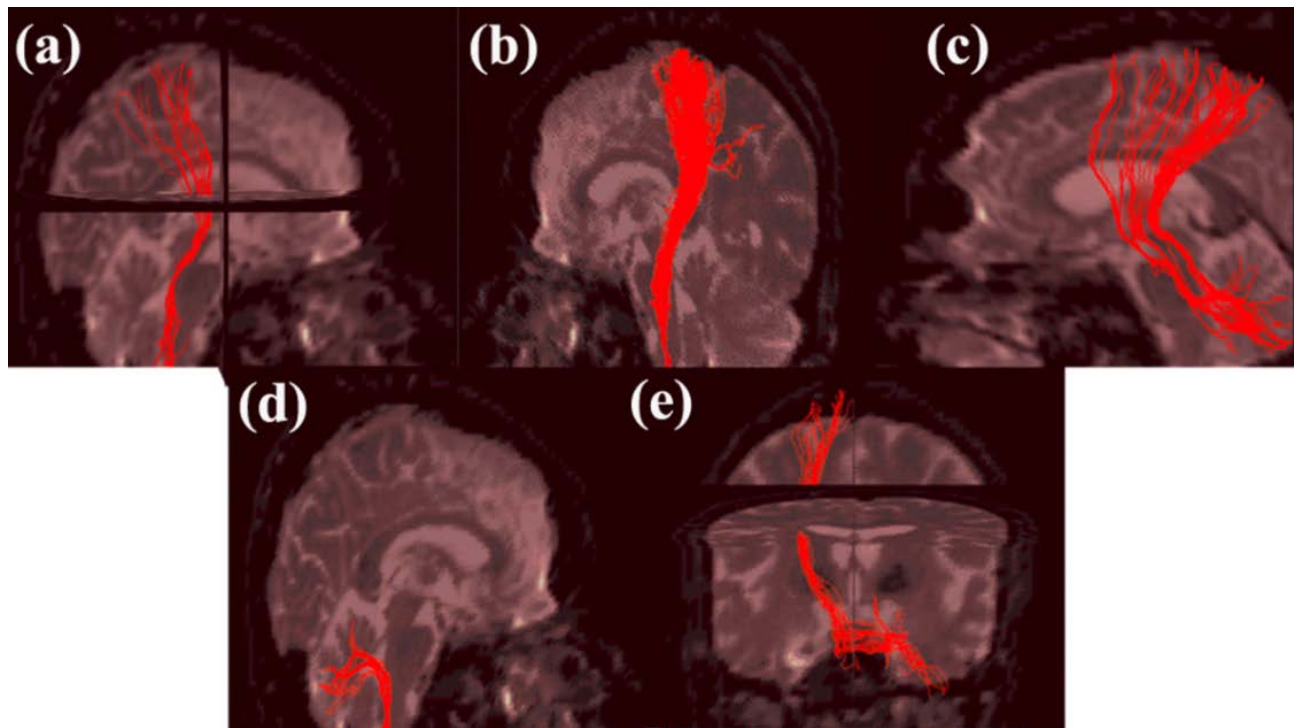


Figure 33: TDF-tractography results in reconstructing (a): the dorsal column-medial lemniscus pathway, (b): the corticospinal tracts, and all major cerebellar afferent/efferent fibers passing the superior, middle, and inferior peduncles (the dentate-rubro-thalamo-cortical or DRTC pathway via the superior cerebellar peduncle in (c); the spinocerebellar tracts via the inferior cerebellar peduncle in (d); the cortico-ponto-cerebellar or CPC pathway via the middle cerebellar peduncle in (e)). Here, both the CPC and DRTC pathways exhibit terminations in the motor cortex.

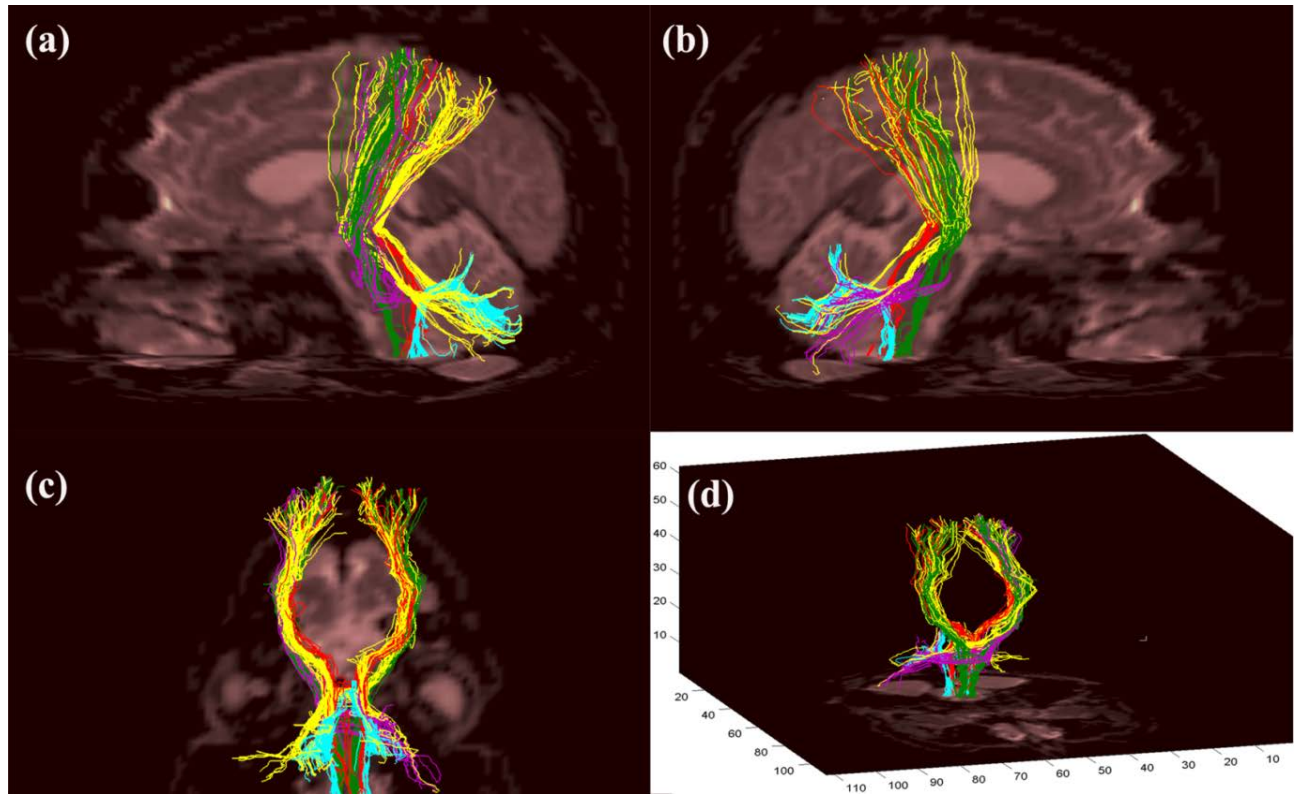


Figure 34: The GUI introduced in Figure 31 allows us to plot and visualize all reconstructed fibers in different colors (green-corticospinal or pyramidal fibers; red-DCML and other ascending sensory pathways; yellow-tracts passing through SCP representing the major cerebellar efferent pathway; light blue-tracts passing through ICP; magenta-CPC pathway/MCP). To better appreciate the anatomy, all fibers were reconstructed bilaterally except for the CPC pathway, shown here to originate on the right hemisphere and reach the contralateral cerebellum.

7.5 Circular Standard Deviation

In this section, we will discuss the issue of fiber incoherence and will show that it cannot be negligible. A lot of studies have relied in their analysis on using the DTI-based FA measure (equation 3.19). However, FA is contaminated by many factors such as spatial resolution and fiber incoherence especially in low resolution acquisitions which will profoundly affects clinical interpretation and comparisons across studies and put limits in the quantification of the underlying physiology. Zhan et al. have lately defined a

TDF-based FA (Zhan et al. 2009) which we have found to possess a lower dependence on spatial resolution as well as on fiber incoherence. To strengthen our proof, we have designed the circular standard deviation as a measure of fiber incoherence. For sake of convenience, we are going to refer to the DTI-based FA as FA^{DTI} and the TDF-based FA as FA^{TDF} .

We begin by first defining the FA^{TDF} , given a TDF function $P(D(\boldsymbol{\theta}, \boldsymbol{\lambda}))$ with $\boldsymbol{\theta} = (\theta_1, \theta_2)$ and $\boldsymbol{\lambda} = (\lambda_1, \lambda_2)$, the average eigenvalues are defined as:

$$\bar{\lambda}_i = \frac{\int P(D(\boldsymbol{\theta}, \boldsymbol{\lambda})) \lambda_i d\boldsymbol{\lambda}}{\int P(D(\boldsymbol{\theta}, \boldsymbol{\lambda})) d\boldsymbol{\lambda}}, i = 1, 2 \quad (7.5)$$

And the FA^{TDF} is defined as:

$$FA^{TDF} = \int P(D(\boldsymbol{\theta}, \boldsymbol{\lambda})) FA(D(\boldsymbol{\theta}, \boldsymbol{\lambda})) d\boldsymbol{\theta} d\boldsymbol{\lambda} \quad (7.6)$$

where

$$FA(D(\boldsymbol{\theta}, \boldsymbol{\lambda})) = \sqrt{\frac{(\bar{\lambda}_1 - \bar{\lambda}_2)^2 + (\bar{\lambda}_1 - \bar{\lambda}_3)^2 + (\bar{\lambda}_2 - \bar{\lambda}_3)^2}{2(\bar{\lambda}_1^2 + \bar{\lambda}_2^2 + \bar{\lambda}_3^2)}} \quad (7.7)$$

From the literature of directional statistics (Fisher 1993), we propose to compute the mean fiber direction vector \mathbf{R} of all detected fiber directions $\boldsymbol{\theta}^i$ at a given voxel as follows:

$$\mathbf{R} = \max_{eigenvector} \left\{ eigenvector \left\{ \sum_i TOD(\boldsymbol{\theta}^i) \boldsymbol{\theta}^i [\boldsymbol{\theta}^i]^T \right\} \right\} \quad (7.8)$$

Here, \mathbf{R} corresponds to the eigenvector corresponding to the largest eigenvalue of the matrix produced by the weighted sum of the self-inner product of the different fiber directions. Then, the CSD can be computed as:

$$CSD = \sqrt{-2 \log(\|\mathbf{R}\|)} \quad (7.9)$$

where $\|\cdot\|$ sign denotes the Euclidian norm.

The variation in the FA^{DTI} values have been thoroughly studied along different fiber bundles. It has been found that fiber orientational incoherence contaminates results. In (Fillard et al. 2003; Gilmore et al. 2007), the FA^{DTI} values have been computed along the CC fibers in the genu region in order to investigate early neonatal development of the CC. The authors have reported that FA^{DTI} depends on tract organization. In our analysis, we have constructed the genu fibers in a low and high spatial resolution data of a healthy subject (see Appendix A) using FACT tractography algorithm built-in the DTISTUDIO software (<http://cmrm.med.jhmi.edu/>) as well as using our TDF-TRACT algorithm. FA^{DTI} , FA^{TDF} , and CSD were computed along the constructed fibers. Figure 35 plots the average FA^{DTI} values against the geodesic distance across the reconstructed genu fibers obtained from DTISTUDIO in low and high spatial resolution data. Even though the low resolution data and its higher reconstruction were acquired in the same session using the same parameters, the FA^{DTI} values are higher in the higher spatial resolution data. Such increase can be explained by the existence of a higher degree of fiber incoherence due to the curving nature of the genu fibers which trace the trajectory of a U shape, thus a larger voxel would capture more of the curving trajectory. Such dependence on the image resolution puts limitations on the quantification of the underlying physiology. In contrast to FA^{DTI} , FA^{TDF} does not exhibit such great change in values from low to high resolution data (Figure 36) which supports the hypothesis that low FA^{DTI} values in low spatial resolution data is contaminated by a higher degree of fiber incoherence due to the larger voxel size. In order to strengthen this hypothesis, we computed CSD in low resolution data along the genu fiber bundle and expect the opposite effects to FA^{DTI} with respect to the geodesic distance (i.e., high degree of fiber incoherence leads to higher CSD values but lower FA values). Indeed, this is shown in Figure 37 where the blue line of the FA^{DTI} closely follows the trend of the inverse CSD plotted in red.

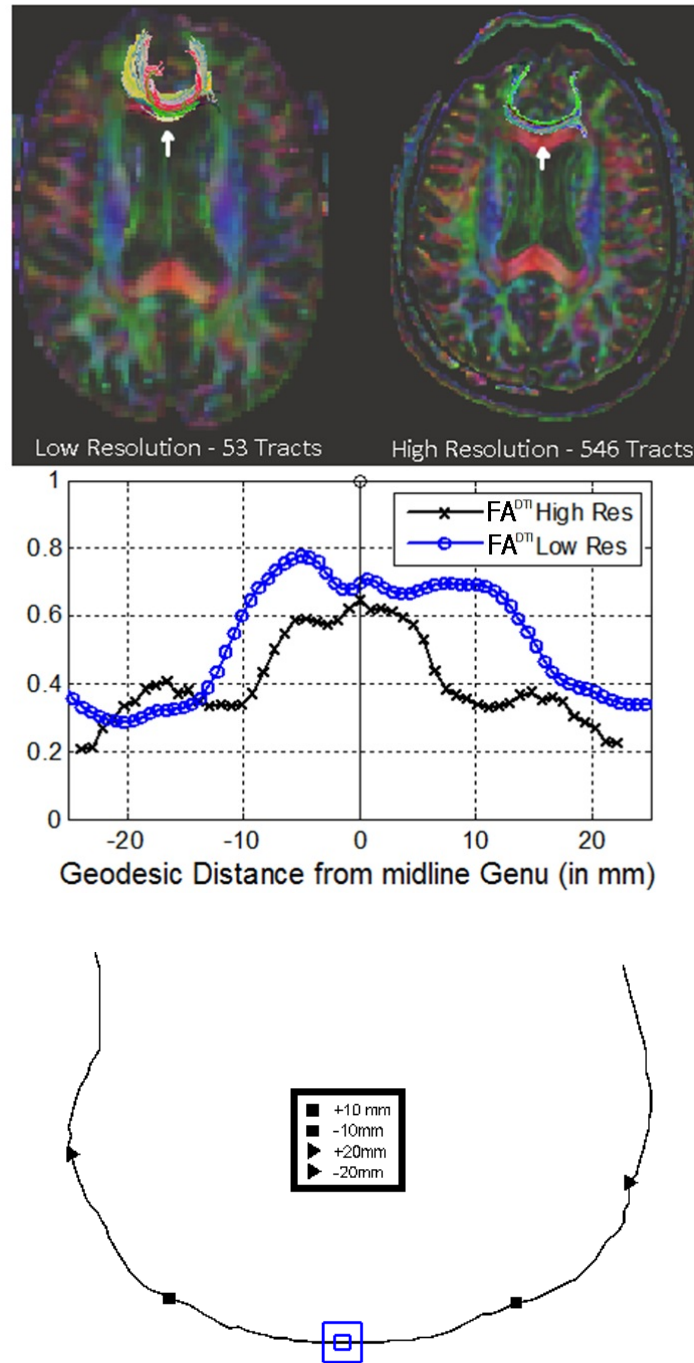


Figure 35: The averaged FA^{DTI} values (second panel) with respect to the geodesic distance from the mid-sagittal point (marked with white arrows, top panel) across all reconstructed commissural fibers in the genu of CC (top panel). We notice that the FA^{DTI} values are much higher for the higher spatial resolution data, especially in the central portion of the plot (i.e., around the mid-sagittal point). All results in this figure were produced using the DTI Studio software. Third panel shows the mid-sagittal point, the geodesic distance, and the low and high spatial resolution voxel sizes (the blue squares) with respect to a typical commissural fiber in the genu of CC.

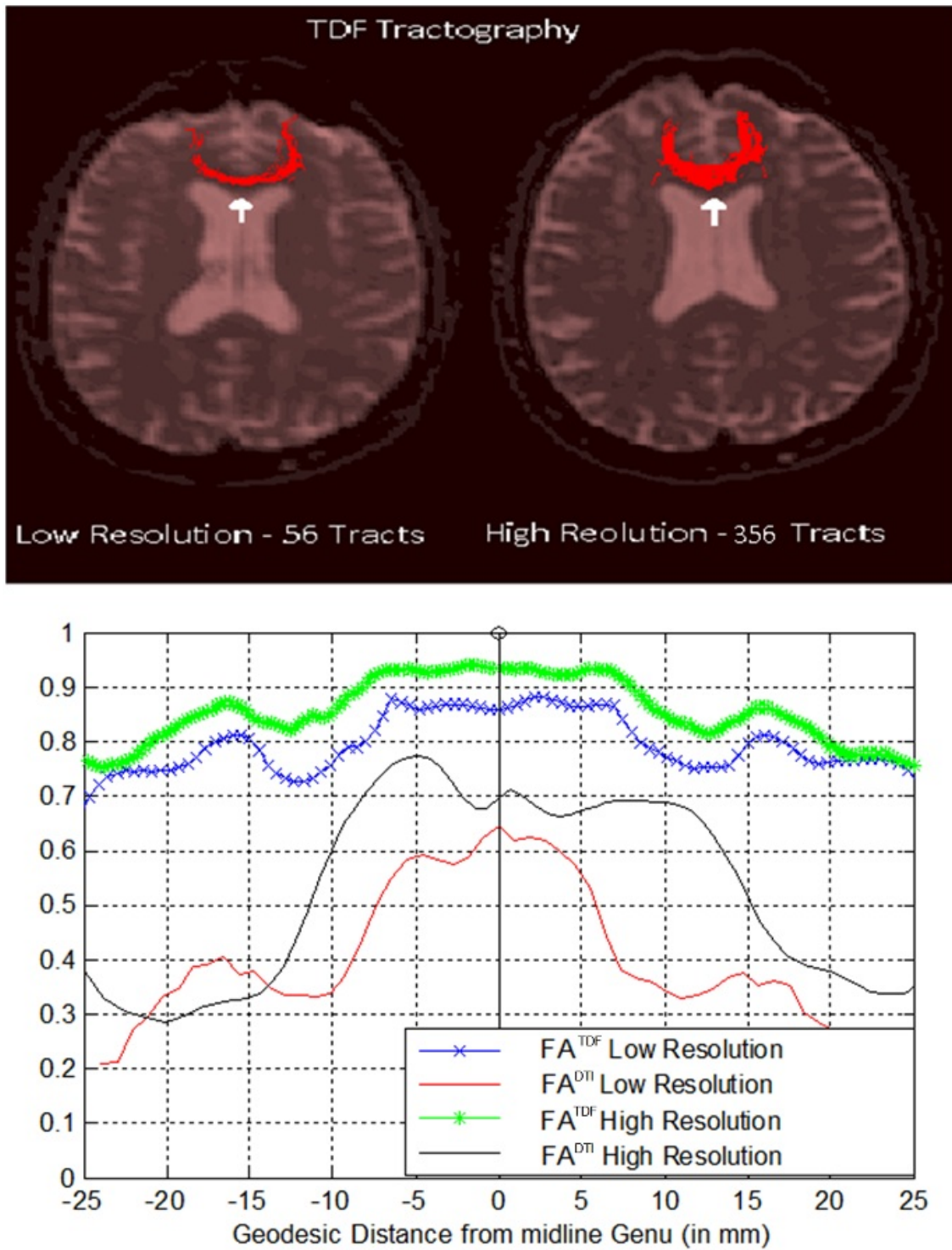


Figure 36: FA^{TDF} versus FA^{DTI} for both low and high resolution data (lower panel). Tracts were generated using our TDF-tractography program, and used to extract FA^{TDF} values along the curves (upper panel). Here, we notice that for the low resolution dataset, FA^{TDF} also has values higher than the FA^{DTI}. Moreover, FA^{TDF} has minimal dependence on the spatial resolution. This supports our hypothesis that the low FA^{DTI} values in low spatial resolution data are a direct result of the higher degree of fiber incoherence due to the larger voxel size.

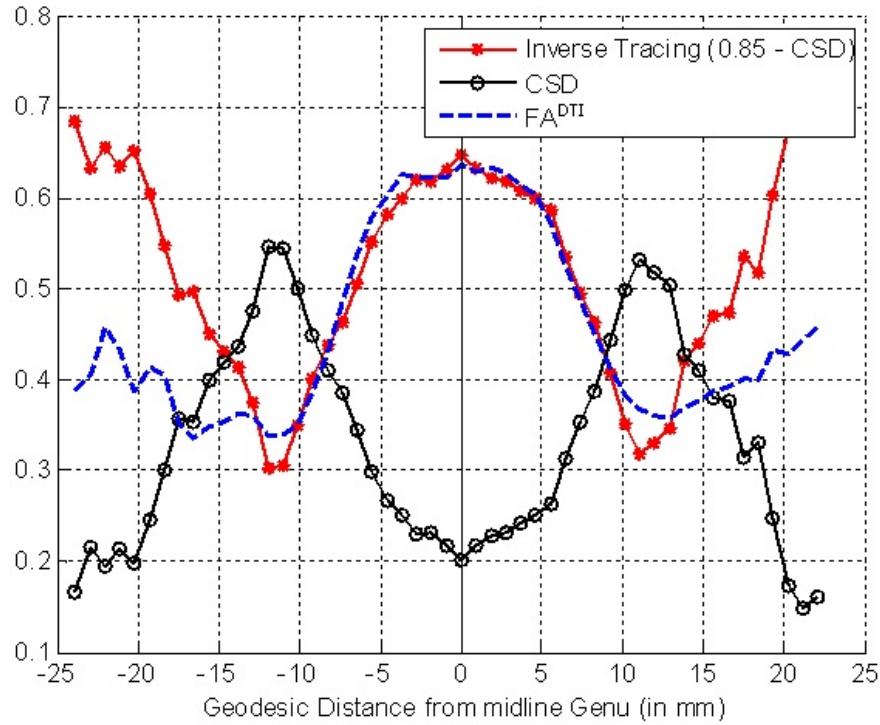


Figure 37: CSD and average FA^{DTI} plotted against the geodesic distance from the mid-sagittal point, across all reconstructed fibers, for the low spatial resolution data. The CSD is interpreted as a measure of the degree of fiber incoherence. Here, the FA^{DTI} tracing (dotted blue line) closely follows the trend of the inverse CSD tracing (red line) within 15 mm from the mid-sagittal point. Thus, FA^{DTI} values along tracts are highly correlated with, and dependent upon, the degree of fiber incoherence. This is more pronounced in lower spatial resolution images.

7.6 Conclusion

In this chapter, we have presented a new tractography algorithm (TDF-TRACT) which possesses a unique probabilistic aspect unlike other deterministic algorithms. The algorithm is capable of reconstructing many important fiber bundles. Moreover, we have developed a new metric (CSD) to measure fiber incoherence and used it to proof the dependence of FA^{DTI} on fiber incoherence especially in low spatial resolution data with large voxel size. We recommend the adoption of HARDI-based analysis techniques in future clinical studies of white matter integrity in order to avoid the problems found in FA^{DTI} .

VIII. EXTRACTING THE BRAIN COMMUNITY STRUCTURES

The work in this chapter has been presented in:

- 1- **Johnson GadElkarim**, Olusola Ajilore, Dan Schonfeld, Liang Zhang, Paul Thompson, Jamie Feusner, Anand Kumar, Lori Altshuler, and Alex Leow. 'Investigating brain community structure abnormalities in bipolar disorder using PLACE (Path Length Associated Community Estimation).' Human Brain Mapping, 2013 Jun 25:0. doi: 10.1002/hbm.22324,
- 2- **Johnson GadElkarim**, Dan Schonfeld, Olusola Ajilore, Liang Zhang, Jamie Feusner, Aifeng Zhang, Paul Thompson, Tony Simon, Anand Kumar, and Alex Leow. 'A Framework for Detecting Community Structure Group Differences in Brain Connectivity Networks.' MICCAI 2012, LCNS, Vol 7511, p 193-200.
- 3- Alex Leow, Liang Zhan, Olusola Ajilore, **Johnson GadElkarim**, Aifeng Zhang, Donatello Arienzo, Teena Moody, Jamie Feusner, Anand Kumar, Paul Thompson, Lori Altshuler, 'Measuring inter-hemispheric integration in bipolar affective disorder using brain network analysis and HARDI', International Symposium of Biomedical Imaging, ISBI 2012.

8.1 Introduction

In this chapter, we are going to study the brain on the macro-level. Through the concept of connectome, presented in chapter 5, the brain can be abstracted as a network. Using the connectome, one can use various metrics from graph theory to study topological, integration and clustering properties of brain networks (Rubinov and Sporns 2010). Assessment of such properties will allow us to describe a realm where healthy brain network lies in. Thus, we will be able to make group studies on various neuropsychological diseases in order to understand structural changes on the network level occurring in disease connectomes. For example, studying the community structure of the brain has lately shed light on alterations related to aging (Fair et al. 2009; Meunier et al. 2009) and schizophrenia (Bassett et al. 2008; Liu et al. 2008; Lynall et al. 2010; van den Heuvel et al. 2010; Alexander-Bloch et al. 2012). This could help assessing the effectiveness of therapeutical processes on the connectional level of the brain.

In this chapter, we are going to present two main contributions to both graph theory as well as to connectome studying fields. We will present new metrics to measure the modular integration of modular networks. These new metrics will rely on the notion of path length previously defined in chapter 5. The metrics will be used to measure the integration of brain networks in a group study of the bipolar disease based on the hypothesis that bipolar patient suffers a significant hemispheric dis-integration. Moreover, we are going to present a new metric, Ψ^{PL} , to extract the community structure of a network (review chapter 5). Using this metric, a complete framework is formulated based on the extracted brain community structures in the form of top-down binary trees (also known as dendrograms). The framework allows us to statistically detect significant community alterations on both: the nodal and community levels for group comparison studies using a nodal “consistency metric” designed to quantify differences in nodal affiliation between trees at each node. We named the new framework PLACE, which stands for “*Path Length Associated Community Estimation*”. The framework was used to perform two group studies on a sample of depression patients as well as a sample of bipolar patients.

The chapter is arranged as follow: first, in the methods section, we will describe the pipeline to generate a connectome, followed by the presentation of the new metrics that measure networks modular integration, followed by the description of PLACE. Second, we are going to present results of the application of the new metrics and PLACE on group studies. Third, a discussion to the findings will be presented. Finally, a mathematical variation of Ψ^{PL} will presented at the end of the chapter.

8.2 Methods

8.2.1 Constructing Brain Connectivity Network

Since the current state of the art imaging technologies do not allow access to the micro-level of neurons and axons, brain networks are generated on the macro-level by defining different brain regions on the GM and using results of the tractography process. To generate brain structural networks, a pipeline is followed which integrates multiple image analysis techniques. Figure 38 shows a simplified version of this pipeline. First, DW images are eddy current corrected using an image registration tool. Typically, one uses the $b0$ image as a reference for the other DW images acquired at the different gradients directions. In this thesis, we have used the automatic image registration (AIR) tool built-in the DTISTUDIO program (<http://www.mristudio.org>). This is followed by the generation of full brain tractography. One can choose from the different types of tractography presented in chapter 7. In this thesis, we have computed the DT then deterministic tractography using the FACT algorithm (Jiang et al. 2006) built into the DTISTUDIO program.

T1-weighted images are usually used to generate label maps in which the GM is divided into different ROIs. Though multiple atlases exist, one of two atlases is commonly used in literature, the automated anatomical labeling (AAL) (Tzourio-Mazoyer et al. 2002) or the one built-in the Freesurfer software package (<http://surfer.nmr.mgh.harvard.edu/>). Both generate label maps composed of ROIs in the order of 90. In this thesis, we have used the Freesurfer package. The resultant label maps contain 87 ROIs which include cortical, subcortical regions as well as the brainstem and cerebellum; the ROIs are listed in Appendix E. From a network point of view, each ROI is considered as being a node, brain networks are generated by counting the number of fibers connecting each node pair. Before performing the counting

process, the label map must be first registered in the space of the DW data. This is usually performed by registering the T1 image onto the $b0$ image. The resultant transformation matrix from this registration process is then used to transform the label map to the DW space.

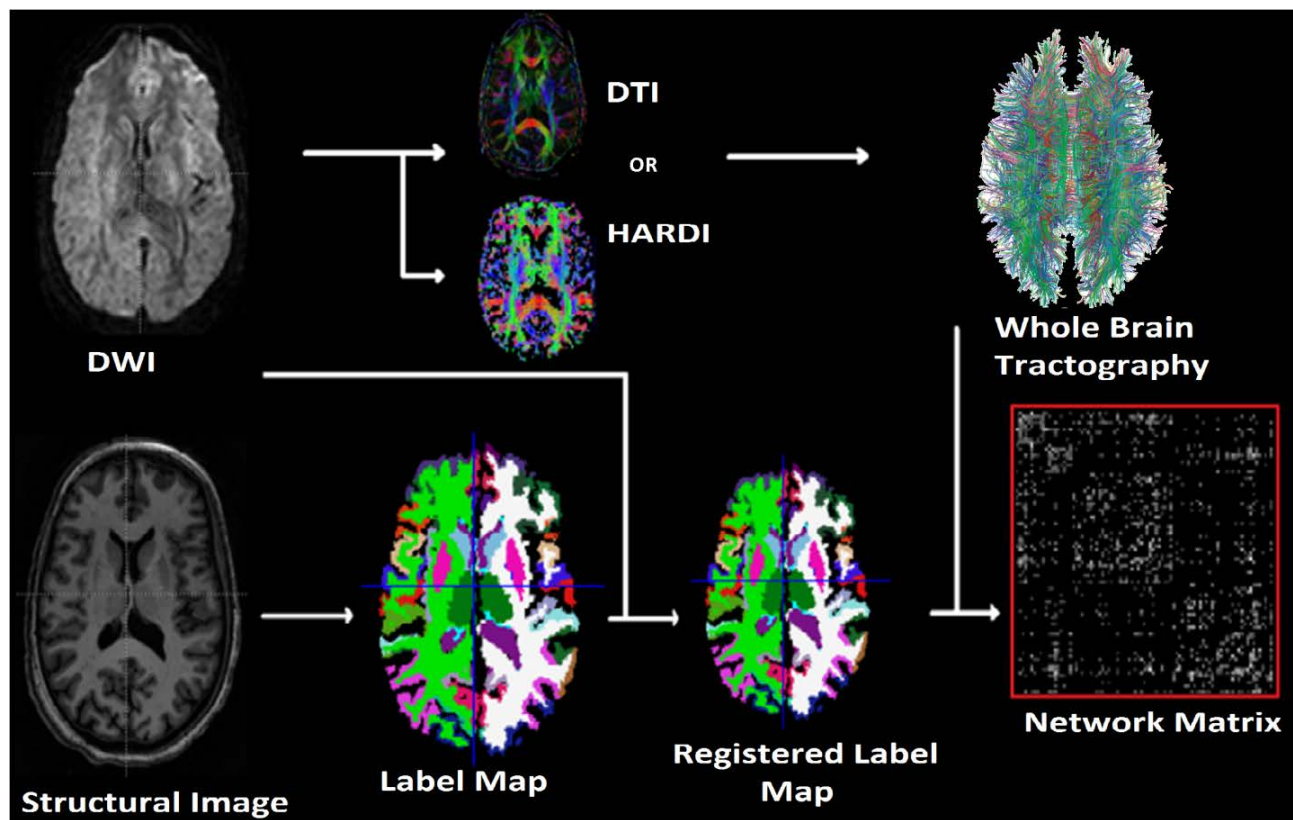


Figure 38: Pipeline used to generate structural brain networks

8.2.2 New Graph Metrics

In order to study modular integration in networks, we introduce a set of four metrics by modifying the definitions of CPL and E_{glob} . The proposed metrics are termed intra/inter modular path length and intra/inter modular efficiency ($Intra_{PL}$, $Inter_{PL}$, E_{intra} , and E_{inter}). The $Intra_{PL}$ is computed by averaging all shortest paths connecting node pairs in the same module. On the other hand, $Inter_{PL}$ is defined as the mean inter-modular distance (e.g., for communities (modules) C_i and C_j , $Inter_{PL}$ is measured by averaging the path lengths of all shortest paths connecting any node in module C_i to any node in module C_j). Mathematically, the $Intra_{PL}$ for module C_i is defined as:

$$Intra_{PL}^{C_i} = \frac{\sum_{n,m \in C_i; n > m} d_{nm}}{(N_i - 1)N_i/2} \quad (8.1)$$

Here N_i denotes the number of nodes in module C_i , and d_{nm} denotes the length of the shortest path connecting nodes n and m . Similarly, the $Inter_{PL}$ between modules C_i and C_j is mathematically defined as:

$$Inter_{PL}^{C_i \leftrightarrow C_j} = \frac{\sum_{n \in C_i, m \in C_j} d_{nm}}{N_i N_j} \quad (8.2)$$

In addition to inter and intra modular path length, we further propose the inter-modular and intra-modular efficiency as measures of network integration, mathematically defined as follows.

$$E_{\text{intra}}^{C_i} = \frac{\sum_{n,m \in C_i} d_{nm}^{-1}}{(N_i - 1)N_i/2} \quad (8.3)$$

$$E_{\text{inter}}^{C_i \leftrightarrow C_j} = \frac{\sum_{n \in C_i, m \in C_j} d_{nm}^{-1}}{N_i N_j} \quad (8.4)$$

In order to construct the distance matrix (whose d_{ij} element denotes the length of the shortest path connecting nodes i and j), an element-wise inverse transformation is applied on the weighted network matrix. Note that a higher edge weight indicates stronger connectivity and a shorter edge length. After applying the inverse mapping to a weighted matrix, the shortest path length is obtained using the well-known Dijkstra's algorithm

(Dijkstra 1959). We are going to apply the suggested metrics on structural brain networks in a group study of bipolar disorder (for description of the acquired data see (Appendix B)).

8.2.3 Path-Length Associated Community Estimation

Starting from the next section up to section 8.2.3.5, we are going to present the different methods utilized in the PLACE framework which detects nodal and modular alterations of networks in group studies.

8.2.3.1 Introducing Ψ^{PL}

In order to extract community structure, we seek to find groups of nodes which are highly interconnected while separated from nodes in other groups. Here, unlike in the modularity metric, the degree to which nodes are integrated (or separated) is measured using shortest path lengths, which encode geodesic distances between nodes in the graph and are calculated by applying the Dijkstra's algorithm to the element-wise inverse of the connectivity matrix. The proposed metric Ψ^{PL} is then defined as the difference between the mean inter and the mean intra modular path lengths ($Inter_{PL} / Intra_{PL}$) defined in the previous section. In the case of two communities (modules), for example, Ψ^{PL} is defined as:

$$\Psi^{PL} = Inter_{PL}^{C_1 \leftrightarrow C_2} - \frac{1}{2} (Intra_{PL}^{C_1} + Intra_{PL}^{C_2}) \quad (8.5)$$

Here, notice that maximizing Ψ^{PL} is equivalent to searching for a partition such that its communities exhibit stronger intra-community integration as well as stronger between-community separation. As such, we argue that Ψ^{PL} may be advantageous over the modularity Q in capturing the global configuration of a network (note that Q is computed by summing over a term that is only defined for node pairs belonging to a same community).

8.2.3.2 Community Structure Estimation

In order to extract community structures, a top-down hierarchical clustering was used to yield binary trees. At each level, nodes are randomly assigned to one of two communities, and the optimal assignment was determined by maximizing Ψ^{PL} using the SA algorithm (Kirkpatrick et al. 1983). At every iteration of

the SA algorithm, one node is randomly chosen to switch affiliation (to the other community). This affiliation switch is then accepted with respect to the following acceptance probability $P(accept)$ for such a change:

$$P(accept) = \begin{cases} 1, & \text{if } \Psi_{new}^{PL} > \Psi_{old}^{PL} \\ \exp\left(\frac{1}{T}(\Psi_{new}^{PL} - \Psi_{old}^{PL})\right), & \text{if } \Psi_{new}^{PL} < \Psi_{old}^{PL} \end{cases} \quad (8.6)$$

where Ψ_{new}^{PL} is the new value of our cost function under optimization computed with the switched affiliation, Ψ_{old}^{PL} is the last accepted value, and T is the artificial cooling temperature and is initially set to 1. The SA process is repeated at each level until the optimal dendrogram is reached (optimal in the sense that no further bifurcation may reveal additional community structure). The artificial temperature was lowered by a factor of 0.95 after a number of iterations equal to the square of the number of nodes. At any level, Ψ^{PL} was computed by considering the entire set of nodes found in the network in order to ensure the solution was globally optimized. Additionally, bifurcation was rejected if the maximum Ψ^{PL} was non-positive, since it indicated that the $Inter_{PL}$ was smaller than the average $Intra_{PL}$.

8.2.3.3 Assessing group-level Community Structure Differences

To quantify node level community differences, we have utilized the *scaled inclusivity* metric from Steen et al. (Steen et al. 2011). Here, the authors presented ζ , as a nodal consistency vector of length equal to the number of nodes in the network (68 in our case), which compares nodes in a *test* tree (i.e., an individual subject's tree) to nodes in a *reference* tree. Mathematically, for each node k belonging to communities C_p and C_q in the *test* and *reference* trees respectively, the scaled inclusivity, ζ , is defined as:

$$\zeta(k) = \frac{(N_c)^2}{N_p N_q}, \quad k = 1, \dots, 68 \quad (8.7)$$

where N_c denotes the number of common nodes between the two communities C_p and C_q , that contain this node k in the *test* and *reference* trees respectively.

8.2.3.4 Statistical Analysis

In order to examine group differences in community structures at the nodal level, we first constructed and qualitatively assessed the two groups mean trees (for control and disease groups under study) by extracting the community structure corresponding to the group mean connectivity matrices (NW_{mean}):

$$NW_{mean} = \frac{1}{N_{sub}} \sum_{i=1}^{N_{sub}} NW_i \quad (8.8)$$

where N_{sub} is the total number of subjects in the group and NW_i is the network matrix of subject i . The mean tree here may also represent the average brain network that summarizes the common network characteristics shared by all normal subjects in this sample (He et al. 2009; Meunier et al. 2009; Power et al. 2011; Zuo et al. 2012). Next, all individual subjects' trees (both disease and control) are compared to the mean tree of the control group (which serves as the reference tree in the previous section). We propose to detect group differences in local community structure using node-wise 2-sample T-tests for ζ , followed by correcting for multiple comparisons. Alternatively, a more powerful test on the community-level can be constructed via a multivariate distribution, for each community in the final level of the binary tree of the mean normal group, by concatenating the ζ vectors of all nodes in this community, on which 2-sample Hotelling's T-squared tests can be conducted. To examine the relationship of community structure with clinical measures, a post-hoc two-tailed partial correlation analysis is performed on ζ in selected nodes-of-interest and duration of illness (years since first mania and years since first major depression) and the number of mood episodes (manic and depressive) controlling for age.

8.2.3.5 Testing for Frequency of Occurrence

Additionally, under a stronger assumption that community structures do not depend on other covariates such as age and gender, one may perform a permutation test (Nichols et al.) in order to detect a change in node affiliation between groups. To this end, we first define an $N \times N$ frequency table for each diagnostic group (healthy and bipolar). For each diagnostic group, the entry f_{ij} of the frequency table

represents the number of times node i and node j are assigned to the same community, normalized by the number of subjects in this group (hence f_{ij} values range from 0 to 1; note that this frequency table is also a symmetric matrix). Secondly, for every node we compute the Euclidean distance of the corresponding frequency vectors for this node between the healthy and disease groups. Mathematically, for node i , the Euclidean distance D_i is defined as:

$$D_i = \sqrt{\sum_{j=1, j \neq i}^N (f_{ij}^H - f_{ij}^D)^2}, \quad i = 1, \dots, N \quad (8.9)$$

where the superscripts H and D stand for healthy and disease respectively. To construct permutation testing, we randomly shuffle subjects between the healthy and disease groups and re-compute the frequency tables as well as their Euclidean distances. This shuffling procedure is repeated 10,000 times and the re-sampled Euclidean distances are recorded. Last, for every node i , the p -value indicating whether there is a group difference in this node's frequency table, can be computed by ranking the observed D_i relative to the re-sampled 10,000 D_i s (e.g., if the observed D_i value ranks at 50 percentile among all re-sampled D_i then the corresponding p -value is 0.5 and, thus, we cannot reject the null hypothesis at a threshold level of 0.05).

8.3 Results

In this section, we are going to present three types of results. First, we are going to present the application of the modular integration metrics on a group study of a sample of bipolar patients. Second, a comparison between community structure extracted using Ψ^{PL} and the Q modularity will be presented by analyzing two real two published networks, the Zachary club (Zachary 1977) and bottlenose dolphins living in Doubtful Sound in New Zealand (Lusseau et al. 2003). Finally, we are going to present results of the application of PLACE to the a bipolar dataset and another population of major depression in order to detect nodal and modular alterations which might occur due to those diseases. Before presenting the results from using PLACE, we are going to discuss the issue of the optimal level that can be used in the hierarchical reconstruction of the human brain community structure in the form of trees.

8.3.1 Applying the New Graph Metrics to Bipolar Disorder

Brain networks were reconstructed as described in the method section using the dataset made of 25 healthy controls and 25 subjects with bipolar disorder described in Appendix B. Focusing only on cortical regions, sub-networks formed of 68 cortical ROIs were reconstructed. The proposed intra/inter modular path length and intra/inter modular efficiency ($Intra_{PL}$, $Inter_{PL}$, E_{intra} , and E_{inter}) were computed between the two hemispheres. After controlling for multiple comparisons (Bonferroni corrections; cut-off p value at 0.05/12 for a total of 12 tests) results showed that bipolar subjects exhibited significantly attenuated inter-hemispheric integration (lower inter-hemispheric efficiency and longer inter-hemispheric path length) relative to control subjects (23.90 ± 4.50 in bipolar versus 28.52 ± 4.37 in control, and $p < 0.001$). Further focus was given to localize corpus colossal abnormalities in inter-hemispheric integration, by separately investigating $Inter_{PL}$ and E_{inter} within the frontal, parietal, temporal, and occipital lobes. Results revealed widespread inter hemispheric integration abnormalities with the most statistically significant deficit in the frontal lobe, thus suggesting prominent corpus colossal abnormality in the genu and anterior body (Table VI).

Table VI: Inter-hemispheric integration analyses in the frontal, temporal, parietal and occipital lobes. This table shows the mean and standard deviation of lobar inter-hemispheric path length and efficiency. Only group differences reaching statistical significance are shown (Bonferroni correction with a total of 16 tests; cut-off p value $0.05/16=0.003$)

			p -value
Inter-hemispheric path length Occipital lobe	Bipolar	0.054 \pm (0.014)	0.0021
	Healthy controls	0.044 \pm (0.010)	
Inter-hemispheric efficiency Frontal lobe	Bipolar	22.9 \pm (4.86)	1.5 $\times 10^{-4}$
	Healthy controls	27.9 \pm (6.26)	
Inter-hemispheric efficiency Temporal lobe	Bipolar	54.6 \pm (17.9)	0.0016
	Healthy controls	71.4 \pm (20.3)	
Inter-hemispheric efficiency Occipital lobe	Bipolar	22.9 \pm (4.86)	0.0024
	Healthy controls	27.9 \pm (6.26)	
Inter-hemispheric efficiency Parietal lobe	Bipolar	54.6 \pm (17.9)	0.0030
	Healthy controls	71.4 \pm (20.3)	

8.3.2 Comparison with Q Modularity

Perhaps one of the most important questions to ask in the analysis of community structure is the relevance and meaning of extracted communities. Several quality functions, such as Q , do exist to assess the goodness of a community. However, it has been shown that higher Q values do not always indicate a meaningful community structure (high Q was found in partitioning random graphs into communities although one would not expect any communities to exist) (Fortunato 2010). In addition, one would expect that the optimization of any quality function yields communities consistent with the underlying criterion inherent in the function being optimized. For this reason, testing an algorithm using real networks whose communities are known *a priori* is paramount.

Here, we tested the proposed framework using two published networks and compared the extracted communities by maximizing Ψ^{PL} at different levels with the corresponding communities having the maximum known Q_w in the literature. The first network was compiled by Zachary (Zachary 1977) as a social network which represents the communication between 34 members of a university karate club, the study of which was done in two years. The nodes represent the club members while the edges represent the strength of the social relation between them. According to Zachary, the club consists of two communities, one around the club's administrator (node 1) and the other around the karate trainer (node 34), as a result of a dispute between them at the beginning of the study. Both Q_w and Ψ^{PL} have successfully recovered the two known communities shown in Figure 39a, b. However, the maximal Q_w reported in the literature is 0.4198 was obtained by a four-module community structure (Aloise et al. 2010) (Figure 39b). On the other hand, the two-level dendrogram computed using Ψ^{PL} yielded the correct community structure at the first level, while revealing a different four-module structure at the second level.

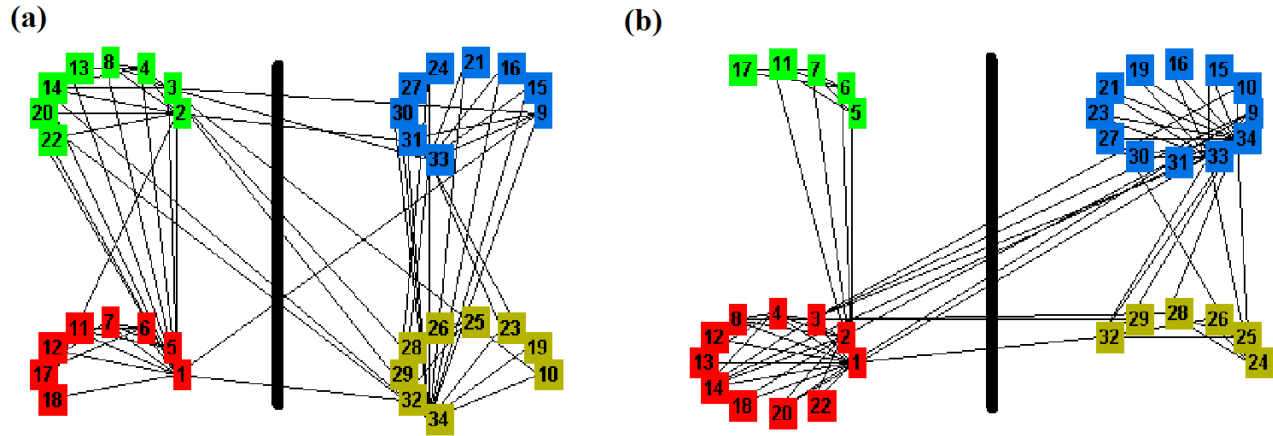


Figure 39: Community structure obtained by maximizing Ψ^{PL} using a two-level binary tree for the Zachary club network (a), and the corresponding community structure obtained by maximizing Q_w at a value of 0.4189 (b). Both strategies correctly identified the 2 main communities as reported by Zachary (indicated by the bold line in the middle).

8.3.3 Optimal Level of Hierarchical Reconstruction

Since bifurcating hierarchical trees are used to represent brain community structure, a relevant question is at what bifurcation level is brain community structure best represented (note that this may depend on the choice of brain atlas and the resolution – number of nodes – using which brain regions are partitioned). To determine the optimal level and avoid choosing a random level, we first constructed hierarchical trees, for all healthy subjects in Appendix B, up to the fifth level (i.e., a total of 32 communities). To assess the separability at each bifurcation step (i.e., the higher the separability, the more evidence this community can be further divided up into smaller communities), we computed the ratio $Inter_{PL}/Intra_{PL}$ which should be considerably greater than 1 if a community can be further divided into two. At each level, this separability metric is computed and averaged across all subjects. We plotted the average separability against the level of bifurcation, and noted that this ratio reached its maximum at the fourth level followed by a significant decrease at the fifth level (Figure 40), indicating that optimal community structure may be attained at the fourth level.

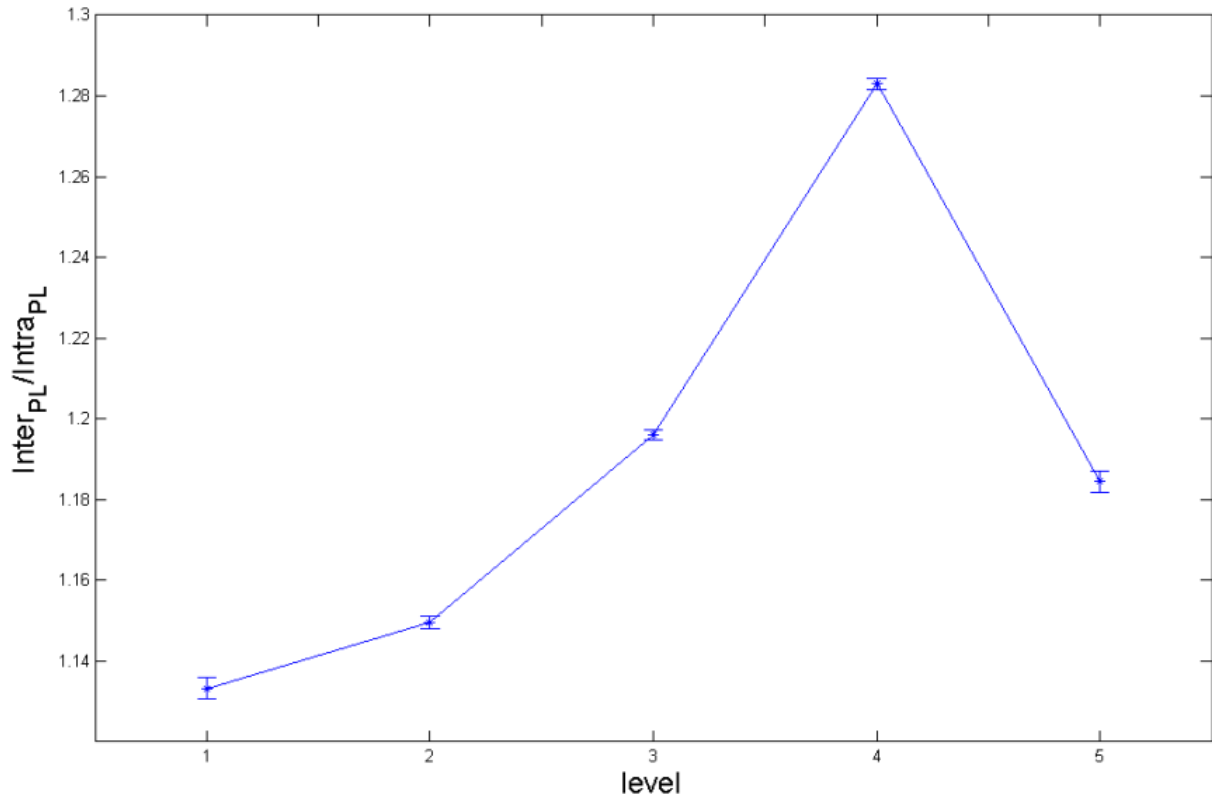


Figure 40: This figure plots the average separability metric $Inter_{PL}/Intra_{PL}$ ratio across all subjects at each level (y axis; brackets indicate standard error) against the bifurcation level up to the fifth level (x axis).

8.3.4 Community Structure Alterations in Bipolar Disorder

Brain networks were constructed using the dataset in Appendix B made out of 25 healthy subjects and 25 participants with bipolar I disorder. Hierarchical trees were generated using only cortical regions (68 nodes, 34 per hemisphere). Consistency metrics were computed to yield 25 ζ vectors for each group as presented in the method section. To detect community structure abnormalities, the Hotelling's T-squared statistics was constructed for all 16 communities in the reference (mean control) tree. Results showed a significant group difference (i.e., lower consistency; $p = 0.0059$, uncorrected) in bipolar versus control for the

community containing the right paracentral gyrus, right posterior cingulate, left paracentral gyrus and left posterior cingulate (Figure 41 upper left, and bottom row). On a node level, conducting 2-sample T-tests on the consistency metric ζ revealed similar findings. In particular, the right paracentral gyrus exhibited the lowest node-level consistency ($p = 0.0005$ & for the T-test, passing Bonferroni correction at $0.05/68$). Qualitative comparison between the two mean community structures reveals that the right and left paracentral gyri, while belonging to the same community in the healthy controls (Figure 41 upper left), are assigned to different communities in the bipolar group (Figure 41 upper right). Additionally the right isthmus cingulate, paracentral gyrus, posterior-cingulate and precuneus are assigned to one community while the same regions in the left hemisphere are assigned to another community (Figure 41 upper right).

Applying the permutation test presented in the methods section 8.2.3.5 also supports the above finding. Here, the right paracentral gyrus exhibits the lowest p -value of 0.0068 (uncorrected) (Figure 42) which indicates that a change in the frequency vector for this node does exist in the bipolar group. For the bipolar group, post hoc analyses were conducted to correlate ζ values with duration of illness. Here, ROIs were informed by the community structure group differences, and thus included the bilateral paracentral gyrus, the bilateral precuneus, and the bilateral posterior and isthmus cingulate. Results revealed that ζ was negatively associated with the number of depressive episodes for the left isthmus cingulate ($r = -0.49$, $p = .017$) and left precuneus ($r = -0.45$, $p = .032$).

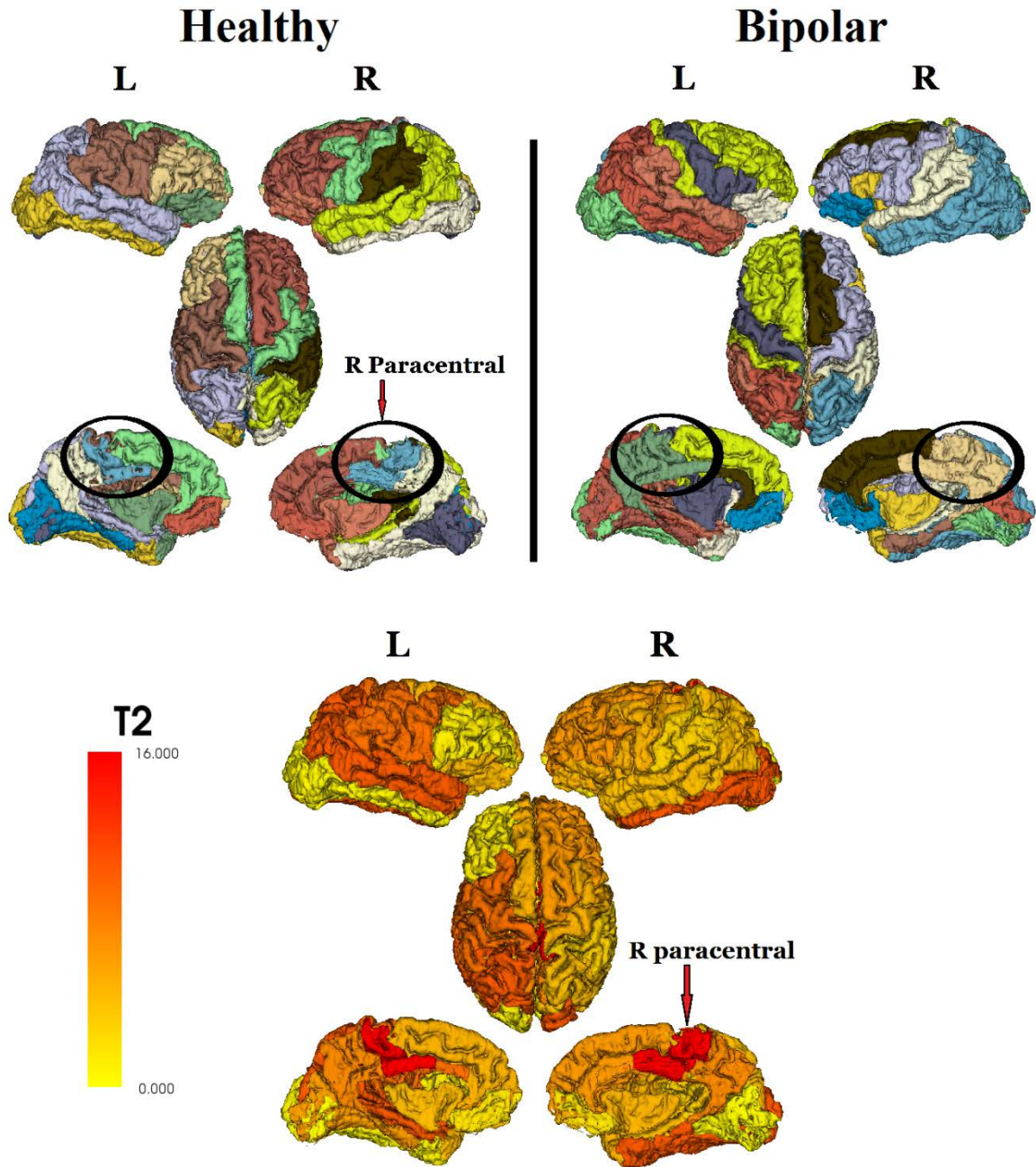


Figure 41: Top: 4-level binary trees showing mean community structures via the proposed metric Ψ^{PL} . Notice that the right paracentral and left paracentral gyrus belong to the same community in the healthy but not in the bipolar group. Additionally, in the bipolar group the isthmus cingulate, the paracentral gyrus, the posterior cingulate and the precuneus are assigned to one single community in each hemisphere. Bottom: Hotelling's T-Squared statistics are overlaid on the 16 communities of the mean healthy control tree, showing the degree of regional group differences between groups. The most significant differences are for the community containing the bilateral paracentral gyri and posterior cingulate (this community is indicated by R paracentral, the only node passing Bonferroni correction in the corresponding 2-sample T-test). This figure is showing a left/right lateral view (top), an axial view (middle) and a left/right mid-line view (at the bottom).

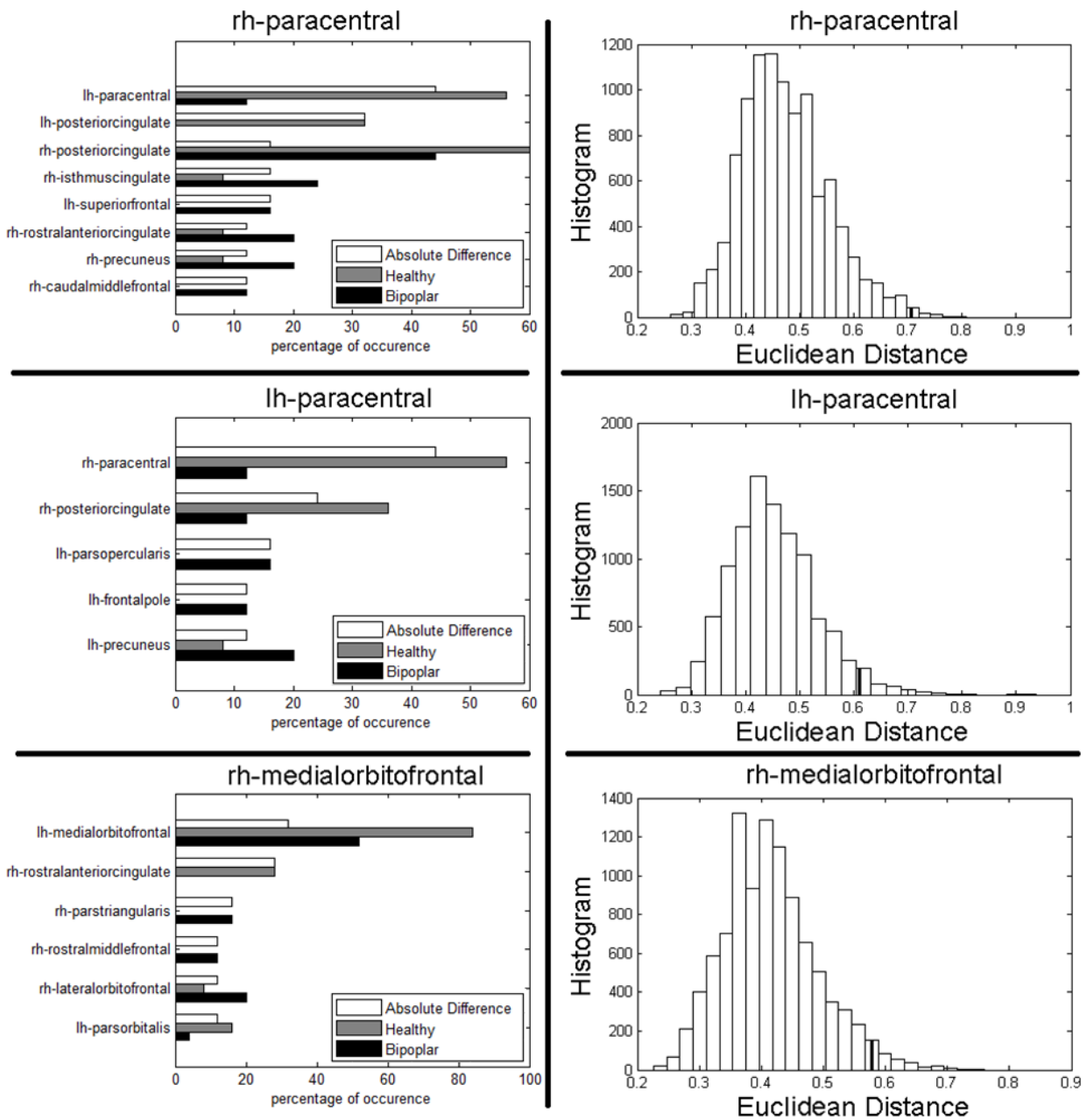


Figure 42: (Left panel) The frequencies at which several brain regions (i.e., nodes; y-axis) belong to the same community as the right and left paracentral gyrus and the right medial orbitofrontal gyrus (all three regions passed the permutation test at 0.05 uncorrected). The frequency (x-axis) was calculated separately for each group (gray and black denote healthy and bipolar respectively, while the absolute difference is denoted in white). The brain regions are arranged according to the magnitude of the absolute difference such that the nodes on top exhibit a larger degree of group difference. (Right panel) Histogram of the resampled test statistics (Euclidean distances). This figure shows only nodes with $p < 0.05$ (uncorrected) in the proposed permutation test, and the observed statistics (without re-shuffling) are indicated using thick solid lines ($p=0.0068$ for the right paracentral gyrus, $p = 0.0333$ for the left paracentral gyrus, and $p = 0.03$ for the right medial orbitofrontal gyrus).

8.3.5 Community Structure Alterations in Depression Disorder

Brain networks were constructed using the dataset in Appendix A made out of 47 healthy subjects and 42 subjects with major depression. Hierarchical trees were generated using only cortical regions (68 nodes, 34 per hemisphere). We constructed the Hotelling T-squared for all 16 communities in the reference tree. Results showed a significantly lower consistency ($p = 0.0079$) in depression versus control for the community containing the right precuneus, superior parietal gyrus, inferior parietal gyrus, inferior temporal gyrus, and isthmus cingulate (Figure 43). On a node level, conducting 2-sample T-test on ζ confirmed such findings (Table VII).

The right precuneus and superior parietal gyrus exhibited the lowest node-level consistency ($p < 0.01$; uncorrected). Comparing the mean community structures between two groups, we note that the right precuneus and right superior parietal gyrus, while belonging to the same community in the healthy controls, are assigned to different communities in the depressed group. Additionally, in depression the bilateral precuneus are assigned to one community, suggesting a stronger structural integration between them.

Table VII: List of nodes which showed significant lower consistency in depression relative to healthy controls at $p < 0.01$ (uncorrected). The table shows mean and standard deviation values using 2-sample T-test (for ζ), and their corresponding p values.

	Healthy	Depressed	p-value
right-precuneus	0.2645 ± 0.1501	0.1784 ± 0.0908	0.0019
right-superiorparietal	0.2374 ± 0.1475	0.1524 ± 0.1106	0.0033

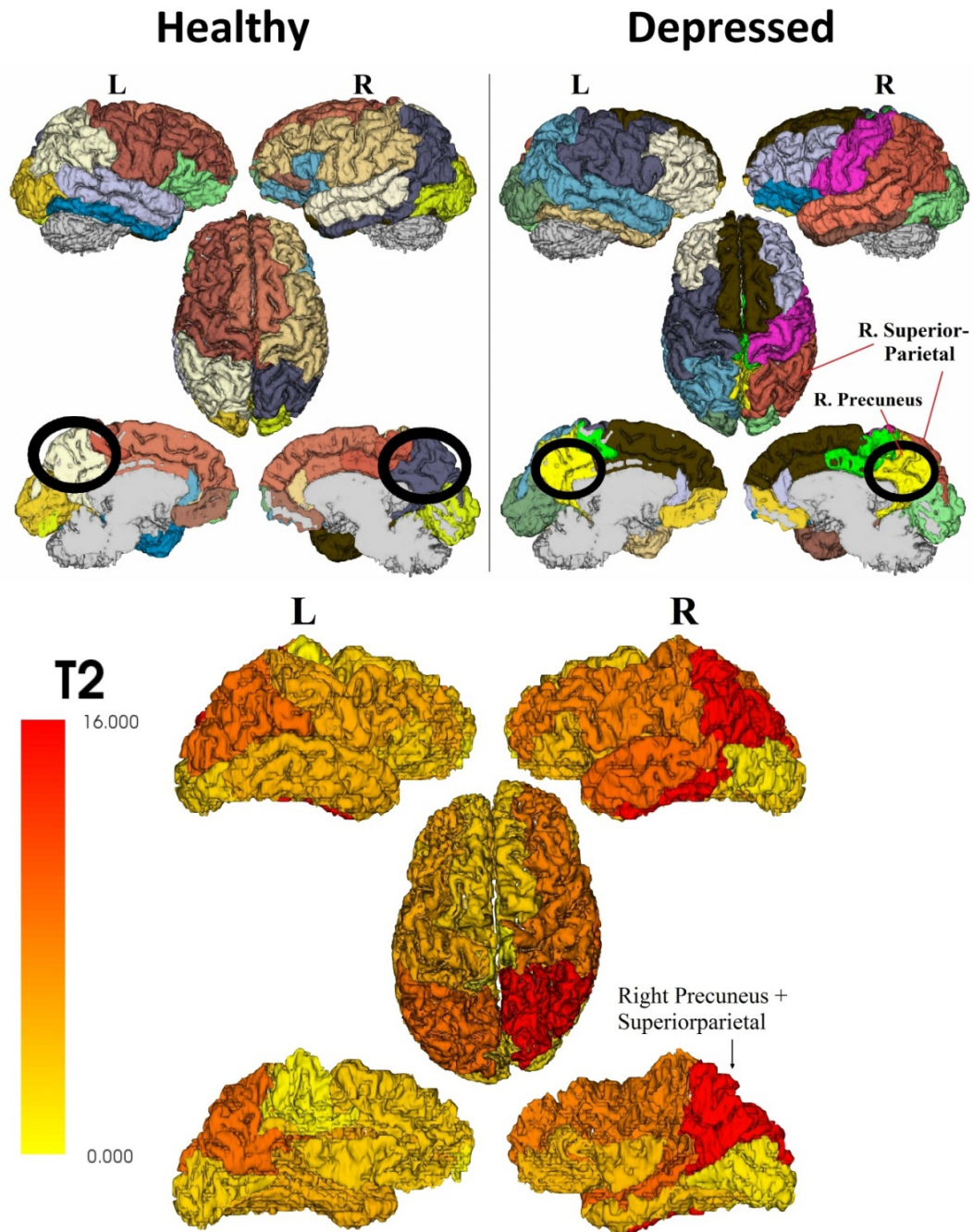


Figure 43: Top row: 4-level binary trees showing mean community structures via the proposed metric Ψ^{PL} . Notice that the right precuneus and right superior parietal gyrus belong to the same community in the healthy controls but not in the depressed group. Additionally, in the depressed group the right and left precuneus are assigned to one single community (which also comprises bilateral isthmus cingulate). Bottom row: Hotelling's T-Squared statistics are overlaid on the 16 communities of the reference tree, showing regional group differences in the community structure between groups. The most significant differences are in the right precuneus and superior parietal gyrus. This figure is showing a left/right lateral view (top), an axial view (middle) and a left/right mid-line view (at the bottom). The community containing the right precuneus and the right superior parietal gyrus is highlighted in red.

8.4 Discussion

The application of the new metrics on brain networks of subjects with bipolar disorder has revealed significant alteration in WM integrity in the corpus callosum. Further analysis has localized the alteration to be more significant in the anterior section of the corpus callosum (i.e., genu and anterior body). In all, these metrics can be applied given any sub-grouping of a network into a non-overlapping set of modules. The results are scientifically relevant and may potentially have significant clinical implications.

Moreover, PLACE was able to identify changes in the community structures between two groups of connectomes on both the nodal and the modular levels. The application of PLACE on the bipolar dataset have revealed that a relative left-right decoupling exists in the community structure of bipolar subjects (i.e., the right paracentral gyrus, right posterior cingulate, left paracentral gyrus and left posterior cingulate form one community in the healthy group, but they are left-right decoupled and separated in the bipolar group). Previous studies in bipolar disorder have consistently implicated deficits in inter-hemispheric communication via corpus callosum (Frazier et al. 2007; Bruno et al. 2008; Wang et al. 2008; Sussmann et al. 2009; Mahon et al. 2010). Moreover, our decoupling finding is also in line with the results from the new graph metrics. In this previous study, although global deficits were found across all regions of the corpus callosum, we detected and reported more prominent deficits in the anterior section of corpus callosum, (similar findings have been reported, e.g. in (Walterfang et al. 2009)).

Furthermore, the application of PLACE on the depression dataset has revealed local community differences in parts of the default mode network (the network of brain regions that are active when the individual is not focused on the outside world and the brain is at wakeful rest), in specific, the right precuneus which has been previously linked to self-awareness and shown to exhibit abnormalities in depression (Lou et al. 2004; Zhu et al. 2012).

8.5 Conclusion

In this chapter we have presented a new contribution to graph theory. A set of four new graph metrics was presented to measure the modular integration of networks. Furthermore, we presented Ψ^{PL} , a new quality function for the goodness of a graph partitioning into communities. The new function was used to extract community structure from graphs in the form of hierarchical binary trees. This was integrated within a new framework that can be used to detect nodal and modular alterations between two groups of graphs. The framework, named PLACE, was applied to brain networks extracted from two datasets, bipolar and depression. Results were consistent with previous clinical findings which strengthen the framework and open a new horizon in the analysis of connectomes. Moreover, a generalization of Ψ^{PL} was presented as well as preliminary results which show its usefulness in the extraction of community structure in graphs.

IX. CONCLUSIONS AND FUTURE RESEARCH

In this thesis, we have studied the brain on three levels: micro, mid and macro. On the micro-level, we tried to describe the complexity of the human brain using two new models based on the theory of AD. The models tried to probe the porosity and tortuosity of the brain tissues by introducing new biometrics. Results have shown the directional dependence of the complexity metric, complexity was found higher in perpendicular directions to the white matter fibers. Further investigation is needed to test the applicability of the model on datasets from other scanners as well as to perform group studies on neuropsychological diseases and test for changes in the new biometrics.

On the mid-level, we have first presented a new tractography algorithm, suggested a new model for the diffusion data in light of the anomalous diffusion theory, and finally described a complete framework to detect alterations in the community structure of brain networks on both the nodal and modular levels. The proposed tractography algorithm in chapter 7, based on the TDF model, has shown a great success in extracting various fiber bundles in the human brain due to its probabilistic nature. Furthermore, the newly defined, CSD, has been used to measure fiber incoherence and was helpful in proofing the dependence of FA^{DTI} on fiber incoherence especially in low spatial resolution data with large voxel size. For that, we recommend the adoption of HARDI-based analysis techniques in future clinical studies of white matter integrity in order to avoid the problems found in FA^{DTI} . Although the TDF is an effective model to solve the crossing fibers problem within voxels, it suffers a computational problem in which the analysis of a single subject might take a day or even two. Decreasing the computational cost of the TDF model would be on the top priorities of future research to allow the model the ease of use needed for group analysis.

On the macro-level, the PLACE framework provides a way to investigate changes that occur in the brain structure on the nodal and modular levels. The framework was applied to the brain networks extracted from two datasets, bipolar and depression. Results were consistent with previous clinical findings which strengthen the framework and open a new horizon in the analysis of connectomes. As a future step, measuring the distance between the space of healthy trees and the space of disease tree would be a prominent

way of finding differences in group analysis which will not be depend on the computation of the mean healthy tree from the mean healthy network. Moreover, a generalization of the Ψ^{PL} metric to non-binary bifurcation is required. Although the choice of binary hierarchical trees may allow us to study small modules which are not discovered by the classical modularity Q , however, real life networks may be non-hierarchical and may contain an odd number of modules.

APPENDICES

Appendix A

Depression Dataset:

We scanned 47 healthy subjects (20 male/27 female; age: 59.74±14.8)) and 42 subjects with major depression as defined by DSM-IV (18 male/24 female; age: 57.64±13.4). A Philips 3.0 T Achieva scanner supplied with 8-channel SENSE head-coil was used to acquire the brain MRI data. High resolution T1-weighted images were acquired with MPRAGE sequence (FOV=240 mm; TR/TE=8.4/3.9 ms; flip angle 8; voxel size 1.1x1.1x1.1mm). Diffusion weighted (DW) images were acquired using SS-SE-EPI sequences (FOV = 240 mm; resolution 0.83X0.83 mm; TR/TE=6994/71 ms; flip angle = 90, 32 gradient directions, b= 700 s/mm² and one minimally DW scan: b0 image). Parallel imaging was also used with a SENSE factor of 2.5 to reduce scan time to 4 min.

Appendix B

Bipolar Dataset:

We scanned 25 healthy subjects (13 male and 12 female; age: 42.2 ± 10.8) and 25 gender and age matched bipolar subjects (14 male and 11 female; age: 41.7 ± 12.6). All bipolar subjects received comprehensive psychiatric evaluations using the structured clinical interview for DSM disorders (SCID; <http://www.scid4.org/>) and met the DSM IV criteria for bipolar I disorder (at the time of image acquisition all subjects have been in an euthymic state for at least 30 days). A Siemens 3T Trio scanner was used to acquire the brain MRI data. High resolution T1-weighted images were acquired with MPRAGE sequence (FOV = 250x250 mm; TR/TE = 1900/2.26 ms; flip angle = 9; voxel size = 1x1x1 mm). Diffusion weighted (DW) images were acquired using SS-SE-EPI sequences (FOV = 190x190 mm; resolution 2x2x2 mm³; TR/TE = 8400/93 ms; 64 gradient directions, $b = 1000$ s/mm² and one minimally DW scan: b0 image). At the time of the MRI scan, 7 participants were on valproic acid, 1 on carbamazepine, 3 on lamotrigine, 14 on antipsychotic medications, 8 on SSRI antidepressant medications, 5 on other antidepressant medications, and 3 on benzodiazepines. None of the study participants was on lithium; two participants were not on any psychotropic medications either at SCID or the time of the MRI scan.

Appendix C

Multi b -value Dataset1:

Multiple b -value dMRI scans were acquired from a healthy subject. The Philips 3.0 T Achieva scanner located at the University of Illinois Medical Center Advanced Imaging Center was used to acquire the brain MRI data using an 8-channel SENSE head-coil. DW images were acquired using double spin-echo (SE) echo-planar imaging (EPI) sequences with TR/TE = 10900/80 ms, FOV = 24 x 24 cm², resolution 0.83x0.83 mm², slice thickness = 2.2 mm. DW images were acquired at sixteen b -values – 0, 100, 200, 300, 400, 500, 700, 800, 1000, 1200, 1500, 2000, 2400, 3000, 4000, 4700 s/mm² – generated by varying the applied gradient amplitude while fixing the pulse width (δ) and pulse separation (Δ) at 21.7 msec and 43.5 msec respectively. In order to increase the SNR, we averaged three acquisitions for the last four b -values. At each b -value, the DW gradient was applied at six non-collinear directions. The whole acquisition took approximately 25 min.

Multi b -value Dataset2:

A healthy subject was scanned on a 3T Siemens “Allegra”. DW were acquired using double SE EPI sequences, TR/TE = 6400/107 ms, slice thickness = 3 mm, matrix 128 x 128, FOV = 23 x 23 cm² and 7 b -values in the range 100 to 5000 s/mm².

Appendix D

Fractional Calculus:

Fractional calculus is the field of mathematics which deals with integrals and derivatives of real numbers. In 1695, the French mathematician L'Hôpital wrote to Leibniz asking him about the n th derivative of a function $f(x) = x$ when $n = \frac{1}{2}$. Leibniz's response was "an apparent paradox from which one day useful consequences will be drawn". This is when fractional calculus was born. Although it dates 300 years back, it is not until the last five decades that fractional calculus have grabbed the attention of researchers. In fact, fractional calculus has been found useful in many applications such as electrical networks, diffusive transport, electromagnetic theory and probability.

Unlike integer-order integrals and derivatives which are well established and have clear physical interpretations. However, since the introduction of this new field in mathematics, there was not any acceptable physical interpretation in the preceding two centuries. Perhaps the most intriguing property of fractional calculus is that fractional integrals and derivatives are not local operators (that act at a point) unlike their integer order counterpart. As we will see, those operators takes into consideration the past and future of the function under action, not just a small neighborhood as used to be in ordinary integer order operators. For that, many definitions have existed for those operators, each have its own use. In this short introduction, we are going to present the different definitions of fractional order integral and derivative operators. Before that, relevant functions are going to be presented which will be used later. Furthermore, a derivative example of some functions will be given for every definition. For more information on fractional calculus, we refer the reader to the monographs by Podlubny (Podlubny 1999), Herrman (Herrmann 2011) and Meerschaert and Sikorskii (Meerschaert Mark and Sikorskii 2011). In addition, an excellent summary of both theoretical models and experimental applications is available in the recent book by Klages *et al.* (Klages et al. 2008).

Appendix D (continued)

Gamma Function:

Gamma function is considered a generalization of the factorial operator for non-integer values to include all positive real numbers. It is defined as the integral:

$$\Gamma(z) = \int_0^{\infty} e^{-t} t^{z-1} dt, z \in +\mathbb{R} \quad (1)$$

Some properties:

$$n! = \Gamma(n + 1), n \in +\mathbb{Z} \quad (2)$$

$$\Gamma(z + 1) = z \Gamma(z) \quad (3)$$

$$\Gamma(z)\Gamma(1 - z) = \frac{\pi}{\sin(\pi z)} \rightarrow \Gamma\left(\frac{1}{2}\right) = \sqrt{\pi} \quad (4)$$

$$\Gamma(z)\Gamma\left(z + \frac{1}{2}\right) = \sqrt{\pi} 2^{2z-1} \Gamma(2z) \rightarrow \text{at } z = n + \frac{1}{2}: \Gamma\left(n + \frac{1}{2}\right) = \frac{\sqrt{\pi}(2n)!}{2^{2n}n!} \quad (5)$$

Mittag-Leffler Function:

The Mittag-Leffler function is a complex function that takes two independent complex numbers, it is named after Gösta Mittag-Leffler. It is defined as:

$$E_{\alpha,\beta}(z) = \sum_{k=0}^{\infty} \frac{z^k}{\Gamma(\alpha k + \beta)}, \alpha, \beta > 0 \quad (6)$$

Some useful modes:

$$E_{1,1}(z) = \sum_{k=0}^{\infty} \frac{z^k}{\Gamma(k + 1)} = \sum_{k=0}^{\infty} \frac{z^k}{k!} = \exp(z) \quad (7)$$

Appendix D (continued)

$$E_{1,m}(z) = \frac{1}{z^{m-1}} \left(e^z - \sum_{k=0}^{m-2} \frac{z^k}{k!} \right) \quad (8)$$

$$E_{\alpha,1}(z) = \sum_{k=0}^{\infty} \frac{z^k}{\Gamma(\alpha k + 1)} = E_{\alpha}(z) \quad (9)$$

Different Definitions:

In this section we consider different definitions of fractional calculus. First, a relationship between the fractional integral and derivative can be identified in the form:

$$\frac{d^{\alpha}}{dx^{\alpha}} = D^{\alpha} = I^{-\alpha}, \alpha \in +\mathbb{R} \quad (10)$$

where the operator I denotes the fractional integration and D^{α} denotes the fractional derivative. In words, we require that the fractional integration to be the inverse of a fractional derivative. One can also define the fractional derivative in the form:

$$D^{\alpha} = D^m D^{\alpha-m} = \frac{d^m}{dx^m} (I^{m-\alpha}), m \in \mathbb{N} \quad (11)$$

This indicates that one may interpret fractional derivative as a fractional integral followed by a classical derivative. An alternative definition could be found by inverting the sequence of operators:

$$D^{\alpha} = D^{\alpha-m} D^m = I^{m-\alpha} \left(\frac{d^m}{dx^m} \right), m \in \mathbb{N} \quad (12)$$

Here, the fractional derivative is interpreted as a classical derivative followed by a fractional integral.

The Fourier Transform:

For a multivariate function $f(\mathbf{x})$, where $\mathbf{x} \in \mathbb{R}^n$, the Fourier transform $\mathcal{F}\{f(\mathbf{x})\}$ is given by:

Appendix D (continued)

$$F(\mathbf{k}) = \mathcal{F}\{f(\mathbf{x})\} = \frac{1}{(2\pi)^{n/2}} \int_{-\infty}^{\infty} f(\mathbf{x}) e^{i\mathbf{k} \cdot \mathbf{x}} d\mathbf{x} \quad (13)$$

And its inverse is given by:

$$f(\mathbf{x}) = \mathcal{F}^{-1}\{F(\mathbf{k})\} = \frac{1}{(2\pi)^{n/2}} \int_{-\infty}^{\infty} F(\mathbf{k}) e^{-i\mathbf{k} \cdot \mathbf{x}} d\mathbf{k} \quad (14)$$

The Fractional Fourier Derivative:

In early 19th century, Fourier has proposed a fractional derivative using his transform (Fourier 1822).

For a univariate function, the derivative of a function is given by:

$$\frac{d^n}{dx^n} f(x) = \frac{1}{\sqrt{2\pi}} \int_{-\infty}^{\infty} F(k) (-ik)^n e^{-ikx} dk \quad (15)$$

Generalizing n to a real value, we get:

$$\frac{d^\alpha}{dx^\alpha} f(x) = \frac{1}{\sqrt{2\pi}} \int_{-\infty}^{\infty} F(k) (-ik)^\alpha e^{-ikx} dk \quad (16)$$

A simple definition conditioned by the existence of $F(k)$ and its fractional inverse of a given function. If the parameter alpha was chosen to be negative, one would get the definition of a fractional integral as defined in equation 10.

Table VIII: Some functions and the corresponding Fourier derivative

$f(x)$	$\frac{d^\alpha f(x)}{dx^\alpha}$
e^{iax}	$(ia)^\alpha e^{iax}$
$\sin(ax)$	$a^\alpha \sin(ax + \frac{\pi}{2}\alpha)$
$\cos(ax)$	$a^\alpha \cos(ax + \frac{\pi}{2}\alpha)$

Appendix D (continued)

Riemann-Liouville Fractional Integral:

Starting from Cauchy's formula of repeated integration which writes as follow:

$${}_aI^n = \int_a^{x_n} \dots \int_a^{x_1} f(x_0) dx_0 \dots dx_{n-1} = \frac{1}{(n-1)!} \int_a^x (x-t)^{n-1} f(t) dt \quad (17)$$

where ${}_aI^n$ is the chosen operator for multiple integration characterized by $\frac{d}{dx}({}_aI)f(x) = f(x)$. Extending equation 15 to the fractional case, one would get:

$${}_aI_+^\alpha = \frac{1}{\Gamma(\alpha)} \int_a^x (x-t)^{\alpha-1} f(t) dt \quad (18)$$

$${}_aI_-^\alpha = \frac{1}{\Gamma(\alpha)} \int_x^b (t-x)^{\alpha-1} f(t) dt \quad (19)$$

Equation 17 is valid for $x > a$ and it is commonly called left-handed while equation 18 is valid for $x < b$ and it is commonly called right-handed. The lower and upper boundaries are determined by the constants a and b . As we have mentioned earlier that fractional operators are not local operators, we can see here that in equation 17, the left-handed integral depends on weighted values for $t < x$ (left from x), while the right-handed integral in equation 18 depends on weighted values for $t > x$ (right from x). Various definitions have emerged from the above equations depending on the values of a and b .

Liouville Fractional Integral and Derivative:

The Liouville fractional integral is defined by setting $a = -\infty$, $b = \infty$:

$${}_LI_+^\alpha f(x) = \frac{1}{\Gamma(\alpha)} \int_{-\infty}^x (x-t)^{\alpha-1} f(t) dt \quad (20)$$

Appendix D (continued)

$${}_L I_-^\alpha f(x) = \frac{1}{\Gamma(\alpha)} \int_x^\infty (t-x)^{\alpha-1} f(t) dt \quad (21)$$

For the case when $0 < \alpha < 1$, one can define the Liouville derivative using equation 11 in the form:

$${}_L D_+^\alpha f(x) = \frac{d}{dx} {}_L I_+^{1-\alpha} f(x) = \frac{d}{dx} \frac{1}{\Gamma(1-\alpha)} \int_{-\infty}^x (x-t)^{-\alpha} f(t) dt \quad (22)$$

$${}_L D_-^\alpha f(x) = \frac{d}{dx} {}_L I_-^{1-\alpha} f(x) = \frac{d}{dx} \frac{1}{\Gamma(1-\alpha)} \int_x^\infty (t-x)^{-\alpha} f(t) dt \quad (23)$$

Table IX: Some functions and the corresponding Liouville derivative

$f(x)$	${}_L D_+^\alpha \{f(x)\}$
e^{iax}	$(ia)^\alpha e^{iax}, a \geq 0$
$\sin(ax)$	$a^\alpha \sin(ax + \frac{\pi}{2}\alpha)$
$\cos(ax)$	$a^\alpha \cos(ax + \frac{\pi}{2}\alpha)$

Riemann Fractional Integral and Derivative:

The Riemann fractional integral is defined by setting $a = b = 0$:

$${}_R I_+^\alpha f(x) = \frac{1}{\Gamma(\alpha)} \int_0^x (x-t)^{\alpha-1} f(t) dt \quad (24)$$

$${}_R I_-^\alpha f(x) = \frac{1}{\Gamma(\alpha)} \int_x^0 (t-x)^{\alpha-1} f(t) dt \quad (25)$$

For the case when $0 < \alpha < 1$, one can define the Riemann derivative using equation 11 in the form:

$${}_R D_+^\alpha f(x) = \frac{d}{dx} {}_R I_+^{1-\alpha} f(x) = \frac{d}{dx} \frac{1}{\Gamma(1-\alpha)} \int_0^x (x-t)^{-\alpha} f(t) dt \quad (26)$$

Appendix D (continued)

$${}_RD_-^\alpha f(x) = \frac{d}{dx} {}_RI_-^{1-\alpha} f(x) = \frac{d}{dx} \frac{1}{\Gamma(1-\alpha)} \int_x^0 (t-x)^{-\alpha} f(t) dt \quad (27)$$

Table X: Some functions and the corresponding Riemann derivative

$f(x)$	${}_RD_+^\alpha \{f(x)\}$
e^{ax}	$\text{sgn}(x)(\text{sgn}(x)a)^\alpha e^{ax} \left(1 - \frac{\Gamma(-\alpha, ax)}{\Gamma(-\alpha)}\right)$
const	$\frac{\text{const}}{\Gamma(1-\alpha)} x^{-\alpha}$

Liouville-Caputo Fractional Derivative:

Using equations 20 and 21 combined with the derivative definition in equation 12, we get:

$${}_L D_+^\alpha f(x) = {}_L I_+^{1-\alpha} \frac{d}{dx} f(x) = \frac{1}{\Gamma(1-\alpha)} \int_{-\infty}^x (x-t)^{-\alpha} \frac{df(t)}{dt} dt \quad (28)$$

$${}_L D_-^\alpha f(x) = {}_L I_-^{1-\alpha} \frac{d}{dx} f(x) = \frac{1}{\Gamma(1-\alpha)} \int_x^\infty (t-x)^{-\alpha} \frac{df(t)}{dt} dt \quad (29)$$

Table XI: Some functions and the corresponding Liouville-Caputo derivative

$f(x)$	${}_L D_+^\alpha \{f(x)\}$
e^{iax}	$(ia)^\alpha e^{iax}, a \geq 0$
$\sin(ax)$	$a^\alpha \sin(ax + \frac{\pi}{2}\alpha)$
$\cos(ax)$	$a^\alpha \cos(ax + \frac{\pi}{2}\alpha)$
constant	0

Caputo Fractional Derivative:

Using Riemann fractional integral in equations 24 and 25 combined with the derivative definition in equation 12, we get:

Appendix D (continued)

$${}_c D_+^\alpha f(x) = {}_R I_+^{1-\alpha} \frac{d}{dx} f(x) = \frac{1}{\Gamma(1-\alpha)} \int_0^x (x-t)^{-\alpha} \frac{df(t)}{dt} dt \quad (30)$$

$${}_c D_-^\alpha f(x) = {}_R I_-^{1-\alpha} \frac{d}{dx} f(x) = \frac{1}{\Gamma(1-\alpha)} \int_x^0 (t-x)^{-\alpha} \frac{df(t)}{dt} dt \quad (31)$$

Note that applying the Riemann fractional derivative on a constant would result in:

$${}_R D_+^\alpha C = \frac{C}{\Gamma(1-\alpha)} x^{-\alpha} \quad (32)$$

while for the Caputo fractional derivative one would obtain 0 similar to classical laws.

Table XII: Some functions and the corresponding Caputo derivative

$f(x)$	${}_c D_+^\alpha \{f(x)\}$
e^{ax}	$\text{sgn}(x)(\text{sgn}(x)a)^\alpha e^{ax} \left(1 - \frac{\Gamma(1-\alpha, ax)}{\Gamma(1-\alpha)}\right)$
const	0

Fractional Derivative of High Order:

In the past sections, we have defined the fractional derivative for orders in $0 < \alpha < 1$, for an arbitrary value of alpha one could define it in the form:

$$D_\pm^\alpha = \begin{cases} \pm D^m {}_a I_\pm^{m-\alpha} f(x), & m-1 < \alpha \leq m, \text{ } m \text{ odd} \\ D^m {}_a I_\pm^{m-\alpha} f(x), & m-1 < \alpha \leq m, \text{ } m \text{ even} \end{cases} \quad (33)$$

Riesz Fractional Integral and Derivative:

Riesz fractional integral is a linear combination of left and right-handed Liouville fractional integrals:

Appendix D (continued)

$${}_{RZ}I^\alpha f(x) = \frac{{}_LI_+^\alpha + {}_LI_-^\alpha}{2 \cos\left(\frac{\pi\alpha}{2}\right)} = \frac{1}{\Gamma(\alpha) \cos\left(\frac{\pi\alpha}{2}\right)} \int_{-\infty}^{\infty} |x-t|^{\alpha-1} f(t) dt, \quad (34)$$

$$\alpha > 0, \alpha \neq 1, 3, 5, \dots$$

In order to write the Riesz fractional derivative, Liouville derivative need to be re-written in an alternative form. Using partial integration, one would get:

$${}_LD_+^\alpha f(x) = \frac{1}{\Gamma(1-\alpha)} \int_0^\infty \frac{f(x) - f(x-t)}{t^{\alpha+1}} dt \quad (35)$$

$${}_LD_-^\alpha f(x) = \frac{1}{\Gamma(1-\alpha)} \int_0^\infty \frac{f(x) - f(x+t)}{t^{\alpha+1}} dt \quad (36)$$

Using equations 35 and 36, the Riesz fractional derivative writes:

$$\begin{aligned} {}_{RZ}D^\alpha f(x) &= \frac{{}_LD_+^\alpha + {}_LD_-^\alpha}{2 \cos\left(\frac{\pi\alpha}{2}\right)} f(x) \\ &= \Gamma(1+\alpha) \frac{\sin\left(\frac{\pi\alpha}{2}\right)}{\pi} \int_0^\infty \frac{f(x+t) - 2f(x) + f(x-t)}{t^{\alpha+1}} dt, 0 < \alpha < 2 \end{aligned} \quad (37)$$

Table XIII: Some functions and the corresponding Caputo derivative

$f(x)$	${}_{RZ}D^\alpha \{f(x)\}$
e^{iax}	$- a ^\alpha e^{iax}$
$\sin(ax)$	$- a ^\alpha \sin(ax)$
$\cos(ax)$	$- a ^\alpha \cos(ax)$

Feller Fractional Integral and Derivative:

Feller fractional integral is a combination of left and right-handed Liouville fractional integrals in the form:

Appendix D (continued)

$${}_FI_\theta^\alpha = \frac{\sin\left(\frac{(\alpha - \theta)\pi}{2}\right)}{\sin(\pi\alpha)} {}_LI_+^\alpha + \frac{\sin\left(\frac{(\alpha + \theta)\pi}{2}\right)}{\sin(\pi\alpha)} {}_LI_-^\alpha \quad (38)$$

The fractional Feller derivative is then given as:

$${}_FD_\theta^\alpha = -\frac{\sin\left(\frac{(\alpha - \theta)\pi}{2}\right)}{\sin(\pi\alpha)} {}_LD_+^\alpha + \frac{\sin\left(\frac{(\alpha + \theta)\pi}{2}\right)}{\sin(\pi\alpha)} {}_LD_-^\alpha \quad (39)$$

The special case when $\Theta = 0$ leads to the definition of Riesz derivative while for $\Theta = 1$ leads to:

$$\begin{aligned} {}_FD_1^\alpha f(x) &= \frac{{}_LD_+^\alpha - {}_LD_-^\alpha}{2 \sin\left(\frac{\pi\alpha}{2}\right)} f(x) \\ &= \Gamma(1 + \alpha) \frac{\cos\left(\frac{\pi\alpha}{2}\right)}{\pi} \int_0^\infty \frac{f(x+t) - f(x-t)}{t^{\alpha+1}} dt, 0 \leq \alpha < 1 \end{aligned} \quad (40)$$

In general, the Feller derivative can be written in the form:

$${}_FD_\theta^\alpha = \begin{cases} \sin\left(\frac{\pi\theta}{2}\right) {}_FD_1^\alpha + \cos\left(\frac{\pi\theta}{2}\right) {}_{RZ}D^\alpha & 0 < \alpha < 1 \\ \sin\left(\frac{\pi\theta}{2}\right) \frac{d}{dx} {}_FD_1^{\alpha-1} + \cos\left(\frac{\pi\theta}{2}\right) {}_{RZ}D^{\alpha-1} & 1 \leq \alpha < 2 \\ \sin\left(\frac{\pi\theta}{2}\right) \frac{d^2}{dx^2} {}_FD_1^{\alpha-2} + \cos\left(\frac{\pi\theta}{2}\right) {}_{RZ}D^{\alpha-2} & 2 \leq \alpha < 3 \\ \dots & \end{cases} \quad (41)$$

Table XIV: Some functions and the corresponding Caputo derivative

$f(x)$	${}_FD_{\theta=1}^\alpha \{f(x)\}$
e^{iax}	$i \operatorname{sgn}(a) a ^\alpha e^{iax}$
$\sin(ax)$	$\operatorname{sgn}(a) a ^\alpha \cos(ax)$
$\cos(ax)$	$-\operatorname{sgn}(a) a ^\alpha \sin(ax)$

Appendix E

List of Brain Regions Defined by FreeSurfer

This list shows different brain regions as defined by the FreeSurfer software, the list is split into two columns which represent the left and right hemispheres, unique regions are not associated with an entry in the other column. The abbreviations ‘ctx’, ‘lh’, and ‘rh’ stand for cortex, left hemisphere and right hemisphere respectively. Highlighted regions are not gray matter and are not considered in the brain network generation. The index column represents the assigned indexes by the FreeSurfer software in the output label map file of the segmentation process. The list was adapted from: http://www.slicer.org/slicerWiki/index.php/Documentation/4.1/SlicerApplication/LookupTables/Freesurfer_1abels

Table XV: List of brain regions as defined by the FreeSurfer software.

Index	Region	Index	Region
Subcortical regions, Ventricles and Brain Stem			
2	Left_Cerebral_White_Matter	41	Right_Cerebral_White_Matter
4	Left_Lateral_Ventricle	43	Right_Lateral_Ventricle
5	Left_Inf_Lat_Vent	44	Right_Inf_Lat_Vent
7	Left_Cerebellum_White_Matter	46	Right_Cerebellum_White_Matter
8	Left_Cerebellum_Cortex	47	Right_Cerebellum_Cortex
10	Left_Thalamus_Proper	49	Right_Thalamus_Proper
11	Left_Caudate	50	Right_Caudate
12	Left_Putamen	51	Right_Putamen
13	Left_Pallidum	52	Right_Pallidum
14	Third_Ventricle		
15	Fourth_Ventricle		
16	Brain_Stem		
17	Left_Hippocampus	53	Right_Hippocampus
18	Left_Amygdala	54	Right_Amygdala
24	CSF		
26	Left_Accumbens_area	58	Right_Accumbens_area
28	Left_VentralDC	60	Right_VentralDC
30	Left-vessel	62	Right-vessel
31	Left-choroid-plexus	63	Right-choroid-plexus
72	Fifth_Ventricle		

Appendix E (continued)**Cortical Regions**

1001	ctx-lh-bankssts	2001	ctx-rh-bankssts
1002	ctx-lh-caudalanteriorcingulate	2002	ctx-rh-caudalanteriorcingulate
1003	ctx-lh-caudalmiddlefrontal	2003	ctx-rh-caudalmiddlefrontal
1004	ctx-lh-corpuscallosum	2004	ctx-rh-corpuscallosum
1005	ctx-lh-cuneus	2005	ctx-rh-cuneus
1006	ctx-lh-entorhinal	2006	ctx-rh-entorhinal
1007	ctx-lh-fusiform	2007	ctx-rh-fusiform
1008	ctx-lh-inferiorparietal	2008	ctx-rh-inferiorparietal
1009	ctx-lh-inferiortemporal	2009	ctx-rh-inferiortemporal
1010	ctx-lh-isthmuscingulate	2010	ctx-rh-isthmuscingulate
1011	ctx-lh-lateraloccipital	2011	ctx-rh-lateraloccipital
1012	ctx-lh-lateralorbitofrontal	2012	ctx-rh-lateralorbitofrontal
1013	ctx-lh-lingual	2013	ctx-rh-lingual
1014	ctx-lh-medialorbitofrontal	2014	ctx-rh-medialorbitofrontal
1015	ctx-lh-middletemporal	2015	ctx-rh-middletemporal
1016	ctx-lh-parahippocampal	2016	ctx-rh-parahippocampal
1017	ctx-lh-paracentral	2017	ctx-rh-paracentral
1018	ctx-lh-parsopercularis	2018	ctx-rh-parsopercularis
1019	ctx-lh-parsorbitalis	2019	ctx-rh-parsorbitalis
1020	ctx-lh-parstriangularis	2020	ctx-rh-parstriangularis
1021	ctx-lh-pericalcarine	2021	ctx-rh-pericalcarine
1022	ctx-lh-postcentral	2022	ctx-rh-postcentral
1023	ctx-lh-posteriorcingulate	2023	ctx-rh-posteriorcingulate
1024	ctx-lh-precentral	2024	ctx-rh-precentral
1025	ctx-lh-precuneus	2025	ctx-rh-precuneus
1026	ctx-lh-rostralanteriorcingulate	2026	ctx-rh-rostralanteriorcingulate
1027	ctx-lh-rostralmiddlefrontal	2027	ctx-rh-rostralmiddlefrontal
1028	ctx-lh-superiorfrontal	2028	ctx-rh-superiorfrontal
1029	ctx-lh-superiorparietal	2029	ctx-rh-superiorparietal
1030	ctx-lh-superiortemporal	2030	ctx-rh-superiortemporal
1031	ctx-lh-supramarginal	2031	ctx-rh-supramarginal
1032	ctx-lh-frontalpole	2032	ctx-rh-frontalpole
1033	ctx-lh-temporalpole	2033	ctx-rh-temporalpole
1034	ctx-lh-transversetemporal	2034	ctx-rh-transversetemporal
1035	ctx-lh-insula	2035	ctx-rh-insula

Appendix F

Rightslink® by Copyright Clearance Center

<https://s100.copyright.com/AppDispatchServlet#formTop>

RightsLink®

Home

Create Account

Help



Title: TDF-TRACT: Probabilistic tractography using the tensor distribution function

Conference Proceedings: Biomedical Imaging: From Nano to Macro, 2011 IEEE International Symposium on

Author: GadElkarim, J.J.; Zhan, L.; Yang, S.L.; Zhang, A.F.; Altshuler, L.; Lamar, M.; Ajilore, O.; Thompson, P.M.; Kumar, A.; Leow, A.

Publisher: IEEE

Date: March 30 2011-April 2 2011

Copyright © 2011, IEEE

User ID
<input type="text"/>
Password
<input type="text"/>
<input type="checkbox"/> Enable Auto Login
<input type="button" value="LOGIN"/>
Forgot Password/User ID?
If you're a copyright.com user, you can login to RightsLink using your copyright.com credentials. Already a RightsLink user or want to learn more?

Thesis / Dissertation Reuse

The IEEE does not require individuals working on a thesis to obtain a formal reuse license, however, you may print out this statement to be used as a permission grant:

Requirements to be followed when using any portion (e.g., figure, graph, table, or textual material) of an IEEE copyrighted paper in a thesis:

- 1) In the case of textual material (e.g., using short quotes or referring to the work within these papers) users must give full credit to the original source (author, paper, publication) followed by the IEEE copyright line © 2011 IEEE.
- 2) In the case of illustrations or tabular material, we require that the copyright line © [Year of original publication] IEEE appear prominently with each reprinted figure and/or table.
- 3) If a substantial portion of the original paper is to be used, and if you are not the senior author, also obtain the senior author's approval.

Requirements to be followed when using an entire IEEE copyrighted paper in a thesis:

- 1) The following IEEE copyright/ credit notice should be placed prominently in the references: © [year of original publication] IEEE. Reprinted, with permission, from [author names, paper title, IEEE publication title, and month/year of publication]
- 2) Only the accepted version of an IEEE copyrighted paper can be used when posting the paper or your thesis on-line.
- 3) In placing the thesis on the author's university website, please display the following message in a prominent place on the website: In reference to IEEE copyrighted material which is used with permission in this thesis, the IEEE does not endorse any of [university/educational entity's name goes here]'s products or services. Internal or personal use of this material is permitted. If interested in reprinting/republishing IEEE copyrighted material for advertising or promotional purposes or for creating new collective works for resale or redistribution, please go to http://www.ieee.org/publications_standards/publications/rights/rights_link.html to learn how to obtain a License from RightsLink.

If applicable, University Microfilms and/or ProQuest Library, or the Archives of Canada may supply single copies of the dissertation.

BACK

CLOSE WINDOW



RightsLink®

[Home](#)
[Create Account](#)
[Help](#)


Title: Fractional Order Generalization of Anomalous Diffusion as a Multidimensional Extension of the Transmission Line Equation

Author: GadElkarim, J.J.; Magin, R.L.; Meerschaert, M.M.; Capuani, S.; Palombo, M.; Kumar, A.; Leow, A.D.

Publication: Emerging and Selected Topics in Circuits and Systems, IEEE Journal on

Publisher: IEEE

Date: Sept. 2013

Copyright © 2013, IEEE

User ID

Password

☐ Enable Auto Login

[Forgot Password/User ID?](#)
If you're a copyright.com user, you can login to RightsLink using your copyright.com credentials. Already a RightsLink user or want to [learn more?](#)

Thesis / Dissertation Reuse

The IEEE does not require individuals working on a thesis to obtain a formal reuse license, however, you may print out this statement to be used as a permission grant:

Requirements to be followed when using any portion (e.g., figure, graph, table, or textual material) of an IEEE copyrighted paper in a thesis:

- 1) In the case of textual material (e.g., using short quotes or referring to the work within these papers) users must give full credit to the original source (author, paper, publication) followed by the IEEE copyright line © 2011 IEEE.
- 2) In the case of illustrations or tabular material, we require that the copyright line © [Year of original publication] IEEE appear prominently with each reprinted figure and/or table.
- 3) If a substantial portion of the original paper is to be used, and if you are not the senior author, also obtain the senior author's approval.

Requirements to be followed when using an entire IEEE copyrighted paper in a thesis:

- 1) The following IEEE copyright/ credit notice should be placed prominently in the references: © [year of original publication] IEEE. Reprinted, with permission, from [author names, paper title, IEEE publication title, and month/year of publication]
- 2) Only the accepted version of an IEEE copyrighted paper can be used when posting the paper or your thesis on-line.
- 3) In placing the thesis on the author's university website, please display the following message in a prominent place on the website: In reference to IEEE copyrighted material which is used with permission in this thesis, the IEEE does not endorse any of [university/educational entity's name goes here]'s products or services. Internal or personal use of this material is permitted. If interested in reprinting/republishing IEEE copyrighted material for advertising or promotional purposes or for creating new collective works for resale or redistribution, please go to http://www.ieee.org/publications_standards/publications/rights/rights_link.html to learn how to obtain a License from RightsLink.

If applicable, University Microfilms and/or ProQuest Library, or the Archives of Canada may supply single copies of the dissertation.



RightsLink®

[Home](#)
[Create Account](#)
[Help](#)


Title: Measuring inter-hemispheric integration in bipolar affective disorder using brain network analyses and HARDI

Conference Proceedings: Biomedical Imaging (ISBI), 2012 9th IEEE International Symposium on

Author: Leow, A.; Zhan, L.; Ajilore, O.; GadElkarim, J.; Zhang, A.; Arienzo, D.; Moody, T.; Feusner, J.; Kumar, A.; Thompson, P.; Altshuler, L.

Publisher: IEEE

Date: 2-5 May 2012

Copyright © 2012, IEEE

User ID

Password

☐ Enable Auto Login

[LOGIN](#)

[Forgot Password/User ID?](#)

If you're a copyright.com user, you can login to RightsLink using your copyright.com credentials. Already a RightsLink user or want to [learn more?](#)

Thesis / Dissertation Reuse

The IEEE does not require individuals working on a thesis to obtain a formal reuse license, however, you may print out this statement to be used as a permission grant:

Requirements to be followed when using any portion (e.g., figure, graph, table, or textual material) of an IEEE copyrighted paper in a thesis:

- 1) In the case of textual material (e.g., using short quotes or referring to the work within these papers) users must give full credit to the original source (author, paper, publication) followed by the IEEE copyright line © 2011 IEEE.
- 2) In the case of illustrations or tabular material, we require that the copyright line © [Year of original publication] IEEE appear prominently with each reprinted figure and/or table.
- 3) If a substantial portion of the original paper is to be used, and if you are not the senior author, also obtain the senior author's approval.

Requirements to be followed when using an entire IEEE copyrighted paper in a thesis:

- 1) The following IEEE copyright/ credit notice should be placed prominently in the references: © [year of original publication] IEEE. Reprinted, with permission, from [author names, paper title, IEEE publication title, and month/year of publication]
- 2) Only the accepted version of an IEEE copyrighted paper can be used when posting the paper or your thesis on-line.
- 3) In placing the thesis on the author's university website, please display the following message in a prominent place on the website: In reference to IEEE copyrighted material which is used with permission in this thesis, the IEEE does not endorse any of [university/educational entity's name goes here]'s products or services. Internal or personal use of this material is permitted. If interested in reprinting/republishing IEEE copyrighted material for advertising or promotional purposes or for creating new collective works for resale or redistribution, please go to http://www.ieee.org/publications_standards/publications/rights/rights_link.html to learn how to obtain a License from RightsLink.

If applicable, University Microfilms and/or ProQuest Library, or the Archives of Canada may supply single copies of the dissertation.

[BACK](#)
[CLOSE WINDOW](#)

JOHN WILEY AND SONS LICENSE TERMS AND CONDITIONS

Oct 08, 2013

This is a License Agreement between Johnson J GadElkarim ("You") and John Wiley and Sons ("John Wiley and Sons") provided by Copyright Clearance Center ("CCC"). The license consists of your order details, the terms and conditions provided by John Wiley and Sons, and the payment terms and conditions.

All payments must be made in full to CCC. For payment instructions, please see information listed at the bottom of this form.

License Number	3244320219104
License date	Oct 08, 2013
Licensed content publisher	John Wiley and Sons
Licensed content publication	Human Brain Mapping
Licensed content title	Investigating brain community structure abnormalities in bipolar disorder using path length associated community estimation
Licensed copyright line	Copyright © 2013 Wiley Periodicals, Inc.
Licensed content author	Johnson J. GadElkarim,Olusola Ajilore,Dan Schonfeld,Liang Zhan,Paul M. Thompson,Jamie D. Feusner,Anand Kumar,Lori L. Altshuler,Alex D. Leow
Licensed content date	Jun 25, 2013
Start page	000
End page	000
Type of use	Dissertation/Thesis
Requestor type	Author of this Wiley article
Format	Print
Portion	Full article
Will you be translating?	Yes, including English rights
Number of languages	1
Languages	English
Total	0.00 USD
Terms and Conditions	

TERMS AND CONDITIONS

This copyrighted material is owned by or exclusively licensed to John Wiley & Sons, Inc. or one of its group companies (each a "Wiley Company") or a society for whom a Wiley Company has exclusive publishing rights in relation to a particular journal (collectively "WILEY"). By clicking "accept" in connection with completing this licensing transaction, you agree that the following terms and conditions apply to this transaction (along with the billing and payment terms and conditions established by the Copyright Clearance Center

Inc., ("CCC's Billing and Payment terms and conditions"), at the time that you opened your RightsLink account (these are available at any time at <http://myaccount.copyright.com>).

Terms and Conditions

1. The materials you have requested permission to reproduce (the "Materials") are protected by copyright.
2. You are hereby granted a personal, non-exclusive, non-sublicensable, non-transferable, worldwide, limited license to reproduce the Materials for the purpose specified in the licensing process. This license is for a one-time use only with a maximum distribution equal to the number that you identified in the licensing process. Any form of republication granted by this license must be completed within two years of the date of the grant of this license (although copies prepared before may be distributed thereafter). The Materials shall not be used in any other manner or for any other purpose. Permission is granted subject to an appropriate acknowledgement given to the author, title of the material/book/journal and the publisher. You shall also duplicate the copyright notice that appears in the Wiley publication in your use of the Material. Permission is also granted on the understanding that nowhere in the text is a previously published source acknowledged for all or part of this Material. Any third party material is expressly excluded from this permission.
3. With respect to the Materials, all rights are reserved. Except as expressly granted by the terms of the license, no part of the Materials may be copied, modified, adapted (except for minor reformatting required by the new Publication), translated, reproduced, transferred or distributed, in any form or by any means, and no derivative works may be made based on the Materials without the prior permission of the respective copyright owner. You may not alter, remove or suppress in any manner any copyright, trademark or other notices displayed by the Materials. You may not license, rent, sell, loan, lease, pledge, offer as security, transfer or assign the Materials, or any of the rights granted to you hereunder to any other person.
4. The Materials and all of the intellectual property rights therein shall at all times remain the exclusive property of John Wiley & Sons Inc or one of its related companies (WILEY) or their respective licensors, and your interest therein is only that of having possession of and the right to reproduce the Materials pursuant to Section 2 herein during the continuance of this Agreement. You agree that you own no right, title or interest in or to the Materials or any of the intellectual property rights therein. You shall have no rights hereunder other than the license as provided for above in Section 2. No right, license or interest to any trademark, trade name, service mark or other branding ("Marks") of WILEY or its licensors is granted hereunder, and you agree that you shall not assert any such right, license or interest with respect thereto.
5. NEITHER WILEY NOR ITS LICENSORS MAKES ANY WARRANTY OR REPRESENTATION OF ANY KIND TO YOU OR ANY THIRD PARTY, EXPRESS, IMPLIED OR STATUTORY, WITH RESPECT TO THE MATERIALS OR THE ACCURACY OF ANY INFORMATION CONTAINED IN THE MATERIALS, INCLUDING, WITHOUT LIMITATION, ANY IMPLIED WARRANTY OF

MERCHANTABILITY, ACCURACY, SATISFACTORY QUALITY, FITNESS FOR A PARTICULAR PURPOSE, USABILITY, INTEGRATION OR NON-INFRINGEMENT AND ALL SUCH WARRANTIES ARE HEREBY EXCLUDED BY WILEY AND ITS LICENSORS AND WAIVED BY YOU.

6. WILEY shall have the right to terminate this Agreement immediately upon breach of this Agreement by you.

7. You shall indemnify, defend and hold harmless WILEY, its Licensors and their respective directors, officers, agents and employees, from and against any actual or threatened claims, demands, causes of action or proceedings arising from any breach of this Agreement by you.

8. IN NO EVENT SHALL WILEY OR ITS LICENSORS BE LIABLE TO YOU OR ANY OTHER PARTY OR ANY OTHER PERSON OR ENTITY FOR ANY SPECIAL, CONSEQUENTIAL, INCIDENTAL, INDIRECT, EXEMPLARY OR PUNITIVE DAMAGES, HOWEVER CAUSED, ARISING OUT OF OR IN CONNECTION WITH THE DOWNLOADING, PROVISIONING, VIEWING OR USE OF THE MATERIALS REGARDLESS OF THE FORM OF ACTION, WHETHER FOR BREACH OF CONTRACT, BREACH OF WARRANTY, TORT, NEGLIGENCE, INFRINGEMENT OR OTHERWISE (INCLUDING, WITHOUT LIMITATION, DAMAGES BASED ON LOSS OF PROFITS, DATA, FILES, USE, BUSINESS OPPORTUNITY OR CLAIMS OF THIRD PARTIES), AND WHETHER OR NOT THE PARTY HAS BEEN ADVISED OF THE POSSIBILITY OF SUCH DAMAGES. THIS LIMITATION SHALL APPLY NOTWITHSTANDING ANY FAILURE OF ESSENTIAL PURPOSE OF ANY LIMITED REMEDY PROVIDED HEREIN.

9. Should any provision of this Agreement be held by a court of competent jurisdiction to be illegal, invalid, or unenforceable, that provision shall be deemed amended to achieve as nearly as possible the same economic effect as the original provision, and the legality, validity and enforceability of the remaining provisions of this Agreement shall not be affected or impaired thereby.

10. The failure of either party to enforce any term or condition of this Agreement shall not constitute a waiver of either party's right to enforce each and every term and condition of this Agreement. No breach under this agreement shall be deemed waived or excused by either party unless such waiver or consent is in writing signed by the party granting such waiver or consent. The waiver by or consent of a party to a breach of any provision of this Agreement shall not operate or be construed as a waiver of or consent to any other or subsequent breach by such other party.

11. This Agreement may not be assigned (including by operation of law or otherwise) by you without WILEY's prior written consent.

12. Any fee required for this permission shall be non-refundable after thirty (30) days from receipt

13. These terms and conditions together with CCC's Billing and Payment terms and conditions (which are incorporated herein) form the entire agreement between you and WILEY concerning this licensing transaction and (in the absence of fraud) supersedes all

prior agreements and representations of the parties, oral or written. This Agreement may not be amended except in writing signed by both parties. This Agreement shall be binding upon and inure to the benefit of the parties' successors, legal representatives, and authorized assigns.

14. In the event of any conflict between your obligations established by these terms and conditions and those established by CCC's Billing and Payment terms and conditions, these terms and conditions shall prevail.

15. WILEY expressly reserves all rights not specifically granted in the combination of (i) the license details provided by you and accepted in the course of this licensing transaction, (ii) these terms and conditions and (iii) CCC's Billing and Payment terms and conditions.

16. This Agreement will be void if the Type of Use, Format, Circulation, or Requestor Type was misrepresented during the licensing process.

17. This Agreement shall be governed by and construed in accordance with the laws of the State of New York, USA, without regards to such state's conflict of law rules. Any legal action, suit or proceeding arising out of or relating to these Terms and Conditions or the breach thereof shall be instituted in a court of competent jurisdiction in New York County in the State of New York in the United States of America and each party hereby consents and submits to the personal jurisdiction of such court, waives any objection to venue in such court and consents to service of process by registered or certified mail, return receipt requested, at the last known address of such party.

Wiley Open Access Terms and Conditions

Wiley publishes Open Access articles in both its Wiley Open Access Journals program [<http://www.wileyopenaccess.com/view/index.html>] and as Online Open articles in its subscription journals. The majority of Wiley Open Access Journals have adopted the [Creative Commons Attribution License](#) (CC BY) which permits the unrestricted use, distribution, reproduction, adaptation and commercial exploitation of the article in any medium. No permission is required to use the article in this way provided that the article is properly cited and other license terms are observed. A small number of Wiley Open Access journals have retained the [Creative Commons Attribution Non Commercial License](#) (CC BY-NC), which permits use, distribution and reproduction in any medium, provided the original work is properly cited and is not used for commercial purposes.

Online Open articles - Authors selecting Online Open are, unless particular exceptions apply, offered a choice of Creative Commons licenses. They may therefore select from the CC BY, the CC BY-NC and the [Attribution-NoDerivatives](#) (CC BY-NC-ND). The CC BY-NC-ND is more restrictive than the CC BY-NC as it does not permit adaptations or modifications without rights holder consent.

Wiley Open Access articles are protected by copyright and are posted to repositories and websites in accordance with the terms of the applicable Creative Commons license referenced on the article. At the time of deposit, Wiley Open Access articles include all changes made during peer review, copyediting, and publishing. Repositories and websites that host the article are responsible for incorporating any publisher-supplied amendments or

retractions issued subsequently.

Wiley Open Access articles are also available without charge on Wiley's publishing platform, **Wiley Online Library** or any successor sites.

Conditions applicable to all Wiley Open Access articles:

- The authors' moral rights must not be compromised. These rights include the right of "paternity" (also known as "attribution" - the right for the author to be identified as such) and "integrity" (the right for the author not to have the work altered in such a way that the author's reputation or integrity may be damaged).
- Where content in the article is identified as belonging to a third party, it is the obligation of the user to ensure that any reuse complies with the copyright policies of the owner of that content.
- If article content is copied, downloaded or otherwise reused for research and other purposes as permitted, a link to the appropriate bibliographic citation (authors, journal, article title, volume, issue, page numbers, DOI and the link to the definitive published version on Wiley Online Library) should be maintained. Copyright notices and disclaimers must not be deleted.
 - Creative Commons licenses are copyright licenses and do not confer any other rights, including but not limited to trademark or patent rights.
- Any translations, for which a prior translation agreement with Wiley has not been agreed, must prominently display the statement: "This is an unofficial translation of an article that appeared in a Wiley publication. The publisher has not endorsed this translation."

Conditions applicable to non-commercial licenses (CC BY-NC and CC BY-NC-ND)

For non-commercial and non-promotional purposes individual non-commercial users may access, download, copy, display and redistribute to colleagues Wiley Open Access articles. In addition, articles adopting the CC BY-NC may be adapted, translated, and text- and data-mined subject to the conditions above.

Use by commercial "for-profit" organizations

Use of non-commercial Wiley Open Access articles for commercial, promotional, or marketing purposes requires further explicit permission from Wiley and will be subject to a fee. Commercial purposes include:

- Copying or downloading of articles, or linking to such articles for further redistribution, sale or licensing;
- Copying, downloading or posting by a site or service that incorporates

advertising with such content;

- The inclusion or incorporation of article content in other works or services (other than normal quotations with an appropriate citation) that is then available for sale or licensing, for a fee (for example, a compilation produced for marketing purposes, inclusion in a sales pack)
- Use of article content (other than normal quotations with appropriate citation) by for-profit organizations for promotional purposes
- Linking to article content in e-mails redistributed for promotional, marketing or educational purposes;
- Use for the purposes of monetary reward by means of sale, resale, license, loan, transfer or other form of commercial exploitation such as marketing products
- Print reprints of Wiley Open Access articles can be purchased from:
corporatesales@wiley.com

The modification or adaptation for any purpose of an article referencing the CC BY-NC-ND License requires consent which can be requested from
RightsLink@wiley.com.

Other Terms and Conditions:

BY CLICKING ON THE "I AGREE..." BOX, YOU ACKNOWLEDGE THAT YOU HAVE READ AND FULLY UNDERSTAND EACH OF THE SECTIONS OF AND PROVISIONS SET FORTH IN THIS AGREEMENT AND THAT YOU ARE IN AGREEMENT WITH AND ARE WILLING TO ACCEPT ALL OF YOUR OBLIGATIONS AS SET FORTH IN THIS AGREEMENT.

v1.8

If you would like to pay for this license now, please remit this license along with your payment made payable to "COPYRIGHT CLEARANCE CENTER" otherwise you will be invoiced within 48 hours of the license date. Payment should be in the form of a check or money order referencing your account number and this invoice number RLNK501131066.

Once you receive your invoice for this order, you may pay your invoice by credit card. Please follow instructions provided at that time.

**Make Payment To:
Copyright Clearance Center
Dept 001**

**P.O. Box 843006
Boston, MA 02284-3006**

For suggestions or comments regarding this order, contact RightsLink Customer Support: customercare@copyright.com or +1-877-622-5543 (toll free in the US) or +1-978-646-2777.

Gratis licenses (referencing \$0 in the Total field) are free. Please retain this printable license for your reference. No payment is required.

SPRINGER LICENSE TERMS AND CONDITIONS

Oct 08, 2013

This is a License Agreement between Johnson J GadElkarim ("You") and Springer ("Springer") provided by Copyright Clearance Center ("CCC"). The license consists of your order details, the terms and conditions provided by Springer, and the payment terms and conditions.

All payments must be made in full to CCC. For payment instructions, please see information listed at the bottom of this form.

License Number	3244240922758
License date	Oct 08, 2013
Licensed content publisher	Springer
Licensed content publication	Springer eBook
Licensed content title	A Framework for Quantifying Node-Level Community Structure Group Differences in Brain Connectivity Networks
Licensed content author	Johnson J. GadElkarim
Licensed content date	Jan 1, 2012
Type of Use	Thesis/Dissertation
Portion	Full text
Number of copies	1
Author of this Springer article	Yes and you are the sole author of the new work
Order reference number	
Title of your thesis / dissertation	From Micro to Macro: A Study of Human Brain Structure Based on Diffusion MRI and Neuronal Networks
Expected completion date	Oct 2013
Estimated size(pages)	170
Total	0.00 USD
Terms and Conditions	

Introduction

The publisher for this copyrighted material is Springer Science + Business Media. By clicking "accept" in connection with completing this licensing transaction, you agree that the following terms and conditions apply to this transaction (along with the Billing and Payment terms and conditions established by Copyright Clearance Center, Inc. ("CCC"), at the time that you opened your Rightslink account and that are available at any time at <http://myaccount.copyright.com>).

Limited License

With reference to your request to reprint in your thesis material on which Springer Science and Business Media control the copyright, permission is granted, free of charge, for the use

indicated in your enquiry.

Licenses are for one-time use only with a maximum distribution equal to the number that you identified in the licensing process.

This License includes use in an electronic form, provided its password protected or on the university's intranet or repository, including UMI (according to the definition at the Sherpa website: <http://www.sherpa.ac.uk/romeo/>). For any other electronic use, please contact Springer at (permissions.dordrecht@springer.com or permissions.heidelberg@springer.com).

The material can only be used for the purpose of defending your thesis, and with a maximum of 100 extra copies in paper.

Although Springer holds copyright to the material and is entitled to negotiate on rights, this license is only valid, subject to a courtesy information to the author (address is given with the article/chapter) and provided it concerns original material which does not carry references to other sources (if material in question appears with credit to another source, authorization from that source is required as well).

Permission free of charge on this occasion does not prejudice any rights we might have to charge for reproduction of our copyrighted material in the future.

Altering/Modifying Material: Not Permitted

You may not alter or modify the material in any manner. Abbreviations, additions, deletions and/or any other alterations shall be made only with prior written authorization of the author(s) and/or Springer Science + Business Media. (Please contact Springer at (permissions.dordrecht@springer.com or permissions.heidelberg@springer.com))

Reservation of Rights

Springer Science + Business Media reserves all rights not specifically granted in the combination of (i) the license details provided by you and accepted in the course of this licensing transaction, (ii) these terms and conditions and (iii) CCC's Billing and Payment terms and conditions.

Copyright Notice:Disclaimer

You must include the following copyright and permission notice in connection with any reproduction of the licensed material: "Springer and the original publisher /journal title, volume, year of publication, page, chapter/article title, name(s) of author(s), figure number(s), original copyright notice) is given to the publication in which the material was originally published, by adding: with kind permission from Springer Science and Business Media"

Warranties: None

Example 1: Springer Science + Business Media makes no representations or warranties with respect to the licensed material.

Example 2: Springer Science + Business Media makes no representations or warranties with respect to the licensed material and adopts on its own behalf the limitations and disclaimers

established by CCC on its behalf in its Billing and Payment terms and conditions for this licensing transaction.

Indemnity

You hereby indemnify and agree to hold harmless Springer Science + Business Media and CCC, and their respective officers, directors, employees and agents, from and against any and all claims arising out of your use of the licensed material other than as specifically authorized pursuant to this license.

No Transfer of License

This license is personal to you and may not be sublicensed, assigned, or transferred by you to any other person without Springer Science + Business Media's written permission.

No Amendment Except in Writing

This license may not be amended except in a writing signed by both parties (or, in the case of Springer Science + Business Media, by CCC on Springer Science + Business Media's behalf).

Objection to Contrary Terms

Springer Science + Business Media hereby objects to any terms contained in any purchase order, acknowledgment, check endorsement or other writing prepared by you, which terms are inconsistent with these terms and conditions or CCC's Billing and Payment terms and conditions. These terms and conditions, together with CCC's Billing and Payment terms and conditions (which are incorporated herein), comprise the entire agreement between you and Springer Science + Business Media (and CCC) concerning this licensing transaction. In the event of any conflict between your obligations established by these terms and conditions and those established by CCC's Billing and Payment terms and conditions, these terms and conditions shall control.

Jurisdiction

All disputes that may arise in connection with this present License, or the breach thereof, shall be settled exclusively by arbitration, to be held in The Netherlands, in accordance with Dutch law, and to be conducted under the Rules of the 'Netherlands Arbitrage Instituut' (Netherlands Institute of Arbitration). *OR:*

All disputes that may arise in connection with this present License, or the breach thereof, shall be settled exclusively by arbitration, to be held in the Federal Republic of Germany, in accordance with German law.

Other terms and conditions:

v1.3

If you would like to pay for this license now, please remit this license along with your payment made payable to "COPYRIGHT CLEARANCE CENTER" otherwise you will be invoiced within 48 hours of the license date. Payment should be in the form of a check or money order referencing your account number and this invoice number RLNK501130830.

Once you receive your invoice for this order, you may pay your invoice by credit card. Please follow instructions provided at that time.

Make Payment To:
Copyright Clearance Center
Dept 001
P.O. Box 843006
Boston, MA 02284-3006

For suggestions or comments regarding this order, contact RightsLink Customer Support: customercare@copyright.com or +1-877-622-5543 (toll free in the US) or +1-978-646-2777.

Gratis licenses (referencing \$0 in the Total field) are free. Please retain this printable license for your reference. No payment is required.

CITED LITERATURE

1. Achard, S. and E. Bullmore (2007). "Efficiency and cost of economical brain functional networks." PLoS Comput Biol **3**(2): e17.
2. Alexander-Bloch, A., R. Lambiotte, et al. (2012). "The discovery of population differences in network community structure: new methods and applications to brain functional networks in schizophrenia." Neuroimage **59**(4): 3889-3900.
3. Alexander, A. L., K. M. Hasan, et al. (2001). "Analysis of partial volume effects in diffusion-tensor MRI." Magn Reson Med **45**(5): 770-780.
4. Alexander, D. C. (2005). "Maximum entropy spherical deconvolution for diffusion MRI." Inf Process Med Imaging **19**: 76-87.
5. Alexander, D. C. (2005). "Multiple-Fiber Reconstruction Algorithms for Diffusion MRI." Ann N Y Acad Sci **1064**(1): 113-133.
6. Alexander, D. C., G. J. Barker, et al. (2002). "Detection and modeling of non-Gaussian apparent diffusion coefficient profiles in human brain data." Magn Reson Med **48**(2): 331-340.
7. Aloise, D., S. Cafieri, et al. (2010). "Column generation algorithms for exact modularity maximization in networks." Phys Rev E Stat Nonlin Soft Matter Phys **82**(4 Pt 2): 046112.
8. Anderson, A. W. (2005). "Measurement of fiber orientation distributions using high angular resolution diffusion imaging." Magnetic Resonance in Medicine **54**(5): 1194-1206.
9. Assaf, Y. and P. J. Basser (2005). "Composite hindered and restricted model of diffusion (CHARMED) MR imaging of the human brain." Neuroimage **27**(1): 48-58.
10. Assaf, Y., R. Z. Freidlin, et al. (2004). "New modeling and experimental framework to characterize hindered and restricted water diffusion in brain white matter." Magn Reson Med **52**(5): 965-978.
11. Barabási, A.-L. and R. Albert (1999). "Emergence of Scaling in Random Networks." Science **286**(5439): 509-512.
12. Barrat, A., M. Barthelemy, et al. (2004). "The architecture of complex weighted networks." Proc Natl Acad Sci U S A **101**(11): 3747-3752.
13. Basser, P., Mattiello, , T. J., R., , et al. (1993). "Diffusion tensor echo-planar imaging of human brain." Proceedings of the SMRM: 584
14. Basser, P. J. (1998). "Fiber-tractography via diffusion tensor MRI (DT-MRI)." Proceedings of the ISMRM.
15. Basser, P. J. and D. K. Jones (2002). "Diffusion-tensor MRI: theory, experimental design and data analysis - a technical review." NMR Biomed **15**(7-8): 456-467.
16. Basser, P. J., J. Mattiello, et al. (1994). "Estimation of the effective self-diffusion tensor from the NMR spin echo." J Magn Reson B **103**(3): 247-254.
17. Basser, P. J., J. Mattiello, et al. (1994). "MR diffusion tensor spectroscopy and imaging." Biophys J **66**(1): 259-267.
18. Basser, P. J., S. Pajevic, et al. (2000). "In vivo fiber tractography using DT-MRI data." Magnetic Resonance in Medicine **44**(4): 625-632.
19. Basser, P. J. and C. Pierpaoli (1996). "Microstructural and physiological features of tissues elucidated by quantitative-diffusion-tensor MRI." J Magn Reson B **111**(3): 209-219.
20. Bassett, D. S. and E. Bullmore (2006). "Small-world brain networks." Neuroscientist **12**(6): 512-523.
21. Bassett, D. S., E. Bullmore, et al. (2008). "Hierarchical organization of human cortical networks in health and schizophrenia." J Neurosci **28**(37): 9239-9248.
22. Behrens, T. E., H. J. Berg, et al. (2007). "Probabilistic diffusion tractography with multiple fibre orientations: What can we gain?" Neuroimage **34**(1): 144-155.
23. Behrens, T. E., M. W. Woolrich, et al. (2003). "Characterization and propagation of uncertainty in diffusion-weighted MR imaging." Magn Reson Med **50**(5): 1077-1088.

CITED LITERATURE (continued)

24. Bennett, K. M., K. M. Schmainda, et al. (2003). "Characterization of continuously distributed cortical water diffusion rates with a stretched-exponential model." Magn Reson Med **50**(4): 727-734.
25. Bergmann, O., G. Kindlmann, et al. (2007). "TWO-TENSOR FIBER TRACTOGRAPHY." ISBI 2007: 796-799.
26. Björnemo, M., A. Brun, et al. (2002). Regularized Stochastic White Matter Tractography Using Diffusion Tensor MRI. Proceedings of MICCAI conference, Springer-Verlag: 435-442.
27. Bloch, F. (1946). "Nuclear Induction." Physical Review **70**(7-8): 460-474.
28. Blondel, V. D., J. L. Guillaume, et al. (2008). "Fast unfolding of communities in large networks." Journal of Statistical Mechanics-Theory and Experiment.
29. Blyth, R., P. Cook, et al. (2003). "Tractography with Multiple Fibre Directions." Proceedings of the International Society of Magnetic Resonance in Medicine: 240.
30. Brandes, U., D. Dellling, et al. (2006). On modularity-NP-completeness and beyond, Citeseer.
31. Brun, A., M. Björnemo, et al. (2002). White matter tractography using sequential importance sampling. ISMRM Honolulu, Hawaii
32. Bruno, S., M. Cercignani, et al. (2008). "White matter abnormalities in bipolar disorder: a voxel-based diffusion tensor imaging study." Bipolar Disord **10**(4): 460-468.
33. Callaghan, P. T. (1991). Principles of nuclear magnetic resonance microscopy. Oxford England, New York, Clarendon Press ; Oxford University Press.
34. Callaghan, P. T., C. D. Eccles, et al. (1988). "NMR microscopy of dynamic displacements: k-space and q-space imaging." Journal of Physics E: Scientific Instruments **21**(8): 820.
35. Campbell, J. S., K. Siddiqi, et al. (2005). "Flow-based fiber tracking with diffusion tensor and q-ball data: validation and comparison to principal diffusion direction techniques." Neuroimage **27**(4): 725-736.
36. Campbell, J. S. W., P. Savadjiev, et al. (2006). Validation and regularization in diffusion MRI tractography. ISBI 2006.
37. Capuani, S., M. Palombo, et al. (2012). "Spatio-temporal anomalous diffusion imaging: results in controlled phantoms and in excised human meningiomas." Magn Reson Imaging: 359-365.
38. Caserta, F., W. D. Eldred, et al. (1995). "Determination of fractal dimension of physiologically characterized neurons in two and three dimensions." J Neurosci Methods **56**(2): 133-144.
39. Catani, M. and M. Mesulam (2008). "What is a disconnection syndrome?" Cortex **44**(8): 911-913.
40. Chao, Y. P., J. H. Chen, et al. (2008). "A multiple streamline approach to high angular resolution diffusion tractography." Med Eng Phys **30**(8): 989-996.
41. Chao, Y. P., C. H. Yeh, et al. (2007). "Multiple Streamline Tractography Approach with High Angular Resolution Diffusion Imaging Data." Proceedings of the ISMRM: 1550.
42. Chen, Y., W. Guo, et al. (2004). "Estimation, smoothing, and characterization of apparent diffusion coefficient profiles from High Angular Resolution DWI." Proceedings of the 2004 IEEE Computer Society Conference on Computer Vision and Pattern Recognition, 2004, **1**: 588-593.
43. Clark, C. A. and D. Le Bihan (2000). "Water diffusion compartmentation and anisotropy at high b values in the human brain." Magn Reson Med **44**(6): 852-859.
44. Clauset, A., M. E. J. Newman, et al. (2004). "Finding community structure in very large networks." Physical Review E **70**(6).
45. Conturo, T. E., N. F. Lori, et al. (1999). "Tracking neuronal fiber pathways in the living human brain." Proc Natl Acad Sci U S A **96**(18): 10422-10427.
46. Danon, L., A. Diaz-Guilera, et al. (2006). "The effect of size heterogeneity on community identification in complex networks." Journal of Statistical Mechanics-Theory and Experiment.
47. Dayan, P. and L. F. Abbott (2001). Theoretical neuroscience : computational and mathematical modeling of neural systems. Cambridge, Mass., Massachusetts Institute of Technology Press.
48. De Santis, S., A. Gabrielli, et al. (2011). "Anisotropic anomalous diffusion assessed in the human brain by scalar invariant indices." Magn Reson Med **65**(4): 1043-1052.

CITED LITERATURE (continued)

49. Dejerine, J. and A. Dejerine-Klumpke (1895). Anatomie des centres nerveux Tome 1, Méthodes générales d'étude-embryologie-histogénèse et histologie. Anatomie du cerveau, Paris, Rueff.
50. Descoteaux, M. (2008). High Angular Resolution Diffusion MRI: From Local Estimation to Segmentation and Tractography, Université de Nice - Sophia Antipolis.
51. Descoteaux, M. and R. Deriche (2007). Q-Ball Images Segmentation Using Region-Based Statistical Surface Evolution. Technical Report. INRIA Sophia Antipolis. **6257**.
52. Dijkstra, E. W. (1959). "A note on two problems in connexion with graphs." Numerische Mathematik **1**(1): 269-271.
53. Du, H., M. W. Feldman, et al. (2007). "An algorithm for detecting community structure of social networks based on prior knowledge and modularity: Research Articles." Complex. **12**(3): 53-60.
54. Einstein, A. and R. Fürth (1956). Investigations on the theory of Brownian movement. New York, N.Y., Dover Publications.
55. Erdős, P. and A. Rényi (1960). "On the Evolution of Random Graphs." Publication of the Mathematical Institute of the Hungarian Academy of Sciences.
56. Euler, L. (1741). "Solutio problematis ad geometriam situs pertinentis." Commentarii academiae scientiarum Petropolitanae **8**: 128-140.
57. Fair, D. A., A. L. Cohen, et al. (2009). "Functional brain networks develop from a "local to distributed" organization." PLoS Comput Biol **5**(5): e1000381.
58. Fick, A. (1855). "On liquid diffusion." Philos. Mag. J. Sci. **10**: 31-39.
59. Fillard, P., J. Gilmore, et al. (2003). Quantitative Analysis of White Matter Fiber Properties along Geodesic Paths. Medical Image Computing and Computer-Assisted Intervention - MICCAI 2003. R. Ellis and T. Peters, Springer Berlin Heidelberg. **2879**: 16-23.
60. Fisher, N. I. (1993). Statistical analysis of circular data. Cambridge [England] ; New York, NY, USA, Cambridge University Press.
61. Fortunato, S. (2010). "Community detection in graphs." Physics Reports-Review Section of Physics Letters **486**(3-5): 75-174.
62. Fortunato, S. and M. Barthelemy (2007). "Resolution limit in community detection." Proc Natl Acad Sci U S A **104**(1): 36-41.
63. Frank, L. R. (2002). "Characterization of anisotropy in high angular resolution diffusion-weighted MRI." Magn Reson Med **47**(6): 1083-1099.
64. Frazier, J. A., J. L. Breeze, et al. (2007). "White matter abnormalities in children with and at risk for bipolar disorder." Bipolar Disord **9**(8): 799-809.
65. Freeman, L. C. (1979). "Centrality in social networks conceptual clarification." Social networks **1**(3): 215-239.
66. Friman, O., G. Farneback, et al. (2006). "A Bayesian approach for stochastic white matter tractography." IEEE Trans Med Imaging **25**(8): 965-978.
67. Gao, Q., G. Srinivasan, et al. (2011). "Anomalous diffusion measured by a twice-refocused spin echo pulse sequence: analysis using fractional order calculus." J Magn Reson Imaging **33**(5): 1177-1183.
68. GESCHWIND, N. (1965). "DISCONNEXION SYNDROMES IN ANIMALS AND MAN." Brain **88**(2): 237.
69. Gilmore, J. H., W. Lin, et al. (2007). "Early postnatal development of corpus callosum and corticospinal white matter assessed with quantitative tractography." AJNR Am J Neuroradiol **28**(9): 1789-1795.
70. Girvan, M. and M. E. J. Newman (2002). "Community structure in social and biological networks." Proceedings of the National Academy of Sciences **99**(12): 7821-7826.
71. Gray, H. (1936). Anatomy of the human body. Philadelphia., Lea & Febiger.
72. Guimera, R. and L. A. Amaral (2005). "Cartography of complex networks: modules and universal roles." J Stat Mech **2005**(P02001): nihpa35573.
73. Guimerà, R., M. Sales-Pardo, et al. (2004). "Modularity from fluctuations in random graphs and complex networks." Physical Review E **70**(2): 025101.

CITED LITERATURE (continued)

74. Habas, C. and E. A. Cabanis (2007). "Anatomical parcellation of the brainstem and cerebellar white matter: a preliminary probabilistic tractography study at 3 T." Neuroradiology **49**(10): 849-863.
75. Hagmann, P. (2005). From diffusion MRI to brain connectomics PhD, ECOLE POLYTECHNIQUE FEDERALE DE LAUSANNE.
76. Hagmann, P., T. Reese, et al. (2004). Diffusion Spectrum Imaging Tractography in Complex Cerebral White Matter: An Investigation of the Centrum Semiovale, International Society for Magnetic Resonance in Medicine. **12**: 623.
77. Hahn, E. L. (1950). "Spin Echoes." Physical Review **80**(4): 580-594.
78. Hall, M. G. and T. R. Barrick (2008). "From diffusion-weighted MRI to anomalous diffusion imaging." Magn Reson Med **59**(3): 447-455.
79. Hall, M. G. and T. R. Barrick (2012). "Two-step anomalous diffusion tensor imaging." NMR Biomed **25**(2): 286-294.
80. Hanyga, A. and M. Seredynska (2012). "Anisotropy in high-resolution diffusion-weighted MRI and anomalous diffusion." J Magn Reson **220**: 85-93.
81. Haroon, H. A. and G. J. Parker (2007). "Using the Wild Bootstrap to Quantify Uncertainty in Fibre Orientations from Q-Ball Analysis." Proceedings of the ISMRM: 903.
82. Hastie, T., R. Tibshirani, et al. (2001). The elements of statistical learning : data mining, inference, and prediction : with 200 full-color illustrations. New York, Springer.
83. Havlin, S., S. V. Buldyrev, et al. (1995). "Fractals in biology and medicine." Chaos Solitons Fractals **6**: 171-201.
84. He, Y., J. Wang, et al. (2009). "Uncovering intrinsic modular organization of spontaneous brain activity in humans." PLoS One **4**(4): e5226.
85. Herculano-Houzel, S. (2009). "The human brain in numbers: a linearly scaled-up primate brain." Front Hum Neurosci **3**: 31.
86. Herrmann, R. (2011). Fractional calculus an introduction for physicists. Singapore; Hackensack, N.J., World Scientific.
87. Hess, C. P., P. Mukherjee, et al. (2006). "Q-ball reconstruction of multimodal fiber orientations using the spherical harmonic basis." Magn Reson Med **56**(1): 104-117.
88. Hirsch, J., S. Schwenk, et al. (2003). "Deviations from the diffusion tensor model as revealed by contour plot visualization using high angular resolution diffusion-weighted imaging (HARDI)." Magnetic Resonance Materials in Physics, Biology and Medicine **16**(2): 93-102.
89. Hörmander, L. (1987). Pseudo-Differential Operators. The Analysis of Linear Partial Differential Operators III. Germany, Springer Berlin Heidelberg: 63-179.
90. Hosey, T., G. Williams, et al. (2005). "Inference of multiple fiber orientations in high angular resolution diffusion imaging." Magnetic Resonance in Medicine **54**(6): 1480-1489.
91. Humphries, M. D. and K. Gurney (2008). "Network 'Small-World-Ness': A Quantitative Method for Determining Canonical Network Equivalence." PLoS One **3**(4): e0002051.
92. Jansons, K. M. and D. C. Alexander (2003). "Persistent Angular Structure: new insights from diffusion MRI data. Dummy version." Inf Process Med Imaging **18**: 672-683.
93. Jbabdi, S., P. Bellec, et al. (2004). "A level set method for building anatomical connectivity paths between brain areas using DTI." ISBI 2004 **1**: 1024-1027.
94. Jbabdi, S., P. Bellec, et al. (2008). "Accurate anisotropic fast marching for diffusion-based geodesic tractography." Int J Biomed Imaging **2008**: 320195.
95. Jbabdi, S., M. W. Woolrich, et al. (2007). "A Bayesian framework for global tractography." Neuroimage **37**(1): 116-129.
96. Jian, B. and B. C. Vemuri (2007). Multi-fiber reconstruction from diffusion MRI using mixture of wisharts and sparse deconvolution. Proceedings of the 20th international conference on Information processing in medical imaging. Kerkrade, The Netherlands, Springer-Verlag: 384-395.
97. Jian, B., B. C. Vemuri, et al. (2007). "A novel tensor distribution model for the diffusion-weighted MR signal." Neuroimage **37**(1): 164-176.

CITED LITERATURE (continued)

98. Jiang, H., P. C. van Zijl, et al. (2006). "DtiStudio: resource program for diffusion tensor computation and fiber bundle tracking." Comput Methods Programs Biomed **81**(2): 106-116.
99. Jones, D., S. Williams, et al. (1997). Full representation of white-matter fibre direction on one map via diffusion tensor analysis. Proceedings of the ISMRM.
100. Kaden, E., T. R. Knosche, et al. (2007). "Parametric spherical deconvolution: inferring anatomical connectivity using diffusion MR imaging." Neuroimage **37**(2): 474-488.
101. Kamali, A., L. A. Kramer, et al. (2010). "Diffusion tensor tractography of the human brain cortico-ponto-cerebellar pathways: a quantitative preliminary study." J Magn Reson Imaging **32**(4): 809-817.
102. Kirkpatrick, S., C. D. Gelatt, Jr., et al. (1983). "Optimization by simulated annealing." Science **220**(4598): 671-680.
103. Klages, R., G. Radons, et al. (2008). Anomalous transport : foundations and applications. Weinheim, Wiley-VCH.
104. Koch, M. A., D. G. Norris, et al. (2002). "An investigation of functional and anatomical connectivity using magnetic resonance imaging." Neuroimage **16**(1): 241-250.
105. Kreher, B. W., J. F. Schneider, et al. (2005). "Multitensor approach for analysis and tracking of complex fiber configurations." Magn Reson Med **54**(5): 1216-1225.
106. Latora, V. and M. Marchiori (2001). "Efficient behavior of small-world networks." Phys Rev Lett **87**(19): 198701.
107. Lazar, M. and A. L. Alexander (2005). "Bootstrap white matter tractography (BOOT-TRAC)." Neuroimage **24**(2): 524-532.
108. Lazar, M., D. M. Weinstein, et al. (2003). "White matter tractography using diffusion tensor deflection." Hum Brain Mapp **18**(4): 306-321.
109. Le Bihan, D. (2003). "Looking into the functional architecture of the brain with diffusion MRI." Nat Rev Neurosci **4**(6): 469-480.
110. Le Bihan, D., E. Breton, et al. (1986). "MR imaging of intravoxel incoherent motions: application to diffusion and perfusion in neurologic disorders." Radiology **161**(2): 401-407.
111. Le Bihan, D., J. F. Mangin, et al. (2001). "Diffusion tensor imaging: concepts and applications." J Magn Reson Imaging **13**(4): 534-546.
112. Lenglet, C. (2006). Geometric and Variational Methods for Diffusion Tensor MRI Processing. PhD, University Nice Sophia-Antipolis.
113. Leow, A. D., S. Zhu, et al. (2009). "The tensor distribution function." Magn Reson Med **61**(1): 205-214.
114. Liu, C., R. Bammer, et al. (2004). "Characterizing non-gaussian diffusion by using generalized diffusion tensors." Magnetic Resonance in Medicine **51**(5): 924-937.
115. Liu, Y., M. Liang, et al. (2008). "Disrupted small-world networks in schizophrenia." Brain **131**(Pt 4): 945-961.
116. Lou, H. C., B. Luber, et al. (2004). "Parietal cortex and representation of the mental Self." Proc Natl Acad Sci U S A **101**(17): 6827-6832.
117. Lusseau, D., K. Schneider, et al. (2003). "The Bottlenose Dolphin Community of Doubtful Sound Features a Large Proportion of Long-Lasting Associations: Can Geographic Isolation Explain This Unique Trait?" Behavioral Ecology and Sociobiology **54**(4): 396-405.
118. Lynall, M. E., D. S. Bassett, et al. (2010). "Functional connectivity and brain networks in schizophrenia." J Neurosci **30**(28): 9477-9487.
119. Magin, R. L., O. Abdullah, et al. (2008). "Anomalous diffusion expressed through fractional order differential operators in the Bloch-Torrey equation." Journal of Magnetic Resonance **190**(2): 255-270.
120. Magin, R. L., B. S. Akpa, et al. (2011). "Fractional Order Analysis of Sephadex Gel Structures: NMR Measurements Reflecting Anomalous Diffusion." Commun Nonlinear Sci Numer Simul **16**(12): 4581-4587.

CITED LITERATURE (continued)

121. Magin, R. L., J. J. GadElkarim, et al. (2013). An Anisotropic Fractional Order Model of Anomalous Diffusion. International Society for Magnetic Resonance in Medicine ISMRM, Croatia.
122. Mahon, K., K. E. Burdick, et al. (2010). "A role for white matter abnormalities in the pathophysiology of bipolar disorder." Neurosci Biobehav Rev **34**(4): 533-554.
123. Maier, S. E., S. Vajapeyam, et al. (2004). "Biexponential diffusion tensor analysis of human brain diffusion data." Magn Reson Med **51**(2): 321-330.
124. Mandelbrot, B. B. (1982). The fractal geometry of nature. San Francisco, W.H. Freeman.
125. Massen, C. P. and J. P. K. Doye (2005). "Identifying communities within energy landscapes." Physical Review E **71**(4).
126. Medus, A., G. Acuna, et al. (2005). "Detection of community structures in networks via global optimization." Physica a-Statistical Mechanics and Its Applications **358**(2-4): 593-604.
127. Meerschaert Mark, M. and A. Sikorskii (2011). Stochastic Models for Fractional Calculus. Berlin, Boston, De Gruyter.
128. Meerschaert, M. M., J. Mortensen, et al. (2006). "Fractional vector calculus for fractional advection–dispersion." Physica A: Statistical Mechanics and its Applications **367**(0): 181-190.
129. Mei, J., S. He, et al. (2009). "Revealing network communities through modularity maximization by a contraction-dilation method." New J Phys **11**.
130. Metzler, R. (2000). "Generalized chapman-kolmogorov equation: A unifying approach to the description of anomalous transport in external fields." Phys Rev E Stat Phys Plasmas Fluids Relat Interdiscip Topics **62**(5 Pt A): 6233-6245.
131. Metzler, R. and J. Klafter (2000). "The random walk's guide to anomalous diffusion: a fractional dynamics approach." Physics Reports **339**(1): 1-77.
132. Meunier, D., S. Achard, et al. (2009). "Age-related changes in modular organization of human brain functional networks." Neuroimage **44**(3): 715-723.
133. Montroll, E. W. and G. H. Weiss (1965). "Random Walks on Lattices. II." Journal of Mathematical Physics **6**(2): 167-181.
134. Mori, S. and P. B. Barker (1999). "Diffusion magnetic resonance imaging: its principles and applications." Anat Rec B New Anat **257**(3): 102–109.
135. Mori, S., B. J. Crain, et al. (1999). "Three-dimensional tracking of axonal projections in the brain by magnetic resonance imaging." Annals of Neurology **45**(2): 5.
136. Mori, S., B. J. Crain, et al. (1998). "3D brain fiber reconstruction from diffusion MRI." International Conference on Functional Mapping of the Human Brain.
137. Mori, S. and P. C. van Zijl (2002). "Fiber tracking: principles and strategies - a technical review." NMR Biomed **15**(7-8): 468-480.
138. Moseley, M. E., Y. Cohen, et al. (1990). "Diffusion-weighted MR imaging of anisotropic water diffusion in cat central nervous system." Radiology **176**(2): 439-445.
139. Mulkern, R. V., H. P. Zengingonul, et al. (2000). "Multi-component apparent diffusion coefficients in human brain: relationship to spin-lattice relaxation." Magn Reson Med **44**(2): 292-300.
140. Neuman, C. H. (1974). "Spin-Echo of Spins Diffusing in a Bounded Medium." Journal of Chemical Physics **60**(11): 4508-4511.
141. Newman, M. E. (2004). "Fast algorithm for detecting community structure in networks." Phys Rev E Stat Nonlin Soft Matter Phys **69**(6 Pt 2): 066133.
142. Newman, M. E. and M. Girvan (2004). "Finding and evaluating community structure in networks." Phys Rev E Stat Nonlin Soft Matter Phys **69**(2 Pt 2): 026113.
143. Newman, M. E. J. (2003). "The structure and function of complex networks." Siam Review **45**(2): 167-256.
144. Newman, M. E. J. (2006). "Modularity and community structure in networks." Proc Natl Acad Sci U S A **103**(23): 8577-8582.
145. Noack, A. and R. Rotta (2009). Multi-level Algorithms for Modularity Clustering. Proceedings of the 8th International Symposium on Experimental Algorithms. Dortmund, Germany, Springer-Verlag: 257-268.

CITED LITERATURE (continued)

146. Onnela, J.-P., J. Saramäki, et al. (2005). "Intensity and coherence of motifs in weighted complex networks." Physical Review E **71**(6): 065103.
147. Ozarslan, E., P. J. Basser, et al. (2006). "Observation of anomalous diffusion in excised tissue by characterizing the diffusion-time dependence of the MR signal." J Magn Reson **183**(2): 315-323.
148. Ozarslan, E. and T. H. Mareci (2003). "Generalized diffusion tensor imaging and analytical relationships between diffusion tensor imaging and high angular resolution diffusion imaging." Magn Reson Med **50**(5): 955-965.
149. Ozarslan, E., T. M. Shepherd, et al. (2012). "Temporal scaling characteristics of diffusion as a new MRI contrast: findings in rat hippocampus." Neuroimage **60**(2): 1380-1393.
150. Özarslan, E., T. M. Shepherd, et al. (2006). "Resolution of complex tissue microarchitecture using the diffusion orientation transform (DOT)." Neuroimage **31**(3): 1086-1103.
151. Palombo, M., A. Gabrielli, et al. (2011). "Spatio-temporal anomalous diffusion in heterogeneous media by nuclear magnetic resonance." J Chem Phys **135**(3): 034504.
152. Palombo, M., A. Gabrielli, et al. (2012). "The gamma parameter of the stretched-exponential model is influenced by internal gradients: validation in phantoms." J Magn Reson **216**: 28-36.
153. Parker, G. J. and D. C. Alexander (2003). "Probabilistic Monte Carlo based mapping of cerebral connections utilising whole-brain crossing fibre information." Inf Process Med Imaging **18**: 684-695.
154. Parker, G. J. and D. C. Alexander (2005). "Probabilistic anatomical connectivity derived from the microscopic persistent angular structure of cerebral tissue." Philos Trans R Soc Lond B Biol Sci **360**(1457): 893-902.
155. Pearson, K. (1905). "The Problem of the Random Walk." Nature **72**(1867): 342-342.
156. Peled, S., O. Friman, et al. (2006). "Geometrically constrained two-tensor model for crossing tracts in DWI." Magn Reson Imaging **24**(9): 1263-1270.
157. Perrin, M., C. Poupon, et al. (2005). "Fiber tracking in q-ball fields using regularized particle trajectories." Inf Process Med Imaging **19**: 52-63.
158. Podlubny, I. (1999). Fractional Differential Equations: An Introduction to Fractional Derivatives, Fractional Differential Equations, Some Methods of Their Solution and Some of Their Applications. San Diego-Boston-New York-London-Tokyo-Toronto, Academic Press.
159. Poupon, C. (1999). Détection des faisceaux de fibres de la substance blanche pour l'étude de la connectivité anatomique cérébrale. PhD, Ecole Nationale Supérieure des Télécommunications.
160. Power, J. D., A. L. Cohen, et al. (2011). "Functional network organization of the human brain." Neuron **72**(4): 665-678.
161. Pujol, J. M., J. Béjar, et al. (2006). "Clustering algorithm for determining community structure in large networks." Physical Review E **74**(1): 016107.
162. Purcell, E. M., H. C. Torrey, et al. (1946). "Resonance Absorption by Nuclear Magnetic Moments in a Solid." Physical Review **69**(1-2): 37-38.
163. Rabi, I., J. R. Zacharias, et al. (1992). "Milestones in magnetic resonance: 'a new method of measuring nuclear magnetic moment'. 1938." J Magn Reson Imaging **2**(2): 131-133.
164. Ramirez-Manzanares, A., M. Rivera, et al. (2007). "Diffusion basis functions decomposition for estimating white matter intravoxel fiber geometry." IEEE Trans Med Imaging **26**(8): 1091-1102.
165. Rattigan, M. J., M. Maier, et al. (2007). Graph clustering with network structure indices. Proceedings of the 24th international conference on Machine learning. Corvalis, Oregon, ACM: 783-790.
166. Richardson, T., P. J. Mucha, et al. (2009). "Spectral tripartitioning of networks." Physical Review E **80**(3).
167. Ruan, J. and W. Zhang (2007). An Efficient Spectral Algorithm for Network Community Discovery and Its Applications to Biological and Social Networks. Proceedings of the 2007 Seventh IEEE International Conference on Data Mining, IEEE Computer Society: 643-648.
168. Rubinov, M. and O. Sporns (2010). "Complex network measures of brain connectivity: uses and interpretations." Neuroimage **52**(3): 1059-1069.

CITED LITERATURE (continued)

169. Sato, K.-i. (1999). Lévy processes and infinitely divisible distributions. Cambridge, U.K. ; New York, Cambridge University Press.
170. Savadjiev, P., J. S. W. Campbell, et al. (2007). "Disambiguation of Complex Subvoxel Fibre Configurations in High Angular Resolution Fibre Tractography." Joint Annual Meeting ISMRM-ESMRMB: 1477.
171. Schuetz, P. and A. Caflisch (2008). "Efficient modularity optimization by multistep greedy algorithm and vertex mover refinement." Physical Review E **77**(4): 046112.
172. Schuetz, P. and A. Caflisch (2008). "Multistep greedy algorithm identifies community structure in real-world and computer-generated networks." Physical Review E **78**(2): 026112.
173. Schumer, R., M. M. Meerschaert, et al. (2009). "Fractional advection-dispersion equations for modeling transport at the Earth surface." Journal of Geophysical Research-Earth Surface **114**.
174. Seunarine, K. K. and D. C. Alexander (2006). "Linear Persistent Angular Structure MRI and non-linear Spherical Deconvolution for Diffusion MRI." International Society for Magnetic Resonance in Medicine: 2726.
175. Smith, T. G., Jr., T. N. Behar, et al. (1991). "A fractal analysis of cultured rat optic nerve glial growth and differentiation." Neuroscience **41**(1): 159-166.
176. Sporns, O., G. Tononi, et al. (2005). "The human connectome: A structural description of the human brain." PLoS Comput Biol **1**(4): e42.
177. Sporns, O. and J. D. Zwi (2004). "The small world of the cerebral cortex." Neuroinformatics **2**(2): 145-162.
178. Steen, M., S. Hayasaka, et al. (2011). "Assessing the consistency of community structure in complex networks." Phys Rev E Stat Nonlin Soft Matter Phys **84**(1 Pt 2): 016111.
179. Stejskal, E. O. (1965). "Use of Spin Echoes in a Pulsed Magnetic-Field Gradient to Study Anisotropic, Restricted Diffusion and Flow." J Chem Phys **43**(10): 3597-3603.
180. Stejskal, E. O. and J. E. Tanner (1965). "Spin Diffusion Measurements: Spin Echoes in the Presence of a Time-Dependent Field Gradient." J Chem Phys **42**(1): 288-292.
181. Sun, Y., B. Danila, et al. (2009). "Improved community structure detection using a modified fine-tuning strategy." Epl **86**(2).
182. Sussmann, J. E., G. K. Lymer, et al. (2009). "White matter abnormalities in bipolar disorder and schizophrenia detected using diffusion tensor magnetic resonance imaging." Bipolar Disord **11**(1): 11-18.
183. Taylor, D. G. and M. C. Bushell (1985). "The spatial mapping of translational diffusion coefficients by the NMR imaging technique." Phys Med Biol **30**(4): 345-349.
184. Torrey, H. C. (1956). "Bloch Equations with Diffusion Terms." Physical Review **104**(3): 563-565.
185. Tournier, J. D., F. Calamante, et al. (2004). "Direct estimation of the fiber orientation density function from diffusion-weighted MRI data using spherical deconvolution." Neuroimage **23**(3): 1176-1185.
186. Tuch, D. (2002). Diffusion MRI of Complex Tissue Structure, Harvard University and Massachusetts Institute of Technology.
187. Tuch, D., J. Belliveau, et al. (1999). "High Angular Resolution Imaging of the Human Brain." Proceedings of the International Society for the Magnetic Resonance in Medicine: 321.
188. Tuch, D. S. (2004). "Q-ball imaging." Magn Reson Med **52**(6): 1358-1372.
189. Tuch, D. S., T. G. Reese, et al. (2002). "High angular resolution diffusion imaging reveals intravoxel white matter fiber heterogeneity." Magn Reson Med **48**(4): 577-582.
190. Tyler, J. R., D. M. Wilkinson, et al. (2003). Email as spectroscopy: automated discovery of community structure within organizations. Communities and technologies, Kluwer, B.V.: 81-96.
191. Tzourio-Mazoyer, N., B. Landeau, et al. (2002). "Automated Anatomical Labeling of Activations in SPM Using a Macroscopic Anatomical Parcellation of the MNI MRI Single-Subject Brain." Neuroimage **15**(1): 273-289.
192. van den Heuvel, M. P., R. C. Mandl, et al. (2010). "Aberrant frontal and temporal complex network structure in schizophrenia: a graph theoretical analysis." J Neurosci **30**(47): 15915-15926.

CITED LITERATURE (continued)

193. Wakita, K. and T. Tsurumi (2007). Finding community structure in mega-scale social networks: [extended abstract]. Proceedings of the 16th international conference on World Wide Web. Banff, Alberta, Canada, ACM: 1275-1276.
194. Walterfang, M., A. G. Wood, et al. (2009). "Corpus callosum size and shape alterations in individuals with bipolar disorder and their first-degree relatives." Prog Neuropsychopharmacol Biol Psychiatry **33**(6): 1050-1057.
195. Wang, F., M. Jackowski, et al. (2008). "Abnormal anterior cingulum integrity in bipolar disorder determined through diffusion tensor imaging." Br J Psychiatry **193**(2): 126-129.
196. Wang, G. X., Y. Shen, et al. (2008). "A vector partitioning approach to detecting community structure in complex networks." Computers & Mathematics with Applications **55**(12): 2746-2752.
197. Watts, D. J. and S. H. Strogatz (1998). "Collective dynamics of 'small-world' networks." Nature **393**(6684): 440-442.
198. Wedeen, V., T. Reese, et al. (2000). "Mapping fiber orientation spectra in cerebral white matter with Fourier transform diffusion MRI." Proc. of the ISMRM: 82-82.
199. Westin, C. F., S. E. Maier, et al. (2002). "Processing and visualization for diffusion tensor MRI." Med Image Anal **6**(2): 93-108.
200. White, S. and P. Smyth (2003). Algorithms for estimating relative importance in networks. Proceedings of the ninth ACM SIGKDD international conference on Knowledge discovery and data mining. Washington, D.C., ACM: 266-275.
201. Wilkinson, D. M. and B. A. Huberman (2004). "A method for finding communities of related genes." Proc Natl Acad Sci U S A **101**(Suppl 1): 5241-5248.
202. Xiang, B., E.-H. Chen, et al. (2009). Finding Community Structure Based on Subgraph Similarity Complex Networks. S. Fortunato, G. Mangioni, R. Menezes and V. Nicosia, Springer Berlin / Heidelberg. **207**: 73-81.
203. Ye, Z., S. Hu, et al. (2008). "Adaptive clustering algorithm for community detection in complex networks." Physical Review E **78**(4): 046115.
204. Yi-Ping, C., Y. Chia-Yen, et al. (2007). Probabilistic Anatomical Connection Derived from QBI with MFACT Approach. Noninvasive Functional Source Imaging of the Brain and Heart and the International Conference on Functional Biomedical Imaging, 2007. NFSI-ICFBI 2007. Joint Meeting of the 6th International Symposium on.
205. Yu, Q., F. Liu, et al. (2011). Analytical and numerical solutions of the space and time fractional bloch-torrey equation. Proceedings of the ASME 2011 International Design Engineering Technical Conferences & Computers and Information in Engineering Conference. N. Jalili. Chicago, Illinois, Elsevier. **3**: 1-10.
206. Yunmei, C., G. Weihong, et al. (2004). "Recovery of intra-voxel structure from HARD DWI." ISBI 2004. **1**: 1028-1031.
207. Zachary, W. W. (1977). "An Information Flow Model for Conflict and Fission in Small Groups." Journal of Anthropological Research **33**(4): 452-473.
208. Zhan, L., A. D. Leow, et al. (2009). "A novel measure of fractional anisotropy based on the tensor distribution function." Med Image Comput Comput Assist Interv **12**(Pt 1): 845-852.
209. Zhan, W., H. Gu, et al. (2003). "Circular spectrum mapping for intravoxel fiber structures based on high angular resolution apparent diffusion coefficients." Magn Reson Med **49**(6): 1077-1088.
210. Zhang, F., E. R. Hancock, et al. (2009). "Probabilistic white matter fiber tracking using particle filtering and von Mises-Fisher sampling." Med Image Anal **13**(1): 5-18.
211. Zhou, X. J., Q. Gao, et al. (2010). "Studies of anomalous diffusion in the human brain using fractional order calculus." Magn Reson Med **63**(3): 562-569.
212. Zhu, X., X. Wang, et al. (2012). "Evidence of a dissociation pattern in resting-state default mode network connectivity in first-episode, treatment-naïve major depression patients." Biol Psychiatry **71**(7): 611-617.
213. Zuo, X. N., R. Ehmke, et al. (2012). "Network centrality in the human functional connectome." Cereb Cortex **22**(8): 1862-1875.

VITA

NAME: Johnson Jonaris GadElkarim

EDUCATION: B.S., Electronics & communications Engineering, Cairo University, Egypt, 2004
M.S., Electrical & Computer Engineering, University of Illinois at Chicago, Chicago, Illinois, 2013

TEACHING: Department of Electrical and Computer Engineering (ECE), University Of Illinois at Chicago, Chicago, Illinois, Teaching Assistant 2009 – 2010

HONORS: Graduate College Full Tuition Fee Waiver, UIC, Fall 2011, Fall 2012
Graduate Travel Award, UIC, 2011
Graduate Student Travel Award, MICCAI 2012

PROFESSIONAL MEMBERSHIP: Institute of Electrical and Electronics Engineers, IEEE

ABSTRACTS: Arienzo D, Brown J, Zhan L, GadElkarim J, Leow A, Feusner JD. ‘Structural brain network analysis in body dysmorphic disorder and its relationship to global and local information processing’. International Obsessive Compulsive Foundation Conference, 2010.
Johnson J. GadElkarim, Dan Schonfeld, Olu Adjilore, Jamie Feusner, Donatello Arienzo, Liang Zhan, Anand Kumar, Paul M. Thompson, Alex D. Leow, ‘Human brain binary tree partitioning using simulated annealing, Human Brain Mapping’, Organization for Human Brain Mapping, OHBM, China 2012.
R. L. Magin, J.J. Gadelkarim, and A.D. Leow, ‘Fractional Calculus Models for Diffusion Tensor Imaging’, Interpore, Indiana, USA 2012.
Richard L. Magin, Johnson J. GadElkarim, Alex D. Leow, Shaolin Yang, Mark M. Meerschaert, and Andrzej Hanyga, ‘An Anisotropic Fractional Order Model of Anomalous Diffusion’, Proceedings of International Society for Magnetic Resonance in Medicine ISMRM, Croatia, 2013.

PUBLICATIONS: GadElkarim, J. J., Zhan, L. ; Yang, S.L. ; Zhang, A.F. ; Altshuler, L. ; Lamar, M. ; Ajilore, O. ; Thompson, P.M. ; Kumar, A. ; Leow, A.: ‘TDF-TRACT: probabilistic tractography using the Tensor Distribution Function’, International Symposium of Biomedical Imaging, ISBI 2011.
Alex Leow, Liang Zhan, Olusola Ajilore, Johnson GadElkarim, Aifeng Zhang, Donatello Arienzo, Teena Moody, Jamie Feusner, Anand Kumar, Paul Thompson, Lori Altshuler, ‘Measuring inter-hemispheric integration in bipolar affective disorder using brain network analysis and HARDI’, International Symposium of Biomedical Imaging, ISBI 2012.

VITA (continued)

Johnson GadElkarim, Dan Schonfeld, Olu Ajilore, Liang Zhang, Jamie Feusner, Aifeng Zhang, Paul Thompson, Tony Simon, Anand Kumar, and Alex Leow. 'A Framework for Detecting Community Structure Group Differences in Brain Connectivity Networks', Medical Image Computing and Computer Assisted Intervention, MICCAI, LCNS, Vol. 7511, p 193-200, 2012.

Leow AD, Zhan L, Arienzo D, GadElkarim JJ, Zhang AF, Ajilore O, Kumar A, Thompson PM, Feusner JD. 'Hierarchical structural mapping for globally optimized estimation of functional networks' Medical Image Computing and Computer Assisted Intervention, MICCAI 2012, LCNS, Vol. 7511, p 228-236.

Won Hwa Kim, Nagesh Adluru, Moo K. Chung, Anand Kumar, Lori Altshuler, Teena Moody, Johnson GadElkarim, Vikas Singh, Alex Leow, 'Multi-resolutional Brain Network Filtering and Analysis via Wavelets on Non-Euclidean Space', Medical Image Computing and Computer Assisted Intervention , MICCAI 2013.

Zhang A, Ajilore O, Zhan L, Gadelkarim J, Korthauer L, Yang S, Leow A, Kumar A., 'White Matter Tract Integrity of Anterior Limb of Internal Capsule in Major Depression and Type 2 Diabetes.' Neuropsychopharmacology. Vol. 38, pp. 1451-1459, February 2013.

Feusner JD, Arienzo D, Li W, Zhan L, GadElkarim J, Thompson P, Leow A. 'White matter microstructure in body dysmorphic disorder and its clinical correlates', NeuroImage, Vol. 211(2) , pp. 132-140, February 2013.

Leow A, Ajilore O, Zhan L, Arienzo D, Gadelkarim J, Zhang A, Moody T, Van Horn J, Feusner J, Kumar A, Thompson P, Altshuler L. 'Impaired Inter-Hemispheric Integration in Bipolar Disorder Revealed with Brain Network Analyses.' Biol Psychiatry, Vol. 73(2), pp. 183-193 (2013).

Arienzo D, Leow A, Brown JA, Zhan L, Gadelkarim J, Hovav S, Feusner JD. 'Abnormal brain network organization in body dysmorphic disorder.' Neuropsychopharmacology. Vol. 38, pp. 1130-1139, (2013).

Johnson GadElkarim, Olu Ajilore, Dan Schonfeld, Liang Zhang, Paul Thompson, Jamie Feusner, Anand Kumar, Lori Altshuler, and Alex Leow. 'Investigating brain community structure abnormalities in bipolar disorder using PLACE (Path Length Associated Community Estimation).' Human Brain Mapping, 2013 Jun 25:0. doi: 10.1002/hbm.22324. (In Press).

Johnson GadElkarim, Richard Magin, Mark M. Meerschaert, Silvia Capuani, Marco Palombo, and Alex Leow. 'Fractional order generalization of anomalous diffusion as a multidimensional extension of the transmission line equation.' IEEE Journal on Emerging and Selected Topics in Circuits and Systems, Vol 3(3), pp. 432-441, (2013) .